RHEOLOGY AND DEPOSITION OF HETEROGENEOUS ORGANIC MIXTURES:

AN EXPANSION OF "COLD FLOW" RESEARCH

by

Mark Ryan Jemmett

A dissertation submitted to the faculty of
The University of Utah
in partial fulfillment of the requirements for the degree of

Doctor of Philosophy

Department of Chemical Engineering

The University of Utah

December 2012

The University of Utah Graduate School

STATEMENT OF DISSERTATION APPROVAL

The dissertation of Mark Ryan Jemmett

has been approved by the following supervisory committee members:

Milind D. Deo	, Chair	August 23, 2012 Date Approved
Jules J. Magda	, Member	August 23, 2012 Date Approved
Richard Roehner	, Member	August 23, 2012 Date Approved
John D. McLennan	, Member	August 23, 2012 Date Approved
Raj K. Rajamani	, Member	August 23, 2012 Date Approved

and by JoAnn S. Lighty , Chair of the Department of Chemical Engineering

and by Charles A. Wight, Dean of The Graduate School.

ABSTRACT

The study of the rheological properties and deposition potential of organic mixtures such as petroleum are explored below the initial wax appearance temperature using a recycled flow loop, an active slurry-making device called the Scraped Exchanger, and a model oil made with mineral oil, paraffin wax, and LVGO wax. Sub-WAT (heterogeneous) oils, when flowed under isothermal (ambient and oil temperatures are the same) and non-isothermal conditions exhibit no deposition and greatly reduced deposition when compared to similar thermal gradients in above-WAT (homogeneous) oils, respectively. Heterogeneous oils form gels during shutdown just as with homogeneous oils, but the gel strength is greatly reduced (>50%) even with very little precipitated material (oil temperature at shutdown just below WAT). Solids content at shutdown appears to show little effect on subsequent gel strength. Particle size distributions measured using CantyVision equipment at shutdown also show little to no effect on subsequent gel strength, suggesting a balance between particle size and particle count, as well as a fundamental difference in gel matrix structure compared to homogeneous gels. In the ranges tested, all heterogeneous gels exhibited cohesive ("center-core") failure manifested as breakage occurring first within the gel instead of at the walls. Breakage patterns explored using laser particle imaging velocimetry.

TABLE OF CONTENTS

LIST OF TABLES

PREFACE

Every modicum of scientific insight is important. Even a small advance or finding in an existing field of thought is of value; without the tiny individual, insignificant piece the larger puzzle is incomplete. These findings represent an area of research that has not been conducted before and therefore provide a bigger picture, a more expanded knowledge base, and a more thorough look at processes that are, for the most part, still poorly understood.

From a personal standpoint, the results and findings of this research are more than just a novel look at an unknown aspect of petroleum science – they are absolutely necessary in the pursuit of quality models and predictions for gelled restart and deposition reduction. If one does not observe the complete picture with both "Hot" and "Cold Flows" (since both exist in basically every waxy oil pipeline), then one cannot possibly hope to obtain a complete theory and model of the behavior in said pipeline. It is with that thought that I present this dissertation, the Rheology and Deposition of Heterogeneous Organic Mixtures: An Expansion of "Cold Flow" Research.

The author would like to personally thank the following for their help with this research: Milind Deo, for giving me this opportunity and constantly giving me chances to excel; Rich Roehner, for keeping me excited with new ideas and innovations; Jaye Magda, for questioning everything; John McLennan, for combing

over this dissertation with a microscope; Raj Rajamani, for being there for me in my hour of need; David Wagner, for his wisdom and skill in the development of the flow loops and Scraped Exchanger; Hyun Lee, of ConocoPhillips, for his assistance with the design of the Scraped Exchanger; Husam El-Gendy, for his support and help with Particle Imaging Velocimetry; Pal Toth, for his help with Particle Imaging Velocimetry; Jessica Earl, for her help with FTIR analysis; Ahmed Elmadhoun, for his tenacity and support of the equipment, namely the CantyVision system; J.M. Canty for their generosity regarding the CantyVision InFlow® system; RPSEA, for the funding for the development of the flow loops; ConocoPhillips, for their offering of an internship and fellowship; Alicia Jemmett, for her constant love and support through this entire process; Kyeongseok Oh, for teaching me flow assurance; Dave Johnson, for convincing me to take this path; and of course Ed and Linda Jemmett, for insisting I do something with my life.

CHAPTER 1

INTRODUCTION TO FLOW ASSURANCE

Petroleum is arguably the most important chemical mixture in the lives of modern humanity. Plastics, energy, pharmaceuticals, clothing, and even food creation and storage rely heavily upon the steady supply and acquisition of petroleum. Disruptions in this supply can cause food shortages, energy shortages, and subsequent increases in prices for practically all industries. Ensuring a stable supply is therefore a priority in petroleum-based companies and, unfortunately, supply issues arise often.

1.1 What Is Oil?

Oil or petroleum is made up of thousands of individual components, and every petroleum source gives a different composition depending on the source materials (biomaterial),[1] ambient temperatures, and ambient pressures surrounding the developing deposits.[2] In general, a major portion of components in petroleum is methane (CH_4) and normal and branched alkanes ranging from ethane (C_2H_6) to C_{60} and beyond. With these alkanes, a term called "carbon number" is used to quickly identify components; for example, carbon number 4 refers to n- and iso-butane (C_4H_{10}) while carbon number 20 refers to n-eicosane ($C_{20}H_{42}$) and its various

isomers. As a general convention, alkanes of carbon number 19 (20 by some sources[3,4]) and higher are called "waxes" (the term "paraffin", while fairly broad its definitions, it often used synonymously with "wax"). In the context of this research, waxes are typically defined as alkanes that precipitate at 0 °C and 14.7 psia, though, of course, non-wax material can and will precipitate at lower temperatures than this. Using gas chromatography,[5-8] one can get a very good (but not complete) estimate of the components inside an oil, such as the examples provided in Figures 1.1 and 1.2.

In Figures 1.1 and 1.2, each of the peaks represents a molecular weight that enters the spectrometer after a specific amount of time after insertion into the chromatography line. These peaks and their times can then be identified using known standards, thereby allowing for estimation of actual composition, and with careful integration weight percents can be obtained.

In addition to alkanes, numerous unsaturated carbon compounds (those containing double covalent bonds), aliphatic and aromatic ringed structures, napthenes (other cyclic structures), and metal-, nitrogen-, and sulfur-containing carbon compounds exist in the various oils found around the world.[9,10] The preponderance of the various components is heavily influenced by the type of source biomaterial (cellulose, fatty acids, cellular structure, mitochondria, chloroplasts, etc.).[1,10]

1.2 How Is Oil Transported?

Once produced from a well oil needs to be transported to a refining facility. While multiple avenues such as shipping by boat (if offshore), train or tanker truck exist and are used frequently, these tend to be expensive and low capacity (relatively speaking). Shipping by in-place, long distance pipelines is ideal, particularly offshore. These pipelines on both land and sea involve tiebacks, which connect the wells to a central pumping-processing station, and a transit line from the station to the refiner; as expected, these pipelines can be exceptionally long. Naturally, each oil company guards their setup closely; Figure 1.3 is simply a generalization of a deepwater production system.

1.3 Flow Assurance

To flow through a long pipeline, it is important to take account of viscosity (measure of a fluid's resistance to flow), acidity, and salt content (particularly in offshore wells) as all of these factors can affect pipeline capacity (typically measured in barrels of oil per day, in which a barrel is 42 US gallons). Ensuring a constant flow of oil despite the many implications these factors can cause is known as Flow Assurance. While Flow Assurance consists of a spectrum of issues, all of which are, ultimately, related and commonly occur simultaneously, there are four main focuses: corrosion, salts, asphaltenes, and waxes.

1.3.1 Corrosion, Salt, and Asphaltene Flow Issues

Oil, even deep in the well and reservoir, is rarely a sterile, pure fluid. SRBs (sulfur-reducing bacteria), sour gas (H_2S, also from SRBs), and seawater (in oceanic wells) can and do find their way into the lines, and once there can cause serious issues.

Acidification of the oil through sour gas and other reductions can directly corrode the pipeline walls, these being made of stainless steel (very resistant to oxidation, but weak to acidity). Corroded pipelines can develop complete perforations, through which oil can be lost and environmental problems can potentially occur.

Salt from seawater can also cause serious flow issues by crystallizing on the walls and cutting off flow. These salt deposits are hard and difficult to break without chemical intervention, but usually the formation of such deposits dooms the pipeline.

Asphaltenes, large, complex carbon-based molecules characterized by groups of interconnected aromatic rings, can cause flow issues, particularly in the wellhead itself as well as in the refinery lines. While fairly well characterized, asphaltene solubility and precipitation is still a subject of considerable research.

For these flow assurance issues, this dissertation only provides a very brief description as shown here, as they are not an integral part of the research. To learn more of these issues, a plethora of literature is available.

1.3.2 Wax-Related Flow Issues

The fourth estate of flow assurance is wax, and this research focuses completely upon the corresponding issues, namely wax deposition during normal operation and, to a greater degree in this research, wax gelation during shutdown. These issues are very costly to prevent and remediate; as such, substantial effort is given industrially and academically to discover more and better ways to deal with waxes.

1.3.3 Important Parameters Regarding Waxes

With regard to wax studies, there are two key parameters that need to be known prior to any other: initial wax appearance temperature and the gel point (or pour point). In addition, it is important, though not to the same degree, to know the solubility of the waxes in the liquid phase with regard to temperature.

1.3.3.1 Initial Wax Appearance Temperature

As mentioned earlier, petroleum oils are a blend of many different components. Alkanes of carbon number 19 and higher, considered generally as waxes, exhibit varied solubility effects depending on concentrations of each carbon number as well as interactions with other components such as asphaltenes.[11,12] The temperature at a given pressure at which the first components come out of solution via precipitation is called the initial wax appearance temperature, or WAT.

WAT is measured using a variety of methods, each with strengths and weaknesses though none being perfect or exact. The fastest method is a simple

visual test outlined in ASTM D2500. This method gives quick results, but the accuracy is suspect due to temperature inconsistencies within the setup. Figure 1.4 provides an artistic representation of the ASTM method (modified slightly to better fit this research). A sample contained in a glass beaker is warmed until the user is confident no solid wax is left, then inserted into a pre-cooled cell where the sample's temperature will drop. Temperature is monitored using a thermometer, and at desired temperature increments (3-4 degrees) the sample is checked for cloudiness. Once cloudiness is found, the test is repeated, though now the temperature increments are smaller. Typically, two to three tests should give the WAT estimate (or one if the operator is obsessive and checks at every degree). Unfortunately, this method is only applicable to transparent oils.

Another method to determine WAT is cross-polarized microscopy, or CPM.[13,14] This method takes advantage of the reflective nature of wax crystal surfaces; as polarized light comes into contact with the wax surface, it is redirected away from the polarized field. The result is bright wax crystals appearing in a darkened field (this is very similar to how the CantyVision InFlow® system works – see section 2.4.3.1). CPM gives fairly accurate, highly repeatable results, but takes a very long time to run (in excess of 24 hours) to alleviate supersaturation issues as much as possible (these issues are still unavoidable to a degree). Furthermore, sample creation is a source of error, as oil must be drawn into a micropipette. Unfortunately for this study, CPM (the most visually entertaining of the methods) was not available.

In addition to some rheometric methods, Roehner and Hanson developed a repeatable and relatively swift method using Fourier-Transform Infrared (FTIR) spectroscopy in 2001.[15] This method, which was used as the primary determination test in this research, operates under the assumption that, as waxes come out of solution, peaks on the FTIR curve will deviate from the linearly trending changes due to density variance.

According to Roehner and Hanson,[15] in a single phase undergoing temperature (and thus density) changes, the absorption of all FTIR signals will change uniformly and linearly. At the moment solid particles appear, these particles will increase the absorbance of IR wavelengths. By calculating the integral area beneath the FTIR curves and a blank control at multiple temperatures and linearly interpolating the two slopes, the WAT can be determined within +/- 0.5 °C, a reasonable error. Figures 1.5 and 1.6 graphically detail the FTIR-WAT measurement process.

Of course, it is best to use multiple methods to validate the results of any test. The ASTM method was used to provide a "ballpark" guess, FTIR was used to determine actual WAT, and rheological and differential scanning calorimetry (see section 1.3.3.3) methods were used to back up the FTIR results; these results are presented in section 2.1 on Model Oil Development.

It should be noted at this point that wax appearance temperatures typically refer to the initial point at which solubility occurs. In reality, waxes appear at a spectrum of temperatures,[16] but it is fallacious to assume that a single component will completely precipitate out of solution at a single temperature. The interaction of

dissolved components is quite complex, and, naturally, is highly variant from blend to blend.

1.3.3.2 Gel Point / Pour Point

As wax continues to come out of solution with decreasing temperature, the crystals formed via precipitation grow larger and larger. At a certain temperature these crystals begin to interact – literally growing into one another, forming a rudimentary matrix of crystals. The point at which this interaction occurs is known as the gel point.[17,18]

In petroleum studies, another term, the pour point (ASTM D97-11), is often used interchangeably with gel point, but this usage is incorrect. Pour point is the specific temperature at which the gel can resist flowing under gravitational stresses. As one would expect, pour point is a lower temperature than gel point for basically all oils, though the difference between the two can be so small as to not be detectable.

In this research, gel point is given consideration as the author feels it is more important in gelled restart research. However, pour point testing, as will be shortly explained, is not without purpose as it serves as an excellent validation tool for gel point measurement, particularly with model oils (see the second chapter for an explanation on model oils).

Gel point can be measured using a variety of means, though none exhibits any particular superiority. Two means used in this research to measure gel point were crossover method[18] using cone-and-plate rheology and flow loop rheology.

Using a standard cone-and-plate rheometer, a sample of oil can be cooled using a controlled, quantified rate under very gentle oscillatory stress. This means that, at the sample cools down, the cone is oscillated back and forth at a stress low enough to provide minimal impedance to natural gel formation, all the while the storage and loss moduli are measured from the resistance provided by the oil.[18] As the gel takes form, the storage modulus (a measure of negative response to motion, or resistance to flow under stress via elasticity) will start to increase, and as a gel completely forms it will exceed the loss modulus (a measure of positive response to motion, or yielding to flow under stress via viscosity). Figure 1.7 provides an example of this transition using the rheometer used in this study. The crossover point method of finding gel point is quite good, but with most tests it is wise to have a backup method to verify results.

One alternate means of measuring gel point devised by the author involves using a flow loop setup. As will be explained further along in this thesis, a recycled flow loop was built and used to study deposition and gelled restart of a model oil. By preparing the oil to be above WAT at shutdown (pumps shut off, fluid entrained in pressure-controlled test section) and subsequently forming a gel under the same cooling rate conditions as in the rheometer, a three-dimensional gel can be made (the rheometer applies stress via rotation, which is more of a two-dimensional test). Once the gel is made and subjected to the same aging conditions and stress loading conditions, it can be broken while measuring the upstream and downstream pressures with the downstream flow unimpeded by valves. The maximum difference between upstream and downstream pressures is recorded as the yield

pressure, which can be transformed into a yield stress using Equation 1.1.[19,20] By recording the restart pressure at various temperatures and extrapolating forward, the gel point can be estimated (roughly) as the point where the extrapolated line crosses zero. Fortunately, tests conducted using both methods aforementioned give exceptionally similar and repeatable results, indicating the flow loop method is good.

$$\Delta P_{yield} = \frac{4L}{D}\tau_{yield} \tag{1.1}$$

In Equation 1.1, L is the total length of the gel, D is the inside diameter of the gel, ΔP is the maximum pressure differential during breakage, and τ_{yield} is the yield stress of the gel (as would be observed in a standard rheometer). Equation 1.1 is a general correlation and is used as the standard in industry; however, it should be noted that the author feels it is incomplete with regard to potential for multiple yield stresses within a long gel, particularly in the case of nontraditional gels (in this dissertation, nontraditional refers to heterogeneous, or slurry-formed gels). Regardless, it is a good, reliable model and is used extensively in this research.

Pour point, the temperature at which gravitational forces can no longer shear apart a gel, is measured using the long-standing ASTM D97-11 test. For the purposes of this research, a modified pour point test has been devised to give, the author feels, better results.

The modified pour point test involves placing a sample in a specialized glass container sealed with cork while a mercury thermometer is submerged near the top surface of the sample. The glass container is then placed inside a temperature-controlled cell, and the sample is allowed to cool. At a certain temperature, the sample is removed and gently tilted; if the oil flows, a gel has not yet formed, and it must be reheated and recooled to a different temperature (if no flow occurs, this process must be repeated as well). Once the temperature at which flow first stops when tilted horizontally for three seconds, the pour point is said to be that temperature plus one degree. Figure 1.8 presents a graphic depicting the pour point testing setup.

The ASTM method is fairly quick and gives a surprisingly close result to the rheometer and flow loop methods – but generally only for model oils, as these typically have steep solubility curves (model oils tend to have a limited wax range, and the WAT and Gel Point are very close – within two or three degrees in many cases). For waxy crudes, the difference can be varied depending on the composition and slope of the solubility curve (described in the following section), but the pour point, being lower, will give the most conservative estimate of when a stable gel will form.

1.3.3.3 Wax Solubility

In the prior subsections the term solubility has been used in relation to WAT and gel point. Solubility refers to the degree to which components in solution stay in solution; in other words, solubility refers to the thermodynamically driven solids

content in a mixture. At any thermodynamic state (temperature, pressure, composition), equilibrium between phases exists; in some cases the entire mixture will exist as a single phase, but in certain cases multiple phases can exist at equilibrium. In the case of a complex mixture such as petroleum, this multiphase equilibrium behavior is broad, encompassing a large spread of temperatures.

To illustrate the previous point, consider Figures 1.9 and 1.10 made using differential scanning calorimetry (DSC). Figure 1.9 presents a simple phase transition of indium metal, while Figure 1.10 presents the phase transition of a model oil. In both case the only phases present are solid and liquid; no light-end gases are present.

What Figure 1.10 demonstrates is that solid-liquid equilibrium with an oil is hardly cut-and-dry, and solid precipitation occurs more as a spectrum rather than an event. With this in mind, the solubility of waxes in an oil is inherently important if one is to understand the various wax issues related to flow assurance. As such, it is important to know the solubility, via model or experiment, prior to engaging in wax research.

Experimentally measuring solubility is no simple feat; over the years, many methods of attempting to measure solids content have been tried, with only a handful avoiding rejection. Two of these methods are cross-polarized microscopy (CPM) and differential scanning calorimetry (DSC).[21-23] Various direct measurement means (i.e., forcibly removing waxes from an oil) have been attempted in the past and even present[24] but are not attempted in this research.

CPM-based solubility measurement is the one of the preferred means of estimating solubility outside of a well-tuned thermodynamic model due to very low data scatter and repeatability; unfortunately, a CPM system was not available during this research. The downside to CPM is that cooling rates must be very low (0.1 °C or less) as to prevent supersaturation inside the smooth microtube.

In the absence of CPM, DSC can be used to develop a solubility curve, though the exact solubility is not completely achieved.[25] DSC, simply put, measures the heat flow of a sample as ambient conditions change. During phase change, a spike in heat flow (positive for liquid-to solid, negative for solid to liquid) appears; for a single-component substance, this spike is sudden, intense, and abrupt (see earlier Figure 1.9). For a multicomponent substance such as petroleum, the phase change is much more gradual (see earlier Figure 1.10). With the heat flow measured for a sample in phase transition, one can use a cumulative integral ratio and known wax amounts (via model oil development and/or high-temperature gas chromatography) to develop a solubility curve according to Equation 1.2.

$$F_S(x) = C_S \frac{\int_0^x f(x)dx}{\int_0^\infty f(x)dx} \tag{1.2}$$

In Equation 1.2, F_S is the cumulative fraction, C_S is the solid content constant used to properly scale the curve to the known values (this must be known just as with CPM), and f(x) is the data curve. The numerator of the fraction is the portion

being analyzed, while the denominator is the total integral value of the data as shown in Figure 1.11. Figure 1.11 was chosen purposely (it also happens to be a DSC curve for the model oil used in this research) since it shows the difficulty inherent with estimating solubility.

In Figure 1.11, and unlike the earlier 5% model oil DSC curve (Figure 1.10), the heat flow curve trends upwards (mostly due to mechanical limitation inherent with the equipment). This means that the baseline through which one bases the integration must be adjusted accordingly. For simplicity sake (and to avoid unnecessary complications) it is acceptable to use a linear baseline; considering that virtually all precipitable solid wax will come out of solution at roughly -15 to -20 °C, this line can be drawn from the point of initial transition to the user-decided point of transition completion (in this case, the curve becomes horizontal again at about -14 °C). The actual numerical results are not presented here, rather they are shown in section 2.1.3 to great detail.

A major drawback to DSC is that heating and cooling rates must be fast enough for the equipment to capture all heat flow and minimize losses to the surroundings. If too slow (less than 0.334 °C for most DSC machines used by the author) the heat flow is so subtle that the machine is unable to register it before being lost. As such, there is some disparity between DSC solubility results and deep-sea pipeline solubility, though the difference is generally small. As one can see, for higher cooling rates DSC is superior, while for lower cooling rates CPM is preferred. Furthermore and apparent when observing the results in Figure 1.11 is the lack of measured heat flow near WAT (in this case, WAT is 19.5 °C) likely due to

supersaturation[25] inside the testing cell, making it an inappropriate method for measuring WAT. However, with the actual WAT known one can adjust the data appropriately to obtain solubility (see section 2.1.3 for details).

A third method using FTIR[15] is also fairly common, though the results tend to overestimate solubility if testing conditions are not carefully controlled. This method utilizes the same results of the aforementioned WAT test, and from these results a solubility curve is constructed.

1.3.4 Wax Deposition

During regular flow through a pipeline, wax can build up on pipe walls via deposition. In order for deposition to occur a thermal gradient between the outside ambient conditions and the internal oil flow must exist, and the internal wall temperature due to the gradient must be below the initial wax appearance temperature.[26-32] In addition, internal shear forces in the flow must be low enough to allow crystal growth, a case that is almost universally true in active pipelines.[33-41]

Wax deposits, left unchecked, can grow and restrict flow. While it is rare for deposition to completely shut down a pipeline, the loss in production capacity is a cause of concern. Furthermore, wax deposits are hard and strong; if not addressed early in formation, these can be almost impossible to remove without extensive heating (which, particularly for standard oceanic lines, can be difficult if not impossible). Various groups have already conducted considerable study on the topic of deposition, but some questions particularly regarding deposition under slurry-type flow (this will be touched upon later) still exist.

Concerning the measurement of deposition in-line, direct measurement (i.e., removing a section of the line and physically measuring with a ruler) is the most conclusive means, though an indirect method using pressure drop across the line is also acceptable. In the case of a recycled loop system with a temperature-controlled test section in which deposition occurs, the author has developed a modification of the common 1846 Hagen-Poiseuille equation (Equation 1.3) for smooth pipeline pressure drop. This modification, which the author calls the Modified Hagen-Poiseuille equation (Equation 1.4), incorporates a sudden contraction mass balance to account for the noticed increases in head pressure while downstream pressure remains relatively constant during deposition. This model assumes that the deposition is a rigid mass with no slope; in other words, the deposition is assumed to immediately start and immediately end with no heterogeneous surface behavior (a very poor assumption in terms of what really occurs, but quite good when trying to predict deposition thickness as per the results soon to be shown). In addition, a scaling constant C is added to ensure zero deposition height when it is known (i.e., base condition) that no deposition exists.

$$\Delta P = \frac{8\mu LQ}{\pi r^4} \tag{1.3}$$

$$\Delta P = \frac{8\mu LQ}{\pi r^4} + \rho V_m^2 \frac{A_f}{A_d}\left(\frac{A_f^2}{A_d^2} - 1\right) + C \tag{1.4}$$

In Equation 1.3, ΔP is the pressure drop across the pipe, μ is the dynamic viscosity, L is the length of the pipe, Q is the volumetric flow rate through the pipe, and r is the radius of the clean pipe. In the Modified Hagen-Poiseuille equation (Equation 1.4) the previous terms are carried through, In addition, ρ is the density of the fluid, V_m is the maximum fluid velocity (found in the section with deposition), A_f is the free-pipe cross-sectional area, A_d is the cross-sectional area of the deposition-constricted pipe (i.e., the area open to flow), and C is the scaling constant.

Of course, proper validation must be made with the modified Equation 1.4 to make sure that it is, in fact, a valid model. To do this, early testing used laser particle imaging velocimetry (see section 2.4.2 for more details) to measure fluid velocity (for the modified Hagen-Poiseuille equation) and comparison to an incompressible flow model (equation 1.5).

$$Q_f = V_f A_f = V_d A_d; \quad \therefore A_d = \frac{Q_f}{V_d} \tag{1.5}$$

In Equation 1.5, Q_f is the free-pipe volumetric flow rate (which by conservation equals the flow rate through the deposited pipe); therefore, using incompressible fluid assumptions the cross-sectional area of the deposited pipe must equal the volumetric flow rate divided by the average velocity V_d of the deposited layer. It should be stated that the reason this model is not used in place of Equation 1.4 is that measuring velocity in a certain section of a pipeline is not always available; furthermore, using PIV in an industrial line is not realistic.

However, if Equation 1.4 can be shown to be valid then it is possible to know the deposition thickness with only flow rate and pressure drop.

Figures 1.12 and 1.13 compare the results found using Equation 1.5 (incompressible fluid model) and that found using the modified equation. Figure 1.12 was made possible by an artifact of the pipeline used for measurements. Due to an unforeseen collection of stuck fluorescent particles at the bottom of the tube, the deposition layer formed first at the bottom of the pipeline. Gradually the deposition grew and moved up the sides – giving the PIV system a clear, open look into the fluid for a number of hours. Once the deposition layer covered the top of the tube, the PIV was rendered useless.

As seen in Figure 1.13, the absolute knowledge of the incompressible model (Equation 1.5) confirms that the modified Hagen-Poiseuille model (Equation 1.4) is a good model (at least for laminar flow). With this conclusion reached, a final step can be made to remove velocity measurement completely from Equation 1.4 by utilizing a common heuristic of laminar flow: Equation 1.6, which states that the average velocity of a flow is roughly one-half the maximum velocity. With that in mind, Equation 1.4 can be adjusted to Equation 1.7 - desirable in that the only unknown values required to detect are pressure drop and flow rate (it is assumed that one knows the viscosity and density of the oil at various temperatures, as well as the geometry of the pipeline).

$$V_m = 2V_a = 2\frac{Q}{A_d} \tag{1.6}$$

In equation 1.6, V_a represents the average fluid velocity. Substituting Equation 1.6 into 1.4, one can solve this final Equation 1.7 for A_d, from which the thickness of deposition can be calculated. To do this, the author prefers using Excel's SOLVER function or a custom-made MATLAB solver (ideal for large amounts of data).

$$\Delta P = \frac{8\mu LQ}{\pi r^4} + 4\rho \frac{Q^2}{A_d^2}\frac{A_f}{A_d}\left(\frac{A_f^2}{A_d^2} - 1\right) + C \tag{1.7}$$

1.3.4.1 Mechanics of Wax Deposition

In order for deposition to occur 1) a thermal flux must exist, 2) the temperature range (flow and ambient temperatures) must extend into the solubility curve explained earlier, and 3) shear forces must be low enough to not break up any solid deposits.[26-41]

An interesting development proposed by Singh et al. (2000)[26] regarding internal diffusion inside the deposition layer itself lends, in the opinion of the author, intuitive information regarding the formation of the deposition layer itself. The proposed mechanism (Equation 1.8) seeks to explain the diffusion of waxes through the already-formed deposition.

$$J_{GD} = -D_e \frac{dC_{WS}}{dT}\frac{dT}{dr} \tag{1.8}$$

Equation 1.8 is interesting to the author in that it seems to have direct applicability to deposition formation as well. While the turbulent flowing oil of an industrial pipeline hardly lends itself to diffusion, in order for depositional flux J_{GD} to occur an equivalent diffusional mass transfer must occur in some form or another (the constant D_e represents this mass transfer coefficient). A thermal flux dT/dr exists, but this is not sufficient to fully explain deposition since deposition under identical thermal gradients – though different solubility states – is markedly different. Therefore, as seen in Equation 1.8, to obtain a mass transfer gradient dC_{WS}/dr, where C_{WS} represents mass of solid waxes precipitated, one needs to know the particular solubility dC_{WS}/dT (in this research this term is simplified as dC/dT) at each axial position. This concept is of importance to the purposes of this research, and will be touched upon later in section 4.1.

While some deposition study was conducted as part of this research, it needs to be said that deposition mechanics were not of critical study or importance to the research. As mentioned earlier, various groups have already conducted extensive study towards deposition mechanics. The deposition purposes in this research revolve around a concept known as “Cold Flow” which will be detailed further along in this introductory chapter.

1.3.5 Gelation

The concept of gelation has already been briefly explained, but repetition is the foundation of learning. If a flowing, waxy oil pipeline is shut down and subjected to cooling, waxes will come out of solution once internal temperatures drop below

the initial wax appearance temperature of the oil. If internal temperatures drop further, these precipitated wax particles will grow, these being the primary nucleation site for phase transition. These crystals will continue to grow as temperature drop, and once the crystals begin to interact (i.e., "grow" into each other), a solid matrix will form within the liquid phase[42]. This solid matrix within a liquid phase is known as a gel, and in general the more wax comes out of solution the stronger the gel will become (more pressure required to restart flow).[43-48] Gels in pipelines tend to be long, on the order of miles; for weak gels, restart may be an option, but for strong gels the amount of pressure required to rapidly (or even slowly) restart flow exceeds the safety factors of the pumps and/or pipeline.[49-51] Figure 1.14 presents the general process through which a gel forms.

Like deposition, the formation of gels from waxy oils has been studied extensively as well for decades, but many questions still exist and as such waxy gels are a common topic in flow assurance research, including this dissertation.

In terms of gel strength measurement, for a rheometer this is done by rotating the cone at a controlled rate until free movement occurs. In a pipeline system, gel strength is found by measuring the maximum difference between upstream and downstream pressures (both outside of the gel boundary) prior to gel movement and back calculating using Equation 1.1.

1.3.5.1 Gel Strength Considerations

Ultimately the determining factor in gel strength is available amounts of wax in solution.[42,43] For example, an oil with only 3% total wax content by mass will

generally (and practically always) have a weaker gel strength than an oil with 5% total wax content by mass at any given temperature and pressure. In short, more wax = more/larger crystals = stronger crystalline matrix. Furthermore, gels formed under slower cooling rates will exhibit larger crystals and higher strength than gels formed under fast cooling rates.[20,43,45,51] Smaller crystals, while more numerous, can exhibit shallower penetration into other crystals, resulting in weaker and actually fewer cross-links and, ultimately, weaker gels (i.e., lower-quality crystal-crystal interactions).[42,43] The pressure required to break a homogeneous gel is observed to increase linearly with higher pressure loading rates (psi/s) for a particular gel temperature.[43-47]

1.3.5.2 Gel Breakage: Adhesive and Cohesive Failure

According to the paper by Lee et al. (2008), depending on the quality of the gel matrix through cooling rate, specific failure types will be seen.[20] These failure types are known as adhesive and cohesive failure.

Adhesive failure is a failure of gel-wall interactions. This type of failure occurs when the crystal-crystal interactions in the main body of the gel are stronger than those at the wall, and occurs when the gel matrix is formed under lower cooling rates, thereby forming larger crystals and more interactions (in other words, a higher quality gel). As the gel fails under this case, the body of gel moves as a plug for a time before breaking up in the resumed flow.[20,52]

Cohesive failure occurs when the internal crystal-crystal interactions are on the whole weaker than those between crystal and wall.[20] This type of failure occurs

when the internal gel matrix is weaker than that at the wall. As expected, this type of failure occurs with a low gel quality as seen with fast cooling rates, smaller crystals, and a smaller number of crystal-crystal interactions. Cohesive failure would be marked by an internal failure somewhere between the wall and the center (by definition, there is no shear stress as the center of the pipe, so a true "center" failure cannot explicitly occur).

In a series of tests conducted by Lee et al. (2007) results appear to show a transition point, based on cooling rate, at which failure switches from adhesive to cohesive. This transition is marked by a maximum strength at the transition point. While this result is somewhat incomplete, it is a rousing and reasonable result. That said, one question that comes to mind is this: what other factors could lead to failure type change besides cooling rate?

For the record, a paper by El-Gendy et al. (2012) used particle imaging velocimetry (PIV) to show conclusive evidence of adhesive failure at the wall of a model oil with 7 wt% wax.[52] Part of this research builds off that study as will be seen later on.

1.3.6 Methods of Wax Control - Historical

As part of this research a literature review was conducted using industry reports and papers donated by RPSEA, the group involved with early funding on this project; as it stands, permission has been given to expound generally upon the topics therein, but no references or titles are allowed to be given as to protect the

interests of the participating parties. Therefore, much of the following is done without explicit referencing and with very general language.

A great amount of effort has been and is being given to finding methods of eliminating wax issues in pipelines.[53-57] Primarily, the most successful and reliable means of dealing with wax is mechanical removal of deposits through pigging. Chemical additives to reduce gel points and crystal-crystal interaction are also largely successful in avoiding major issues. However, in both of these cases costs become burdensome, particularly in the latter. Heavy insulation is also used frequently with considerable success, but again costs come in to play, and ultimately the insulation cannot stop deposition completely (a thermal flux will eventually get through to the flowing oil).

A series of tests involving line heating, microwave heating, acoustic treatment, ultrasonic treatment, and a variety of surface coatings were conducted over a number of years. The brief, generalized results are as follows.

1.3.6.1 Line Heating

Line heating, whether by an immersed cable (electric resistance heating) or bundled lines, works to prevent deposition and gelation by keeping wall temperatures above WAT and/or gel point. However, this method is very expensive and requires specialized pipeline designs. With heat loss improvements this method should be considered as a means of stopping wax and hydrate (water ice crystal surrounding a hydrocarbon) issues.

1.3.6.2 Microwave Heating

This method was based on the notion that microwaves could cause molecules in the oil to vibrate, heating up the oil and dissolving waxes. Apparently, this method was abandoned due to no discernible benefits or effects.

1.3.6.3 Acoustic Treatment

The use of high-amplitude sound waves was considered as a means to disrupt gels during formation as well as a means of breaking up deposits. No positive results were recorded, and the method has apparently been abandoned.

1.3.6.4 Ultrasonic Treatment

Similar to acoustic treatment, ultrasonic treatment utilizes extremely high frequency sound waves to try and break up deposits and gels. This method has been shown to work in cleaning systems (sonicators, for example), but experiments on pipelines have shown few if any positive results. Because of success in other applications, this method should be given some attention in the future, but for now the groups pursuing largely abandoned it as a means of wax control.

1.3.6.5 Surface Coatings

Experiments with surface coatings yielded some interesting results. Theoretically, by coating the inside surface of the pipeline with a material that inhibits waxes from depositing, one could permanently stop deposition from occurring. A number of coatings, all of which technically should inhibit wax bonding,

were tested in a pipeline. Surprisingly, while all coatings stopped deposition from forming for a short time, none could stop deposits from ultimately forming. According to the researchers, the best effect the coatings provided was insulation.

1.3.7 "Cold Flow" as a Means of Wax Control

While aspects of isothermal flow have been looked at in some degree or another for the better part of a century, only recently has it been seriously considered as a means of preventing deposition in flowing pipelines. In 2007, Larsen et al. coined the term "Cold Flow"[58]: isothermal flow (internal oil temperatures matching external ambient temperatures, thus eliminating the thermal gradient) while internal temperatures are below initial WAT. In other words, "Cold Flow" is flowing the oil as a solid-liquid slurry at cold, ambient temperatures.[16,58,59]

Often times the term "Cold Flow" is used to describe the flow of an oil below WAT but not necessarily at isothermal conditions with the surroundings[60]. In this dissertation, both isothermal and nonisothermal "Cold Flow" are considered and studied.

1.3.7.1 How Does "Cold Flow" Work?

Iso- and nonisothermal "Cold Flow" prevent and/or reduce wax deposition by 1) removing much of the heavier waxes from solution via sub-WAT conditions and 2) eliminating or greatly reducing the thermal gradient between the oil and the ambient surroundings.[16,58-60]

As mentioned earlier, the work of Singh et al. (2001) in describing internal diffusion[26] is directly applicable, to a degree, to the deposition formation itself. According to Equation 1.8, if a thermal gradient dT/dr is limited to zero, the mass flux to the wall will also be limited to zero. Hence, "Cold Flow" eliminates deposition by eliminating thermally-driven mass transfer gradients (a.k.a. the Ludwig-Soret effect or thermophoresis effect developed in 1879) in the flowing oil.

1.3.7.2 How Is "Cold Flow" Accomplished?

While using "Cold Flow" to stop deposition is fairly simple to understand, getting "Cold Flow" conditions is not so simple. Any attempt to traditionally cool an oil (flowing across cold surfaces such as a coil) will result in wax buildup on the surfaces.[16,43,60] This buildup is dangerous because it removes waxes from solution, permanently changing the oil composition and thermodynamic properties and thereby corrupting any deposition testing results. As such, this buildup must be physically removed (in the previous section, it was found that surface coatings are less-than-effective at stopping buildup).

While in a laboratory setting with an easily accessible reservoir and a cooling coil this buildup is simple to manually remove, any such attempts at a deep-sea system would be out of the question. Therefore, while cooling surface de-waxing can be done by hand, an automated and constant means of de-waxing is desirable.

The author designed and built such a device, known as the Scraped Exchanger. The Scraped Exchanger is a pipe-in-pipe heat exchanger with a rotating

blade that cleans the cooling surface constantly. This cleaning preserves the integrity of the fluid for rheological testing.

1.3.7.3 Is "Cold Flow" Successful?

According to virtually all studies,[16,58-60] as well as industry and proprietary research, "Cold Flow" is completely successful as a means of deposition control. Isothermally, deposition is completely eliminated, while nonisothermal "Cold Flow" (as described in other papers) results in significant deposition rate reduction.

There is, however, a major downside to "Cold Flow": fluid viscosity increases greatly. If the fluid is too cold, viscosity can increase well beyond 100 cP and make flow extremely cumbersome and costly pump-wise. Any attempt at implementing "Cold Flow" in the field would need to account for this difficulty.

1.3.7.4 What Is Unknown about "Cold Flow"?

While "Cold Flow" has been shown to slow/stop deposition, research on gels formed in the case of "Cold Flow" shutdown (subsequent cooling occurs only after shutdown) has been curiously overlooked. It is true and generally known that gels made from solid-liquid slurries such as those used in "Cold Flow" are weaker than those formed from hot, "clear" oil at shutdown.[43,49] However, due to the same limitations on "Cold Flow" operation in the laboratory (wax sequestration in cooling systems, crystal "grinding" in rheometers, etc.), the in-depth and meaningful study of these slurry-formed or "heterogeneous" gels has been avoided.

1.3.8 Heterogeneous and Homogeneous Conditions

With the advent of "Cold Flow" studies, an aspect of way oil flow in cold situations has reopened. Slurry (solid components in a liquid) flow has been around as long as waxy oils have been flowing, but relatively little attention has been paid to slurry flow because of the assumed lack of flow assurance issues attached to it. However, in the opinion of the author, it is time to examine slurry, or heterogeneous, flow.

In this dissertation, two types of flow are considered: heterogeneous (solid-liquid slurry) and homogeneous (pure liquid state). No water, asphaltene, or salt interaction is considered. In general, homogeneous oil is a Newtonian fluid, but heterogeneous oil exhibits largely Newtonian behavior (due to relatively low numbers of small, soft crystals) until a few degrees above gel point. Nevertheless, given that heterogeneous flow consists of suspended wax particles it is treated as a non-Newtonian, shear-thinning fluid.

In a flowing pipeline, for instance a deep-sea pipeline with a cold, sub-gel point ambient temperature, deposition potential is highest where the thermal flux is highest and internal flow temperature is below the heaviest component's solubility limit.[26-30] If flow is stopped, Figure 1.15 presents the likely resulting gel formations.

So what is the difference between the gels formed from oil in a homogeneous state and a heterogeneous state? The author prefers to refer to this difference as being natural versus unnatural gel formation. As shown earlier in Figure 1.14, gels formed from a homogeneous flow start as seed crystals forming as wax solubility decreases via dropping internal temperatures. With these seeds formed, further

precipitation occurs at these seeds as they provide the most ideal nucleation sites (aside from a rough pipe wall surface). As the growing crystals increase in size, the space between crystal outgrowths diminishes, and eventually, at gel point, the outgrowth from one crystal will mesh or grow into the outgrowth of another crystal. At the wall, the crystals formed on the wall likewise extend into other crystals.

With heterogeneous flow, however, wax crystals already exist in the flow in various state of morphology due to shearing forces and agglomerations. These preexisting, sheared crystals do not have the same morphology as naturally-forming crystals during cooling. The resultant interaction between natural and preexisting sheared wax crystals disrupts the natural gel formations. It is speculated that these disruptions create weak points inside the gel that reduce the gel strength overall. While the nature of this interaction is not known, the results of this research will give insight and will be shown to have serious implications to the theories of heterogeneous gel matrix development.

One question that must be asked and answered is this: how do preexisting, sheared crystals affect the gel point? It is suspected that these preexisting crystals do in fact participate in the gelation process and the gel matrix, but what is not known is whether or not the presence of these crystals lowers the gel point as opposed to simply lowering the slope of the gel strength versus fluid temperature curve.

1.3.8.1 Difficulties in Managing Constant Heterogeneous Conditions with Traditional Rheological Systems

Part of the problem with studying oils in a heterogeneous state is maintaining constant properties during testing. Simply achieving a heterogeneous state without compromising compositional integrity via wax sequestration on cooling surfaces is a challenge. Attempts at studying heterogeneous fluids inside a typical rheometer provide poor repeatability and high time-dependent behavior (the small space between surfaces in a rheometer can "grind" wax crystals), but the use of a flow loop is much more promising due to lower shear stresses and larger volume. Still, wax sequestration is an issue even in flow loop systems.

To overcome this problem, a device was created to automatically generate heterogeneous conditions while constantly cleaning the cooling surface. This device is called the Scraped Exchanger, and will be explained in great detail in Chapter 2 and in Appendix B.

1.4 Thesis

The purpose of this research and this thesis is to explore several questions regarding deposition under "Cold Flow" and slurry-type flow in general, as well as the more unknown and unexplored heterogeneous gel breakage and rheology. It is also necessary to briefly explore settled restart ("Cold Flow" shutdown without further cooling, followed by allowing suspended particles to settle) and the effect on slurry conditions on gel point.

1.4.1 "Cold Flow" and Slurry-type Flow Deposition

1) Is thermally-drive deposition truly eliminated when operating under true "Cold Flow" conditions?
    a. It is expected that this research will yield the same results as other studies, i.e., no deposition under "Cold Flow"
2) Does deposition still occur under slurry-flow conditions when a thermal gradient is present? If so, is the rate of deposition different when compared to normal (non-slurry) flow?
    a. It is predicted that slurry-type flow deposition rates will be reduced when compared to normal flow.

1.4.2 Heterogeneous Gels Formed from the Cooling of a Slurry

1) To what degree is a heterogeneous gel weaker than a homogeneous gel formed under similar conditions?
    a. It is expected that heterogeneous gels always will be weaker than homogeneous gels, although conditions such as loading rate and particle size may greatly affect the magnitude of this difference.
2) What is the effect of solids loading (via slurry temperature) on heterogeneous gels?
    a. It is expected that increased solids at shutdown will lead to decreased gel strength due to a higher degree of gel irregularity and reduction in precipitable dissolved waxes.

3) Do heterogeneous gels exhibit linear pressure loading rate versus gel temperature curves? Is there an adhesive/cohesive effect with stress loading rate?
    a. A distinct change in slope of the loading rate versus gel temperature is expected to be seen at the transition point between adhesive and cohesive flow, should such a transition exist.
4) Can one visualize the physical breakage of a heterogeneous gel in the case of cohesive (center-core) failure?
    a. PIV may be a way to see into the gel matrix and detect internal breakage.
5) What is the effect of wax crystal size distribution on gel strength?
    a. It is hypothesized that as crystal size diminishes the yield strength of the heterogeneous gel approaches that of the homogeneous gel.

To concretely answer these questions and further the knowledge of multiphase fluids, a model pipeline flow system complete with visualization and sensor systems has been constructed. This system has a controlled test section in which gels are formed and broken. The most important component of the system is the Scraped Exchanger (referred to as the SCE). This device facilitates the creation and maintenance of sub-WAT slurry conditions. Particle sizes are measured using CantyVision InFlow®. This is a cross-polarized, flow-through microcamera that measures particle sizes based on clarity, brightness, and circularity in a live flow. To visualize restart profiles, a clear test section has been created to allow laser particle imaging velocimetry, and provide insight into gel breakage in general.

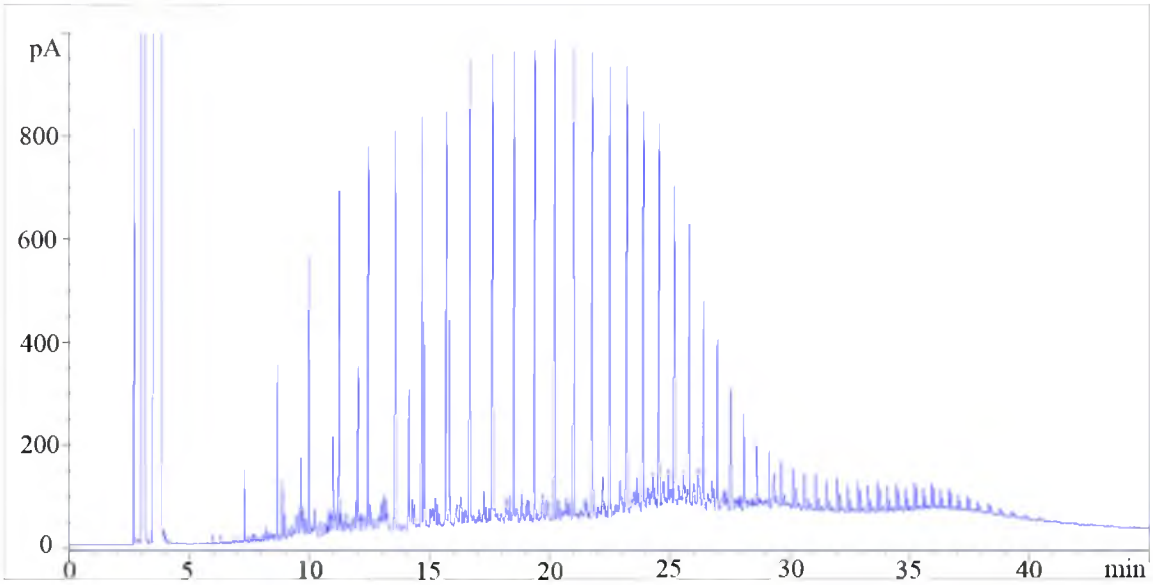

Figure 1.1. Typical gas chromatogram of a crude oil. This result is from a crude oil used early in the research development.

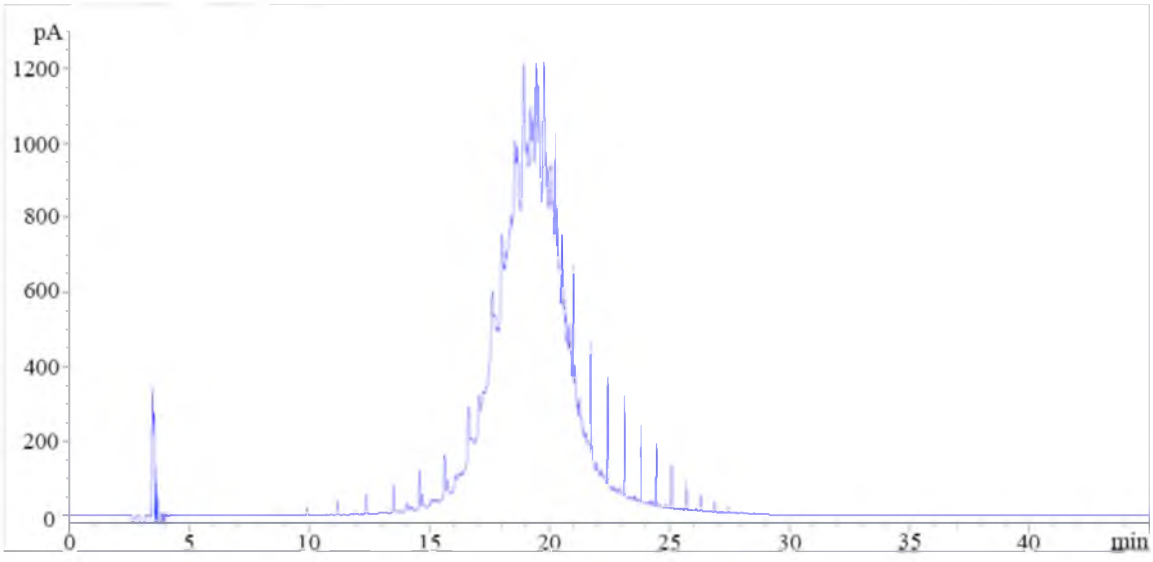

Figure 1.2. Gas chromatogram of the model oil (waxes added to a mineral oil) used in this research. The narrowness of the chromatogram is typical of simple model oils due to limited composition compared to crudes.

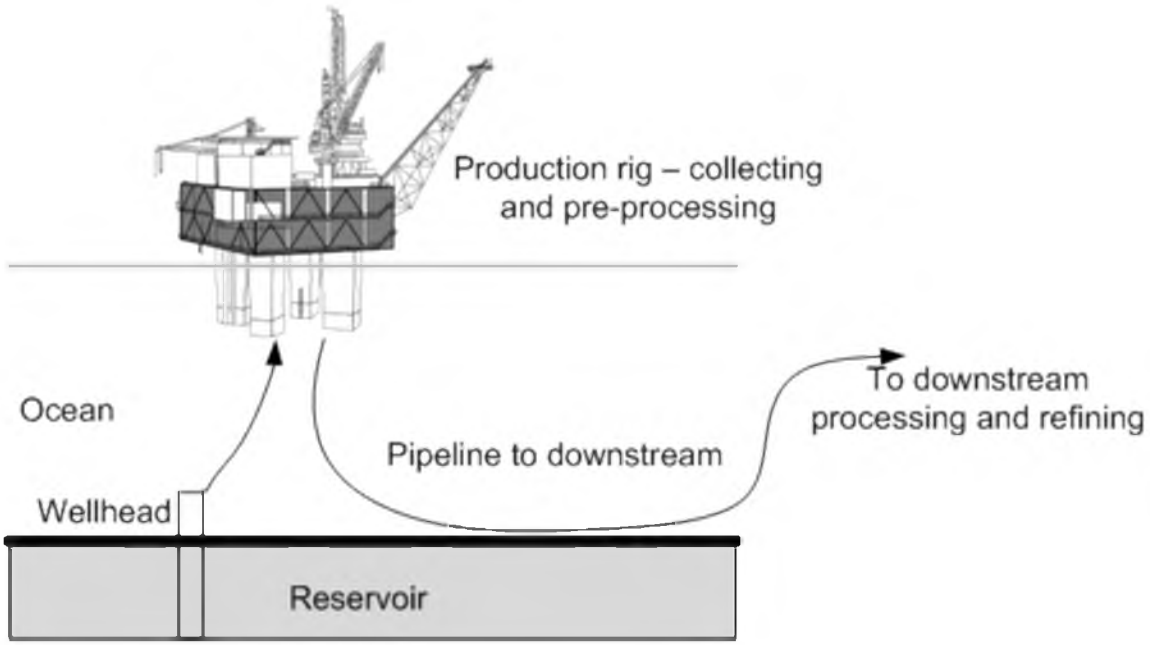

Figure 1.3. Cartoon depicting the transport of oil from the reservoir, wellhead, rig, and eventually refinement via pipeline.

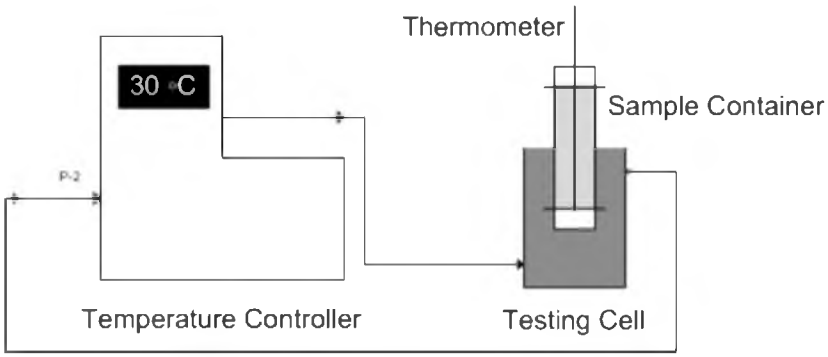

Figure 1.4. Cartoon depicting the modified ASTM D2500 setup used in this research to measure WAT.

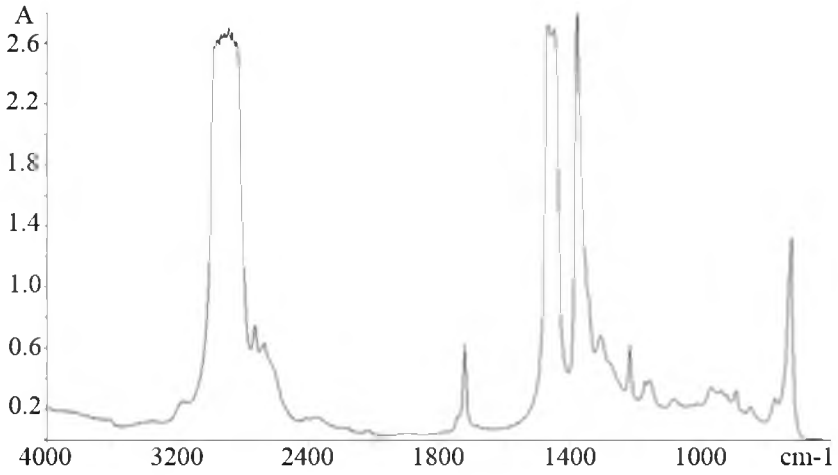

Figure 1.5. FTIR raw data curve for model oil at 20 °C. A curve at each temperature increment is needed to construct integrals used to develop Figure 1.6. Raw data is normalized against a blank background standard. Image pulled directly from FTIR software.

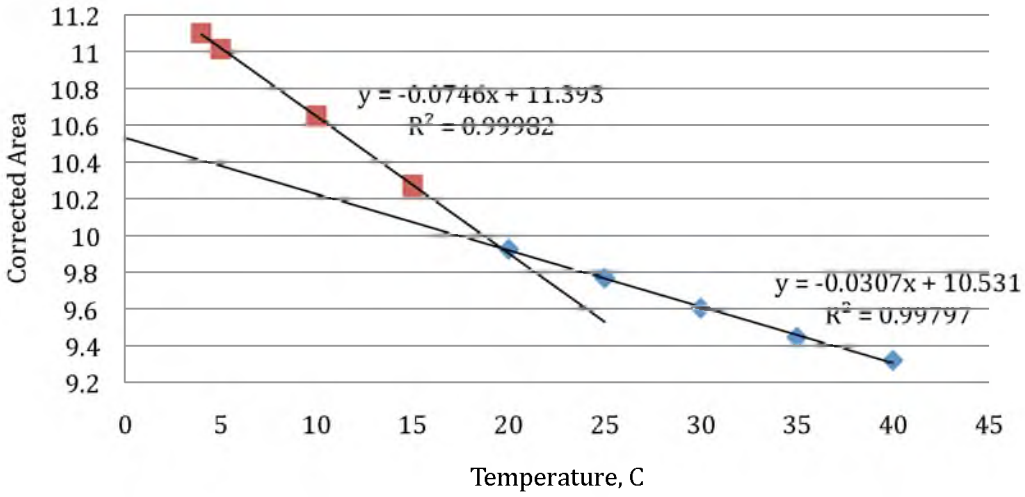

Figure 1.6. Demonstration of using FTIR analysis to determine WAT. Here, wax appearance occurs when the slope of the absorbance curve integrated area suddenly changes.

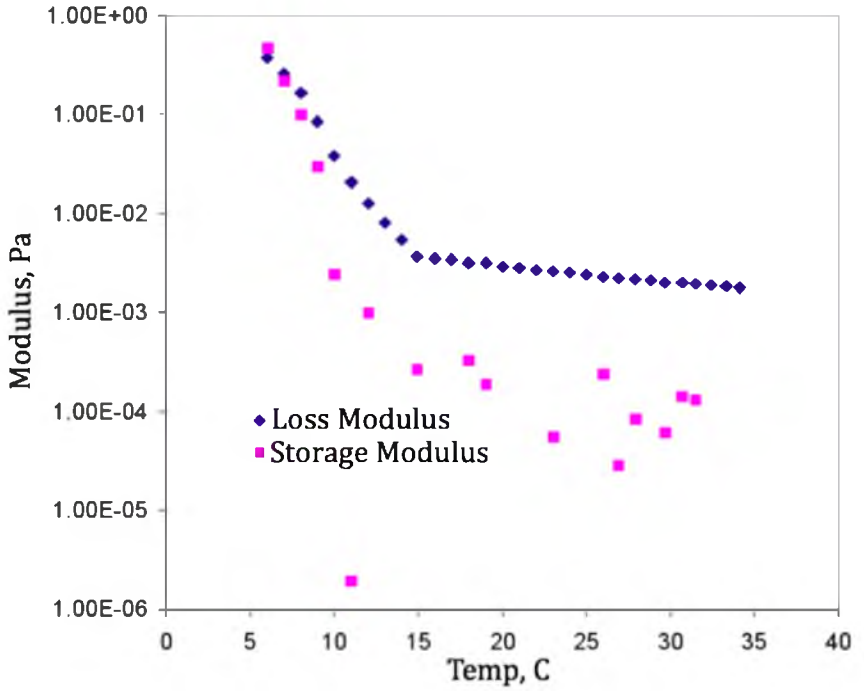

Figure 1.7. Demonstration of using the crossover of the storage (elastic) and loss(viscous) moduli to predict gel point. Gel point shown here is approximately 7 °C.

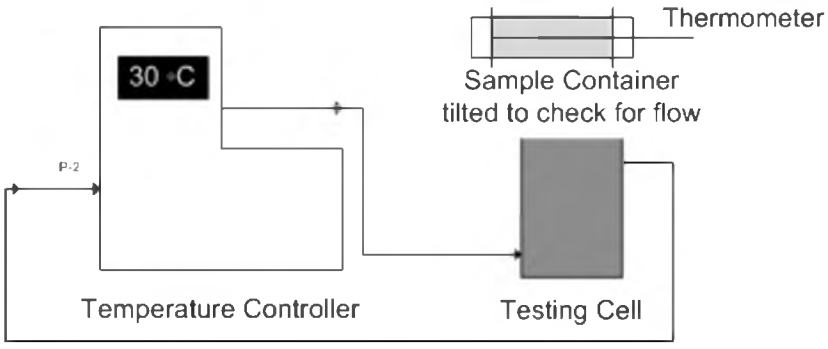

Figure 1.8. Cartoon depicting setup of ASTM D97-11 method for determining pour point.

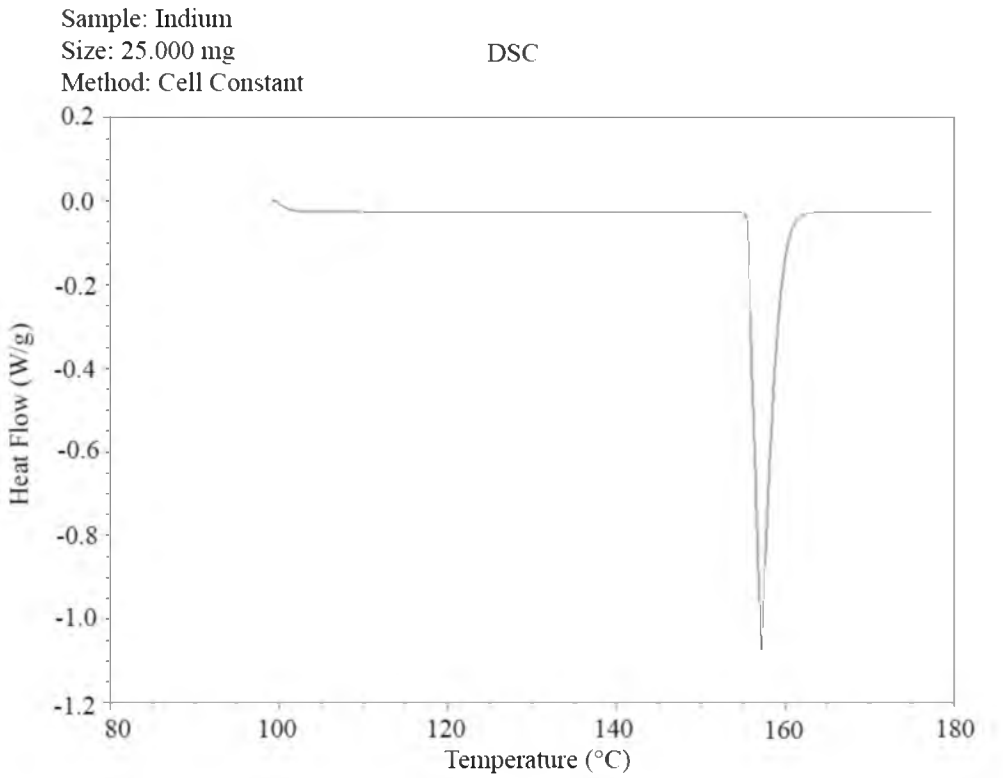

Figure 1.9. Screen capture of Indium metal calibration curve generated using DSC. Note the sharp curve and rapid equilibration, indicating a fast transition and singular composition.

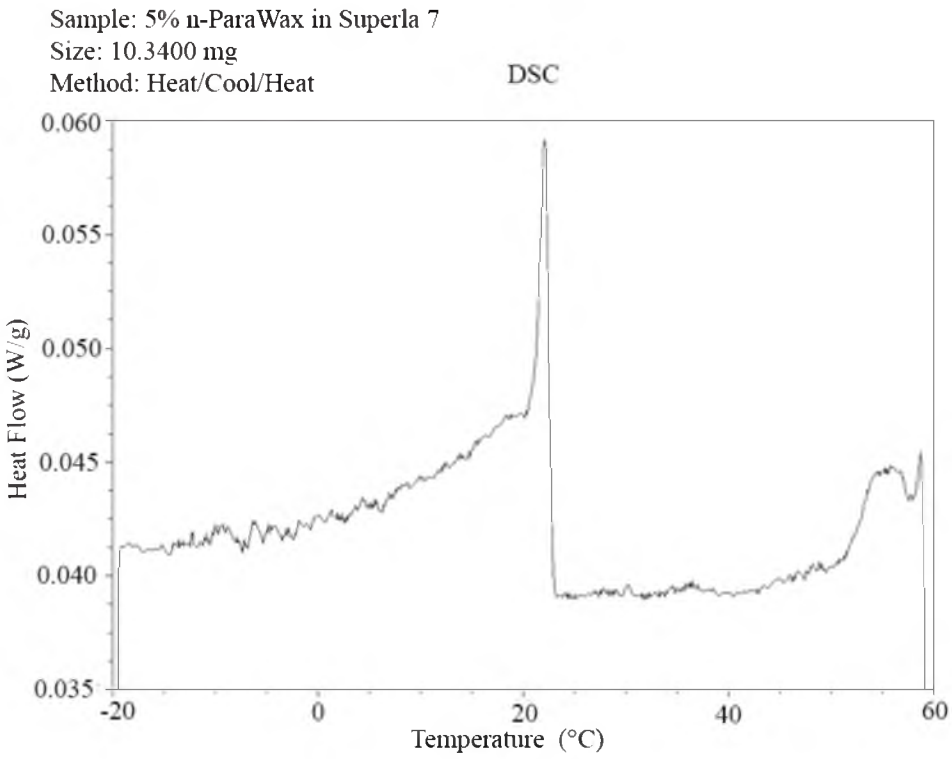

Figure 1.10. Screen capture of model oil heat flow curve generated using DSC. Model oil consists of 5% wax in mineral oil. Phase transition begins at approximately 23 °C, but transition does not stop until -20 °C.

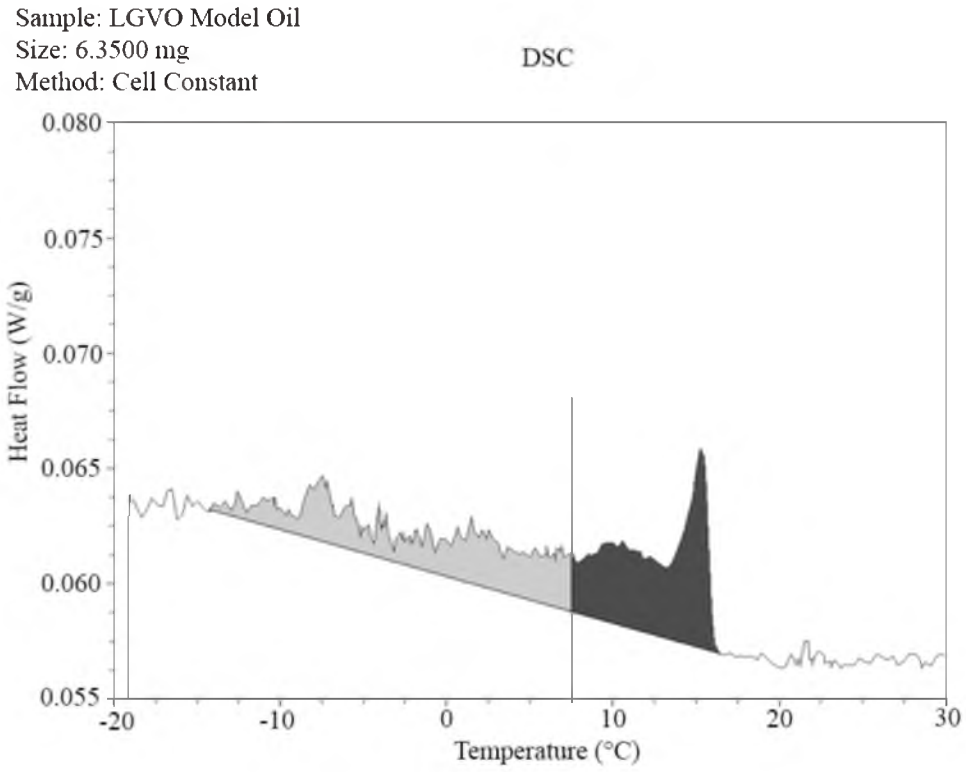

Figure 1.11. Screen capture of model oil heat flow curve generated using DSC. Cumulative integral calculated (here shown at 8 °C) is the darker shaded area divided by the total lighter gray area plus the darker area. This process is continued at every temperature increment until a complete solubility curve is generated.

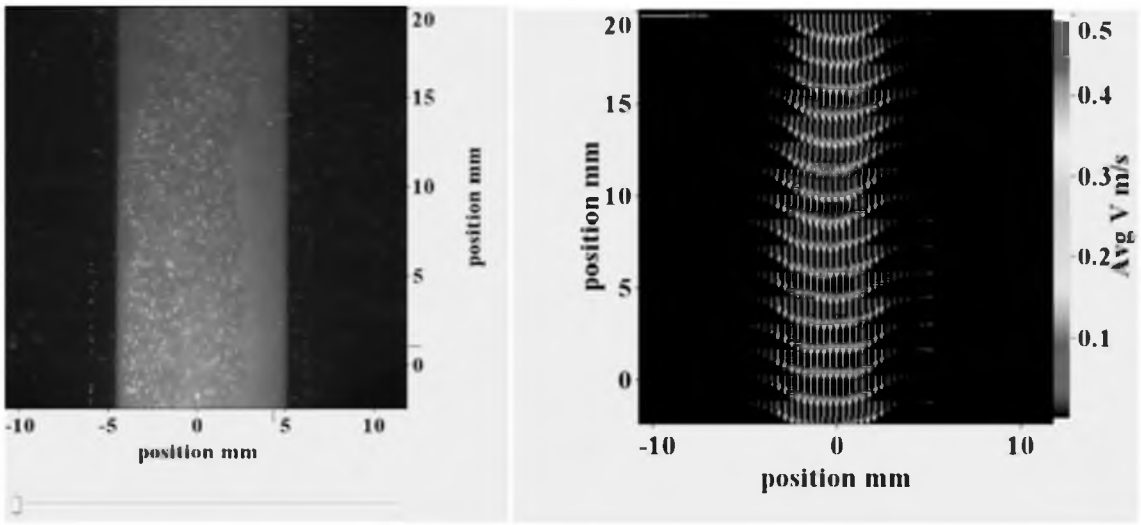

Figure 1.12. PIV results showing live image with deposition (left) and velocity profile (right). With velocity profile defined, the average velocity (as well as maximum velocity V_m) can be measured.

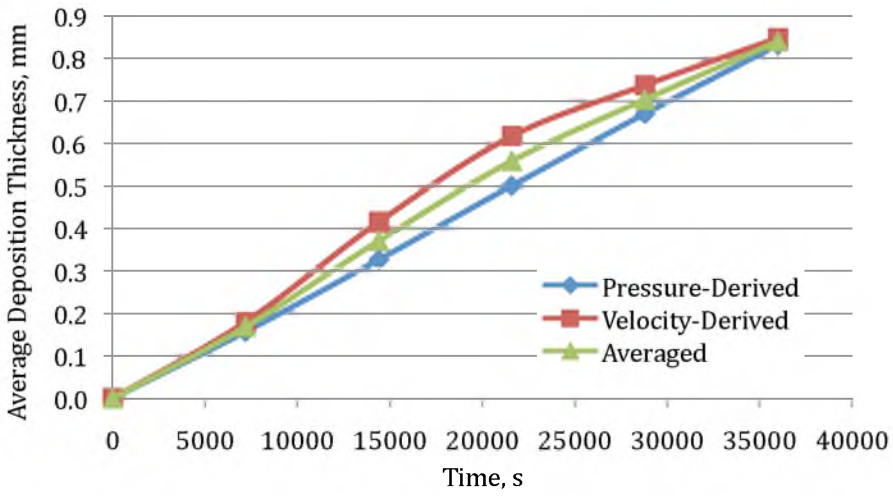

Figure 1.13. Calculated deposition thickness using results from Figure 1.12. Operating conditions are 10 °C ambient, 17 °C fluid (sub-WAT), and 0.7 gpm. "Pressure-Derived" thickness is found using the Modified Hagen-Poiseuille model (Equation 4); "Velocity-Derived" thickness is found using the incompressible model (Equation 5).

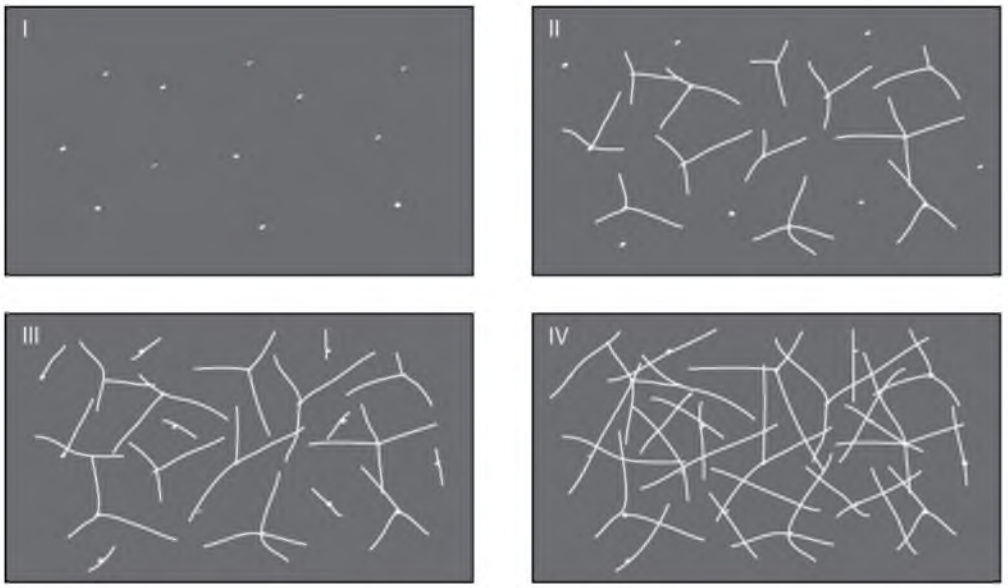

Figure 1.14. General process of gelation. In I, seed crystals composed of the highest carbon numbers come out of solution at WAT. As temperature drops in II and II, additional carbon numbers precipitate upon the seed crystals, creating larger and larger crystals. At gel point in IV, the crystals have extended further and grown into one another, creating a crystal-crystal interaction matrix.

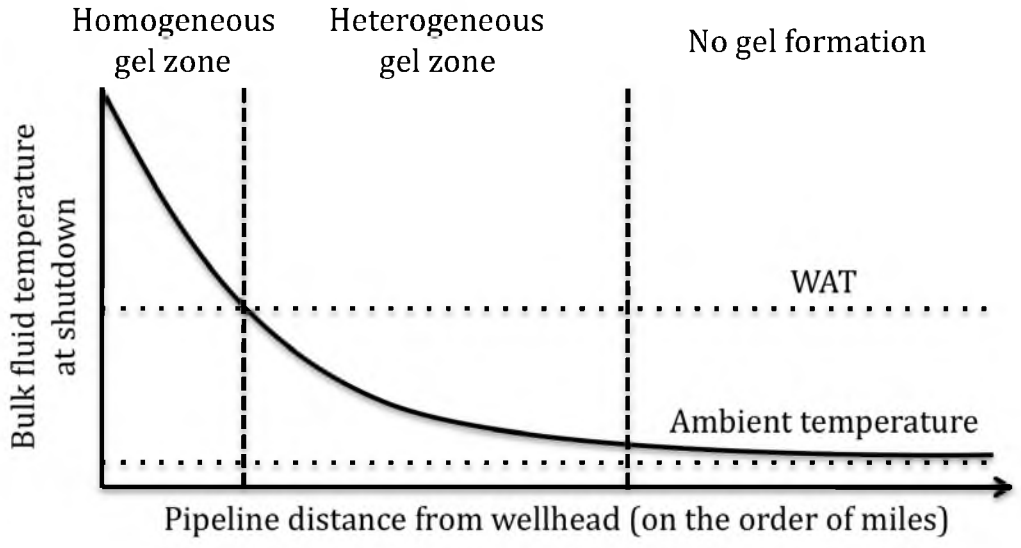

Figure 1.15. Graphical representation of the gel types formed at shutdown in a pipeline for a waxy oil. Ambient conditions are assumed to be below gel point.

CHAPTER 2

EQUIPMENT AND MATERIALS

2.1 Model Oil Development

Use of a model oil instead of a crude oil in research is a common practice. While attempting to correlate specific findings between a model oil and a crude oil is a poor decision, qualitative correlation between the two is an excellent, safe, and inexpensive way to predict general crude oil behavior. For this research, while the deposition and restart pressure results are only quantitatively applicable to the model oil, the trends and qualitative results tell us what to expect in a crude oil system. Furthermore, considering the inventive and exploratory nature of this project, particularly with regard to the Scraped Exchanger as well as the lack of heterogeneous rheological knowledge in general, the use of a model oil is highly appropriate. Naturally, the next step after this completed research is to apply the theories and expectations to crude oils using the same or similar equipment.

To appropriately study the effects of heterogeneity on deposition and gels, it is important to use a model fluid with desirable properties. For this study, the desirable properties of the model fluid are:

- Lower viscosity (0-200 cP in temperature range of study)
- High clarity above WAT
- Multiple degree difference between initial WAT and gel point
- Nontoxic, nonreactive components
- Inexpensive components

Crude oils rarely exhibit clarity (although some gas condensates are fairly clear right out of the well). As such, using PIV to visualize restart profiles as well as any visual confirmation using the clear test section with a crude oil would be ineffective. Additionally, many crudes have higher concentrations of light ends (methane, ethane, propane, butane) and exhibit some toxicity. Therefore, the obvious answer is to use a benign model oil to develop a prediction of how a crude oil would behave. A problem with model oils is that they are typically too simple in composition to achieve comparable properties to a crude oil.[42]

Model oils are developed with simplicity to control cost and to avoid variation in composition; however, a simple two-component oil (wax-free mineral oil, food-grade wax) gives very small range between WAT and gel point, generally no greater than 3-4 °C. Since waxy crude oils feature a wide range of carbon numbers from C-19 up to C-150 and beyond, a crude generally exhibits a WAT-gel point difference of at least 30 °C.

2.1.1 Components and Key Properties

As previously mentioned, two-component model oils, while simple and inexpensive, tend to have exceedingly steep solubility curves, thus leading to a small

temperature difference between WAT and gel point. To overcome the poor WAT-gel point range, a third component was considered. As seen in Figure 2.1, food-grade wax has a strict, short range between C-20 and C-34. LVGO (Light Vacuum Gas Oil) Wax was procured at low cost from Silver Eagle Refinery in Woods Cross, Utah. As seen in Figure 2.2, the LVGO wax features a lower and broader distribution. Figure 2.3 presents a simplified view of these waxes.[61]

These waxes are mixed into Chevron Superla-7 white mineral oil; this mineral oil is colorless, odorless, and contains very low concentrations of wax (components over carbon number 19). The downside of using a mineral oil is a virtual absence of components smaller than C-12 (this mineral oil ranges from C-15 to C-18, with the majority component being C-16).

Using a controlled-stress rheometer (gel point)[18] and FTIR spectroscopy (WAT)[15] to measure the oil properties, the combination of these two waxes gives a variety of results; higher food-grade wax concentrations lead to higher WAT and gel point, while higher LVGO wax concentrations lead to a greater difference between WAT and gel point, but lower WAT.

The final and accepted composition used in this study was 1.5 wt% food-grade wax, 6% LVGO Wax, and 92.5% Superla-7 mineral oil. This provided a total wax percentage of roughly 7%, which was more than enough to ensure gelation. This formulation ensures a WAT of 19 °C and a gel point of 7.5 °C, giving a difference of about 12 °C. Figure 2.4 presents the WAT measurement of the accepted composition for this research, and Figure 2.5 shows the gel point measurement.

2.1.2 Viscosity and Density

With the formulation complete, a full analysis of viscosity and density was made. Early viscosity testing was conducted using a standard controlled-stress rheometer, but as explained earlier these rheometers have issues when measuring properties of slurries. As such, viscosity of the oil under clean and slurry conditions was also measured using the flow loop explained in the following section.

Density can be measured using a vibrational densitometer. The Anton Paar densitometer used in this research takes a sample loaded into a thin tube. This tube is vibrated electromagnetically while the vibrational period T_v is measured and output in μs. By changing the temperature of the cell and allowing a steady state to be reached, the output signal can be correlated to density in g/cc using Equation 2.1.

$$\rho = AT_v^2 + B \tag{2.1}$$

In Equation 2.1, parameters A and B are functions of temperature and ρ is the physical density. In order to generate accurate and realistic results a complete listing of A and B parameters for all temperatures tested must be compiled. To obtain these constants, at least two known samples (i.e., dry air, deionized water, pure ethanol, etc..) can be loaded and tested at each temperature. Since density is exactly known in these cases, A and B can be selected such that the parameters are identical between the tested substances. This selection can be done with analytical software such as MATLAB, Polymath, or Excel. The general setup of the densitometer is presented in Figure 2.6.

The vibrational densitometer is difficult to use with multiphase solutions, i.e., precipitated waxes. During phase transition, the behavior of the vibrating tube can be unpredictable; as such, all density measurements must be done above WAT. However, it is reasonable to assume that a linear model used to predict density holds for multiphase solutions.

Figures 2.7-2.9 show the rheometer and densitometer results for the final model oil composition. In Figure 2.9, the viscosity is shown as a series of curves; this is because an oil below its WAT is technically no longer a Newtonian fluid. With precipitated wax crystals the oil exhibits non-Newtonian, shear-thinning behavior.

2.1.3 Wax Solubility

Using the DSC method explained in section 1.3.3.3, as well as the commonly-used FTIR method of Roehner and Hansen (2001),[15] estimates for the solubility of the model oil were generated (as previously explained, CPM was not available for this research). Figures 2.10-2.13 present the steps for finding the experimentally measured solubility of the model oil using DSC. Figure 2.14 is the solubility derived using FTIR.

In Figure 2.10 a higher cooling rate was used since it generated smoother and more reliable and repeatable results. However, there is some supersaturation within the sample cell which reduced the apparent WAT. There will be some error due to rapid precipitation once the supersaturation barrier is overcome.

In Figure 2.11, the raw data are adjusted to the actual WAT. Furthermore, all data deemed not related to phase transition is removed. The adjusted data are fitted

with a linear baseline from the adjusted apparent WAT and the point at which the sample reaches a steady state (affected by the bias and best guess of the operator). With the data normalized as shown in Figure 2.12, the DSC data can be subjected to a cumulative integration (Equation 1.2) to develop an estimate of solubility.

In Figure 2.13, the solubility curve obtained via DSC is scaled to the actual WAT and the total known wax concentrations. Given that the majority of the wax in the model oil is from LVGO (which has a lower carbon number distribution than normal food-grade wax) this result is fairly believable. Furthermore, considering the presence of LVGO wax content below C-19, it is reasonable to assume precipitation would continue below 0 °C.

As a means of comparison, the method developed by Roehner and Hansen (2001)[15] was also employed. These results are show a shallower onset below WAT than the DSC results, and are shown in Figure 2.14.

The trouble with the shallowness of the slope of Figure 2.14 is that it should approach zero (horizontal) when nearly all the wax is out of solution. The solubility of the model is likely found somewhere between these results (DSC tends to underestimate solubility, while FTIR tends to overestimate[25], though these data would suggest the opposite). Taking this in mind, the best-guess curve from the DSC results was selected as the solubility of the model oil for further use in this research.

2.2 Flow Loop Design

For the purposes of this research, a series of flow loops were created. The final design, FLv3.2 (Flow Loop version 3.2), was used for the bulk of all

experiments. Appendix A describes the development of the flow loops in their entirety; presented here are the details of FLv3.2.

2.2.1 Design FLv3.2

As shown in Figures 2.15 and 2.16, FLv3.2 is a recycled flow loop. Fluid is constantly recirculated during conditioning (and deposition testing) by pumping from a central reservoir, through the conditioning and experimental test sections, and then back to the reservoir. Pressure and temperature measurements are made at key locations; transducers are situated at the inlet and outlet of the two four foot experimental, pipe-in-pipe heat exchanger test sections (one made with stainless steel, the other clear acrylic). Both have a flow diameter of 0.4 inches, while temperature is measured near the same locations. A third, high-accuracy temperature measurement taking place just before the test section inlet. Figures 2.15 and 2.16 show the actual setup.

2.2.2 Design Components

FLv3.2 utilizes a number of high-quality components to ensure the best and most repeatable results. Table 2.1 presents these components.

The ISCO syringe pump requires a calibration to match volumetric flow rate to pressure loading rate. For this research a single rate from the ISCO was used (the needle valve soon to be described was used much more extensively due to a higher range of use). The rate of 80 mL/min in the syringe pump equates to a shear stress loading rate of 0.5 Pa/s (this accounts for the length of the gel).

The high-control needle valve used for some restart tests requires a calibration to know exactly what pressure loading rate (or shear stress loading rate through calculation of Equation 1.1) is being applied at each setting. Table 2.2 presents this calibration.

2.2.3 Benefits of Design FLv3.2

The flow loop FLv3.2 is designed to conduct both deposition and gelled restart tests with a minimal amount of error. This is accomplished by using high-quality transducers for pressure measurements, low shear/impact pumping systems, and a large fluid volume to reduce irregularities. With two test sections side by side with a linked (by three-way valve) coolant system, FLv3.2 is robust and able to conduct a variety of rheological tests under varied cooling and pressure loading conditions. Furthermore, the inclusion of PIV and particle sizing hardware give it a very wide functional range.

Early in flow loop testing, it was found that while the Moyno progressive cavity pumps were indeed effective at constant flow delivery, a pulsing effect still occurred with each revolution. This pulse was detectable by the transducers with a pressure scatter of +/-0.4 psig – an unacceptable value. To overcome this issue, a simple pulse dampening system was devised.

The pulse dampening system is simple and required no specialized equipment, aside from the proper Swagelok fittings and connections. Coming out of the pump, the fluid is forced into a 90-degree turn before splitting off to the test sections. At the 90-degree turn, a section of pipe was added vertically and in line

with the incoming flow. This straight pipe is capped with a high-quality needle valve that leads to the pressure loading system, but when closed this cap forces a large section of air to remain in the vertical section. As fluid moves towards the 90-degree turn, the pulses press against the air section, which compresses slightly reducing the pulse scatter down to +/-0.02-0.05 psig.

Two types of test sections were incorporated into the flow loop, these being a stainless steel test section and an acrylic section of identical dimensions. While there was some concern over the comparability of results from these (wall roughness between the two sections is different, and at pressures above 3 psig gels in the clear section start to "slip", and there is a reduced thermal conductivity across the acrylic walls), overall the results presented in Chapter 4 show that the difference in gel strengths between the two sections is negligible. This difference was less than 5% of the higher value.

2.2.4 Downsides of Design FLv3.2

Flv3.2 is a low pressure (0-75 psig) system. It is not intended for high pressure flow, hydrates, or extremely strong gels. Unlike some of the previous versions (see Appendix A), FLv3.2 only incorporates two pressure transducers per test section; this means that axial pressures inside the gel cannot be measured. Furthermore, like many lab-scale flow loops, FLv3.2 cannot generate turbulent flow due to the oil viscosity, used pump capacity, and pipeline diameter. This means that all deposition tests fall within the laminar regime (Re < 2000) – something that field pipelines rarely exhibit in deposition-prone environments (virtually all turbulent).

2.3 Conditioning Loop Design

As seen in Appendix A, a number of designs were made to generate desired oil conditions prior to testing. All methods encountered the same problem: wax sequestration on cold surfaces. When wax is sequestered on a cold surface, it is literally removed from the experiment – effectively changing the composition of the oil. To eliminate this problem and to facilitate "Cold Flow" testing en masse, a separate but connected conditioning loop was devised.

The conditioning loop consists of a line running from the central reservoir through a Moyno progressive cavity pump, after which it is fed into a device known as the Scraped Exchanger (SCE), a pipe-in-pipe heat exchanger with a rotating blade that removes wax deposits (described in detail in the next section). This loop is responsible for all cooling/heating of the oil, and the SCE makes it possible to extend testing into the sub-WAT range.

2.3.1 Design Components

The conditioning loop utilizes a number of high-quality components to ensure the best and most repeatable results. See section 2.4.1 (The Scraped Exchanger) as this section presents these components and their details.

2.3.2 Benefits of the Conditioning Loop

The testing loop and conditioning loop provide two independent yet coexisting flows tied into the same reservoir. This is beneficial because the pressure

effects of one do not influence the other. Temperature effects are the only aspect shared between them.

In addition, the large volume of the SCE requires a high flow rate to generate meaningful cooling effects on the total reservoir volume. With a high flow rate, considerable mixing and avoidance of oil stagnation (unwanted warming to room temperature) is accomplished, generating more uniform oil properties.

2.3.3 Downsides of the Conditioning Loop

The internal volume of the oil side of the SCE is large compared to the diameter of the experimental loop tubing. This results in a fairly slow cooling process, especially when compared to a regular submersed coil setup. As a result, conditioning takes a long time relative to testing time. However, this is beneficial since it gives comparable cooling conditions to in-field pipelines.

The SCE internal blade does not come into direct contact with the wall. While this prevents fatal failure of the SCE, a thin layer of insipient gel would be expected to persist on the wall. The original SCE testing showed no discernible wax layer after cooling (SCE was opened and visually inspected immediately after a cooling procedure), and the WAT and gel point match rheological data. Both of these observations indicate that if this layer exists, it either is short-lived (i.e., the blade is removing it with the removal of larger deposits) or it has such a small amount of wax that it is not affecting the composition of the oil in any detectable way.

2.4 Specialized Equipment

Three highly specialized pieces of equipment were used in this research to achieve the desired conditions and to detect and record important parameters: the Scraped Exchanger, the Particle Imaging Velocimetry system, and the CantyVision InFlow® system.

2.4.1 The Scraped Exchanger

The SCE was designed and constructed for one purpose: prepare an oil for testing at any desired, reasonable condition (reasonable being conditions seen industrially). As mentioned, it is a simple pipe-in-pipe heat exchanger with a "twist": a rotating blade, vane configuration, that removes wax deposits during cooling. The blade is held in place with two bearing shaft seals at both ends of the exchanger. The path of these blades completely covers the cooling surface to prevent buildup. It is rotated at 5 rpm with a low-speed motor. Figure 2.17 shows the SCE installed; see Appendix B for details on the development and design of the SCE.

As wax is mechanically removed it returns to the flow (testing has shown no buildup on the blades), thus preserving as best as possible heterogeneous flow conditions. The SCE was designed using heat transfer principles, and this development can be also found in Appendix B.

The inside wall of the oil side of the SCE is cold, and wax forms on it as the oil sweeps across. Immediately after formation, a rotating vane blade moves across the deposit. If the deposit is thick enough it will be forcibly removed, and if it is weak enough the shearing forces created by the blade and flow will disrupt and remove it.

The dimensions and components of the SCE are presented in Table 2.3. Given that the SCE is the major component of the conditioning loop, both are presented together.

2.4.2 Particle Imaging Velocimetry

Particle Imaging Velocimetry (PIV) is a novel means of measuring velocity flow profiles in transparent mixtures such as oil, water, gases, etc..[52,62] In this project, some PIV work with deposition was conducted (primarily in verifying the thickness model in Equation 1.7). The larger us of PIV was in the visualization of the movement of the gels under restart conditions. Figure 2.18 presents an artistic representation of PIV.

2.4.2.1 Basic Function of a PIV System

Generally speaking, PIV works by reflecting manipulated laser light off reflective particles (melamine) and into a camera system. Once captured, these images can then be analyzed for frame-by-frame deformation. To save memory and increase efficiency, timing selection in PIV studies is key. There are two time constants that need to be set carefully to gather quality images: step time and delta time.

In PIV, each step consists of two images being captured at high speed. Step time represents the time between the end of the previous step's second image and the start of the current step's first image. Delta time dt is the time between the two images of the current step. For high speed flow, a small delta time is critical to

gather good vectors; conversely, at low speed flow a larger delta time is needed. Delta time must be smaller than step time, but a question with regard to visualizing gel breakage is what exactly should one choose to be that delta time?

Considering that the movement of gel fragments at restart is exceptionally slow, picking too small a delta time will result in an undifferentiated velocity vector field. This was an issue in previous studies,[52] but, since we are looking specifically for a moment in time in which the gel breaks (and not profiles when flow resumes), it is possible to use the first image of each step (in other words, the step time) to create vector fields. This is a difficult maneuver; if the step time is too large, it is entirely possible to miss the breakage event. If the breakage is missed incorrect conclusions can be reached. Step time was universally chosen to be 100 ms. Delta time was varied from 0.5 to 10 ms; the longer delta time gave the best results but was still too small for slow pressure loading rates.

2.4.2.2 Laser Light Considerations

Using PIV for gaseous flows is fairly simple and requires little overhead. Visualizing liquid flow, particularly through multiple layers and/or if the fluid is cloudy, can be difficult without precautions. First and foremost, the laser light being emitted by the New Wave Research SOLO PIV system is at a frequency of 514.5 nm. This light is dangerous and can cause burns and blindness; at full power it can burn away metal and etc.h plastics. As such, material designed specifically to block out 514.5 nm light must be employed for personal protection (i.e., goggles) and as a filter for the camera. While this may seem counterintuitive (wouldn't the material

block light out from the camera?), this method results in splendidly clear fluid images. As laser light collides with the reflective particles the photon frequency is slowed down slightly, causing the particles to become illuminated even through the protective material. Furthermore, since all of the laser light at the normal frequency is blocked out, all that remains are the bright specks in the recorded images.

2.4.3 CantyVision InFlow® Particle Visualization System

The use of cross-polarized microvideography with CantyVision's InFlow® camera system has allowed the study of wax particle size effects on subsequent gel strengths. Of particular benefit is the fact that the InFlow® camera was designed to be a live-flow system – directly tapped from the main flow rather than a batch system. This means that crystal sizes can be measured almost exactly as they are when entering the test section(s). Figure 2.19 is a photograph of the CantyVision system as it is arranged for this research.

2.4.3.1 Basic Function of CantyVision InFlow®

In section 2.2.1, the schematic of FLv3.2 shows the CantyVision as a slipstream off the mainline. This allows a low speed stream of the fluid to enter the CantyVision camera under the same conditions as it is when entering the test sections. As the fluid enters the camera, a small window is recorded; in this window, each screen pixel represents ~0.7 microns. The window is situated between two flat, glass plates separated approximately 2-3 mm apart. By carefully focusing the

camera's focal point directly between these plates, one can obtain the highest quality images of wax particles.

For a transparent model oil, it is difficult to view precipitated particles: the wax particles and the accompanying fluid have basically the same color and opacity. This makes optical viewing of the crystals extremely difficult, if not impossible. To eliminate this problem, the CantyVision system can be fitted with a cross-polarizing filter. When light passes through the filter, it is polarized – all light rays are limited to a single direction. As this light hits a flat crystal face it is reflected in a new direction causing it to "shine" in a field of darkness (the fluid itself does not distort the polarized light, causing it to appear darkened).

With the wax particles illuminated, the CantyVision system can be adjusted to capture light particles instead of dark particles. With the system ready, a video of the flow is recorded, and the software begins looking for particles that fit the user-determined particle criteria. Simply stated, the CantyVision software takes various measurements of the captured particles according to brightness thresholds specified by the user. If the threshold is too low, no particles will be counted; if it is too high, the background will also be included, giving wildly inaccurate results. The key is to choose a threshold that will capture the brightest, clearest particles; even though not all particles in the images are captured (this is anticipated since the focal point is in the center of the flow space) enough images will give a good, repeatable representation of particles.

CantyVision software collects numerous data surrounding the captured particles, but the most useful and speedy measure of particle size is to look at the

mean equivalent circular diameter. This number (given in microns) is not the actual size of the particles, but rather a measure of the mean particle size based on the number of particles measured and the distribution of the particle sizes (equivalent circular diameter is a useful way to represent the size distribution). Wax crystals are rarely circular. For more information regarding the function of the CantyVision InFlow® system, please view the product literature on the CantyVision website (www.jmcanty.com).

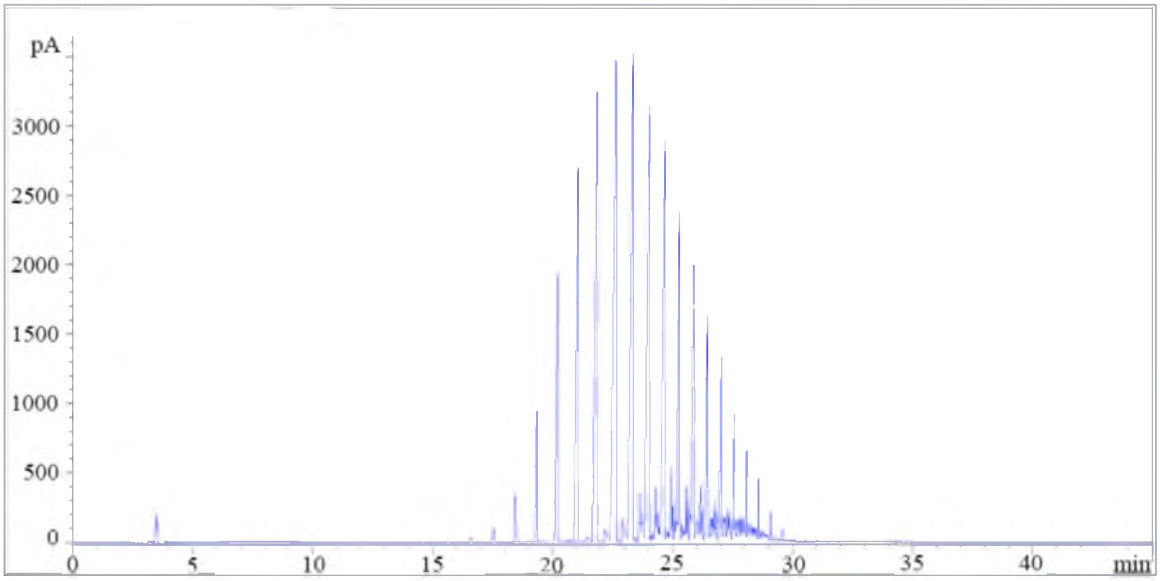

Figure 2.1. Gas chromatogram of the paraffin wax used in this research. Note the narrow range of peaks, indicating a limited polydispersity.

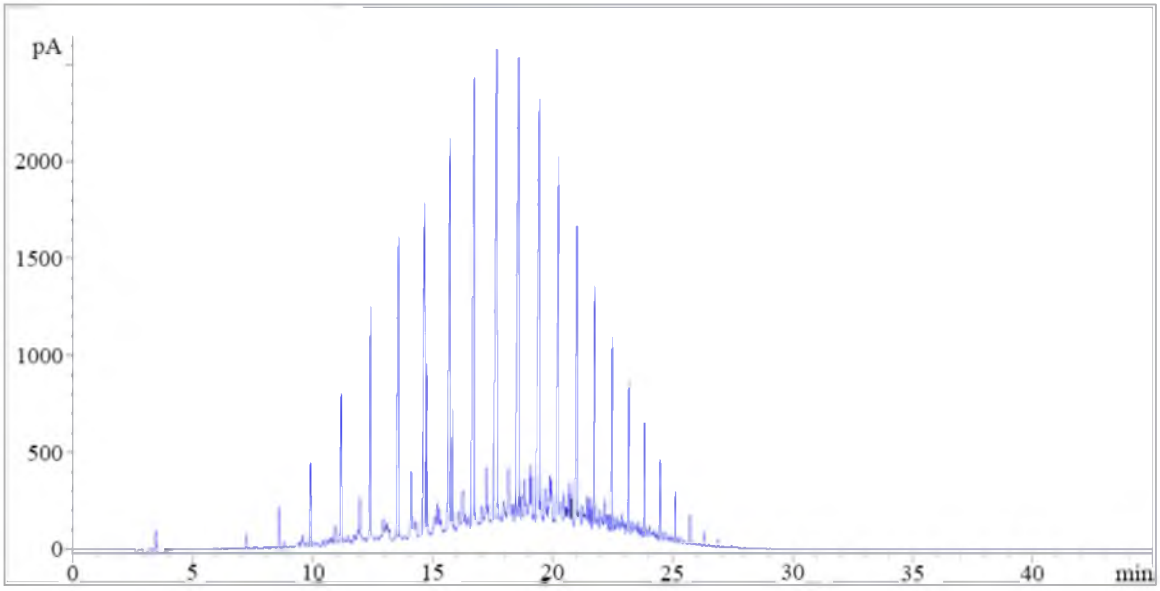

Figure 2.2. Gas chromatogram of the LVGO wax used in this research. Note the broadness of the range of peaks compared to the paraffin wax.

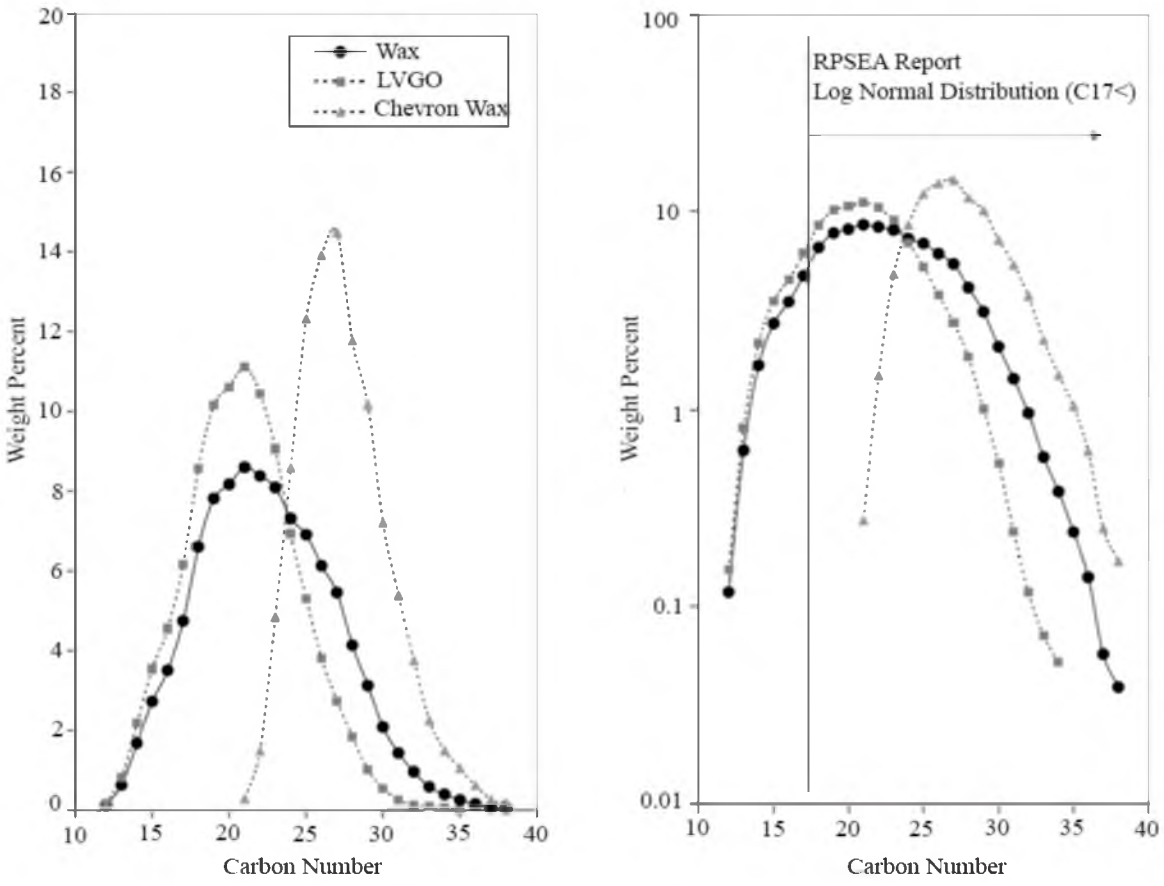

Figure 2.3. Carbon number distribution for Food-Grade Chevron Wax, Silver Eagle LVGO Wax, and the final blend (here simply called "Wax"). Not the broadness of the final composition compared to regular food-grade wax. Distribution image prepared for RPSEA report, "Wax Control in the Presence of Hydrates"[61] by the research team.

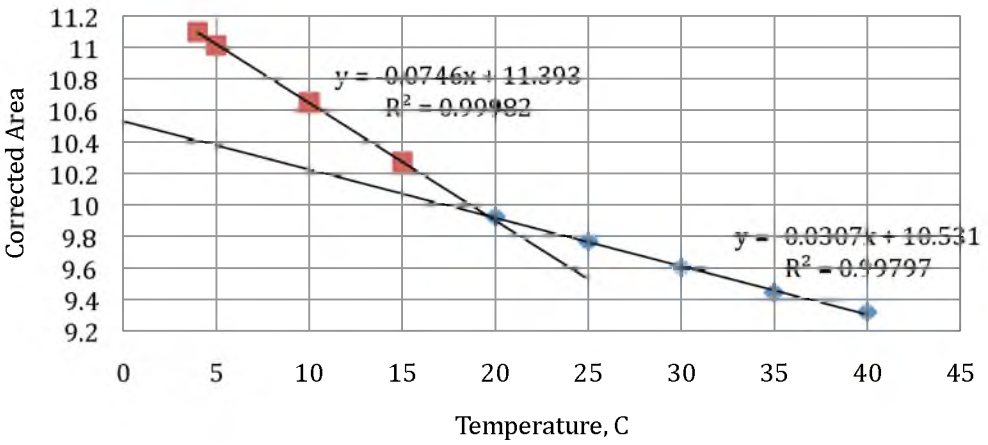

Figure 2.4. WAT measurement using the FTIR method of Roehner and Hansen (2001).[15] Accepted model oil composition gives a WAT of approximately 19 °C for a very slow cooling rate (>0.1 °C/min).

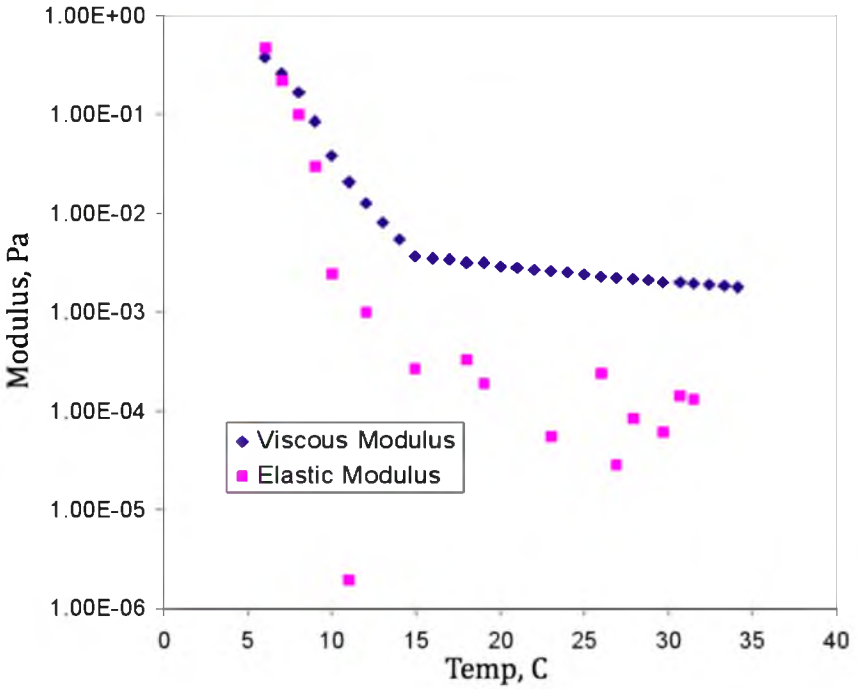

Figure 2.5. Gel point measurement using a controlled-stress cone-and-plate rheometer using the crossover method.[18] This method gives a gel point of approximately 7.5 °C ±0.5 °C (value confirmed with flow loop restart data).

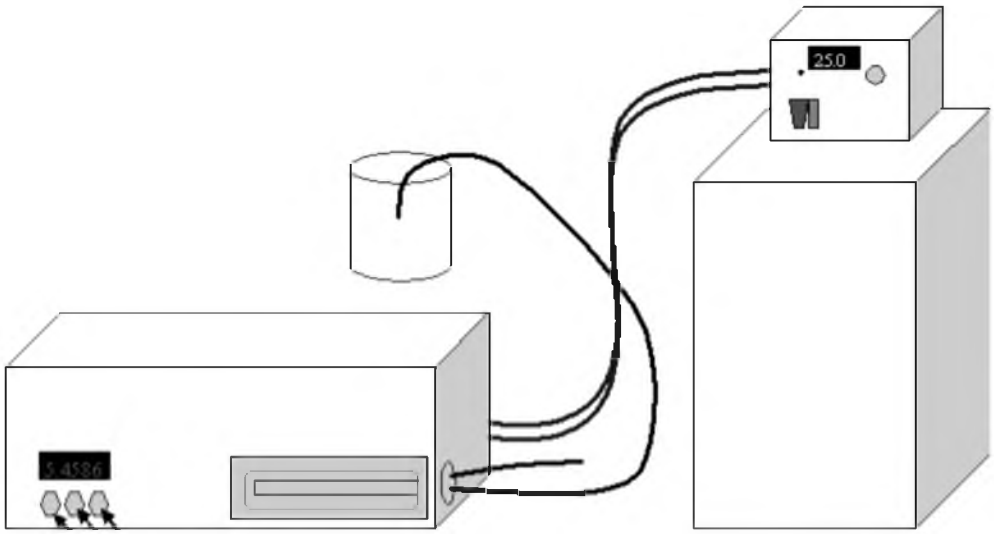

Figure 2.6. Densitometer setup. Sample is added to u-tube through open line at the bottom center.

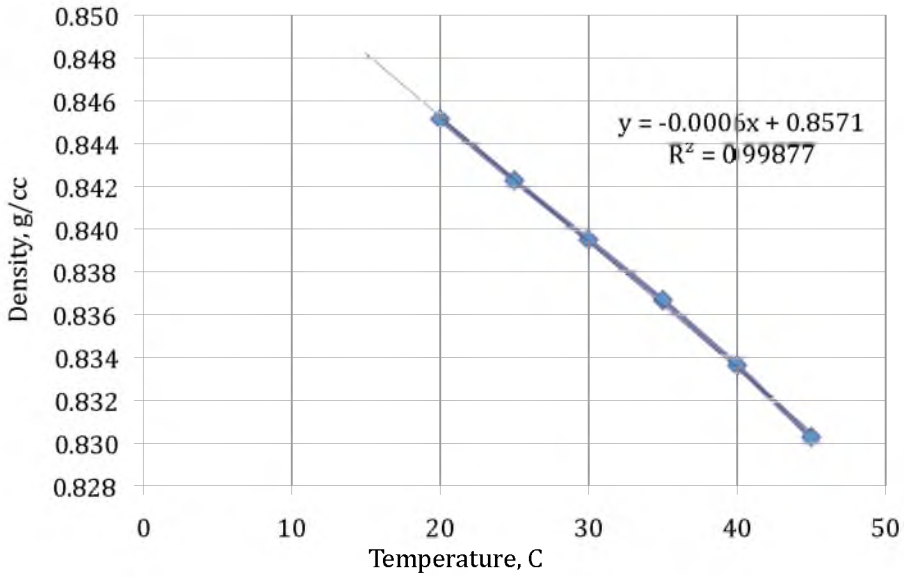

Figure 2.7: Measured density of LVGO model oil using Anton Paar densitometer. Inset equation is the linear model for predicting density based on the recorded data.

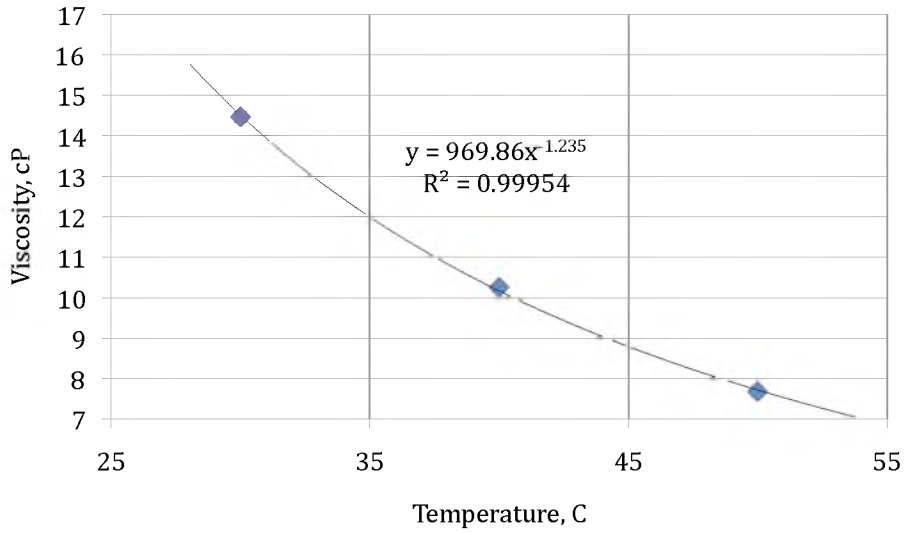

Figure 2.8. Newtonian-range viscosity measured using TA Instruments controlled-stress rheometer. Inset equation is a power law model for predicting viscosity based on recorded data.

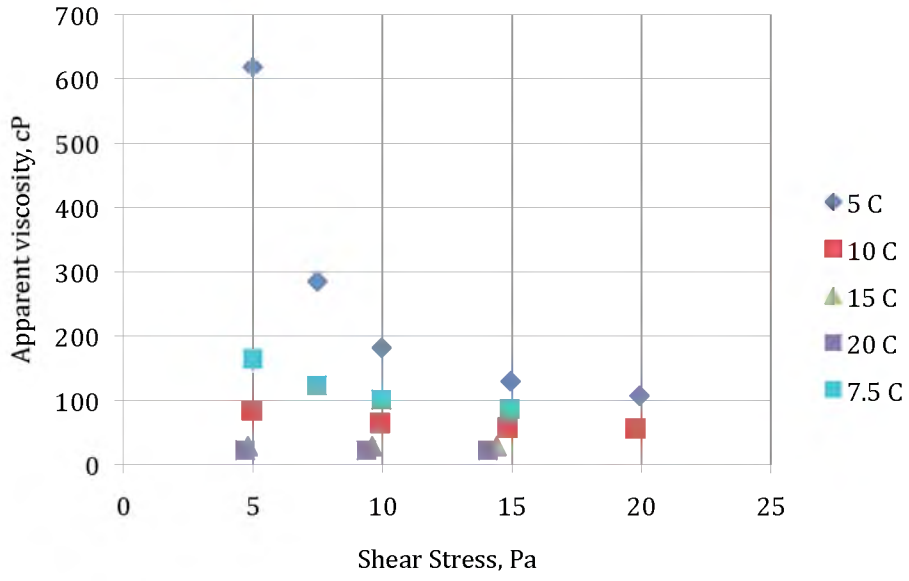

Figure 2.9. Non-Newtonian-range viscosity (T<20 °C) measured using TA Instruments controlled-stress rheometer. X-axis presents the shear stress applied to the fluid at each temperature. Note the sharp jump in viscosity at 7.5 °C marking the onset of gelation.

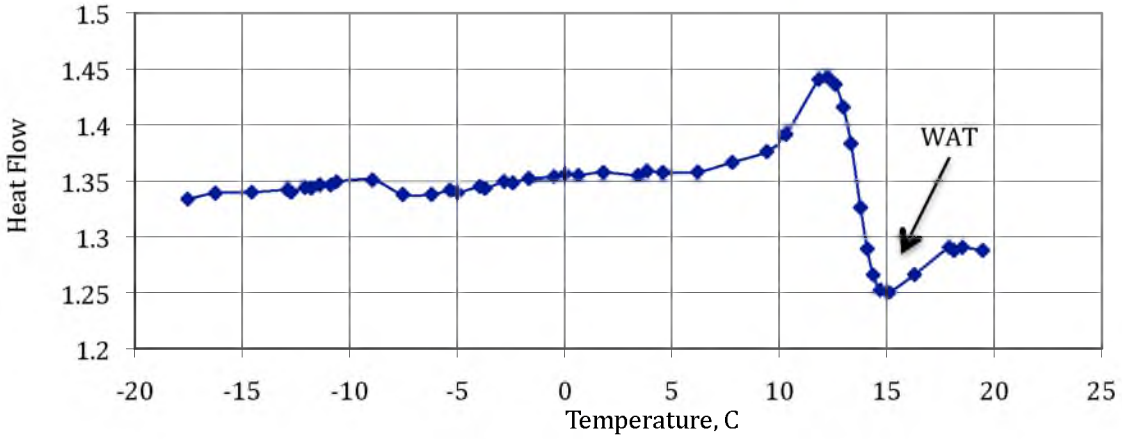

Figure 2.10. Raw DSC data obtained from model oil using a cooling rate of 5 °C/min. Note the apparent WAT is nearly five degrees lower than the FTIR-measured value.

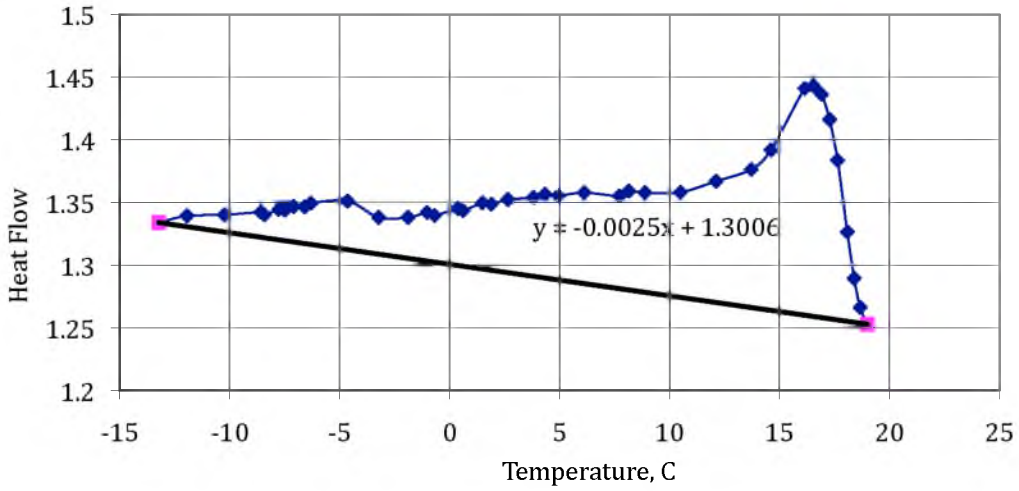

Figure 2.11. Adjusted DSC data including linear baseline. Using FTIR WAT result, data are scaled so that the apparent WAT matches the actual WAT.

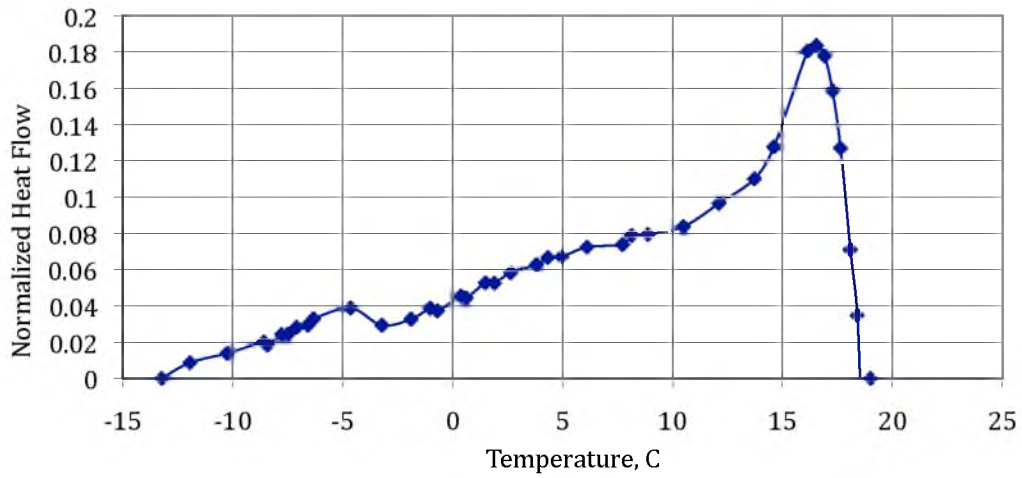

Figure 2.12. Normalized DSC data found by subtracting the adjusted data from the linear baseline.

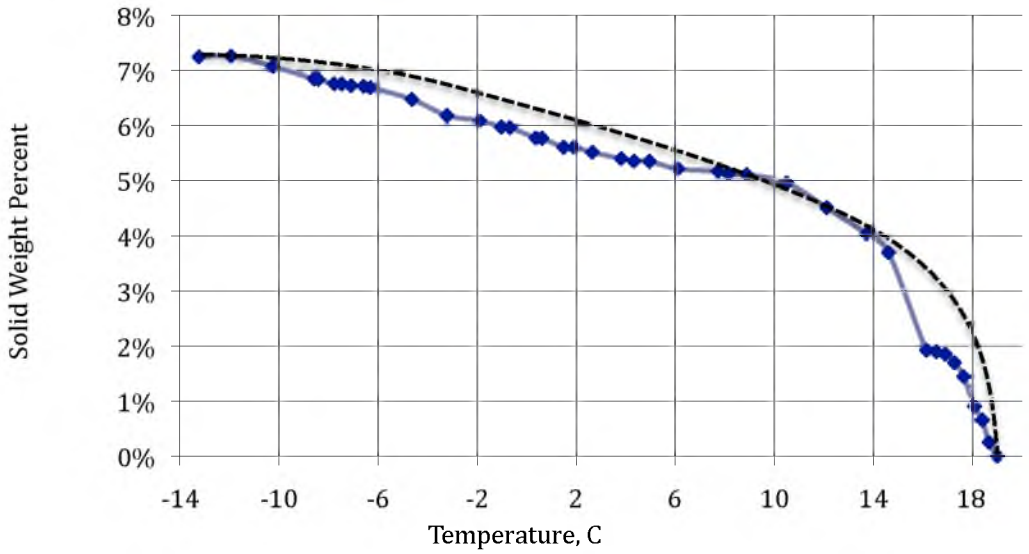

Figure 2.13. Finalized solubility curve generated from DSC results. Dashed line represents best-guess estimate for actual solubility based on the data and supersaturation correction.

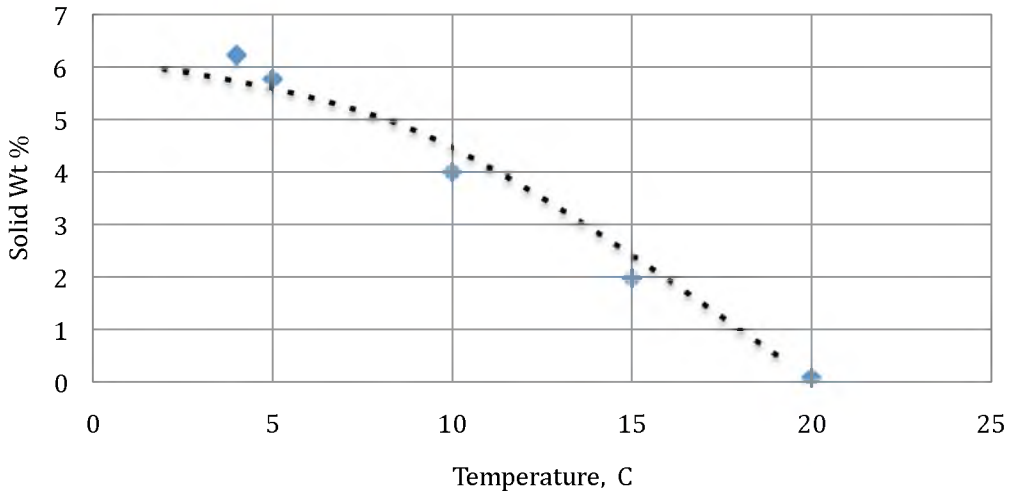

Figure 2.14. FTIR-obtained solubility with estimated best-guess solubility (dotted line). Data obtained from WAT measurement (Figure 2.4 of section 2.1.1).

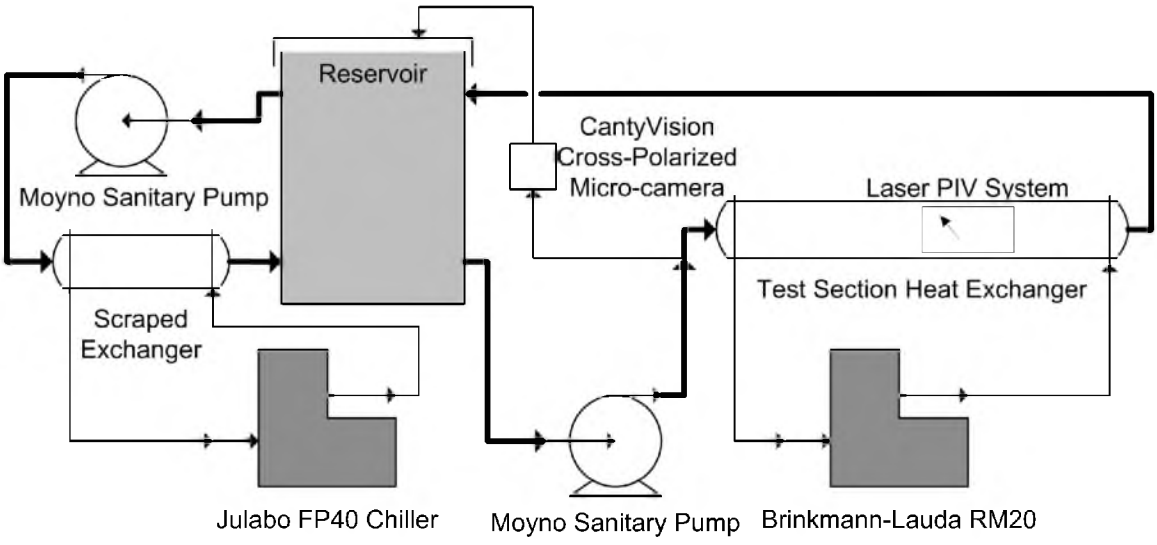

Figure 2.15. Schematic drawing of FLv3.2. The main experimental loop is seen to the right of the reservoir, while the conditioning loop is to the left. Bold lines represent the main oil flow and directions, while thinner lines represent the coolant and slipstream oil flow for the CantyVision InFlow equipment.

Figure 2.16. Photograph of FLv3.2 showing most of the experimental flow lines. Portions of the conditioning loop are visible in the upper center portion of the image. The CantyVision system is visible at the far left, while the PIV system is at the upper left corner. The silver tank in the upper left is the reservoir, and the two temperature controllers at visible at the bottom. The two test sections (steel and acrylic) are seen in the center.

Table 2.1. Flow Loop version 3.2 component list with comments.

Flow Loop Component	Comment
IKA RW20DZH mixer motor	Mixing device for reservoir
Arrow Engineering 3" rotor	3" impeller for 9" reservoir to ensure excellent mixing
Moyno 500 Sanitary pump	Progressive cavity pump for test section, Baldor motor
Dayton 4Z829H DC control	Pump speed control for test section
Moyno 34408 pump	Progressive cavity pump for conditioning loop, Baldor motor
AC Tech M1105SB microinverter	Pump speed control for conditioning loop
Julabo FP40 with HP control	Temperature controller for oil, 50/50 ethylene glycol/water mix, pt100 RTD sensor
Brinkmann Lauda RM20	Temperature controller for test section, pure ethylene glycol, 4 gpm
Omega J-type thermocouple	General temperature measurement
Omega PX309 transducers	General pressure measurement, 0-15 psig range
National Instruments NIcDAQ-9174	Data acquisition system, 4 card input
Rex Engineering 3103 low speed motor	SCE blade motor, 0-5 rpm
Dixon Sanitary clamps	SCE seal clamps, high pressure, synthetic rubber gasket
Solo PIV Nd:YAG laser	PIV laser assembly, 514.5 nm laser light
LaTech PIV software	PIV software for image capture and analysis
InFlow VD-4192-352	CantyVision camera setup
Omega HFL7102A	Flow meter, 0-2 gpm range
Omega HFL7120A	Flow meter, 0-20 gpm range
Nupro SS-4BMG	Special needle valve for controlled-rate restart
ISCO 500 D	Teledyne ISCO pump for low rate restart
Swagelok fittings and tubing	1/2" and 3/4" for various components
High-density plastic tubing	1/2" for various components, up to 75 psig
Steel Test Section	0.4" ID, 0.5" OD, 1.5" jacket tube, stainless steel, ¾" coolant ports, 4' length
Acrylic Test Section	0.4" ID, 0.5" OD, 1.5" jacket tube, clear acrylic, ¾" coolant ports, 4' length
Reinforced plastic hose	3/4" for pump loading and conditioning loop

Table 2.2. Needle valve loading rate calibration. Wall shear stress loading rate calculated utilizing Equation 1.1.

Valve Setting	Pressure loading rate, psi/s	Shear stress loading rate, Pa/s
9	0.117	1.7
10	0.328	4.7
15	0.724	10.4
20	1.12	16.1
25	1.37	19.7
30	1.62	23.3
40	1.99	28.6
50	2.6	37.3

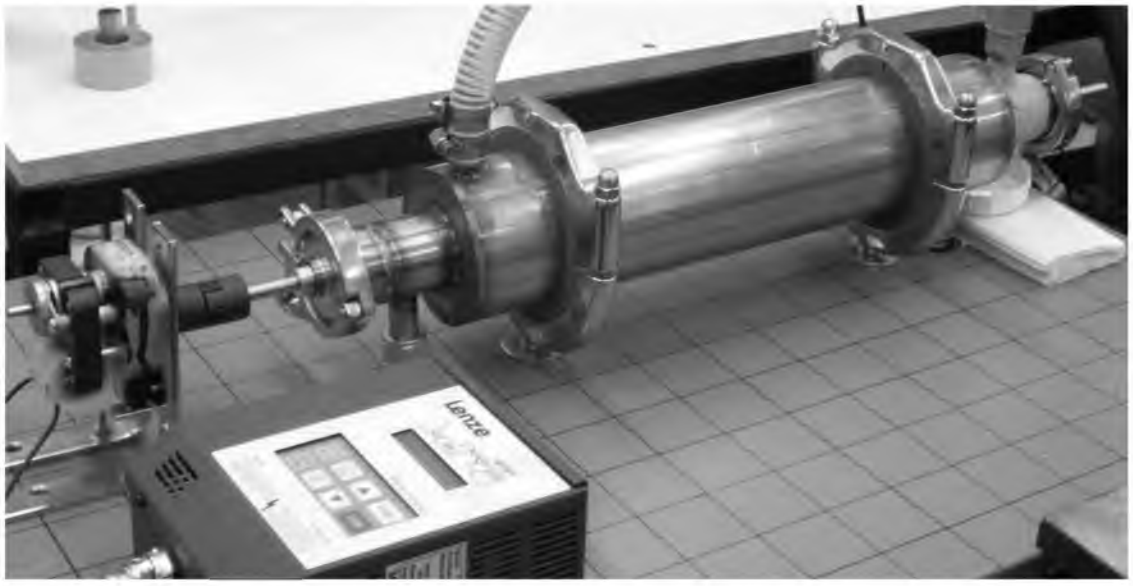

Figure 2.17. Photograph of the Scraped Exchanger attached to the Flow Loop version 3.2. Blade motor is on the left, and the conditioning loop pump box is at the bottom of the image.

Table 2.3. List of SCE and conditioning loop components.

Design Component	Characteristics
Inner pipe (oil flow)	2" OD stainless steel pipe, 1/8" wall, length 21"
Outer pipe (coolant annular flow)	4" OD stainless steel pipe, 1/8" wall, length 18"
Fluid ports (oil and coolant)	3/4" stainless steel pipe, 4 count, 1/16" wall
Tubing	High-pressure reinforced plastic tubing, 3/4" ID
Rotating scraper blade	18.2" vane length, 4 vanes, 1/8" thickness, 0.05" tolerance
Rotating shaft seals	Low pressure bearing (<20 psig), 1/4" diameter
Seal-SCE clamps	High-strength sanitary clamps, stainless steel, rubber gasket
Scraper motor	Low speed (~5 rpm) one-directional motor, AC power
SCE pump	Moyno progressive cavity pump, model 34408
SCE pressure measurement	Omega PX309 0-15 psig

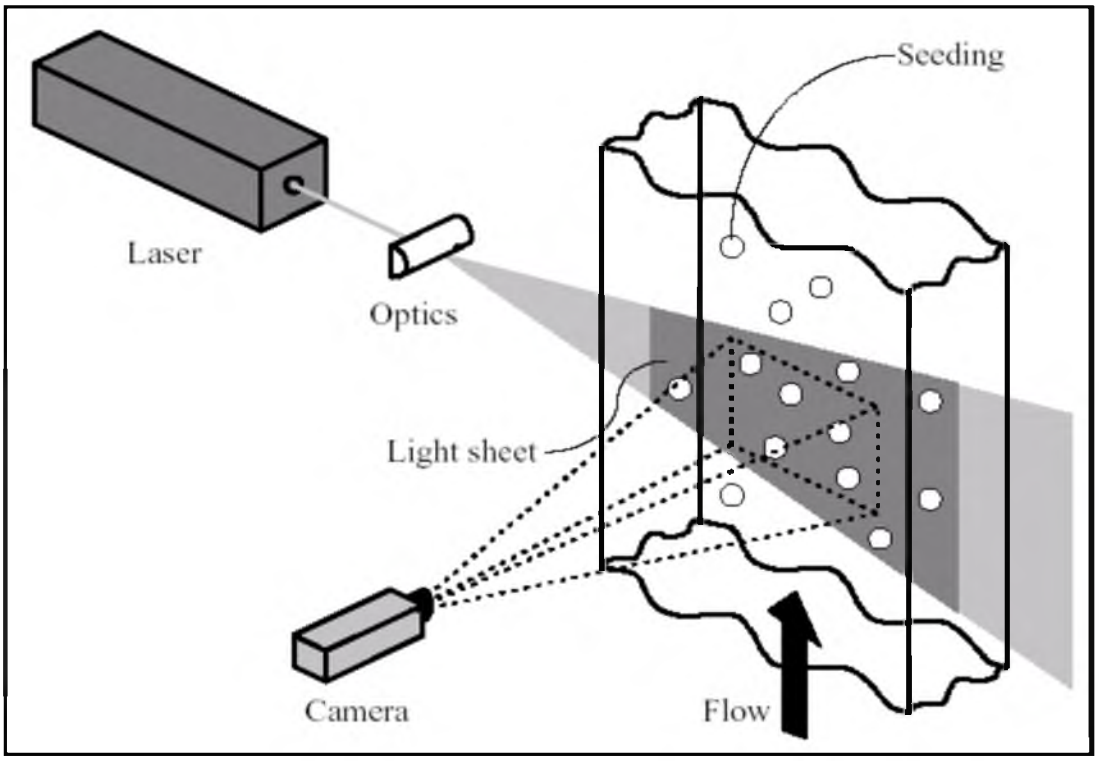

Figure 2.18. Basic function of the PIV system. Laser light is broadened into a beam that passes through the fluid seeded with fluorescent particles. A camera is arranged perpendicular to the laser light and records the light as it bounces off from the fluorescent particles.

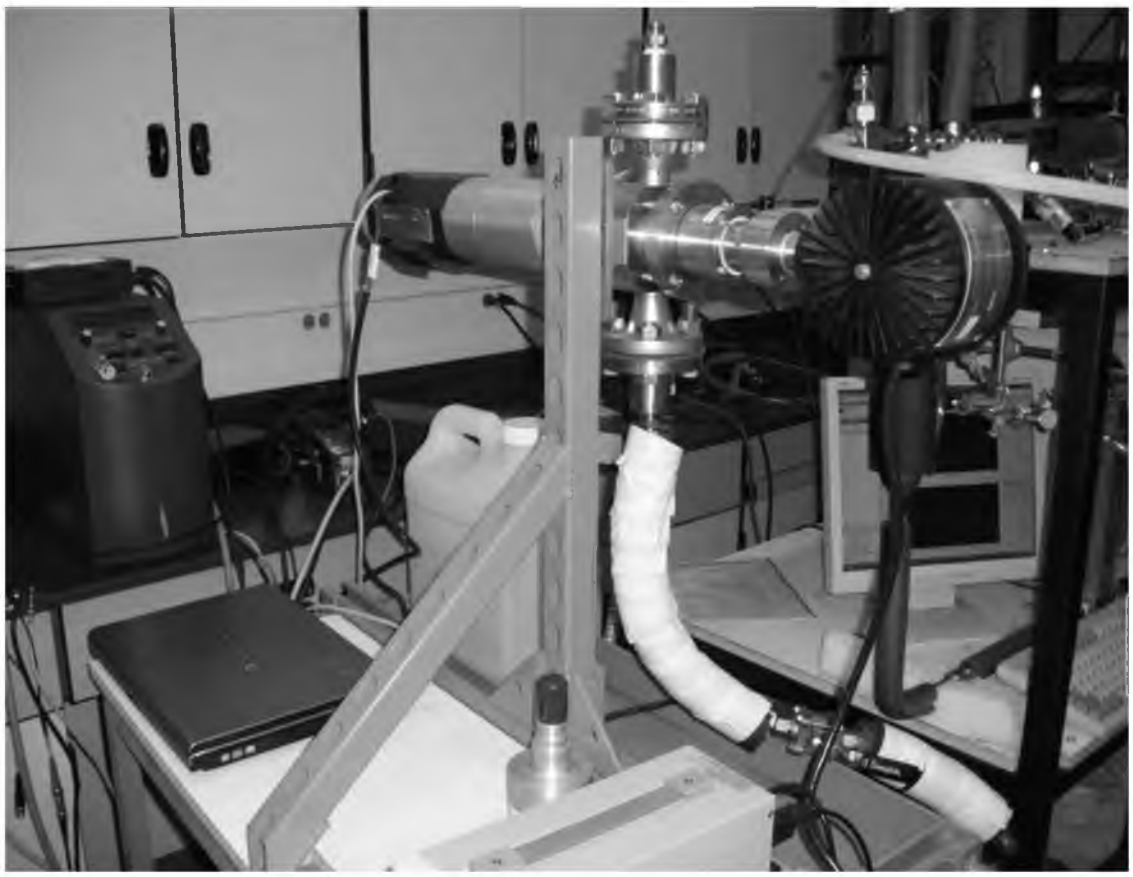

Figure 2.19. CantyVision InFlow ® camera system. In this arrangement, oil flows up into the camera through the white, insulated tube, after which is passes through the recording system and out the top. Cylindrical object to the right is the light source, while the assembly to the left of the central recording area is the camera.

CHAPTER 3

EXPERIMENTAL PROCEDURES

A specific procedure was followed to ensure the best results for each test. Beginning with a conditioning step to remove shear history (previous particle agglomerations, unnatural particle agglomerations, etc.), care was taken to properly cool the oil as needed without exceeding reasonable limits of cloud point depression[16] exhibited through the cooling process in the SCE. To assist in understanding the procedures, Figure 3.1 presents a more detailed view of the flow loop schematic with key valves numbered.

3.1 Conditioning Procedure (General)

All tests are started in the same fashion. All tests require a clean, hot oil to erase any shear history relics from previous tests. Furthermore, ensuring a constant starting point improves repeatability and gives better confidence in the results. The steps involved in preparing the oil for testing are as follows:

1. Start mixing oil in the reservoir at 450-500 rpm (care must be taken to not mix too aggressively; this prevents air bubbles from entraining into the liquid phase; these bubbles can corrupt restart results)

2. Start oil flowing through the experimental test section (acrylic or steel, whichever is to be tested) at 0.5-0.75 gpm; ensure proper valves are open (1, 2, and 4) to ensure flow between reservoir, experimental section pump, test section, and back to the reservoir
3. Start oil flowing through the conditioning loop at 1.5 gpm; ensure valve from reservoir to conditioning pump (5) is open
4. Set conditioning loop temperature controller to 50 °C
5. Turn on scraping mechanism for the SCE at full power (or as desired for particle size control) and turn on the cooling fan for the blade motor
6. Set experimental test section controller to 35 °C; adjust coolant valve to proper test section
7. Allow system to run in this configuration until oil temperature is at 35 °C (~17 °C above initial WAT); all four temperature sensors (three thermocouple, one RTD) should read at or above 35 °C
8. Begin cooling procedure specific to test

3.2 Heterogeneous versus Homogeneous Deposition

To perform a deposition test, flow through the test section and constant test section coolant temperature must be maintained. The following steps will ensure a good, repeatable deposition test. For heterogeneous testing, the oil during the actual data recording session must be a solid-liquid slurry, as explained earlier in this dissertation. For homogeneous testing, the oil must be hot (i.e.,above WAT during the entire data recording session).

1. Follow conditioning procedure
2. Adjust test section coolant valve to the experimental test section NOT being used
3. Set experimental test section coolant temperature to the desired ambient temperature for deposition testing
4. Adjust flow of experimental section pump to desired flow rate for deposition testing
5. Lower the conditioning loop coolant temperature to 10-15 °C below desired oil temperature for heterogeneous (slurry) testing (for example, to test deposition in a 15 °C fluid, the conditioning loop coolant section would need to be set to approximately 0 °C – of course, room temperature will have an effect, so this needs to be watched carefully)
    a. For homogeneous testing, lower the conditioning loop coolant temperature a few degrees below desired set point
    b. An automatic controller can be set to external input based on the RTD output
6. Once oil temperature has been reached, start the LabView software and record the inlet and outlet temperature and pressure for the appropriate test section
7. Once data are being recorded, switch the pre-cooled test section coolant line back to the test section being used to officially begin the deposition test
8. Take care to monitor the oil temperature until a definitive steady-state condition has been reached

a. Since the conditioning loop response time is fairly slow, manual adjustment of the conditioning loop test section may be required to prevent overcooling/overheating of the oil (and very poor control)

9. Maintain oil temperature until testing is complete
10. Analyze pressure data using equation 1.7 to determine deposition thickness and rate of growth

3.3 Heterogeneous Effect on Gel Point

Prior to any gel tests, it is important to know just how much slurry-type heterogeneity affects the gel point of the model oil. If the gel point is lowered too far with each degree (i.e.,if the clear oil's gel point is 7 degrees, what is the gel point if the oil is a slurry with temperature below WAT at shutdown?), the conclusions surrounding heterogeneous gels may be convoluted.

1. Follow conditioning procedure using a flow rate of 0.75 gpm for consistency
2. Lower experimental test section coolant temperature to 20 °C, with valve set to the section being used
3. Lower conditioning loop temperature to approximately 15 °C below target shutdown temperature (for example, to reach a fluid temperature of 16.6 °C, a coolant temperature of 1 °C will suffice – although care must be taken to watch the temperature with manual adjustments as needed)
4. When oil temperature reaches 20 °C, lower the experimental test section coolant temperature by 0.5 °C; repeat this sequence until the new experimental section

set point becomes the target oil temperature (this simulates cold flow conditions in flow with no deposition)

5. When the flowing oil temperature reaches the set point (thus matching the new experimental test section coolant temperature) shut off all pumps, the mixer, and the SCE blade and close the upstream valve (suction side) of the pump (2); also shut off the conditioning loop temperature controller
6. With flow stopped, change the experimental test section coolant temperature to the desired temperature; for gel point testing, start at 9 °C, with the next test being at 8 °C and so on
7. When the final temperature is reached, allow one hour for steady state to be reached inside the fluid
8. With the air regulator valve closed (and air loading system equilibrated with atmospheric pressure), start recording pressure data on the test section being used and open the loading valve (6) to valve setting 20 (1.12 psi/s)
9. With the air cylinder open and the regulator set to ~30 psig (the valve leading to the low pressure gauge should be closed, and the 3-way valve on the ISCO pump must be directed to the loop, not to vent) open the regulator valve; the fluid inside the test section will now be pressurized
10. Monitor the maximum pressure differential between upstream and downstream

3.4 "Cold Flow" Settled Restart

When considering "Cold Flow" shut down, the first condition to look at is isothermal settling. This involves wax particle settling with no subsequent cooling,

and theoretically no gel formation. Once settled, pressure is applied and the settled particles are observed visually. This test is only conducted once as a demonstration of "Cold Flow" settled restart.

1. Follow conditioning procedure
2. Lower experimental test section coolant temperature to 20 °C, with valve set to the section being used (in this case, use the clear acrylic test section)
3. Lower conditioning loop temperature to approximately 15 °C below target shutdown temperature (for example, to reach a fluid temperature of 16.6 °C, a coolant temperature of 1 °C will suffice – though care must be taken to watch the temperature with manual adjustments as needed); for this test, the target temperature must be below WAT
4. When oil temperature reaches 20 °C, lower the experimental test section coolant temperature by 0.5 °C; repeat this pattern until the new experimental section set point becomes the target oil temperature (this simulates cold flow conditions in flow with no deposition)
5. When the flowing oil temperature reaches set point (thus matching the new experimental test section coolant temperature) shut off all pumps, the mixer, and the SCE blade and close the upstream valve leading out of the pump (2); also shut off the conditioning loop temperature controller
6. Maintain experimental test section coolant temperature for approximately 36-48 hours (settling takes a long time)

7. When the wax crystals are completely settled (the oil should be clear), open the experimental pump valve (2), set the pump to the lowest setting, and carefully increase the pump setting until flow occurs

3.5 Heterogeneous versus Homogeneous Effect on Restart Pressure – Constant Slurry Temperature

This is the first and most basic of the gel tests. First, a slurry is created which is cooled to a prescribed temperature, aged, and broken. The key to these tests is utilizing the same slurry temperature for multiple gel temperatures.

3.5.1 Heterogeneous Testing

1. Follow conditioning procedure using a flow rate of 0.75 gpm for consistency
2. Lower experimental test section coolant temperature to 20 °C, with valve set to the section being used
3. Lower conditioning loop temperature to approximately 15 °C below target shutdown temperature (for example, to reach a fluid temperature of 16.6 °C, a coolant temperature of 1 °C will suffice – though care must be taken to watch the temperature with manual adjustments as needed)
4. When oil temperature reaches 20 °C, lower the experimental test section coolant temperature by 0.5 °C; repeat this pattern until the new experimental section set point becomes the target oil temperature (this simulates cold flow conditions in flow with no deposition)
5. When the flowing oil temperature reaches set point (thus matching the new experimental test section coolant temperature) shut off all pumps, the mixer,

and the SCE blade and close the upstream valve leading out of the pump (2); also shut off the conditioning loop temperature controller

6. With flow stopped, change the experimental test section coolant temperature to the desired gel point temperature
7. When gel point temperature is reached, allow one hour for aging
8. Start recording pressure data for test section being used
9. Using whichever loading system desired (ISCO pump for very low loading rates, gas-valve system for higher loading rates), apply a constant loading rate to the gel
10. Monitor restart pressure
11. Repeat test using the same slurry temperature with a different gel point

3.5.2 Homogeneous Testing

1. Follow conditioning procedure using a flow rate of 0.75 gpm for consistency
2. Lower experimental test section coolant temperature to the prescribed above-WAT shutdown temperature of the oil
3. Lower conditioning loop temperature such that the oil temperature reaches the desired shutdown temperature
4. Shut down flow and close the upstream valve leading out the pump (2); also shut off conditioning loop pump and temperature controller, and the SCE blade
5. Set the experimental test section coolant temperature to the desired gel point temperature
6. When gel point temperature is reached, allow one hour for aging

7. Start recording pressure data for test section being used
8. Using whichever loading system desired (ISCO pump for very low loading rates, gas-valve system for higher loading rates), apply a constant loading rate to the gel
9. Monitor restart pressure
10. Repeat test using the same homogeneous temperature with a different gel point

3.6 Solids Loading Effect on Restart Pressure – Constant Gel Temperature

Similar to the previous test type, in the solids loading tests it is desired to observe the effect of solid content (i.e., precipitated wax crystals) on the gel strength. This is not quite the same as particle size testing, although the conclusions are very likely linked together. Instead, this testing type focuses completely on the amounts of wax precipitated. To maintain consistency, the slurries must be formed using the same shearing conditions (mixing speed, blade speed, flow rates).

3.6.1 Heterogeneous Testing

1. Follow conditioning procedure using a flow rate of 0.75 gpm for consistency
2. Lower experimental test section coolant temperature to 20 °C, with valve set to the section being used
3. Lower conditioning loop temperature to approximately 15 °C below target shutdown temperature (for example, to reach a fluid temperature of 16.6 °C, a

coolant temperature of 1 °C will suffice – though care must be taken to watch the temperature with manual adjustments as needed)

4. When oil temperature reaches 20 °C, lower the experimental test section coolant temperature by 0.5 °C; repeat this pattern until the new experimental section set point becomes the target oil temperature (this simulates cold flow conditions in flow with no deposition)
5. When the flowing oil temperature reaches set point (thus matching the new experimental test section coolant temperature) shut off all pumps, the mixer, and the SCE blade and close the upstream valve leading out of the pump (2); also shut off the conditioning loop temperature controller
6. With flow stopped, change the experimental test section coolant temperature to the desired gel point temperature
7. When gel point temperature is reached, allow one hour for aging
8. Start recording pressure data for test section being used
9. Using whichever loading system desired (ISCO pump for very low loading rates, gas-valve system for higher loading rates, or the experimental pump for very high {~4 psig/s} loading rates), apply a constant loading rate to the gel
10. Monitor restart pressure
11. Repeat test using the same gel point temperature with a different slurry temperature

3.6.2 Homogeneous Testing

1. Follow conditioning procedure using a flow rate of 0.75 gpm for consistency
2. Lower experimental test section coolant temperature to the prescribed above-WAT shutdown temperature of the oil
3. Lower conditioning loop temperature such that the oil temperature reaches the desired shutdown temperature
4. Shut down flow and close the upstream valve leading out the pump (2); also shut off conditioning loop pump and temperature controller, and the SCE blade
5. Set the experimental test section coolant temperature to the desired gel point temperature
6. When gel point temperature is reached, allow one hour for aging
7. Start recording pressure data for test section being used
8. Using whichever loading system desired (ISCO pump for very low loading rates, gas-valve system for higher loading rates), apply a constant loading rate to the gel
9. Monitor restart pressure
10. Repeat test using the same homogeneous temperature with a different starting above-WAT shut down temperature

3.7 Particle Size Effect on Restart Pressure

It was suspected that there is an inverse relationship between particle size and gel strength. In order to test this hypothesis, the use of various shearing techniques and CantyVision InFlow ® particle size imaging were employed using

the following steps. Once particles are formed the gel is formed using the common steps in the previous tests.

1. Follow conditioning procedure
2. Lower experimental test section coolant temperature to 20 °C
3. Lower conditioning loop temperature to approximately 15 °C below target shutdown temperature (for example, to reach a fluid temperature of 16.6 °C, a coolant temperature of 1 °C will suffice – though care must be taken to watch the temperature with manual adjustments as needed)
4. Adjust flow rate, blade speed, mixing speed while cooling as necessary to achieve varied particle size distribution – make sure to pay close attention to fluid temperature
5. As oil cools, maintain test section coolant temperature to match
6. When desired oil temperature is reached, start the CantyVision software and open the Canty valve (3) to capture particle images
7. Take 3-4 videos of 5-10 seconds each of different flows; for each flow, close the valve and allow fluid to reach temperature again (some heating up will occur); verify each video is clear and focused – air bubbles passing in front of the window will cause white-outs of the screen
8. Once videos are captured, shut off all flow, close upstream valve (2) and lower test section coolant temperature to desired gel temperature
9. When gel point temperature is reached, allow one hour for aging
10. Start recording pressure data for test section being used

11. Using whichever loading system desired (ISCO pump for very low loading rates, gas-valve system for higher loading rates) apply a constant loading rate to the gel
12. Monitor restart pressure
13. Using the CantyVision software, set brightness thresholds to accurately capture as many particles without "melding" and obtain a distribution; utilize the equivalent mean circular diameter as an estimate for average particle size
14. Repeat test using the same slurry and gel point temperatures, varying only the conditions needed to change particle size distributions

3.8 Pressure Loading Rate Effect on Restart Pressure

This is the most in-depth of all testing procedures, although the formation of the gels is identical to the other tests. The purpose of using PIV, as earlier explained, is to catch a glimpse inside the gel as breakage occurs and characterize the movement profile. As laser equipment is used in this test procedure, adequate protection for the eyes and a darkened laboratory are necessary.

1. Follow conditioning procedure
2. Create a gel using one of the previously described methods; what is important from test to test is to maintain the same gel temperature and slurry temperature, as well as mixing conditions (flow rate, conditioning time, etc.)
3. When gel is ready for breakage, arm the laser PIV system with the lab lights darkened and the delta time between images set to 10,000 microseconds

4. Start the LabView software recording the pressure data from the test section being used
5. Using whichever loading system desired (ISCO pump for very low loading rates, gas-valve system for higher loading rates) apply a constant loading rate to the gel; at the exact time pressure is loaded, start the laser and record the images of the breaking gel
6. Monitor restart pressure
7. Repeat test using identical conditions, but break the gel with a different, known loading rate; compare results from different loading rates by vector analyzing the processed PIV images; observe the breakage profiles and determine the type of failure: adhesive (initial failure at the wall), or cohesive (initial failure inside the gel)

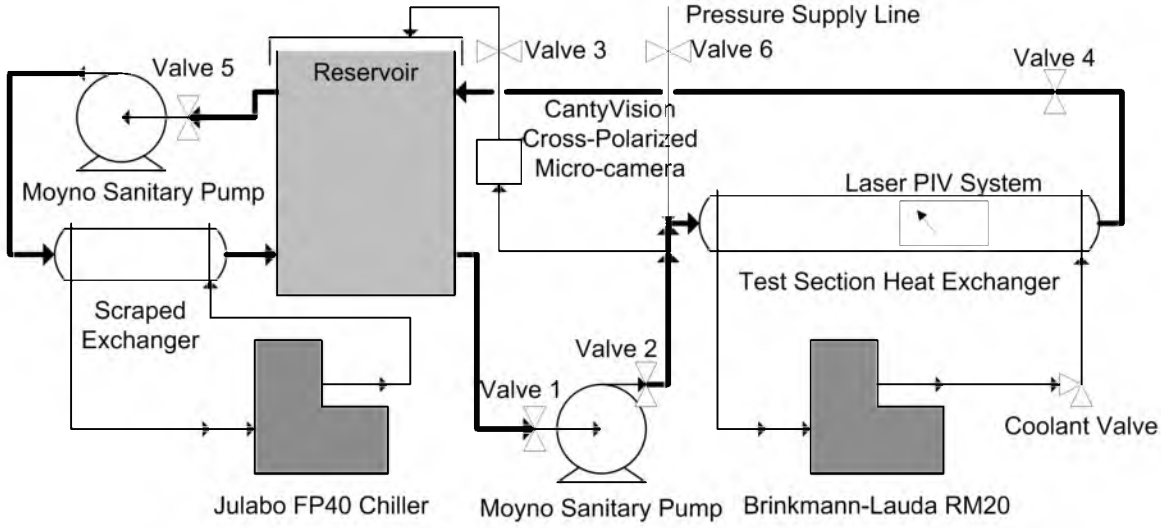

Figure 3.1. Flow Loop version 3.2 schematic with noted valves.

CHAPTER 4

RESULTS

4.1 Heterogeneous versus Homogeneous Deposition

At the start of this research a series of isothermal "Cold Flow" tests were conducted. These short-term tests (3-12 hours) validated the conclusions of previous researchers,[59-62] showing that isothermal "Cold Flow" worked well to indefinitely prevent active deposition. Figures 4.1 and 4.2 sum up these data, although it is fairly mundane and uneventful. Isothermal "Cold Flow" was also used as a means of validating the SCE function; this is presented in Appendix B.

Any test purporting to be "Cold Flow" in nature requires significant temperature control. Even minor fluctuations in laboratory conditions (i.e., heater or air conditioning coming on or quitting suddenly) can lead to changes in the bulk oil temperature. These changes can affect density of the oil, but more importantly they can change viscosity. Said changes can and will disturb the differential pressure between the inlet and outlet of the test section, and these can give false positives or negatives regarding wax deposition presence. In all test results shown here, oil temperature was maintained despite ambient changes using a feedback control system tied into the reservoir temperature controller and the inlet oil temperature via RTD.

Figure 4.2 shows a number of tests detailing the discovery of the "nearly Cold Flow" effect, or flow with a temperature difference of less than 2 °C between oil and ambient. This effect exhibits no deposition even in the presence of a small thermal gradient even though common software packages such as PVTsim predict deposition. Testing at low flow rates and "nearly Cold Flow" conditions (such as shown in Figure 4.2) suggest that shear forces are not contributing to this effect. In a study surrounding this effect, it was discovered that a possible cause of the "nearly Cold Flow" effect is system cooling[16]. In short, the act of cooling an oil to a certain sub-WAT condition requires a cooling surface colder than the final target temperature. The crystals that form near this colder surface contain more precipitated wax than would exist at the final temperature, and because of the kinetic barrier of melting an apparent thermodynamic equilibrium is observed. This pseudo-equilibrium leads to waxes to be precipitated out, preventing them from diffusing to and depositing on the walls.

4.1.1 The "Hot Flow" versus "Cold Flow" Debate – An Informal Report

Concerning conditions in which deposition is expected, this section contains portions of a report prepared regarding a debate over "Hot Flow" and "Cold Flow" deposition rates.

4.1.1.1 Summary

Recently a debate among those who study wax has emerged regarding the effect of precipitated waxes on the rates of deposition, while holding constant the

thermal gradient as well as shear stress at the walls. In an attempt to resolve this debate, data have been prepared showing the deposition rates for two distinct conditions: "Hot Flow" tests in which no solid crystals are present in the flow, and "Cold Flow" tests in which crystals are present. While the individual temperatures are different between the tests, the thermal gradient dT/dr is the same ensuring an identical ΔT across the pipewall between tests. Reynolds number was also held constant between the tests by increasing the flow rate for the "Cold Flow" tests accordingly, thus matching shear conditions at the wall. The deposition rates for the "Cold Flow" tests were considerably lower than for the "Hot Flow" tests, suggesting that the thermal gradient dT/dr is not solely responsible for deposition mechanics. Singh et al. (2000) indicated that, in addition to the necessary thermal gradient, a solubility parameter dC/dT must also be accounted. This implies that there is a thermally-dependent mass transfer gradient, dC/dr, that regulates the "pull" of waxes to the wall. Without this pull there can be no deposition, as seen in isothermal "Cold Flow" tests. The results obtained through this project support that theory.

4.1.1.2 Theory

Although wax deposition on pipe walls during industrial transport is a fairly well-documented phenomena, study of sub-WAT flows has opened up more questions that experimentalists and theorists have yet to answer concretely. One of these questions involves the rate of wax deposition between above-WAT (a.k.a. "Hot Flow") and sub-WAT (a.k.a. "Cold Flow") flowing conditions under identical thermal

gradients. Are the two rates identical given that the thermal gradients are identical? If so, why, and if not, why not?

Recently, a study (awaiting review and publication – authors withheld) seemed to show that deposition rates did not change between "Hot Flow" and "Cold Flow" conditions as long as the thermal gradients were identical (in this case, an identical temperature differential ΔT between the bulk fluid and the ambient). This result seems to show heat transfer dominance in deposition, all but eliminating any mass transfer effects. This would imply that solid wax in the flow has little to no effect on deposit growth. However, prevailing deposition theory describs deposition as a thermally-driven mass transfer process, i.e., the thermal gradient dT/dr drives deposition according to the solubility of wax dC/dT, where C is the solid wax precipitate concentration. Unfortunately a degree of contention has arisen over these results; this short study seeks to allay this contention.

4.1.1.3 Results

The difference between "Hot Flow" and "Cold Flow" tests using identical thermal gradients dT/dr are presented in Figures 4.3 and 4.4. Two gradients were used: 7 °C and 5°C. It is expected for there to be some radial differences between "Hot Flow" and "Cold Flow" tests due to slightly varied thermal conductivity, but the matched Reynold's number should minimize these effects by increasing convection in the "Cold Flow" case. In Figure 4.3, the oil was flowed at 20 °C at 0.75 gpm while the ambient conditions were held at 15 °C for "Hot Flow", and for "Cold Flow" the oil was flowed at 16.6 °C at 0.9 gpm while the ambient temperature was held at 11.6 °C.

In Figure 4.4, the oil was flowed at 20 °C at 0.75 gpm with an ambient of 13 °C for "Hot Flow"; for "Cold Flow" the oil was at 16.6 °C and 0.9 gpm with the ambient temperature at 9.6 °C. All coolant flow rates were greater than 4 gpm to mimic an infinite cooling medium such as the ocean.

It is very clear from these results that, even in the presence of the same thermal gradient, the rates of deposition for "Cold Flow" are greatly reduced from those of "Hot Flow". Clearly, something more than just heat transfer is going on. In observing the solubility curve again in Figure 4.5, a reason for this rather large difference may be visible.

From Figure 4.5, the amount of mass available to deposit in the thermal gradient in the "Hot Flow" case is roughly 4.5%. However, in the corresponding "Cold Flow" case the amount of mass available to deposit is reduced to 3%. More important is the overall slope of the solubility curve in the temperature intervals shown. When the slope of the solubility curve, dC/dT, is multiplied with the thermal gradient, dT/dr, it gives a mass transfer gradient, dC/dr. If dC/dT is larger, i.e., the solubility curve has a steeper slope, this multiplied mass transfer gradient dC/dr would also be greater, and this would be seen in the data as an increased deposition rate. The data would appear to confirm this theory; the "Hot Flow" cases all show a greater rate of deposition, and all have a steeper overall solubility segment associated with them, not to mention greater amounts of available precipitable material.

It should be mentioned that actual deposition mechanics are more complicated than this simplified model, but the underlying driving force of

molecular diffusion via thermal gradients is sound. As such there is no reason to dispute – larger solubility gradients lead to higher deposition rates.

4.1.1.4 Conclusions

Without a heat transfer gradient deposition will not occur. However, based on the results of this study, heat transfer is not the only factor controlling deposition rates. Thermal gradient combined with solubility determines the rate of deposition growth. If thermal gradients are the same between two cases with different solubility conditions, the solubility condition will determine the relative rate of deposition. Two solubility conditions may be responsible for the differences seen: the amount of available precipitable material in the thermal interval, ΔT, and the overall slope of the solubility curve in the thermal interval.

4.2 Heterogeneous Effect on Gel Point

Prior to any gel testing, it must be ascertained what effect heterogeneous flow has on subsequent heterogeneous gels and their gel points. The initial hypothesis was that as wax came out of solution in the form of suspended crystals, these waxes would no longer have any real contribution to gel structure.

A very poor heuristic regarding the slowly-cooled gel point of an oil is that, for a crude oil, precipitation of about 6% of the total oil mass will result in a gel, while for a model oil about 3% is needed. In other words, a solids content of 6% - meaning a minimum of 6% total wax content – must be present in the crude oil in order for it form a gel. Of course, a cursory look at the solubility and known gel point

of the model oil used in this study would suggest a total precipitated solids amount of about 5% total mass is needed to create a gel. With this belief, coupled with the initial hypothesis precipitated solids not participating in the gel structure, the expected observation would be a significant drop in gel point.

As can be seen in Figure 4.6, according to this heuristic the gel point for a slurry held at 16.6 °C would be -10 °C! However, Figure 4.7 shows a simple plot of the restart pressures for gels formed from slurries at various gel temperatures. Of course, none of the reported values is necessarily the gel point; however, should a large temperature offset exist between the slurry curves then gels are experiencing trouble forming. Any restart pressure above 0.1 psig would suggest that at least some gelation is occurring, disproving the heuristic.

As shown by Figure 4.7 the gel point is not reduced as extremely as the poorly founded heuristic would predict. Instead, the gel point is slightly reduced in the presence of suspended, sheared crystals via heterogeneous flow and shutdown, indicating that the preexisting crystals do in fact participate in the gel matrix structure.

Regardless of the actual effect of slurries on gel point, the ultimate result is that slurries do not lower the gel point significantly. Furthermore, it would appear that the precipitated waxes are participating in the gel structure. With this conclusion reached, the research can go on unimpeded.

4.3 "Cold Flow" Settled Restart

Isothermal "Cold Flow" settled restart is a sort of outlier in this research, explored very briefly. Intuitively, if a heterogeneous flow is shut down and allowed to sit quiescently for a long time, the suspended wax crystals would settle rather than form a gel. The reason for this is that without any further cooling (it is isothermal at all times) there is no further precipitation of solids, leaving the solids already precipitated as the only solids in the system. With no further growth, there is no mechanism for the crystal-crystal in-growth that is necessary for gelation. As such, one would expect to see a complete settling of all particles, and when flow is resumed these particles would immediately disperse.

A 3-day test was conducted with the shut-in heterogeneous oil at 16.6 °C and held with ambient conditions likewise at 16.6 °C, thereby eliminating thermal gradients. The precipitated wax settled slowly (three days were required), after which flow was resumed by restarting the Moyno progressive cavity pump. The settled particles neither resisted restart nor exhibited any sludging (precipitated crystals sticking together en masse). Instead, the settled particles dispersed immediately, and no yield stress was measurable. Figures 4.8-4.10 detail this settling effect photographically.

As expected, with no thermal gradient at any time, there was no mechanism for sludge growth or gel growth. No reason exists that would delay restart in this case.

4.4 Heterogeneous versus Homogeneous Effect on Restart Pressure – Constant Slurry Temperature

When homogeneous (clean) gels are formed at the same shutdown temperature but different final temperatures, the resulting gel strength versus final temperature plot is predictably linear[45]. When different cooling rates are applied, the resultant data are again linear, but with a different slope. It was expected that heterogeneous gels, formed at the same final temperatures but sub-WAT shutdown conditions, would also show linearity but with greatly reduced slopes compared to homogeneous gels. Figures 4.11 and 4.12 present the results of the gel strength versus final temperature of the model oil in both homogeneous and heterogeneous states of shutdown. Here, as with most other results, the data from both the clear acrylic section and steel section are presented.

The original prediction was correct – heterogeneous gels are considerably weaker than homogeneous gels, and heterogeneous gels exhibit linear gel strength versus final temperature curves. It is interesting to note the degree to which the slope changes even for a slurry temperature of 17.2 °C. This temperature is just below WAT, yet there is a severe drop-off in gel strength. Dropping an additional degree to 16.2 °C shows virtually no difference in gel strength. The following solids loading effect testing (section 4.5) should give considerable insight into what exactly is happening.

In Figures 4.11 and 4.12, there is a discernible jump is slope at 0 °C for the slurry tests. As of this point the cause is not known as it is not seen in the remaining tests, though it is believed that below 0 °C the natural gelation mechanism may be overcoming the heterogeneous effects caused by suspended particles.

4.5 Solids Loading Effect on Restart Pressure – Constant Gel Temperature

By comparing the gel strength of gels formed under identical cooling rates and final temperatures and differing solubility conditions (i.e., slurry temperature at shutdown), one can gain additional insight into the rheology of these heterogeneous gels. As seen in Figure 4.13-15, a precipitous drop-off in restart pressure occurs immediately below WAT.

Two pressure loading conditions were tested here: Case 1) Moyno pump restart (very high rate, some lack of control) in Figures 4.13 and 4.14; Case 2) carefully-controlled needle valve restart (1.12 psi/s pressure loading rate or 16.1 Pa/s shear stress loading rate) in Figure 4.15. Case 1 was used very early in the research before Case 2 was acquired; however, both testing methods give qualitatively similar results The lower loading rate will give a lower gel restart pressure[45]; this conclusion is confirmed in section 4.7 of this chapter. Case 2, as presented in Figure 4.15, provides a more detailed look at the solids loading effect on gel strength near WAT.

The drop-off in gel strength immediately below WAT is a curious result. Early predictions were that with a small amount of precipitated wax the gel strength would be relatively close to the homogeneous (clean) gel condition. The reality is that the gel strength is greatly reduced in the presence of any precipitated wax contamination at the moment of shutdown. Furthermore, while the data do appear to have a slight downward trend as shutdown temperature decreases this may be an artifact of the reproducibility issues inherent to gelled restart testing. This, coupled with the sharp drop-off below WAT, suggests that while more crystals at shutdown

may lower the subsequent gel strength slightly, what matters most is the presence of crystals generally.

This preexisting, sheared, crystalline presence appears to have a destabilizing effect on the gel structure. This comes not just by disrupting a number of cross-links between naturally-forming wax crystals, but also by disrupting the way in which waxes come out of solution themselves by being the dominant precipitation sites. Figures 4.16 and 4.17 provide a suggested explanation as to why heterogeneous gels behave in the way seen in the data. In other words, the gel structure of a heterogeneous gel is distinctly different than a homogeneous gel due to the preexisting crystals' effect on precipitation patterns. It is still expected that the effect would still be nearly asymptotic as one approaches WAT from the cold side.

As shown in Figure 4.17, the gel matrix formation is completely different when subjected to the presence of preexisting crystals. As mentioned earlier, these crystals act as the primary nucleation sites for new crystal growth, and this in turn limits the number of free-forming crystals. This leads to lower numbers of cross-links, though not necessarily lower gel point as cross-linking will still occur.

4.6 Particle Size Effect on Restart Pressure

Early in the development of this project a major question related to the determination of the effect that particle morphology (shape, size) had on subsequent heterogeneous gel strength. For example, would a heterogeneous gel whose wax particles were twice the size of another heterogeneous gel have a

weaker gel strength? CantyVision InFlow® particle visualization system was used to gain insight into this question

As already explained, the CantyVision system incorporates a cross-polarized light filter to obtain clearer images of wax particles. The resulting images were somewhat surprising: not only were wax particles of a heterogeneous flow rounder after being sheared through flow, but they were also agglomerated – very rarely was a single suspended crystal seen that was not stuck to at least one other. Furthermore, the heterogeneous flow gave very heterogeneous results in regards to wax crystals concentrations. These was very little macroscopic uniformity since the wax crystals had distinct populations. Figures 4.18-4.21 illustrate these findings.

The degree of particle agglomerations in the heterogeneous flows was unexpected, particularly that shown in Figure 4.21. However, it is assumed that the aforementioned findings also exist in some form or another in industrial pipelines (non-uniform particle sizes, agglomerations, etc.). In this study, gels were formed from these heterogeneous flows using a variety of methods intended to adjust the overall particle size distributions. Table 4.1 presents the method and subsequent expected effect.

A drawback to using mechanical methods to control particle size is unavoidable and unintended input. For example, using an increased test section flow rate to promote larger crystals reduces the fluid's cooling rate by displacing fluid faster into the warmer test sections compared to the conditioning loop flow rate which remains unchanged. This should, overall, increase particle size. However, the unintended consequence is an increased shearing rate due to pump and wall-

fluid friction. This has the effect of reducing particle size – which introduces difficulties in controlling and predicting particle size.

Prior to testing one hypothesis was that smaller particles would lead to higher gel strength. Without taking away from the conclusion of the previous section (i.e., that preexisting, precipitated wax particles may be acting as the dominant precipitation site for dissolved waxes, thereby changing the nature of the gel matrix itself), the foundation of this hypothesis was that smaller crystals would result in less disruption of the naturally formed gel matrix. Larger crystals would, then, cause more disruptions by way of having a larger projected surface area (Figures 4.22 and 4.23).

With this in mind, a prediction of how yield stresses should behave was formulated (Figure 4.24 – dotted line). The actual results, however, showed that this hypothesis was wrong – particle size distribution changes seem to have little to no effect on restart pressure as seen in Figure 4.24.

The conclusion that this hypothesis was incorrect was suspected early on due to the remarkable repeatability of gel strength testing in the previous procedures. While the results were consistent between tests, not every test was performed with perfection. However, no such discrepancies were found, and the specific particle size testing led to the reasonable conclusion: particle size and particle number balance each other in regard to gel strength.

To illustrate this conclusion, consider that when more wax particles exist, conservation of mass requires that these particles be smaller in size, while larger particles result in an overall lower number of crystals. There is no reason to believe

that a larger crystal would cause less natural matrix disruptions than a smaller crystal, yet as seen in the results the particle size has apparently very, very little effect on gel strength. This suggests quite strongly that while the larger crystals have a more pronounced reducing effect on gel strength, the lower number of particles reduces the overall effect. Similarly, while smaller crystals have a less pronounced effect on lowering gel strength, the higher number of crystals amplifies that effect. Such a balance is reasonable and consistent with the laws of conservation of mass and energy, and as such there is no reason to discount it. Equation 4.1, while somewhat simplistic, explains this effect mathematically.

$$\tau_{yield} \approx \delta_C N_C \bar{\varepsilon}_C + \delta_W N_W \bar{\varepsilon}_W$$

$$\delta_C = \begin{cases} 0, N_C\bar{\varepsilon}_C > N_W\bar{\varepsilon}_W \\ 0.5, N_C\bar{\varepsilon}_C = N_W\bar{\varepsilon}_W \\ 1, N_C\bar{\varepsilon}_C < N_W\bar{\varepsilon}_W \end{cases}; \quad \delta_W = \begin{cases} 0, N_C\bar{\varepsilon}_C < N_W\bar{\varepsilon}_W \\ 0.5, N_C\bar{\varepsilon}_C = N_W\bar{\varepsilon}_W \\ 1, N_C\bar{\varepsilon}_C > N_W\bar{\varepsilon}_W \end{cases} \tag{4.1}$$

In Equation 4.1, yield stress is approximately equal to the sum of all interactions; N_C is the number of crystal-crystal interactions, (i.e., "cross-links") ε_C is the average strength per crystal-crystal interaction in Pa/interaction, N_W is the number of crystal-wall interactions, and ε_W is the average strength per crystal-wall interaction in Pa/interaction. The values δ_C and δ_W account for the magnitudes of the wall-crystal and crystal-crystal interactions; should one be stronger than the other, the weakest interactions would naturally break first, rending the stronger interactions moot in regards to initial failure. Naturally, the strength of each individual interaction is exceptionally small, but the large number of interactions

magnifies that strength. Consequentially, if N is larger and ε is smaller, the overall gel strength will be roughly the same if N is smaller and ε is larger. A variety of results would be expected for different oils and different compositions, but for a single oil with a constant composition, the results obtained in this research seem to indicate the aforementioned balance according to this simple model.

Of course, there would come a point that, as particle size approaches that of the molecule itself, gel strength would rapidly approach the homogeneous, natural gel strength as shown in Figure 4.25. Unfortunately particle size control is exceptionally difficult, and attempts to reach such a threshold may not be possible even in a laboratory setting.

There is some concern as to whether or not the particle size distributions were measured correctly and/or varied enough to show a significant difference. CantyVision particle sizing is heavily dependent upon user bias and interpretation (as are most measurement devices in science); however, efforts to improve particle sizing have resulted in relatively small differences between analysis methods. It may end up that particle size has more of an effect than is being shown in this research; the author welcomes improvements by others and recognizes the need for more investigation into this aspect of heterogeneous gels.

4.7 Pressure Loading Rate Effect on Restart Pressure

In this the final component of the research program, the effects of pressure loading rate were observed in both the restart pressure obtained for each rate as well as the restart profile seen for each rate. It has already been theorized that for a

regular, homogeneous gel the breakage profile switches from adhesive (failure at the wall) to cohesive (internal failure) with increasing cooling rates.[20] Part of this theory was verified[52] by using laser PIV to show that, for a slow cooling rate such as those seen in a deep-sea pipeline, breakage does in fact occur at the wall.

However, early testing with heterogeneous gels appeared to show visual evidence of internal breakage before wall failure, denoting a center-core failure. These results were found in nearly every heterogeneous gel restart test performed, becoming much less apparent when the loading rate was very low. Therefore, a question was raised: "is there a loading rate dependence on failure type with a heterogeneous gel?" At this point there is no reason to debate or question the conclusion of the cooling-rate dependent failure type change with heterogeneous gels (nor can the cooling system for the test sections be changed from 0.33 °C/min); however, such testing may prove interesting in the future, given the proper equipment.

An early theory put forth by the author was that heterogeneous gels, being in some way fundamentally different from homogeneous gels, might show a loading rate versus gel strength slope change at some critical loading rate, this being the changeover point from adhesive to cohesive failure. The early testing suggested that low loading rates on a heterogeneous gel exhibited adhesive failure, while higher loading rates exhibited cohesive failure. With this in mind, it was expected that some slope change would be visible, as shown in Figure 4.26.

All heterogeneous gels formed and broken during this phase of research were made identically from slurries where flow was stopped when oil temperatures

reached 16.6 °C. All gels (both homogeneous and heterogeneous) were cooled to 3°C at a rate of 0.33 °C/min and were allowed one hour to age at 3 °C. Figures 4.27 and 4.28 show the results when these gels were broken using varied pressure loading rates.

What does Figure 4.28 mean? Is there a slope change that is too small to be seen through the data? To further elucidate, PIV was utilized to investigate when the gel failure switches from adhesive to cohesive. Figures 4.29-4.32 present one such case with a restart pressure loading rate of 2.0 psi/s. A dt time step of 10000 μs between dual frames was used as per section 2.4.2.

In Figures 4.30 and 4.31, the image has been enhanced to more clearly show particle movement and subsequent velocity vectors in gel breakage. Given that these velocities are extremely low the actual magnitude of these vectors is neglected. The relative magnitude of each is utilized to determine breakage profiles.

Table 4.2 summarizes the results of the PIV restart tests with observations. For comparison and observation of adhesive failure, the breakage of a homogeneous gel formed under the same cooling rate and final temperature is shown in Figures 4.33-4.35. It should be noted that the loading rate used in the homogeneous breakage test is 1.62 psi/s – slightly lower than the heterogeneous test shown. An adhesive failure would be marked by movement of the entire gel as a plug with some initial movement (difficult to detect) visible at the walls. It should also be noted that Figures 4.33-4.35 appear different than the heterogeneous results for a reason: the lens used for the heterogeneous tests was not available at the time of the homogeneous tests. As such the images are not able to be cropped to the size of the

others. However, the results are clear enough to understand readily, and did allow for a higher vector resolution.

Contrary to the original theory, not only was there no slope change, but there was no adhesive failure at all: all heterogeneous gel failure, even at very low loading rates, was cohesive. Heterogeneous gels, by definition it would seem, break through the center rather than at the wall. A reason for this may be that the wall-crystal interaction between homogeneous and heterogeneous gels is relatively the same. In the homogeneous case, this interaction is the weakest in the gel matrix; in the heterogeneous case, however, the crystal-crystal interactions around the center of the gel matrix appear to be weakest, leading to failure of internal cross-links before the relatively unchanged wall interactions.

Despite early assumptions, heterogeneous gels and homogeneous gels appear to be nothing alike in terms of failure and structure. It becomes apparent that typical modeling methods for standard, stronger homogeneous gels may not (and likely do not) suffice for heterogeneous gels. Another interesting observation is that, unlike the extended plug-like flow of adhesive failure[20, 52] the cohesive failure almost immediately resulted in parabolic flow, as though the gel was completely shattered immediately after restart.

It should be noted that PIV was used primarily as evidence for this hypothesis; the gel breakage recorded by the PIV was actually best viewed optically without any vector analysis. In other words, the gel breakage was simple enough to see in the images with the naked eye that it almost made the use of PIV moot. It is suspected that the vector analysis software had difficulty with blurry gels.

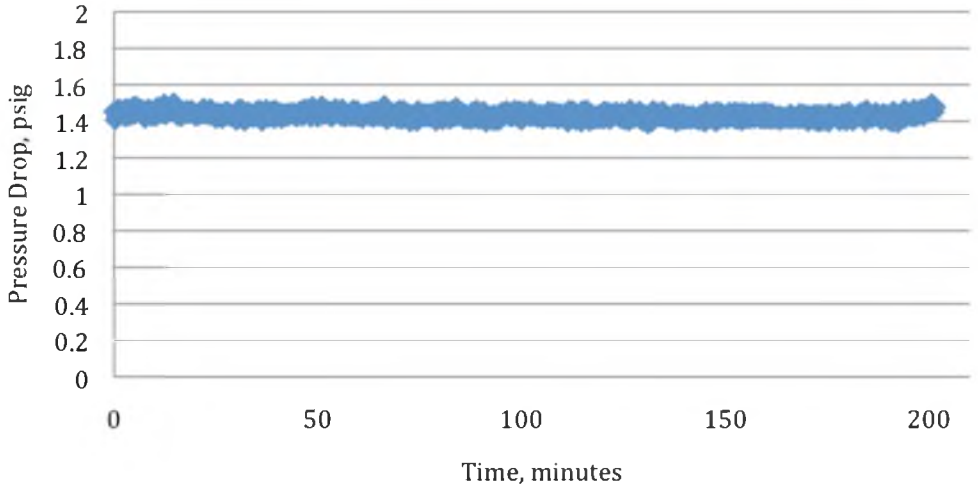

Figure 4.1. Isothermal "Cold Flow" test results. Oil and coolant were both flowed at 13.5 °C (midway between WAT and gel point). Oil flow rate was 1 gpm. No significant pressure drop increases seen signifying the lack of wax layer deposition.

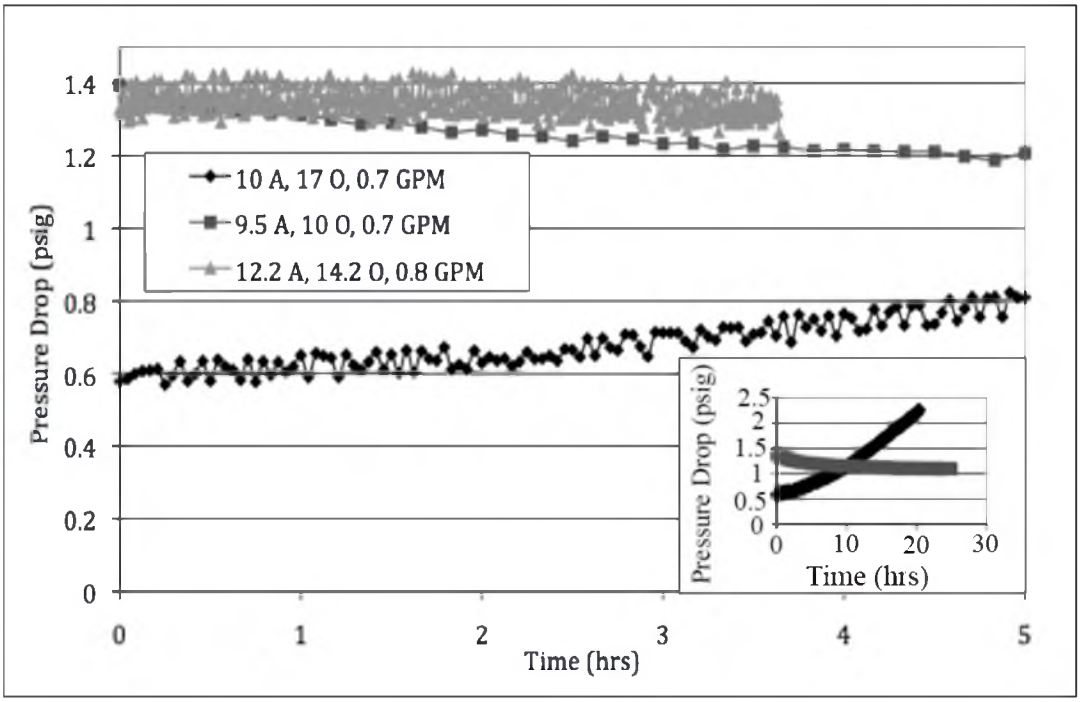

Figure 4.2. Compilation of "nearly Cold Flow" tests compared to non-isothermal "Cold Flow" test. Inset shows long term results. "Nearly Cold Flow" tests show no deposition, contrary to theory.

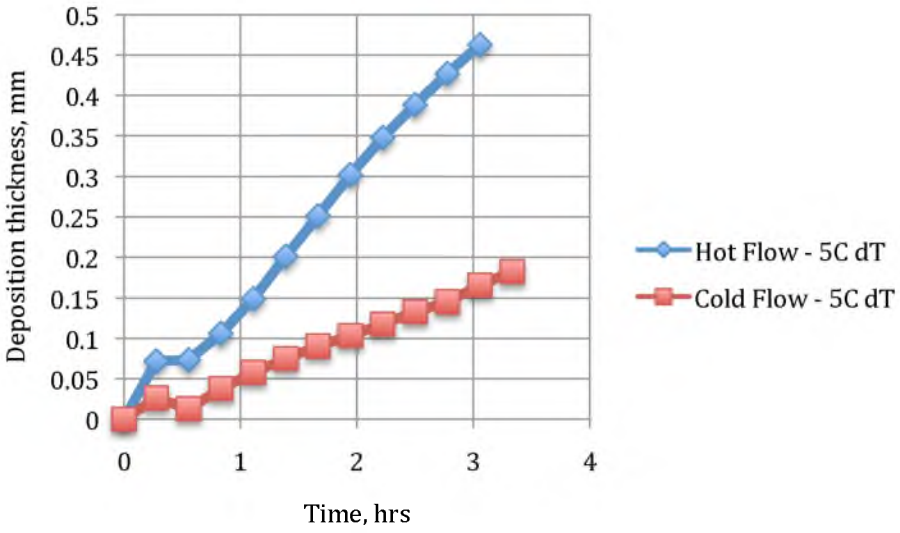

Figure 4.3. Deposition thickness for ΔT=5 °C case.

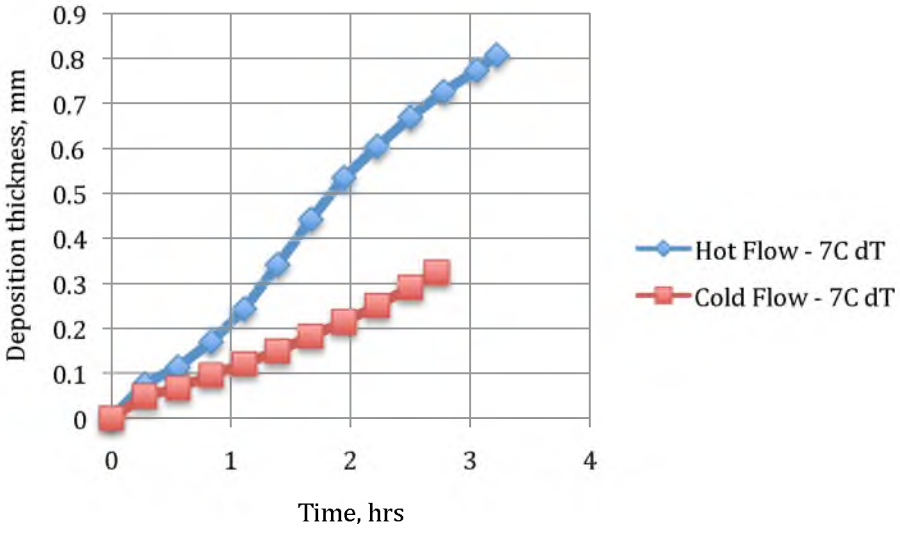

Figure 4.4. Deposition thickness for ΔT=7 °C case.

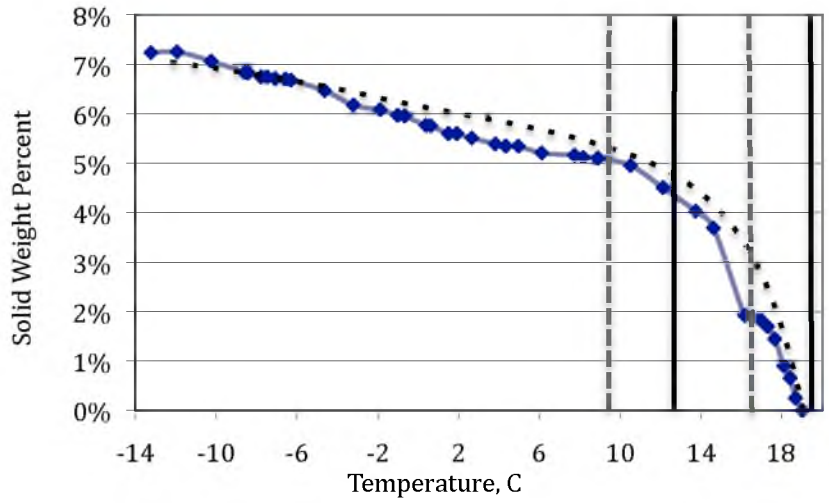

Figure 4.5. Solubility with temperature differentials marked. Dark black lines represent the ΔT=7 °C "Hot Flow" case, while the gray dashed lines represent the corresponding "Cold Flow" case.

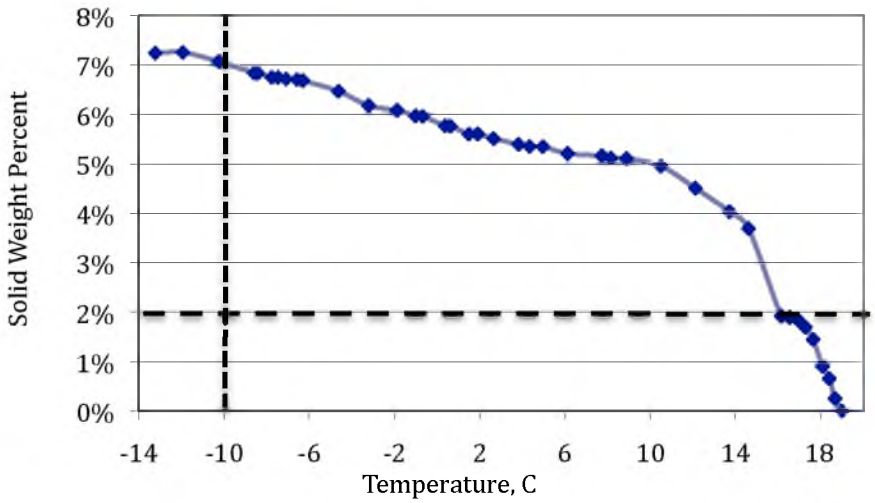

Figure 4.6. Heuristic-determined gel point of 16.6 °C slurry. At 16.6 °C approximately 2% total mass has precipitated, and if an additional 5% is needed to achieve a gel the gel point would be reduced from 7.5 °C to -10 °C. Clearly, this would be a problem for the research.

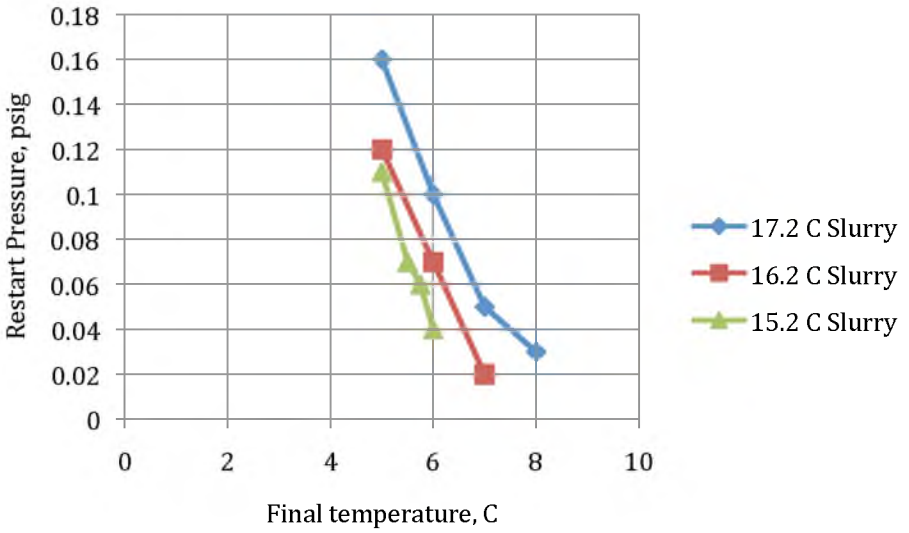

Figure 4.7. Restart pressures for slurry formed gels near homogeneous gel point. Small offset between slurry curves disproves heuristic of Figure 4.6 by showing drop in gel point equivalent to the offset.

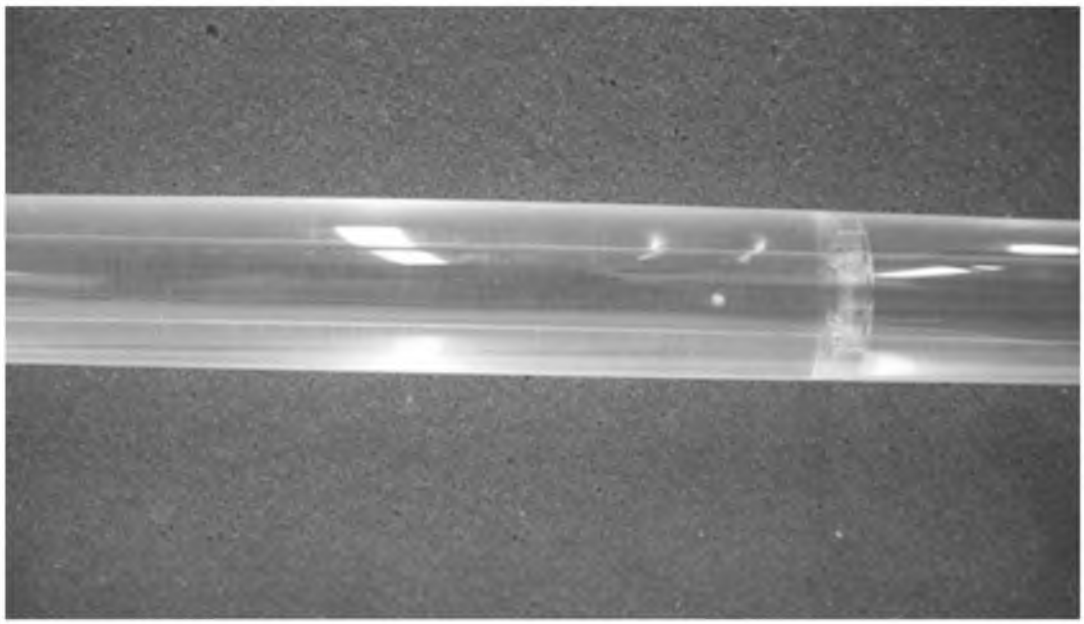

Figure 4.8. Oil flowing above WAT for "Cold Flow" settled restart test. Oil is flowing through the center tube. Note transparency of oil and lack of any sedimentation (the apparent lightening at the bottom of the center tube is a reflection of the table).

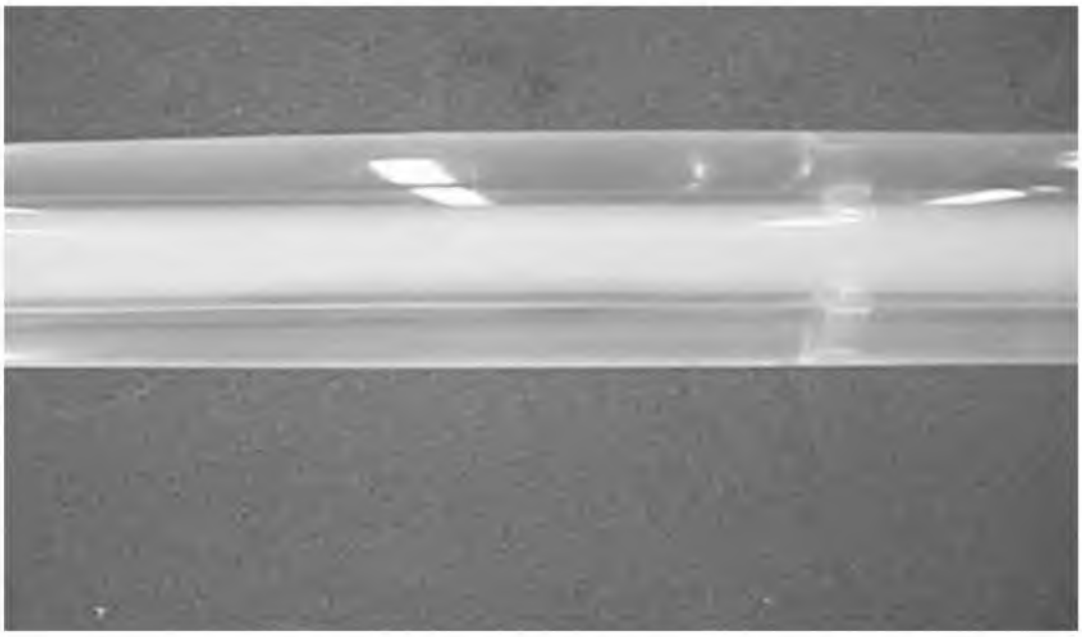

Figure 4.9. Several hours after flow shut down, wax particles are still dispersed and suspended in flow.

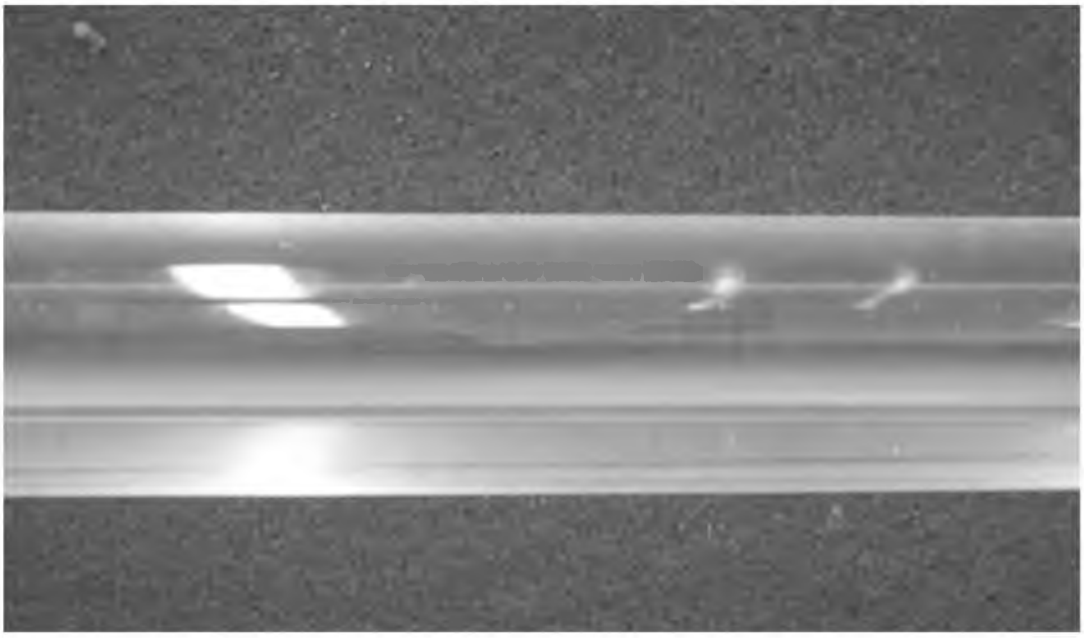

Figure 4.10. After 36 hours the wax present at isothermal shutdown has settled to the bottom of the tube, leaving clear oil above. No gel was formed, and no structure of any type was observed when flow was resumed.

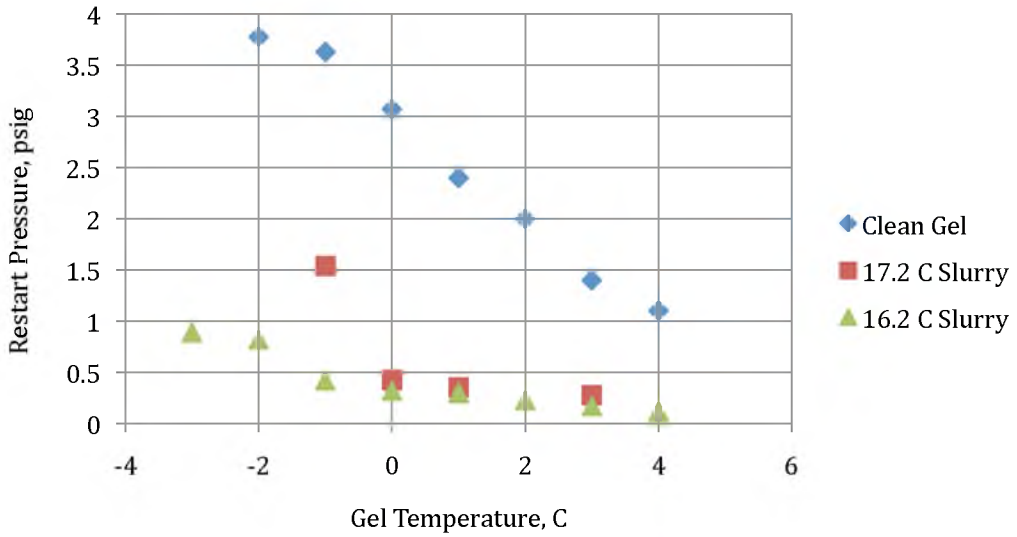

Figure 4.11. Clear acrylic section results for heterogeneous versus homogeneous gel strength testing. Note the linearity of the results. There is negligible difference exists between 17.2 and 16.2 °C slurry-formed heterogeneous gels.

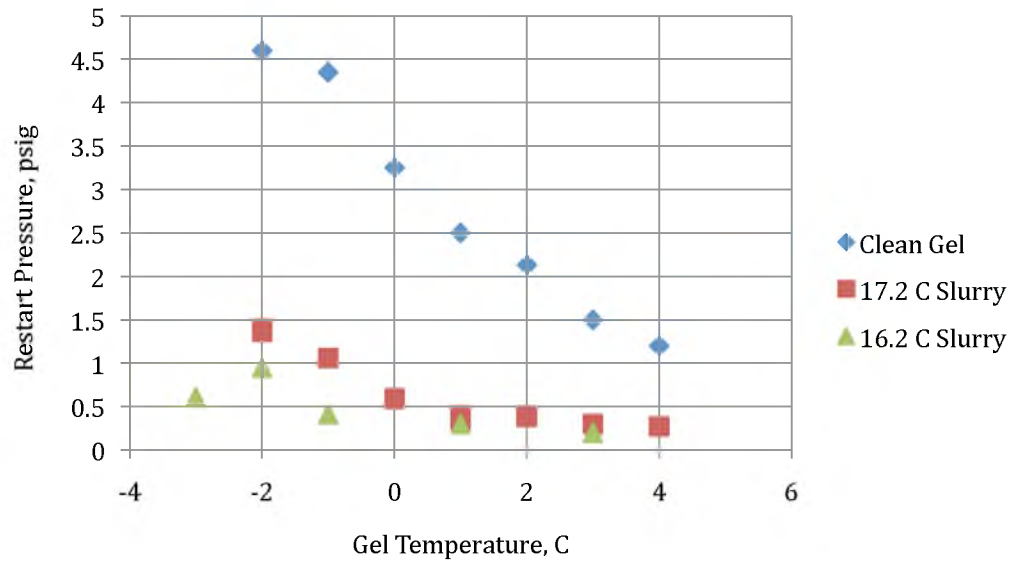

Figure 4.12. Stainless steel section results for heterogeneous versus homogeneous gel strength testing. Like the acrylic testing, the two slurry-formed heterogeneous gels show little difference.

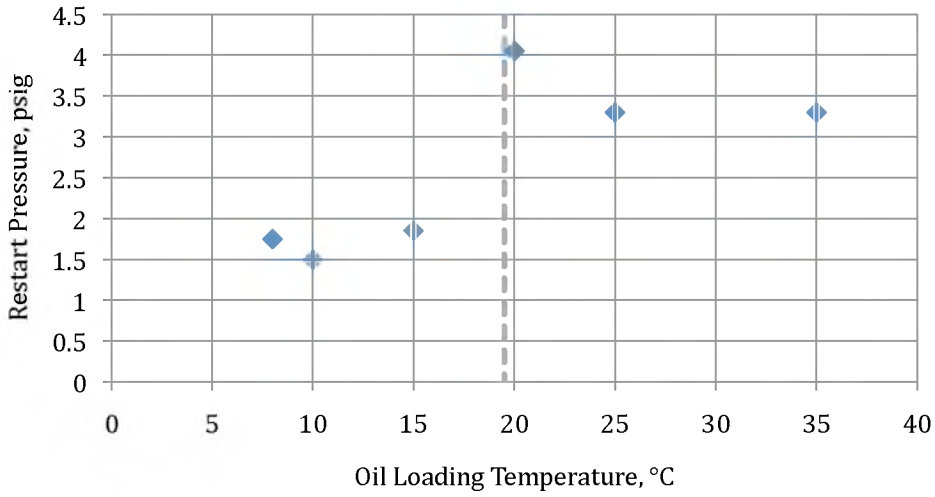

Figure 4.13. Solids loading effect on restart pressure I. Tests conducted in steel test section using Moyno pump restart (loading rate is greater than 4 psi/s). Dashed line represents WAT.

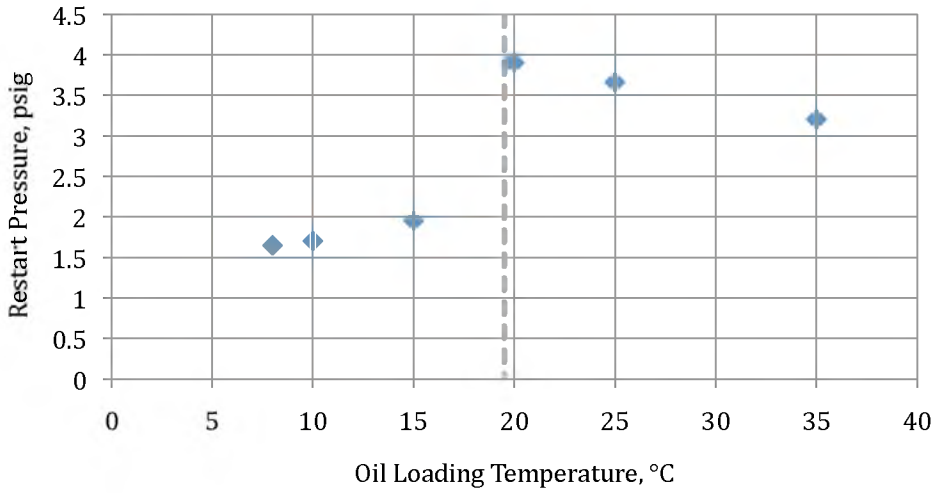

Figure 4.14. Solids loading effect on restart pressure II. Tests conducted in clear acrylic test section using Moyno pump restart (>4 psi/s). Dashed line represents WAT.

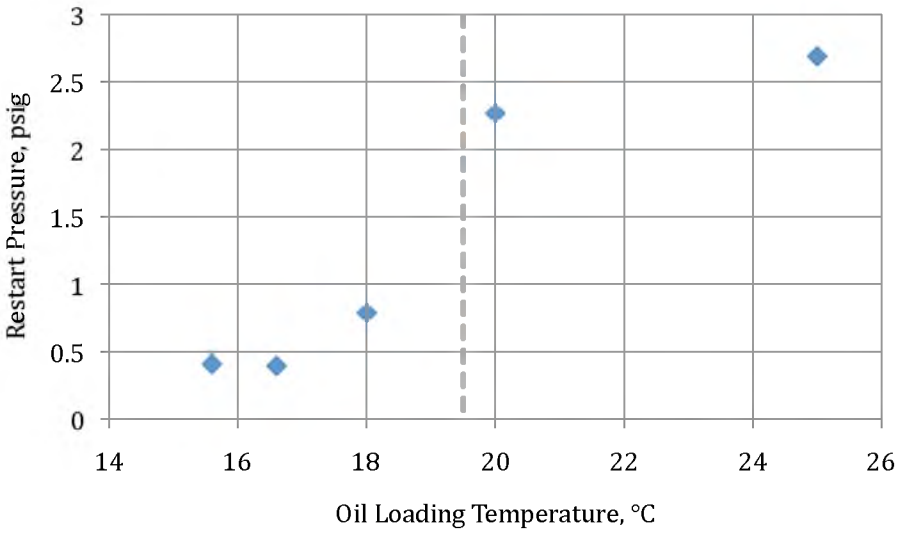

Figure 4.15. Solids loading effect on restart pressure III. Tests conducted in steel test section using needle valve setting 20 (1.12 psi/s). Dashed line represents WAT. Note the reduced scale of the x-axis giving a closer look at the behavior near WAT.

Figure 4.16. Cartoon of natural gel matrix formation with no preexisting crystals. Such a gel matrix features a large number of high quality cross-links between wax crystals.

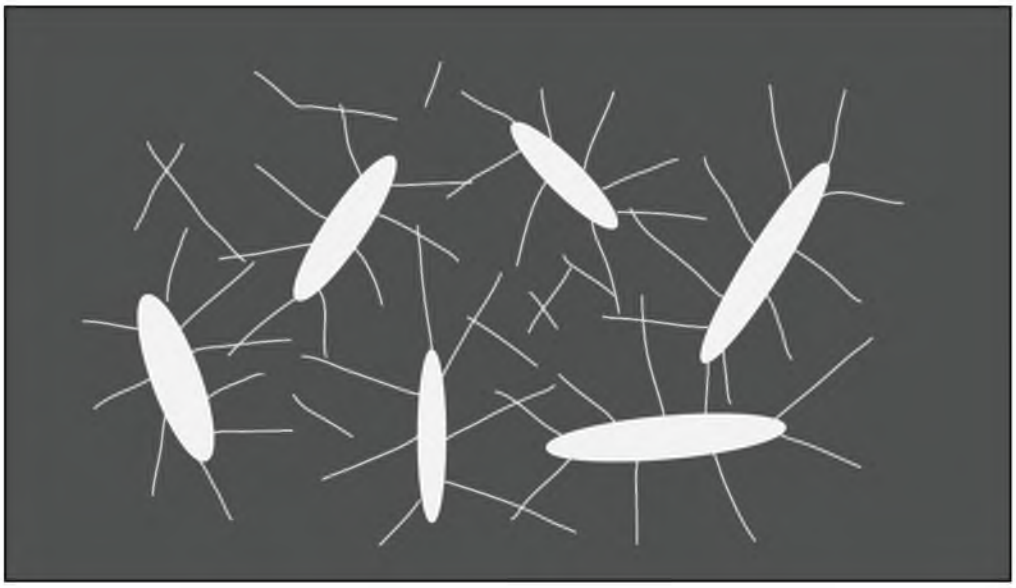

Figure 4.17. Cartoon of suggested theory of the heterogeneous effect on gel matrix formation. Solubility is the same as in Figure 4.15, but preexisting crystals act as primary precipitation sites for waxes. This effect theoretically reduces the number and quality of cross-links; a gel still forms at roughly the same temperature, but the strength of the gel is greatly reduced.

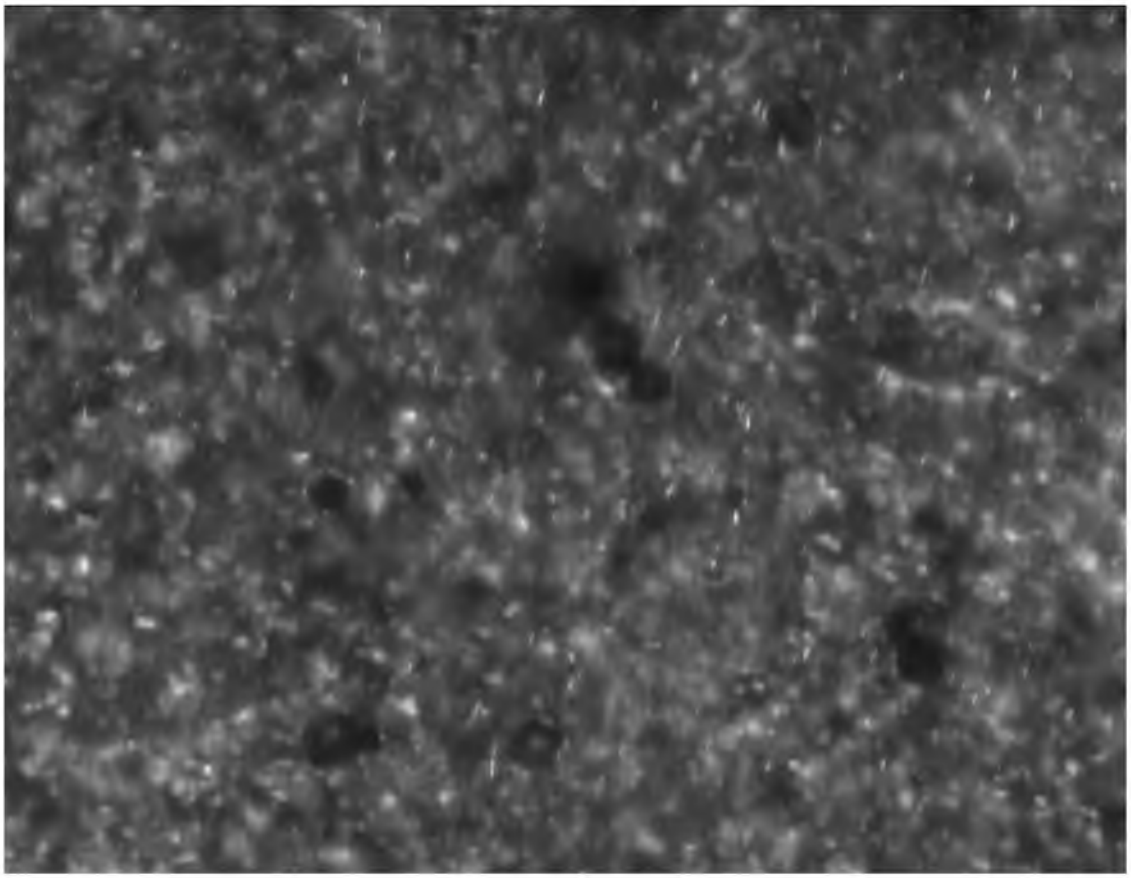

Figure 4.18. Live flow image made using CantyVision InFlow® system. This image shows precipitated wax crystals (lighter spots) in the oil.

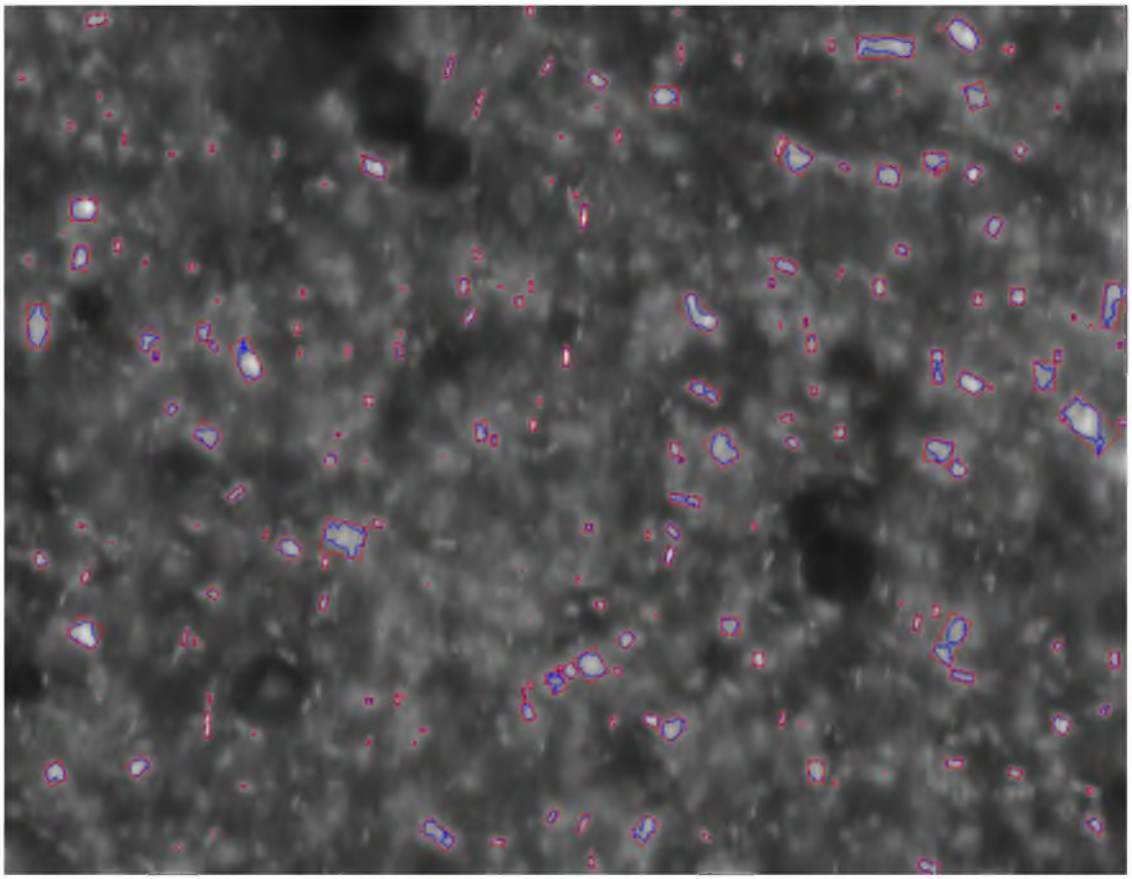

Figure 4.19. Zoomed-in view of bottom right of Figure 4.18 with particle sizing tool activated. Note that not all particles are sized, but only those with the best focus and clarity (many individual images are used in a single particle sizing step). Note the non-uniformity of the particles as well as the presence of agglomerations.

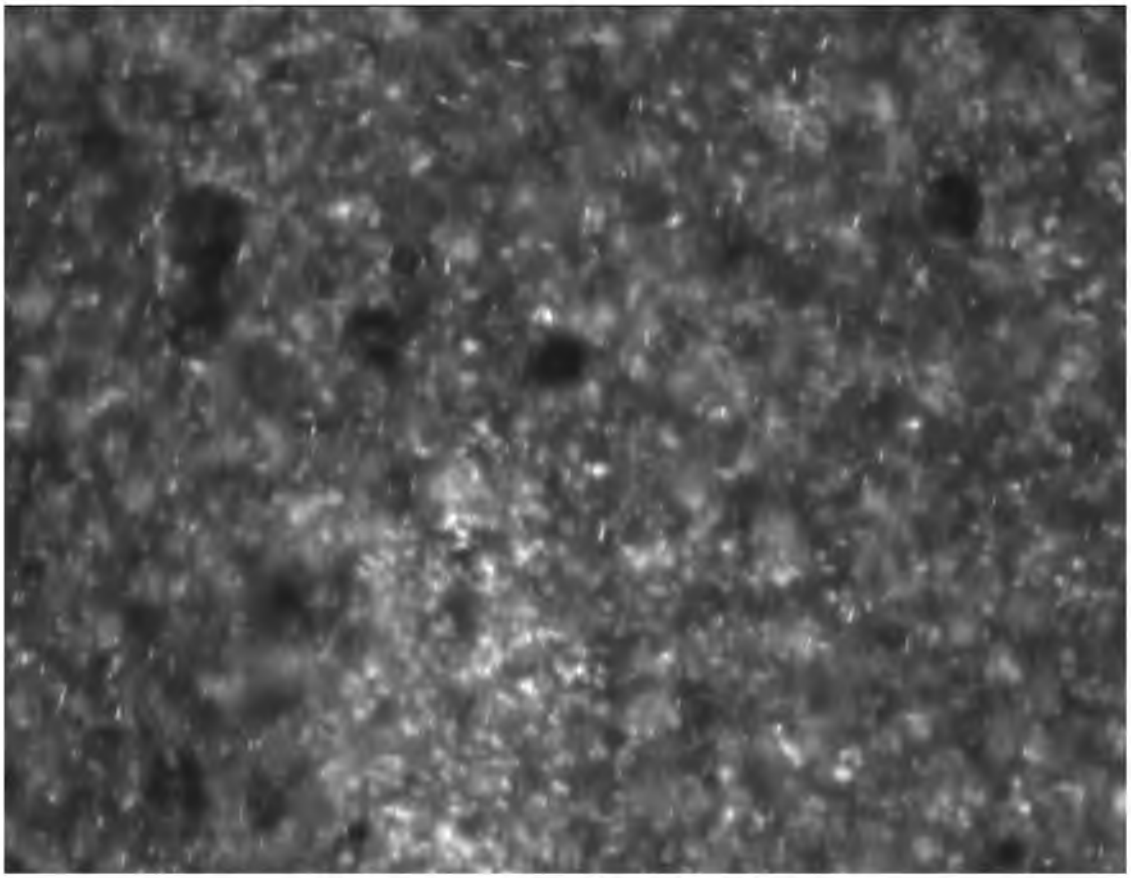

Figure 4.20. Live flow image using CantyVision InFlow® system with a marked wax crystal population center (bottom center-left). These clusters frequently appeared in all tests, reinforcing the need for multiple recordings per particle size test.

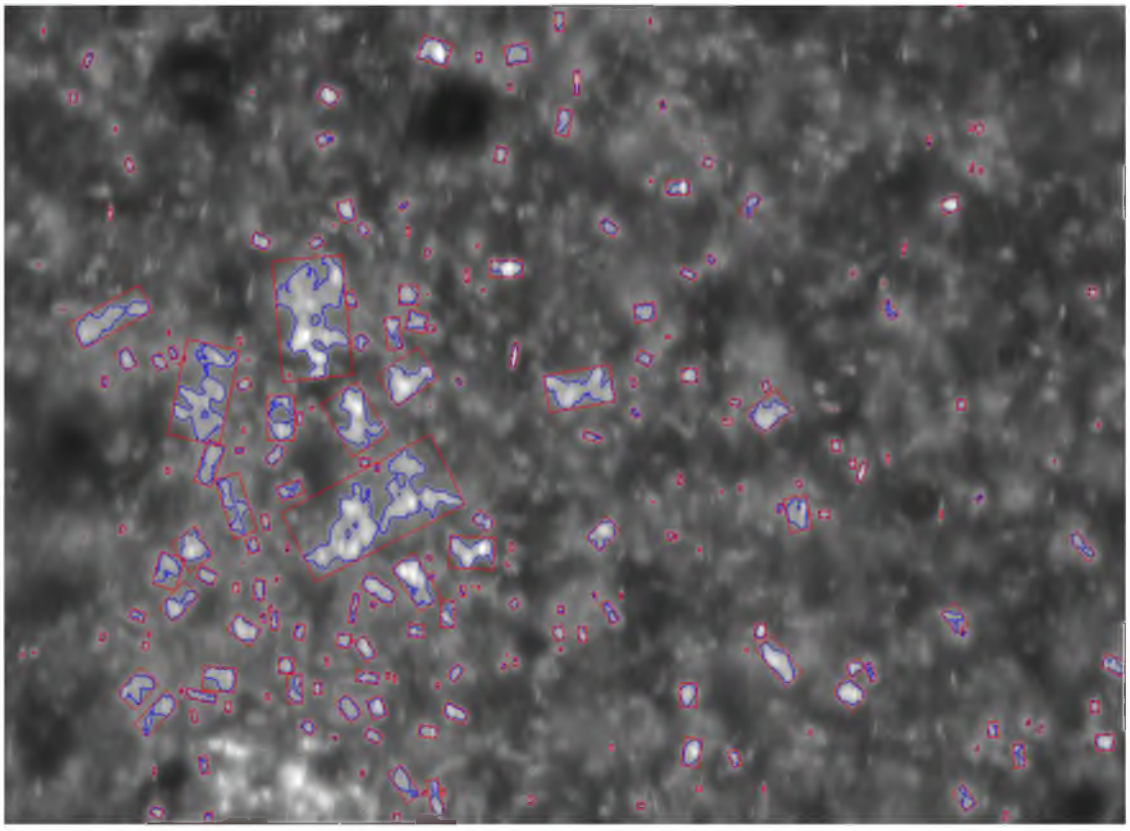

Figure 4.21. Zoomed-in view of wax crystal cluster of Figure 4.20. Note the heavy agglomeration in the cluster, and marked crystal count difference between cluster and main flow surrounding.

Table 4.1. Particle size modification methods and subsequent effects on particle size distribution. A combination of these effects was used to generate the results in Figure 4.24.

Preparation Method	Expected Effect
Increased Test Section Flow Rate	Slower cooling rate - larger crystals
Reduced SCE blade rotation rate	Longer SCE growth time - larger crystals, more agglomerations
Decreased SCE temperature	Faster cooling - smaller crystals
Increased reservoir mixing rate	Increased shear rate - smaller crystals, less agglomerations

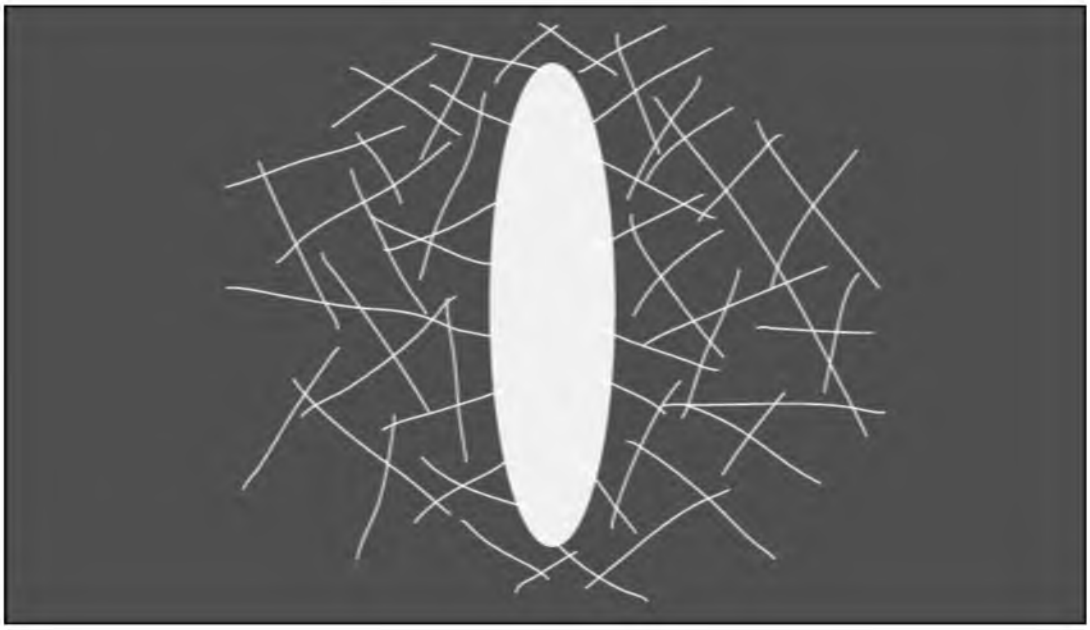

Figure 4.22. Cartoon of theoretical large crystal disruption of gel matrix. Larger crystal impedes cross-linking, and the interactions between the gel matrix and the large crystal are generally shallow and weak compared to the higher quality, natural crystal-crystal interactions.

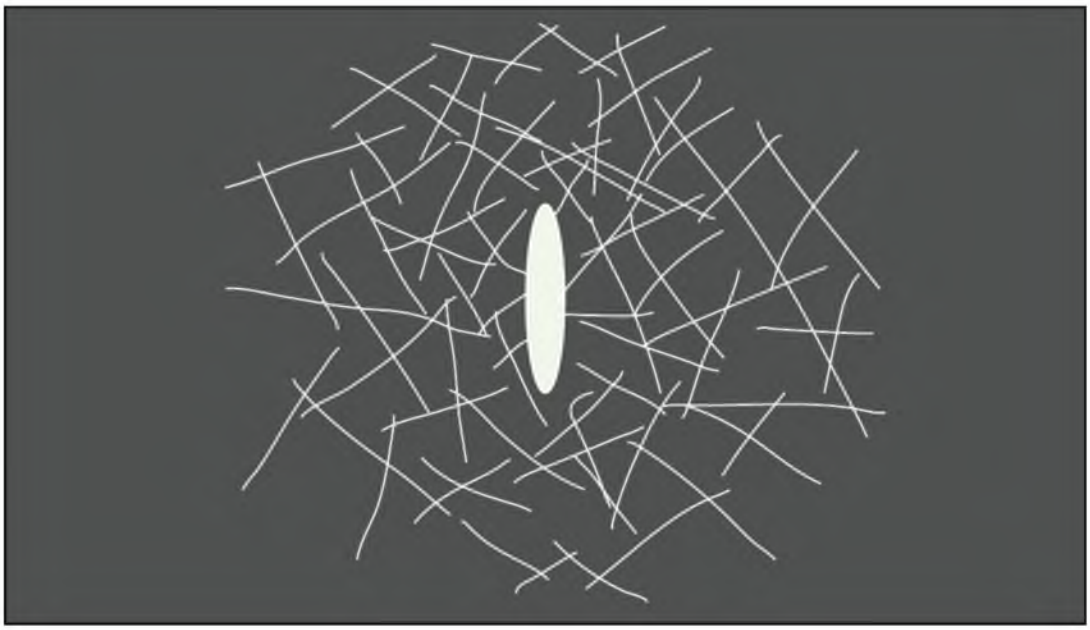

Figure 4.23. Cartoon of theoretical small crystal disruption of gel matrix. Natural gel matrix crystals are same size as those in Figure 4.22, and the small crystal disrupts less cross-links, thereby leading to (theoretically) a stronger gel.

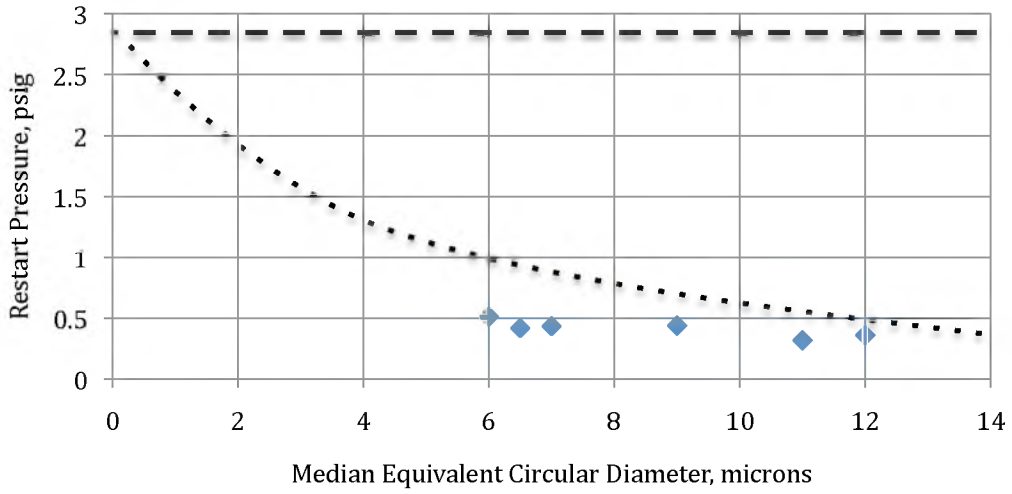

Figure 4.24. Average particle size effect on heterogeneous gel restart pressure. Dashed line represents the homogeneous gel strength, while the dotted line represents the original hypothetical gel strength of the heterogeneous gels with their respective particle size distributions.

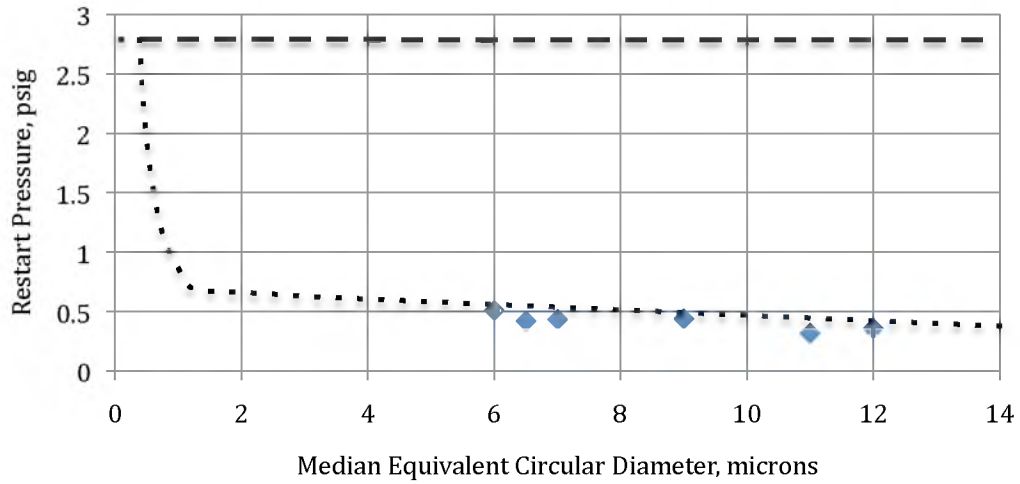

Figure 4.25. Updated plot of particle size effect, including updated hypothetical gel strength (dotted line).

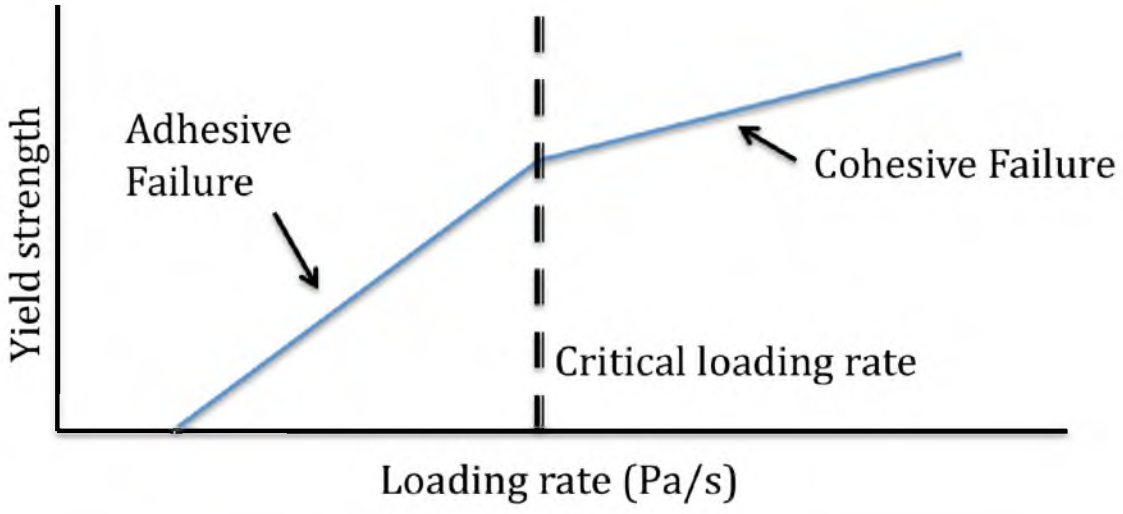

Figure 4.26. Original theoretical heterogeneous failure behavior predicted for increasing pressure loading rate. Homogeneous failure does not exhibit slope change.

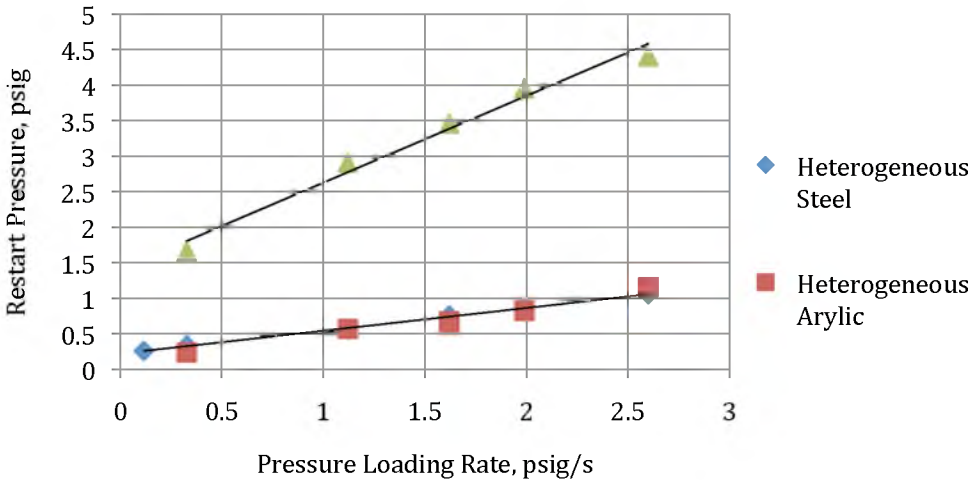

Figure 4.27. Actual restart pressure versus pressure loading rate data for homogeneous and heterogeneous gels. All heterogeneous gels formed from slurries shut down at 16.6 °C and cooled to 3 °C.

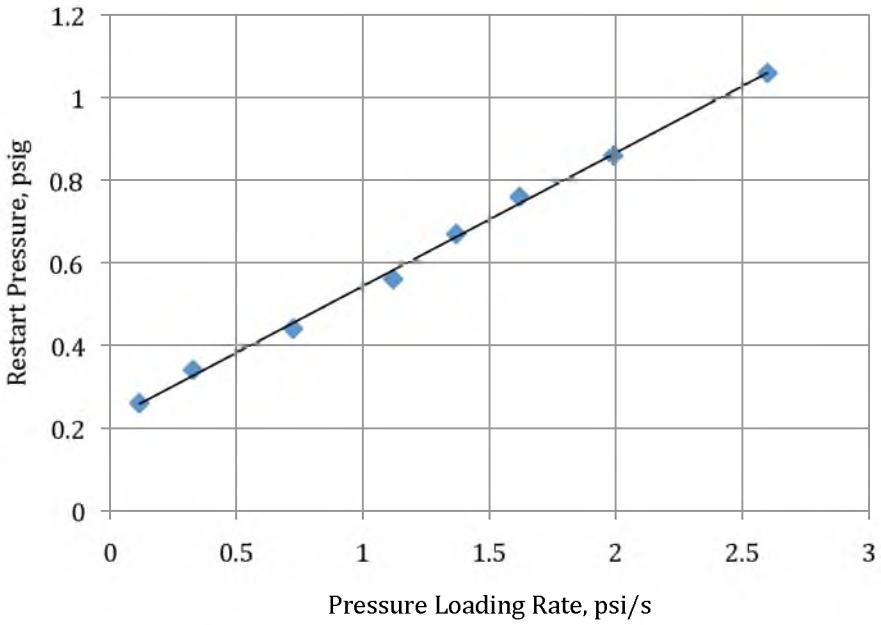

Figure 4.28. Steel section-specific restart pressures versus pressure loading rate for the heterogeneous gel condition. No deviation in slope is detectable.

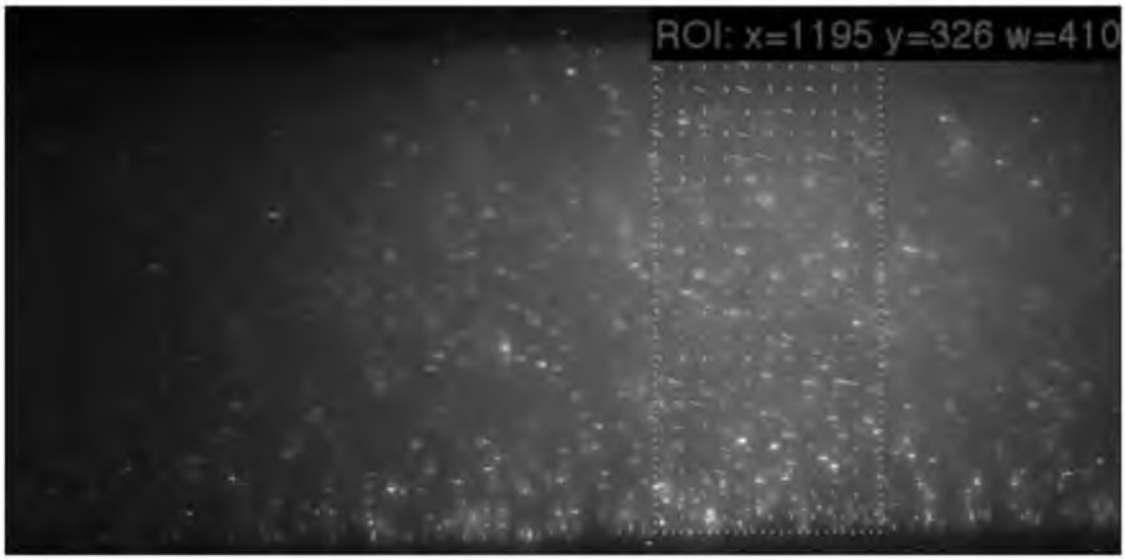

Figure 4.29. PIV image of heterogeneous gel just before breakage. Pressure loading rate of 2.0 psi/s used. Region of interest (ROI) shown between the dotted lines center-right. Arrows are the velocity vectors.

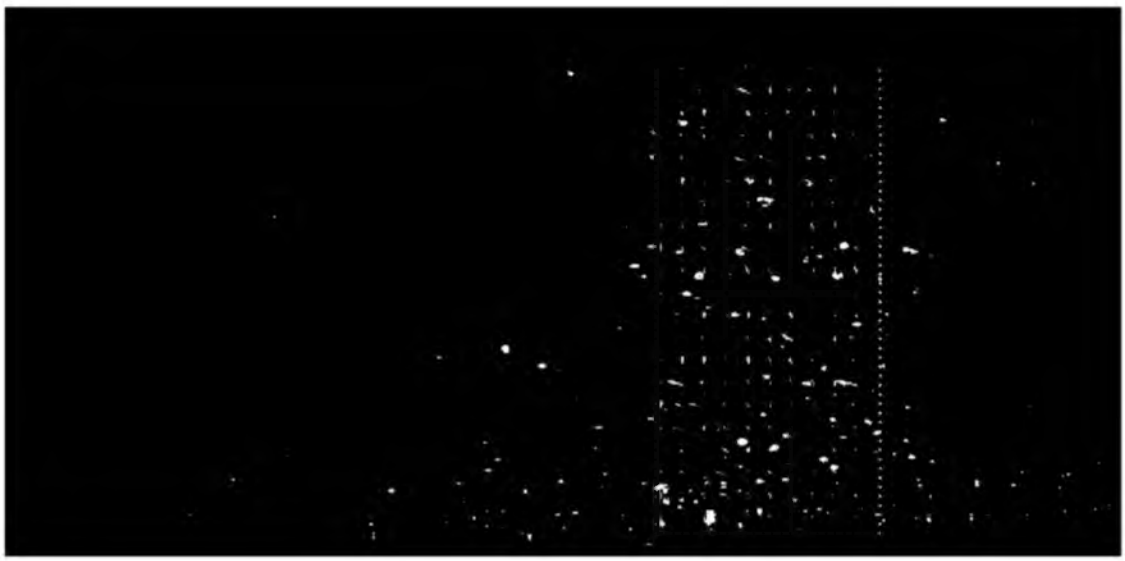

Figure 4.30. Enhanced image of Figure 4.29. Note lack of consistent vectors (due to lack of movement) throughout gel.

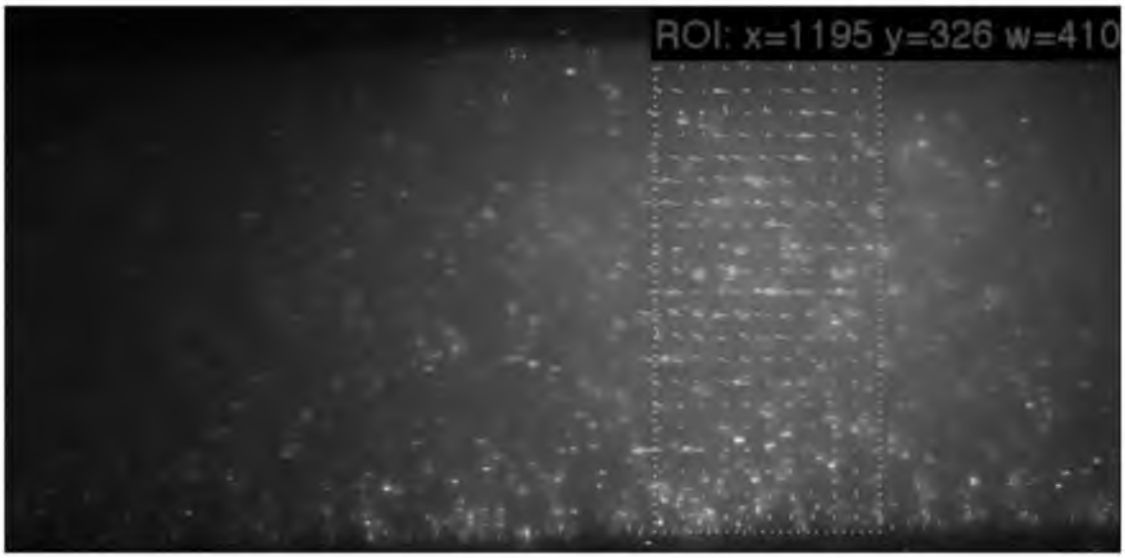

Figure 4.31. PIV image of heterogeneous gel immediately after breakage.

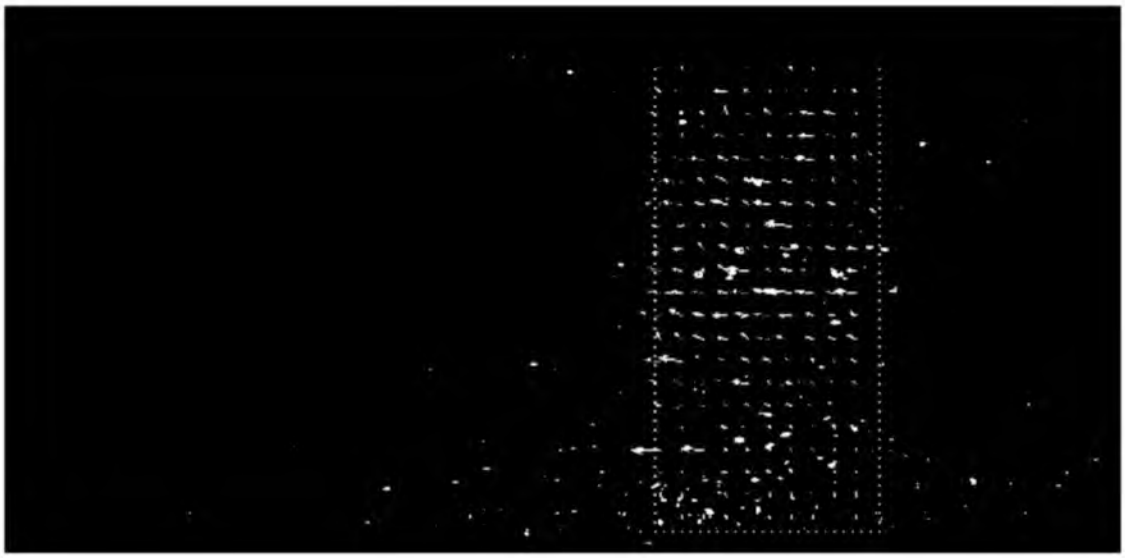

Figure 4.32. Enhanced image of Figure 4.31. Consistent vectors have appeared in the bulk of the gel indicating fracture and flow. No such vectors are seen at the walls (top and bottom of the image) indicating center-core failure.

Table 4.2. Summary of PIV restart experiments with observations.

Loading Pressure Rate, psi/s	Observations and Failure Type
0.328	Slight central movement before wall - possibly cohesive failure
1.12	Full gel movement but with early parabolic profile instead of plug flow - likely cohesive failure with poor image timing
1.37	Central movement before wall - cohesive failure
1.62	Extensive central movement before wall - cohesive failure
1.99	Extensive central movement before wall - cohesive failure
2.6	Central movement before wall - cohesive failure

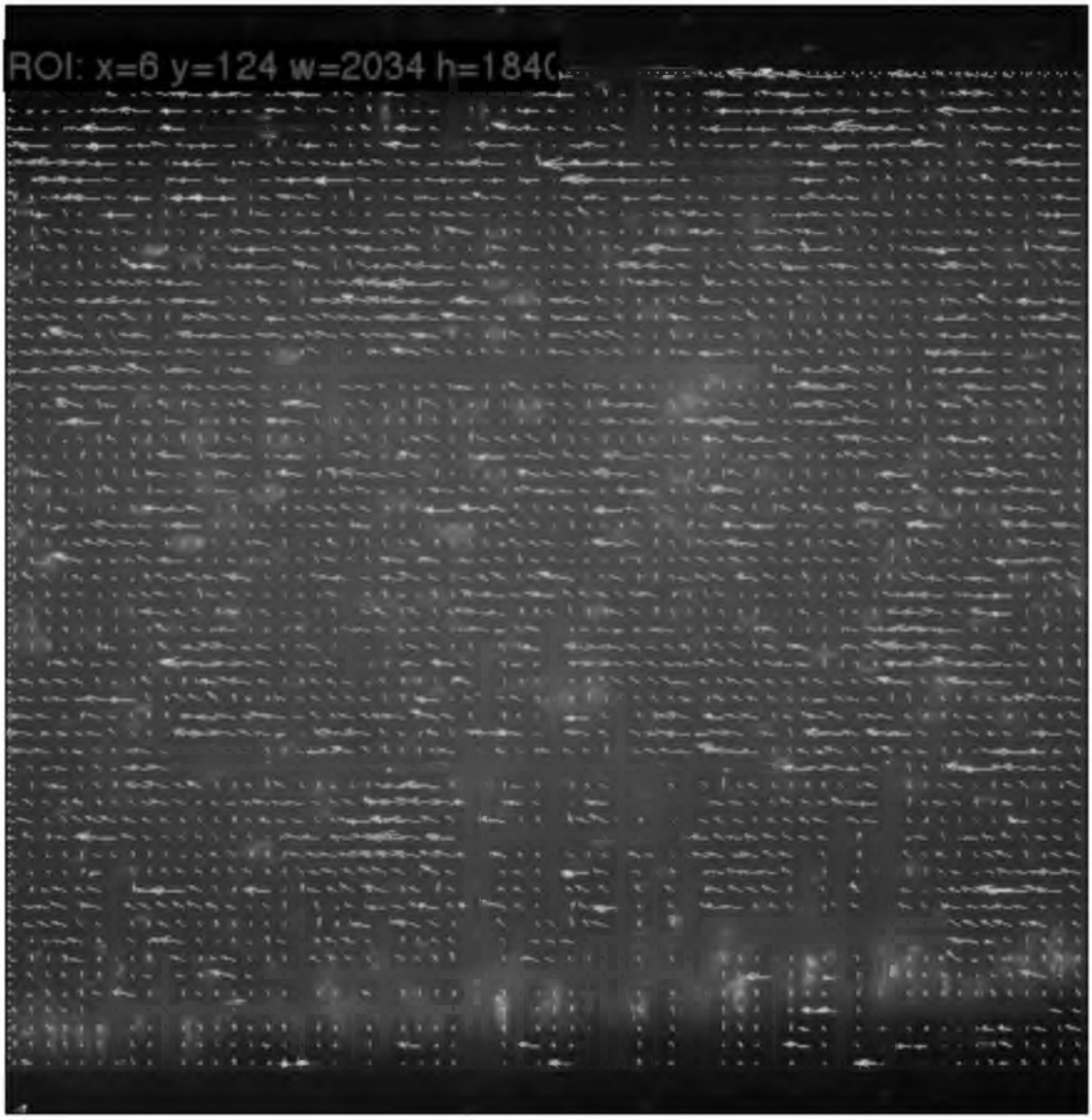

Figure 4.33. PIV image of homogeneous gel just before breakage. Anomalous vectors due to image blurring from the gel dispersing the laser beam. Note the lack of vectors at the walls, particularly the bottom.

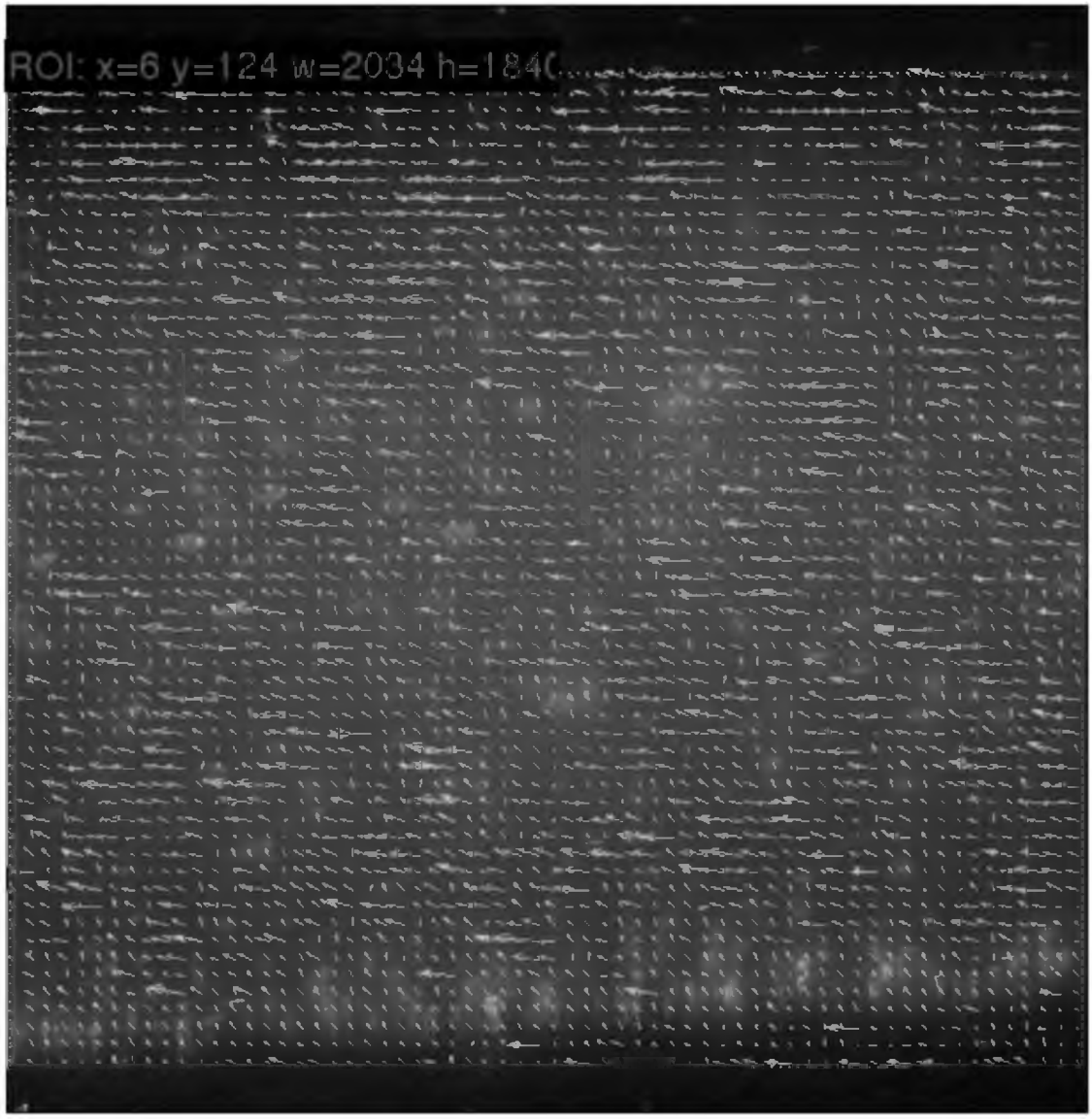

Figure 4.34. PIV image of homogeneous gel just after breakage. While the anomalous vectors are largely unchanged, a definite, distinct (and small) trend change in the vectors overall has occurred, indicating a general movement of the entire gel. Small trend is due to this image being captured very near the moment of breakage. To illustrate, compare the vectors near the bottom of the image to those of Figure 4.33.

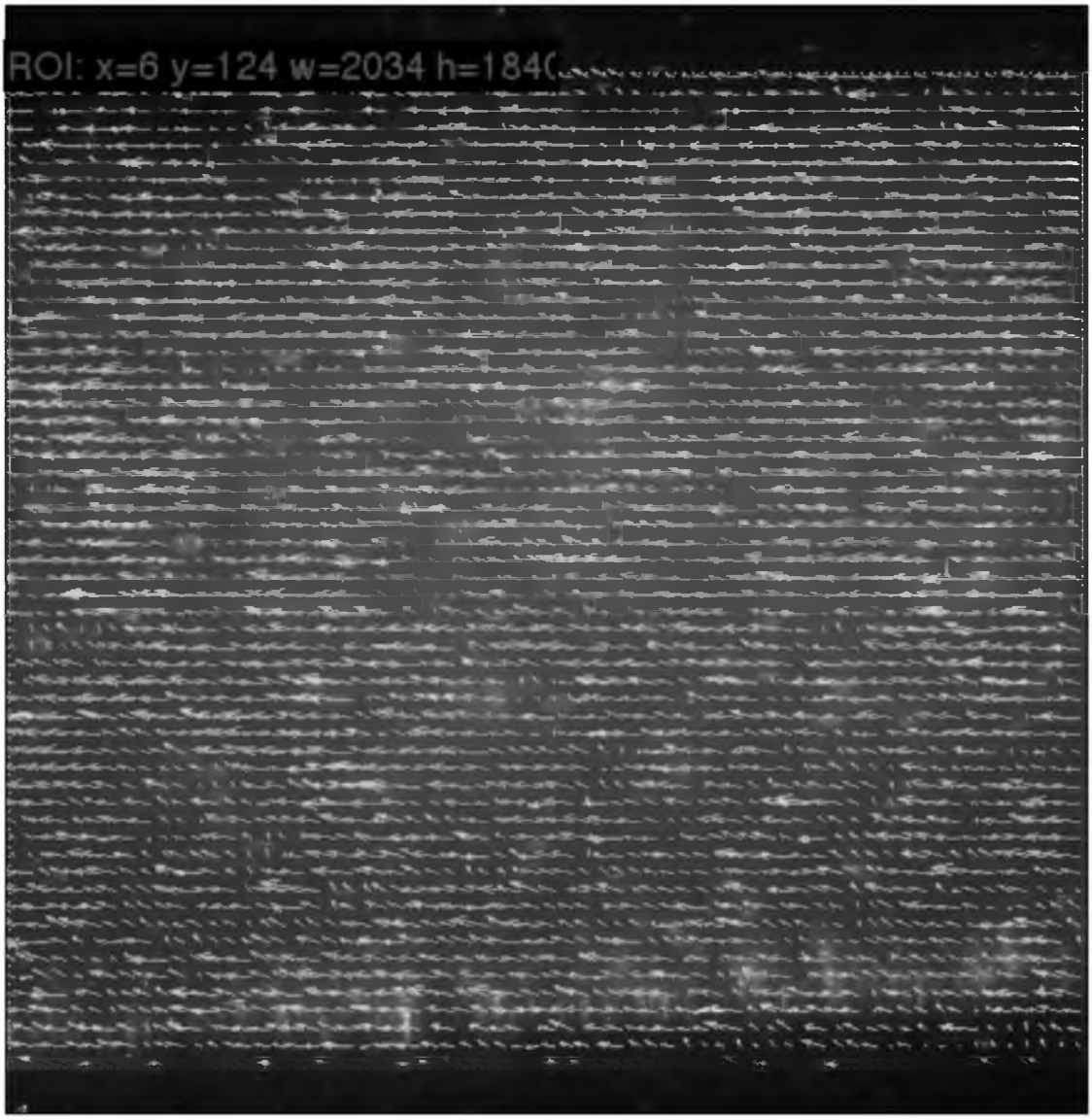

Figure 4.35. PIV image of homogeneous gel 200 ms after breakage. Entire gel is moving at the same velocity suggesting plug-flow movement. Such movement occurs with adhesive failure at the wall.

CHAPTER 5

KEY FINDINGS AND CONCLUSIONS

The conclusions of precipitated wax crystals being the dominant precipitation sites (thus fundamentally changing the way in which the gel matrix is structured) and the particle size effect (balance between particle size and particle number) need to be explained. The fundamental change in gel structure may be the reason for center-core failure since the wall-crystal interactions are basically unchanged, while crystal-crystal interactions are very different.

From this research it has become known that 1) heterogeneous conditions can be created with confidence using the Scraped Exchanger, thereby expanding the range of rheological study of oils, 2) heterogeneous gels are significantly and precipitously weaker than homogeneous gels, 3) heterogeneous gels appear to have a fundamentally different gel matrix structure compared to homogeneous gels, 4) particle size distribution of heterogeneous gels appears to have little to no effect on the overall gel strength due to a tradeoff between particle number and particle size, and 5) heterogeneous gels appear to break cohesively in all pressure loading cases (cooling rate was not tested due to equipment limitations), and possibly in all cases regardless of cooling rate due to the disruptive presence of preexisting shear crystals on the gel matrix.

Regarding the idea that the heterogeneous gel matrix is fundamentally different, the suggested reason for this difference is the change in precipitation patterns in the presence of preexisting crystals as shown in Figure 5.1. These crystals may be acting as the primary precipitation site for waxes, and the unnatural, sheared shape of these preexisting crystals would alter the growth rate and quality of crystal-crystal interactions, all while largely preserving the crystal-pipe wall interactions. It is for this reason that author believes the heterogeneous gels exhibit center-core failure – weaker inner crystal interactions with stronger crystal-wall interactions.

In Figure 5.1 four phases of crystal formation are presented. In I, preexisting crystals exist in the oil at shutdown (sub-WAT). In II, the temperature is dropped and more waxes come out of solution, some in the bulk fluid but the majority on the preferential preexisting crystals. In III, the oil is nearing gel point, again with most waxes precipitating on the preexisting crystals. In IV, gel point is reached, this temperature being very near to the homogeneous gel point temperature.

Concerning deposition and "Cold Flow" in general, it can be said that isothermal "Cold Flow" works without question to prevent deposition, and non-isothermal "Cold Flow" significantly reduces deposition rate by reducing the magnitude of the solubility curve dC/dT.

Ultimately some questions remain – particularly regarding the particle size aspect of this research, this being the weakest portion – and an in-depth, visual exploration into heterogeneous gelation would be invaluable to validating or refuting the claims of this thesis. However, the use of the Scraped Exchanger

coupled with a quality design and excellent sensors (Canty, PIV, etc.) has allowed for groundbreaking rheological research in a difficult phase to study. While some may consider the content of this research banal, a solid understanding of the entire volume of oil – not just that which makes the strongest gels or deposits – is absolutely critical in the design of models and theories for breakage and remediation. Without the complete picture, one cannot have a complete model, and without completeness money can be lost, equipment can be ruined, and safety can be compromised in the field.

Bringing all of this back to the basics and regarding the field of petroleum engineering and Flow Assurance, the results of this research give yet another reason to support "Cold Flow" by showing that deposition can be limited and even eliminated, and gels formed via "Cold Flow" processes are considerably weaker and therefore easier to break. If implemented in field pipelines, these results would predict lower maintenance costs and widespread gelled restart, both of which can greatly reduce costs for both companies and consumers.

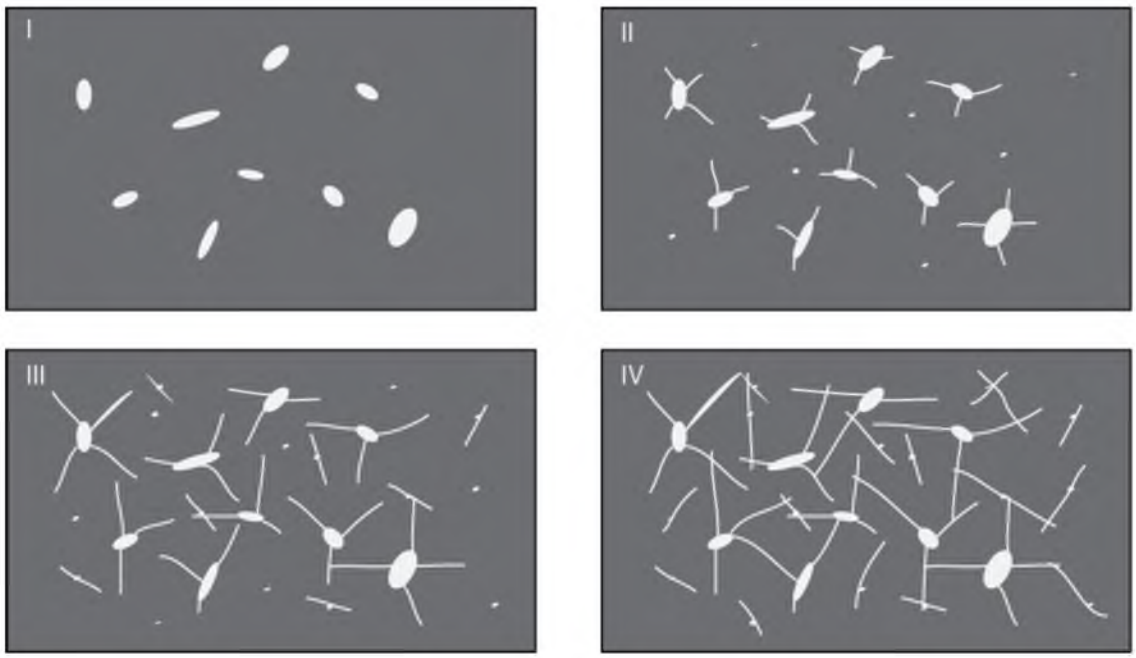

Figure 5.1. Final theoretical effect of heterogeneous conditions on gel matrix development.

APPENDIX A

FLOW LOOP DEVELOPMENT

As mentioned in section 2.2, a number of designs were developed as part of the evolution of the Flow Loop design used in this research. While the grand majority of the data presented in the "Results" section was gleaned from Flow Loop v3.0-3.2, early deposition testing was conducted using Flow Loop v2.1. This section of the appendix presents the development of the Flow Loop models, why they were built in the ways chosen, and the benefits and shortfalls thereof.

A.1 Flow Loop Version 1.0

This version was built by the research team just before the creation of this particular research project, and served as the model for future developments. FLv1.0 (Figure A.1) was designed for the restart of heavy crude oil gels. Oil, heated in a steel drum, was recycled through a 0.5" pipeline until all wax crystals were dissolved. Once ready, flow was stopped and valves one either side of the test section were closed, thus shutting in the oil while it cooled. Temperature profiles at discretized points along the gel were then measured, and once gel was formed and

aged to the operator's wishes the valves were opened and pressure was applied using a syringe (ISCO) pump filled with preheated oil.

FLv1.0 had significant design and control issues, issues serious enough that the flow loop was disassembled and rebuilt into FLv2.0. With no heating or cooling elements, the test section cooling rate was entirely dependent upon ambient conditions in the laboratory (FLv1.0 was in a large warehouse). This resulted in very irreproducible data. Another issue was a complete lack of pressure control and measurement – an aspect partially remedied in FLv2.0. The temperature sensors for this and future designs were J-type Omega thermocouples.

A.2 Flow Loop Version 2.0

The second evolutionary step of the flow loop design was realized with the successful completion and construction of FLv2.0 (Figure A.2). This upgrade featured a unique and powerful new test section design, one that is still being used in FLv2.3 on a different project. This test section comprised of a pipe-in-pipe heat exchanger; annular flow was ethylene glycol circulated through a temperature controller, while the oil flowed countercurrent through the center by means of a variable-speed gear pump. While this design was the important facet control-wise (and a feature used in all subsequent designs), what made the FLv2.0 so powerful was the inclusion of flush-mounted Kulite pressure transducers spaced equally along the length of the test section. These transducers were installed through carefully built ports that extended through the outer jacket into the interior of the oil line. Oil conditioning was conducted using a copper coil installed inside the

reservoir through which coolant would pass. Notably missing from FLv2.0 was the ISCO pump, limiting any restart testing to gear pump-initiation.

The use of these discretized pressure transducers were highly useful to the project preceding this one, as well as the projects afterward, but for the deposition and gelation studies explored in this project they were not necessary. As such, the full rheological capability of FLv2.0 was not used, paving the way for FLv2.1.

A beneficial design concept introduced in FLv2.0 was the pulse dampener to reduce the rather ridiculous scatter in pressure data (+/-1 psig!). Commercial pulse dampeners are expensive and complicated; however, it was determined that these pulses could be removed simply by taking advantage of compressible gases in the presence of an incompressible fluid.

FLv2.0 also incorporated the first attempt at a fully-independent temperature control system by tying in an RTD sensor to the oil inlet of the test section. This sensor fed into the reservoir temperature control system which then would adjust reservoir coolant temperatures to achieve desired results.

A.3 Flow Loop Version 2.1

While the test section of FLv2.0 was fantastic in every regard (so much so that it is still being used extensively), it lacked a crucial property needed in this project: transparency. As such, a new test section was designed to meet this need, this section being constructed out of crystal-clear acrylic tubing. The sensitivity of the material made discretized transducers and thermocouple wells all but impossible, but the clarity opened up the ability to visually detect deposition

formation as well as utilize PIV methods for both deposition growth and gelled restart. Structurally, FLv2.1 and FLv2.0 are identical, but both lacked pressure control as the ISCO pump was no longer present. Figure A.3 shows the clear test section installed, and Figure A.4 shows wax deposition being seen through the material.

While there is a discrepancy in thermal conductivity between the acrylic and steel (0.2 W/(m K) versus 16 W/(m K) respectively), the annular nature of the test section heat exchangers minimizes the effects; in fact, early testing with these heat exchangers showed that while the acrylic test section too slightly longer to cool the gels, the gel strengths produced in both section were exceptionally close – usually within 1-5% of the higher gel strength value.

Most of the deposition testing in the early stages of this research was conducted using FLv2.1. The CantyVision InFlow® camera as installed on FLv2.1 as shown in Figure A.5, but was not used due to pressure limitations (flow through CantyVision system was troublesome due to placement).

A.4 Flow Loop Version 2.2 and 2.3

While not in direct use for this particular project, it is worth noting that FLv2.1 was adapted to include a greater measure of test section temperature control using a programmable recirculator (FLv2.2), and later was fitted with a creep pressure application system (FLv2.3) to allow highly accurate rheological study utilizing creep pressure. FLv2.3 cannot, at this juncture, explore ramping pressure testing.

A.5 Flow Loop Version 3.0

In order to better utilize the acrylic test section from FLv2.1 (as well as improving performance overall), FLv3.0 was created (see Figures A.6 and A.7). The major benefits of FLv3.0 over previous models were a highly-insulated reservoir, low-shear Moyno progressive cavity pump instead of a moderate-shear gear pump, higher capacity temperature controllers, a fully operable CantyVision InFlow® slipstream (complete with cross-polarized filter for wax crystal visualization), and two interchangeable test sections: the aforementioned acrylic section, and an identical stainless steel section. Both these test sections are simultaneously installed, though only one can be utilized at a time.

FLv3.0 was still limited in pressure application for gel research (at this time in the research project, the primary focus was on deposition), and was dependent upon a cooling coil built into the reservoir to condition the oil. This latter aspect proved to be troublesome for any testing below the model oil's wax appearance temperature, as wax would build up on the coils, thus pulling wax out of solution and changing the properties of the oil.

A.6 Flow Loop Version 3.1

The wax sequestration problem was significant enough to require an innovation. Previously, the only way to deal with the sequestration was to manually enter the reservoir and clean the coils every few minutes. This was cumbersome and less effective since the oil went through periods of compositional change

between cleanings. FLv3.1 addressed this problem with the invention of the Scraped Exchanger. Figure A.8 shows the completed SCE and conditioning loop.

As explained in the main body of this dissertation, the Scraped Exchanger utilized an automated scraping blade applied to the cooling surface to constantly remove wax buildup, thereby ensuring constant slurry properties. Furthermore, this addition to the conditioning aspect of the flow loop enabled complete access to the sub-WAT realm of rheological study. Truly, the invention and introduction of the Scraped Exchanger was a game-changer for not only this research project, but for petroleum rheology as well.

A.7 Flow Loop Version 3.2

With the successful installation and operation of the Scraped Exchanger in FLv3.1, the final version FLv3.2 was ready to assemble. While structurally FLv3.2 and FLv3.1 were identical, FLv3.2 included the PIV system for gel restart studies (the PIV system was also temporarily used in FLv2.1 as part of the deposition study), as well as a highly controlled pressure application system. This system consisted of a compressed air supply, an ISCO pump for very low pressure loading rates, and a high-control needle valve for higher pressure loading rates. While not embarked upon in this study, this setup was also designed to handle creep pressure loading conditions. Figure A.9 shows the full and complete construction of FLv3.2.

FLv3.2 was the final design of the flow loop. Future additions would likely include measures for high-pressure flow for hydrate studies.

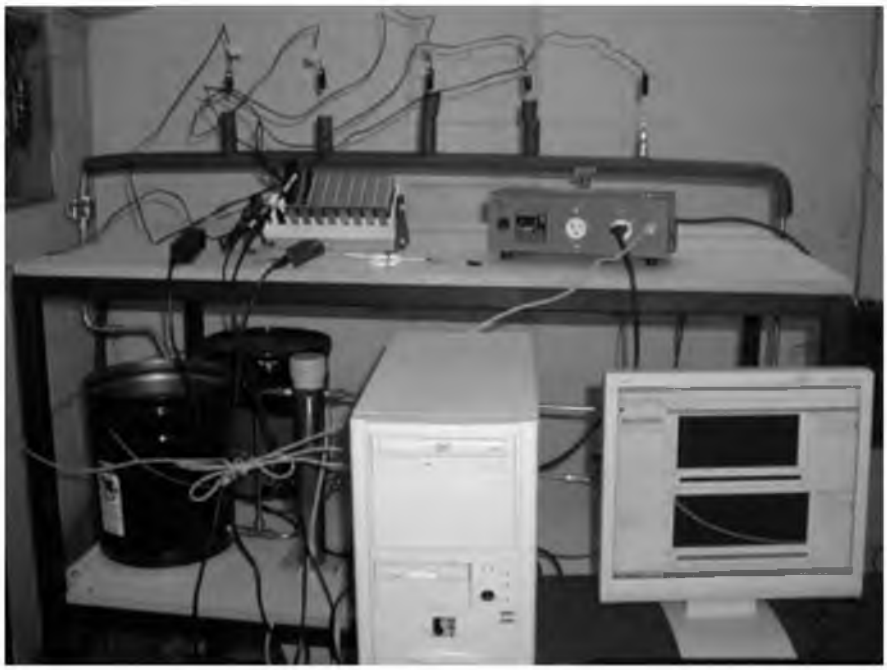

Figure A.1. Flow Loop version 1.0. Two reservoirs for sending and receiving visible to the left. Flow lines proceed from ISCO pump (bottom center-left) up to the left, across through a pipe fitted with transducers, then into the receiving reservoir.

Figure A.2. Flow Loop version 2.0. CantyVision system seen but not installed as of this version. Specialized test section shown on top of the cart covered in insulation, but the sensors are visible. System was unfortunately unkempt in design, leading to plans of a more sleek and streamlined design in FLv3.0.

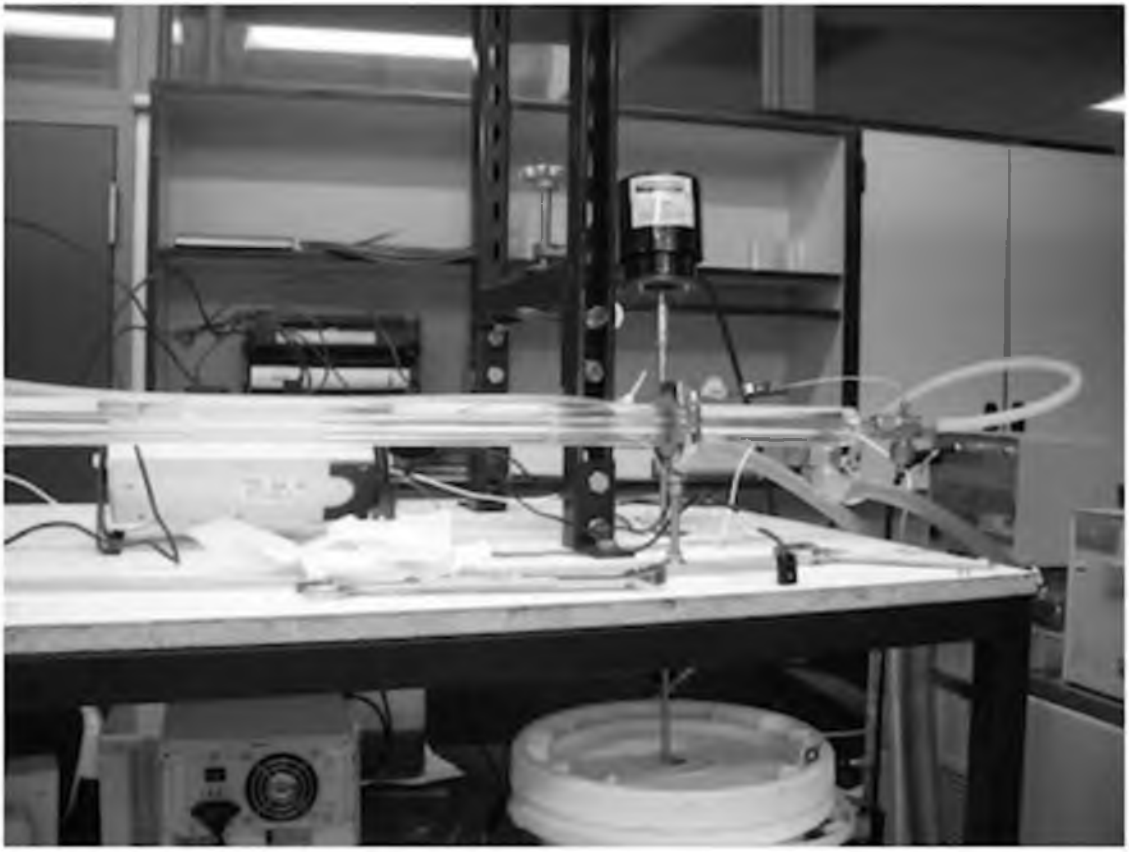

Figure A.3. Flow Loop version 2.1 with clear acrylic test section installed in place of the steel section of FLv2.0. Temperature controllers shown on right edge of image.

Figure A.4. Visualization of wax deposition forming inside the acrylic test section of FLv2.1.

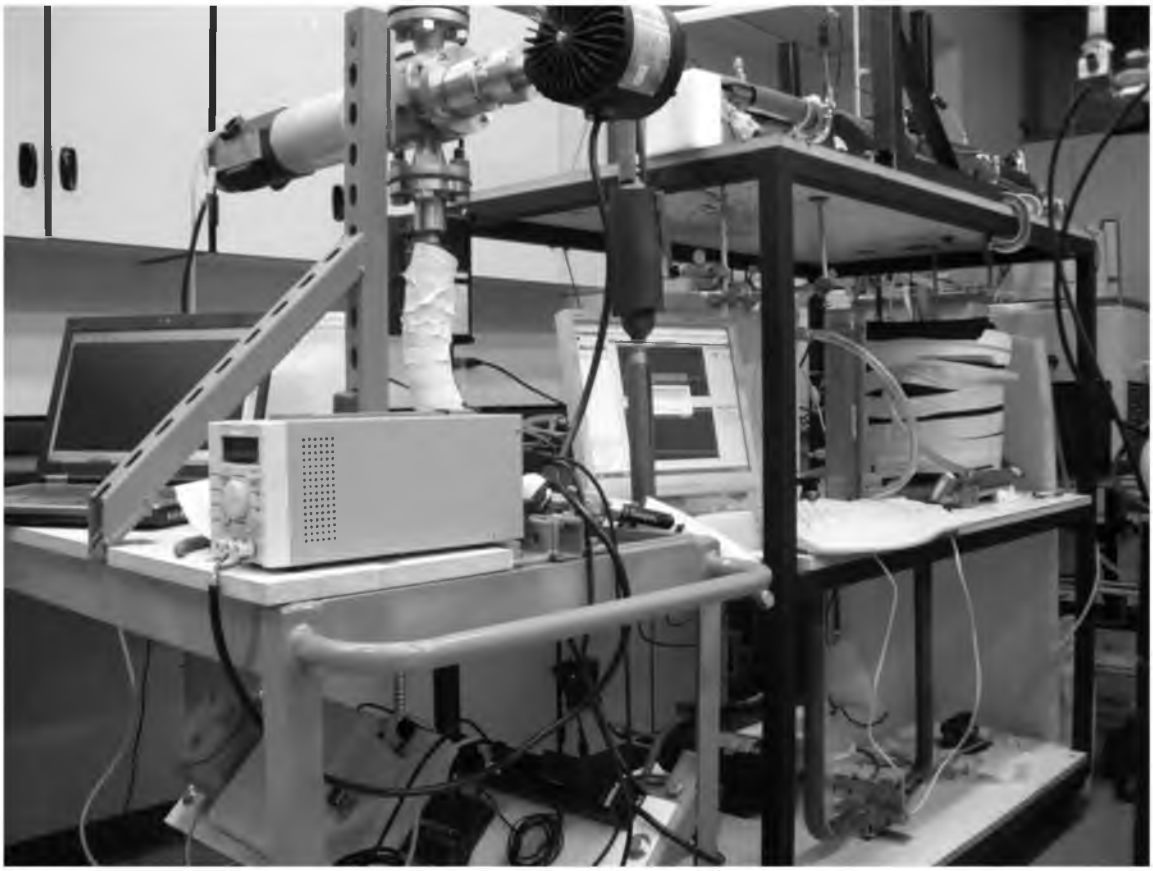

Figure A.5. CantyVision system added to Flow Loop version 2.1. FLv2.1 had flow issues that made the use of CantyVision less than effective. Also shown in this image is the gear pump (bottom right) used to recirculate the oil.

Figure A.6. Flow Loop version 3.0 with both steel and acrylic test sections. A valve at the inlet (further back in the image) diverts flow from one to the other. CantyVision system is seen at the upper left corner, reservoir is just above center, and temperature controllers are on the bottom of the cart.

Figure A.7. Rear-view of Flow Loop version 3.0. Coolant valve seen in bottom left; this valve diverts flow between test sections. Progressive cavity Moyno pump seen to the right on the bottom of the cart.

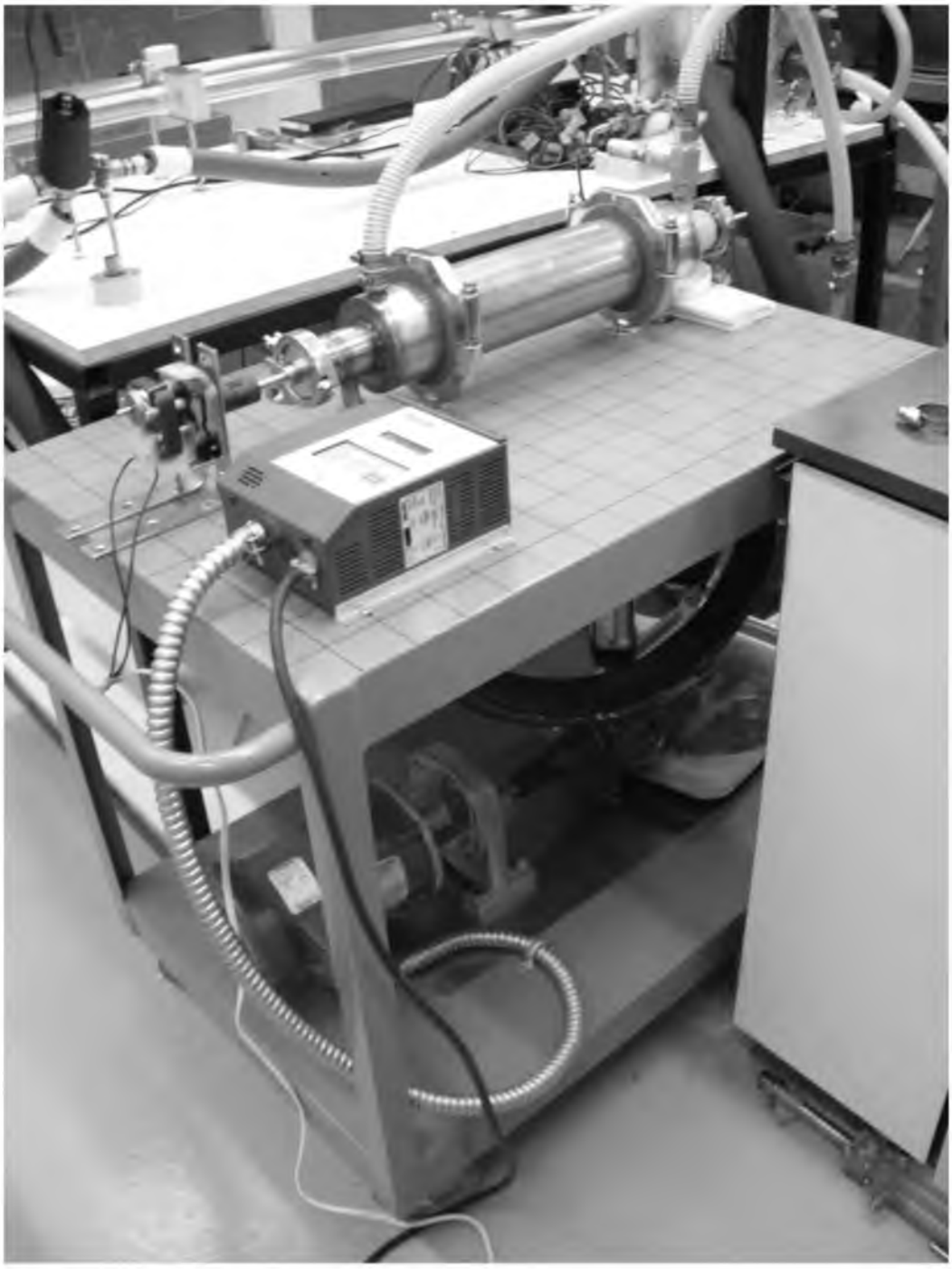

Figure A.8. SCE and conditioning loop of Flow Loop version 3.1. SCE is atop the cart, and the conditioning loop progressive cavity Moyno pump is seen on the bottom of the cart. Oil lines for the conditioning loop are tied into the reservoir on the main cart in the background.

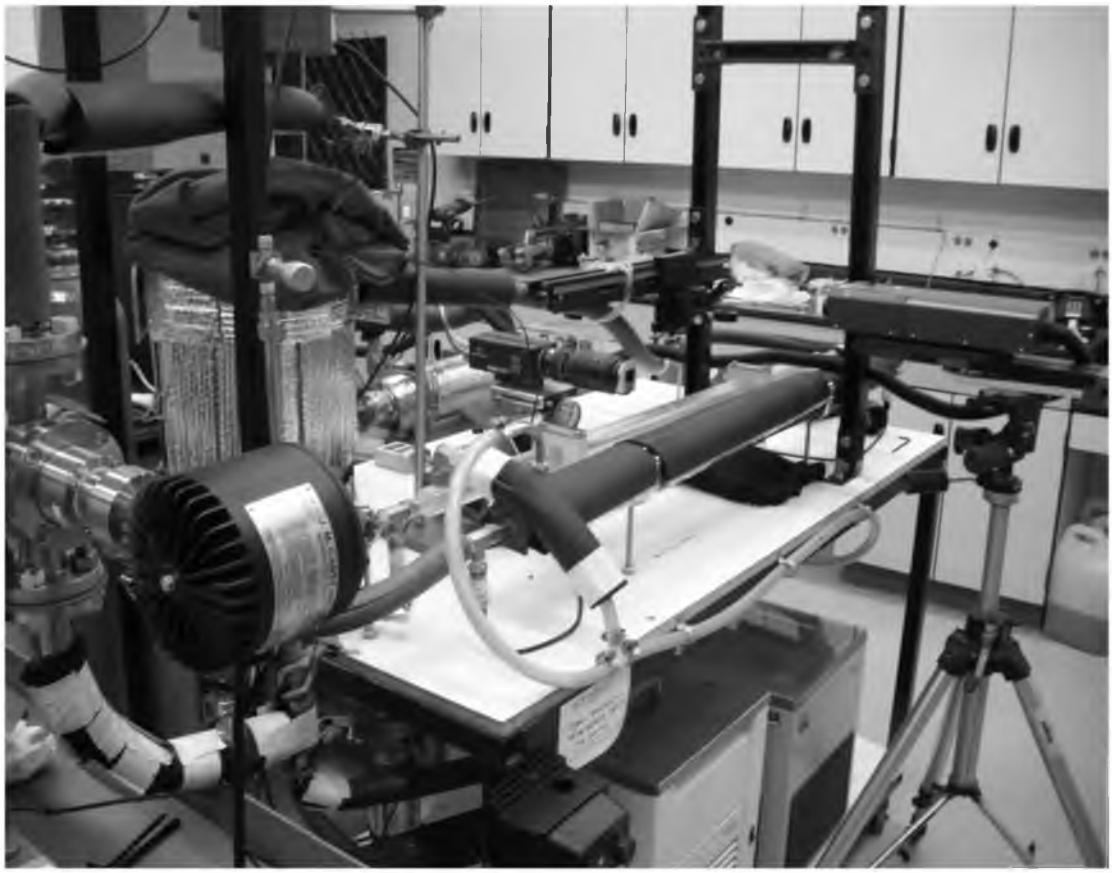

Figure A.9. Flow Loop version 3.2. CantyVision visible to the left, PIV system to the right (PIV camera is in the middle of the photograph), and the SCE unit of the conditioning loop is visible in the background behind the loop.

APPENDIX B

SCRAPED EXCHANGER DEVELOPMENT

To develop the SCE, three projects were undertaken in sequential order: 1) theoretical heat transfer requirements, 2) design and construction, and 3) validation.

B.1 Theoretical Heat Transfer Requirements

Prior to any design or development, an exercise in heat transfer principles was required to properly size the potential equipment. To do this, the text by Incropera et al (2007)[63] was utilized to assemble a series of equations with the intent of sizing the SCE. By assuming a single heat exchanger pass of some immense length and an input equivalent to heat additions from normal circulation, the time required to cool the oil to a specific temperature could be determined for a specific length by cutting the total length into predetermined segments. Each segment became a single pass, and with the desired flow rate a total cooling time could be calculated.

Of course, a series of assumptions need to be made. First, and foremost, the development of this model was conducted with engine oil as the fluid (properties other than density and viscosity were not available for the LVGO model oil). Second,

it was assumed that fluid movement through the SCE was turbulent like an industrial pipeline (this turned out to be false, as all testing regimes with the FL series were laminar). Third, the coolant temperature was assumed to be constant across the exchanger, thereby simplifying the governing equation for heat flux. Fourth, wall resistance to heat transfer was assumed to be negligible due to high conductivity of stainless steel. Fifth, average thermal parameters (between initial and final temperatures) were assumed to be adequate. Finally, it was assumed that the inside wall temperature was constant during the complete process; this assumption is likely the least valid, but it does allow for a much simplified solution.

Perhaps most important to this exercise was the assumption of heat input. A recycled conditioning loop has the oil subjected to zero or positive heat flux for a much longer time than the oil is present in the exchanger for any given pass. The heat additions for the theoretical long exchanger would necessarily be quite high – on the order of kilowatts – and as such the exercise would require this addition to obtain realistic results (as could be imagined, with improper heat input the cooling time is much, much less than reality dictates).

Heat transfer was solved for using an annular flow model with a constant wall temperature assumption. This arrangement and assumption simplified the calculation for the Nusselt number (an error made early in the project was an assumption of turbulent flow when reality gave exclusively laminar results). The worksheet created in excel is shown in Figure B.1 with the assumptions for heat input being on the order of 30 kilowatts.

The model utilized in Figure B.1 is highly idealized; the results are somewhat fantastic, but they did give a good idea of how the SCE would behave. While the model predicted a cooling time of 2 hours to cool from 35 to 16.6 °C, reality gave a cooling time of about 2.5 hours. Regardless, with the model developed (obviously, without the SCE constructed, these results had to be trusted on good faith) the actual design and construction of the SCE could begin.

B.2 Design and Construction

Of course, the aforementioned calculations require heat exchanger dimensions to be input in order to receive any results. Said results shown in Figure B.1 present the final selected dimensions of the exchanger: 20-inch inner tube, 18-inch coolant jacket, 2-inch inside diameter. As a note of interest, these dimensions were chosen for a variety of reasons: 1) available materials; 2) blade sizing considerations; 3) flow rate requirements.

Several generations of SCE design were created. The first plan was developed very early on in the research, and is shown in Figure B.2. This design was simple: fluid and coolant set at countercurrent flow, and a rotating screw to clean the surface. Fluid in this design would be forced to move through the auger space, resulting in a large pressure drop. An alternate thought would be to have a hollow screw – the screw shaft only extended a few inches with the remaining thread suspended in some manner. With the first design in mind (SCEv1), rendering software (SolidWorks®) was used to create a three-dimensional model as shown in Figures B.3 and B.4.

While sound in theory, application and construction of SCEv1 proved to be difficult, most notably regarding screw manufacture. This along with other design issues (bearing plate, for instance) led to the design of SCEv2.

SCEv2 included updates to the arrangement of the fluid ports to give the most efficient countercurrent flow arrangement as well as a proposed alternate screw design. This design would overcome the shaft issues and maximize fluid throughput, but unfortunately the design would be difficult and considerably expensive to build.

Per suggestion of an industry representative, a third design was considered. SCEv3 utilized a four-piece vane format instead of a screw, and this design was ultimately accepted due to ease of manufacture, maximization of throughput, and reduction of radial flow (the axially-arranged vanes would theoretically reduce oil flow towards the walls, thereby reducing to a degree the rate of deposition). This design is shown in Figures B.5 and B.6, with Figure B.7 showing the actual construction.

B.3 Validation

Once constructed and installed as shown in section 2.4.1, it was absolutely necessary to validate the effectiveness and function of the new SCE. This was done in two ways: 1) verifying key parameters with the SCE functioning, and 2) monitoring pressure drop across exchanger during a long-term isothermal "Cold Flow" test.

The key parameters tested in the first validation test were, predictably, WAT and gel point. These values are known exactly for the model oil; by using the clear test section of FLv3.2 an estimate of WAT can be made, and using the restart capability of FLv3.2 an estimate of gel point can be made. Of course, some discrepancy (particularly with WAT) can be expected because this type of validation is akin to the less trustworthy ASTM D2500 method; however, just as with that method it is a good guess. Another benefit of this method is that it can be checked routinely with each and every clear test section experiment.

Results-wise, the WAT validation test gave the following: FTIR-measured WAT – 19.5 °C; the clear section WAT with SCE operation – 18.5 ±0.5 °C. Considering that the FTIR test gave a WAT roughly 1 °C higher than the ASTM D2500 procedure, this is taken as a good result and a successful validation of the WAT parameter.

Validation using gel point is slightly more complicated than WAT, but it too can be done fairly actively. In fact, this validation was done using the first gelation testing of the research coupled with the gel point testing, namely the effect of heterogeneity on gel strength. By using the SCE with the conditioning loop to prepare the oil, the gel point of the heterogeneous gels was just below the rheologically measured gel point of 7.5 °C (see section 4.2). As such, it was concluded that the first step of SCE validation is complete and positive, showing that the SCE is not impeding wax formation.

The second validation test is designed specifically to see if wax is being entrained inside the SCE unit itself. Initially a worry arose that wax would build up on the slow moving blade of the vane. If this was occurring, the built up wax would

impede flow slightly, resulting in an increase in pressure drop – not a huge increase, but one measurable in the range of the transducers. To do this, an isothermal "Cold Flow" test would be necessary to maintain constant oil properties, thereby eliminating any "ghosts" that could give false conclusions from the pressure data. As seen in Figures B.8-B.10, the results of this validation are curious.

From Figures B.8 (pressure drop in the SCE) and B.10 (oil temperature) a periodic behavior emerges after the first day of operation; interestingly there is no such effect seen in the test section pressure drop of Figure B.9, though the minute changes in fluid temperature may be responsible for the small increase in pressure drop. In Figure B.8, the build-up of pressure drop over time is indicatory of some type of restriction to internal flow inside the SCE, but after 40 hours the pressure drop suddenly falls to the original level of the clean SCE. This is followed by another build-up and drop-off, and a very similar response is seen in the temperature data with spikes of cooler temperatures corresponding to the pressure drop reductions. It is suspected that what is occurring is a brief buildup of material on the walls of the SCE, stunted in rate of development by the internal shearing forces of the flow and the moving blade. Once the buildup reaches a certain height on the wall, the moving blade removes the entire deposit (this type of growth, being very slow, would have a weaker adhesive strength {gel to wall} than internal cohesive strength {gel to gel})[20], which then reenters flow. Given that the deposit has been exposed to a very cold surface (about 15 degrees below the oil temperature) this loosened deposit would naturally cause a slight reduction in oil temperature. Then over time, the deposit would rebuild and be again removed, causing yet another temperature drop.

It is therefore the conclusion that while some deposit does build up over time, the SCE is functioning exactly as designed: generating a slurry within the experimentally-derived parameters of WAT and gel point, and is successfully avoiding any permanent internal buildup.

ASSUMPTIONS:
Scraped Heat Exchanger does not induce turbulence
Coolant Temperature is relatively constant
Single exchanger model is adequate
Model oil properties similar to engine oil (property table for engine oil is readily available)
Average physical and thermal parameters are adequate
Wall resistance is negligible due to metal of choice
Inner wall surface temperature is constant at coolant temp

PROCESS TYPE:
Input: 0.3 (Enter 0.4 for heating, 0.3 for cooling, Dietus-Boelter equation constant for turbulent flow)

REQUIRED HEAT EXCHANGER DIMENSIONS:

Internal Shaft Dia.	0.25	in
Inside Dia.	2	in
Unit Length	20	in

(wall thickness, jacket thickness, fittings, etc neglected)

TEMPERATURE SPECIFICATIONS:

Fluid Starting Temp	35	C
Fluid Final Temp	16.6	C
Coolant Temp	1	C

FLUID SPECIFICATIONS:

Average Viscosity	30	cP
Average Density	0.834	g/cc
Flow Rate	1.5	gal/min

(For simplicity, use average properties for calulations)

CALCULATIONS FOR MODEL OIL SYSTEM:

Heat Transfer Area	0.0811	m^2	
Hydraulic Dia.	1.75	in	
Hydraulic Dia. Metric	4.445	cm	
Flow Area	19.952	cm^2	
Corrected Viscosity	0.3	P	
Fluid Velocity	94.635	cm/s	
Di/Do	0.125		
Reynolds Number	1169.4	(pVD/u)	
Average Prandtl	6715		
Nusselt Number, Lam	8.185	(use Incropera et al, Table 8.2 and interpolation to determine value)	
Friction factor	0.0644	(turbulent only, equation 8.21)	
Nusslet Number, Tur	22.587	(from Incropera et al, equation 8.62 (ignore Prandtl requirement))	
Nusselt Number, Used	8.185		
Average k_fluid	0.145	W/m/K, J/m/K/s	
Heat Transfer Coeff	26.7	W/m^2/K	
Mass Flow Rate	0.0789	kg/s	
Q, energy flow, total	-2765.9	W	(if negative, then cooling)
Heat Input from Pump	35000	W	(always positive, REQUIRES INPUT)
Total Q	-37766	W	(amount of heat needed to be removed)
Heat Exchange Length	357.37	m	
Min # of passes	703.49		
Total HX Vol	188.36	gal	
Min HX Duration	125.57	min	
	2.09	hrs	

HELPER SYSTEMS: INPUT KNOWN VALUES
(input lower and higher known values)

Nusselt Helper (Range may need to be adjusted)

Di/Do	Nu
0.25	7.37
0.125	8.185
0.5	5.74

(NOTE: these values are Table 8.2 for laminar flow)

Prandtl Helper (Range may need to be adjusted)

T (K)	Pr
300	6400
298.95	6715
310	3400

k_fluid Helper (Range may need to be adjusted)

T (K)	k, W/m/K
300	0.145
298.95	0.145
310	0.145

c_P Helper (Range may need to be adjusted)

T (K)	c_P, J/kg/K
300	1909
298.95	1904.6
310	1951

Figure B.1. Facsimile of the heat exchanger sizing model. Properties obtained using Incropera et al (2007)[63]. A heat input of 35 kW assumed for pump heating and ambient heating due to reservoir residence and insulated transfer lines. Results shown tailored for starting temperature of 35 °C and a final temperature of 16.6°C using a jacket temperature of 1°C.

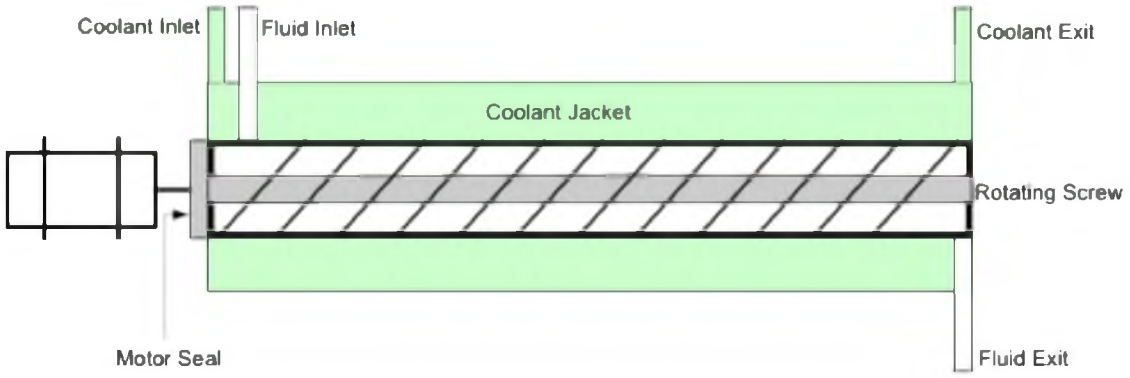

Figure B.2. Initial design of the Scraped Exchanger. Shown here is the concept utilizing a solid-shaft screw mechanism powered by a fixed motor shown at left.

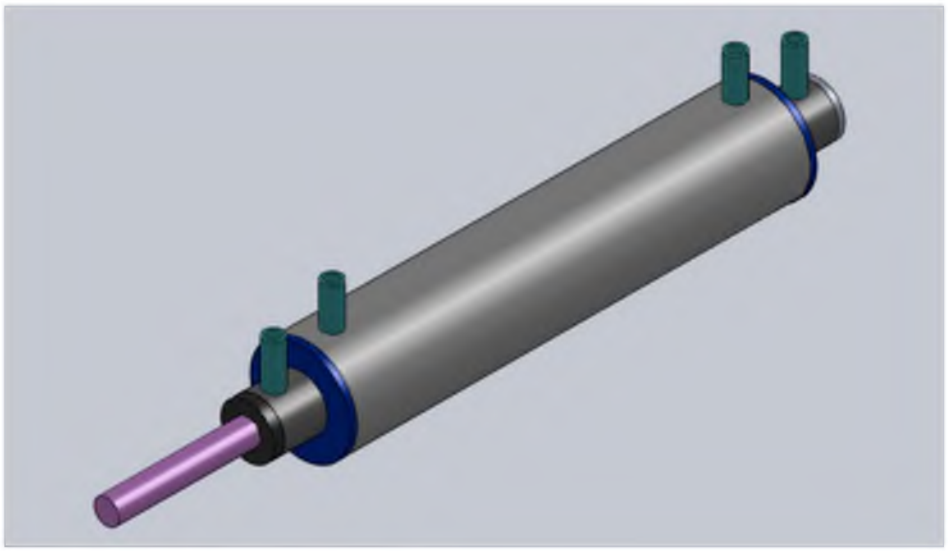

Figure B.3. External view of SCEv1.

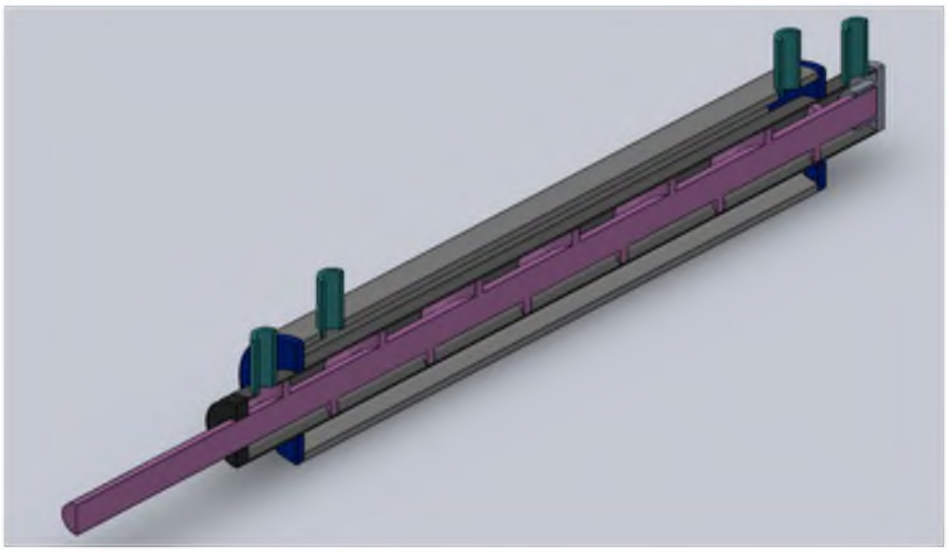

Figure B.4. Cut-view of SCEv1. In conceptual model, the rotating screw shaft is held in place by a rotating seal (black cap on inner tube) and a molded bearing plate (grey cap, inner tube).

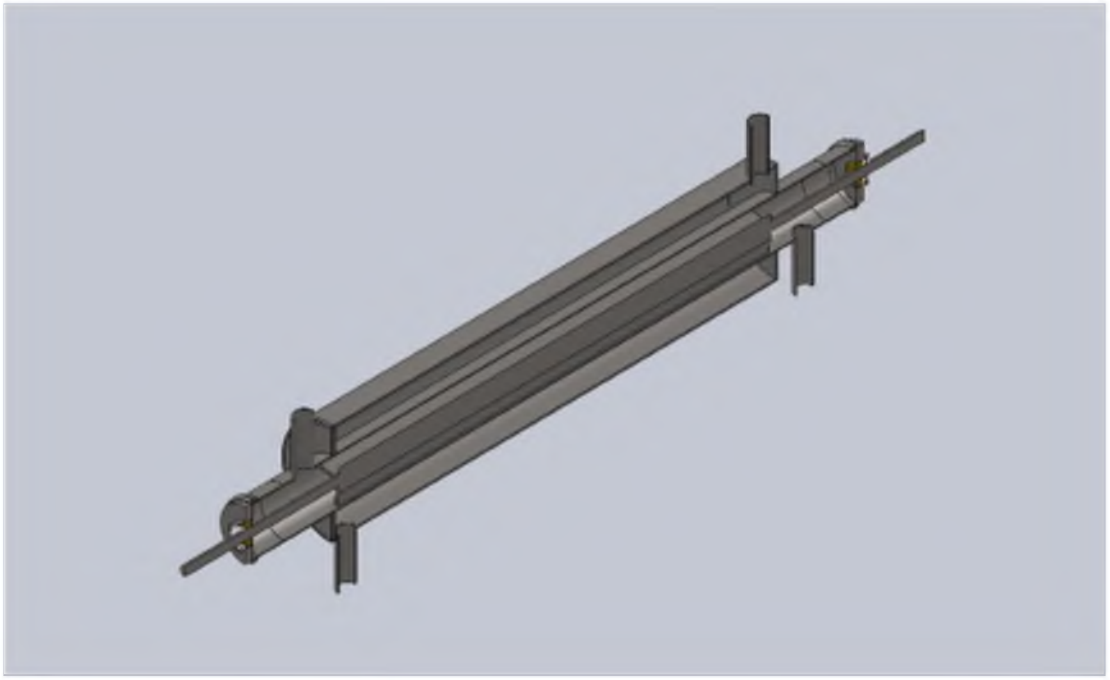

Figure B.5. Cut-view model of SCEv3. Both ends feature rotating shaft bearing held in place with sanitary clamps. Screw design has been replaced with four-blade vane.

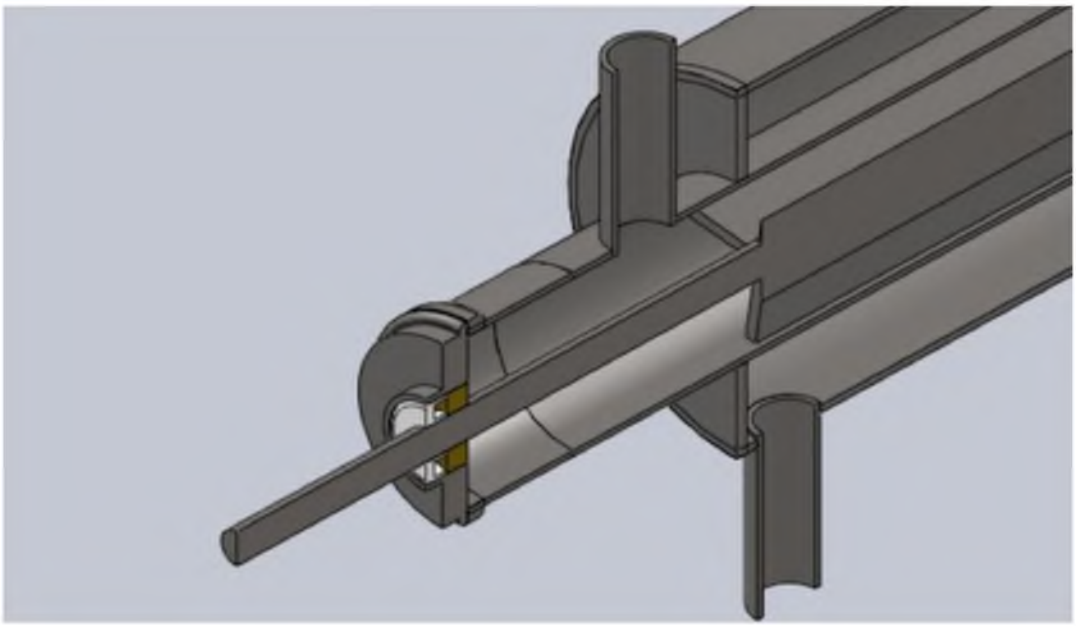

Figure B.6. Close-up view of SCEv3 rotating shaft bearing assembly. Bearing was made using molded steel plate fitted with a low pressure, moderate speed seal as described earlier.

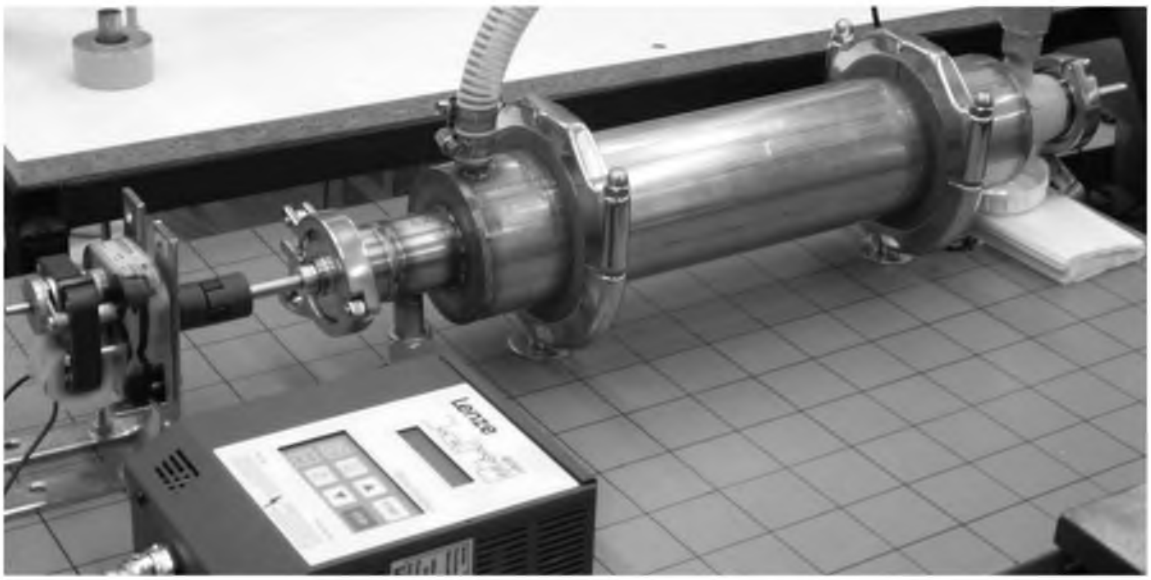

Figure B.7. Photograph of SCE. Blade motor is seen on the left edge, and box on the bottom is the pump controller.

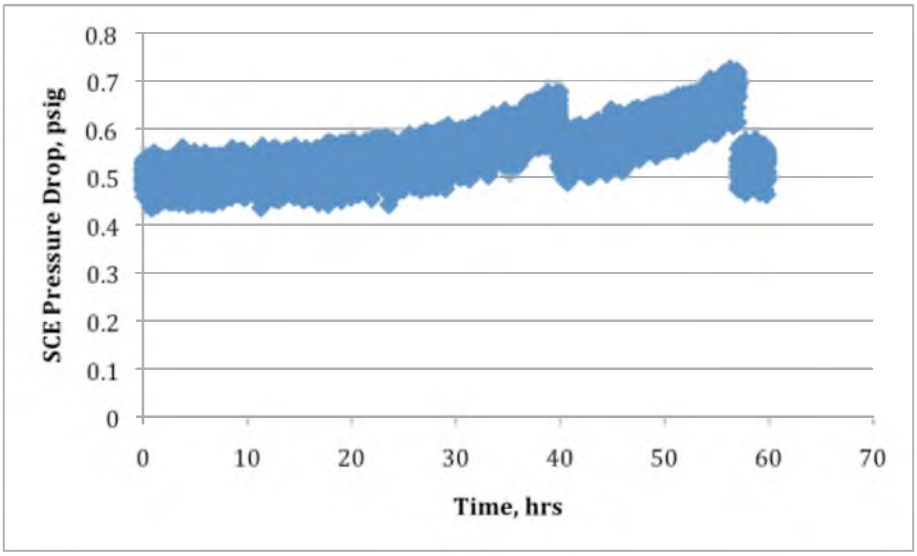

Figure B.8. Pressure drop measured across the SCE in the conditioning loop during isothermal "Cold Flow" validation testing.

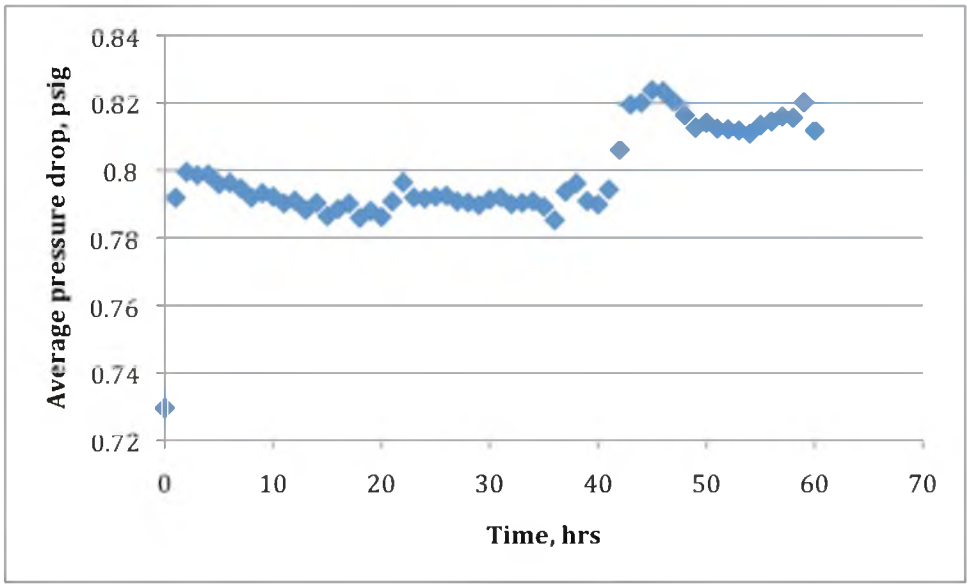

Figure B.9. Averaged pressure drop across test section during isothermal "Cold Flow" validation testing.

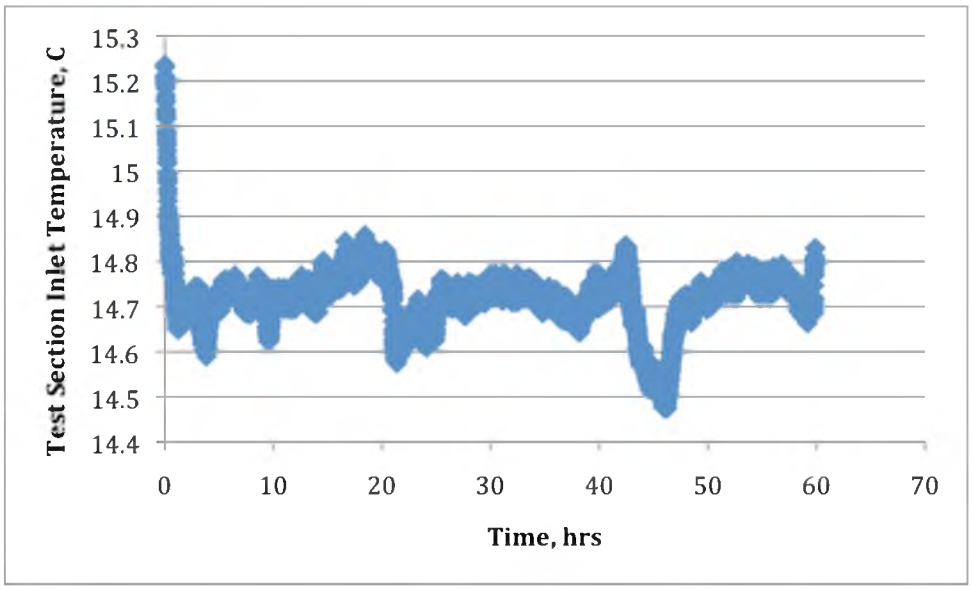

Figure B.10. Experimental test section inlet oil temperature during isothermal "Cold Flow" validation testing.

APPENDIX C

RAW DATA

Presented in this section of the appendix is a collection of the raw data used to derive the conclusions aforementioned. It is very important to note that approximately three months of raw data was lost due to an unfortunate hard drive malfunction of the data acquisition system; all data is presented in some form or another in the main body of this thesis, but the specific raw data for these three months is sadly unavailable. The following data is presented in the same order as the "Results" chapter of this thesis. If the reader is seeking for something stimulating to read, it is suggested to look elsewhere. If the reader is seeking a sedative, continue reading. Narcoleptics are not recommended to proceed with this section.

Many of the plots shown in this section are truncated time-wise in order to remove unnecessary data points from degrading the resolution of the meaningful data. As it takes time between the start-up of data acquisition to the actual performing of the experiment, some tests are truncated anywhere from fifteen seconds to over a minute.

C.1 Heterogeneous versus Homogeneous Deposition

Presented in this section is the raw data for the four deposition tests presented in the informal report of section 4.1. These data comprise Figures C.1-C.4. In each plot, raw recorded pressures are presented with their corresponding pressure drop. Note that while the upstream pressure increases, downstream pressure remains constant for all tests. Data prepared for "Cold Flow" tests are present in their entirety in the body of the dissertation and as such are not included in this section.

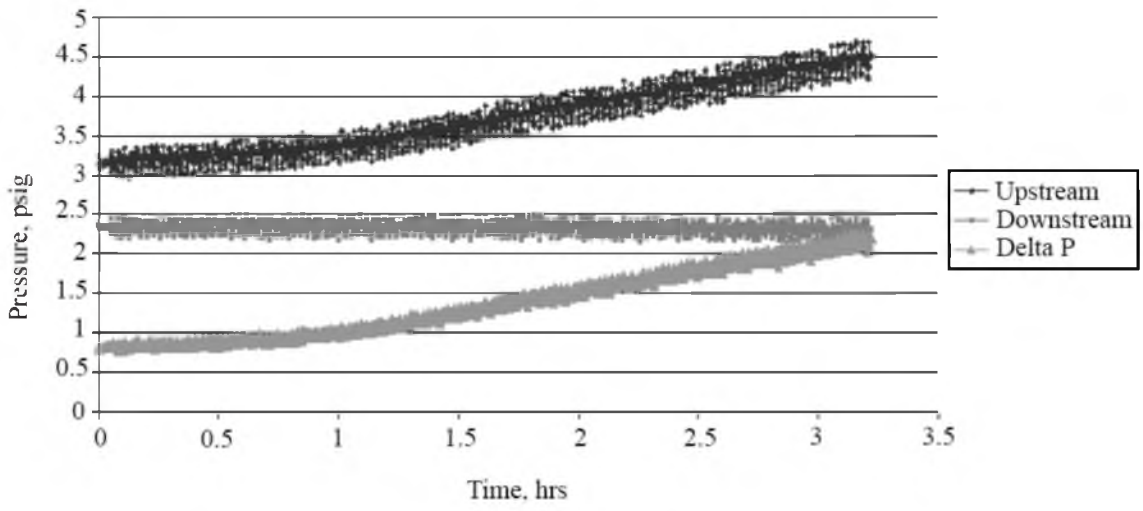

Figure C.1. Pressure profiles and pressure drop for "Hot Flow" test with 7 °C temperature differential. Oil temperature is 20 °C, jacket temperature is 13 °C, flow rate is 0.75 gpm.

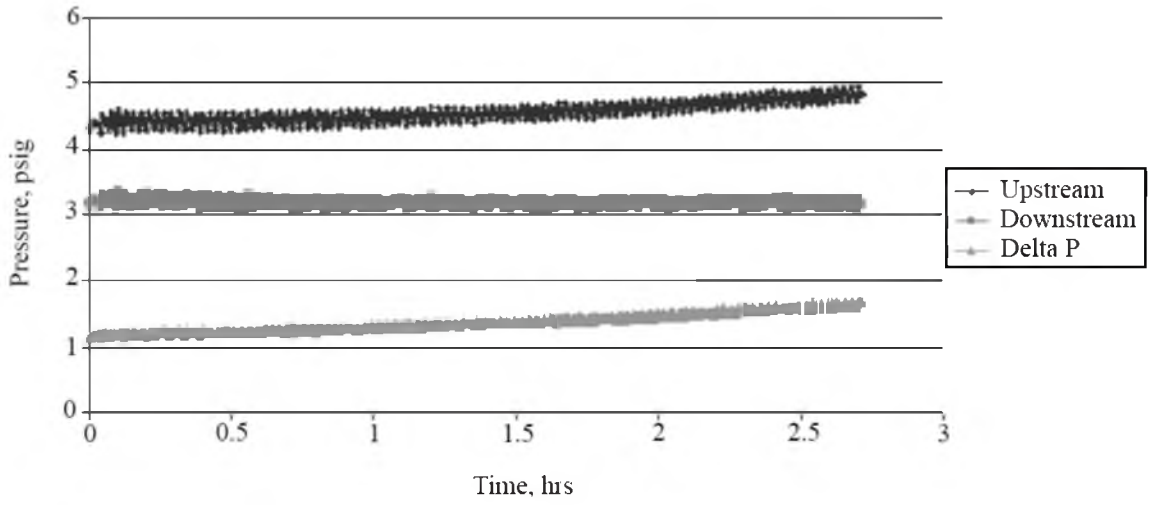

Figure C.2. Pressure profiles and pressure drop for "Cold Flow" test with 7 °C temperature differential. Oil temperature is 16.6 °C, jacket temperature is 9.6 °C, flow rate is 0.9 gpm.

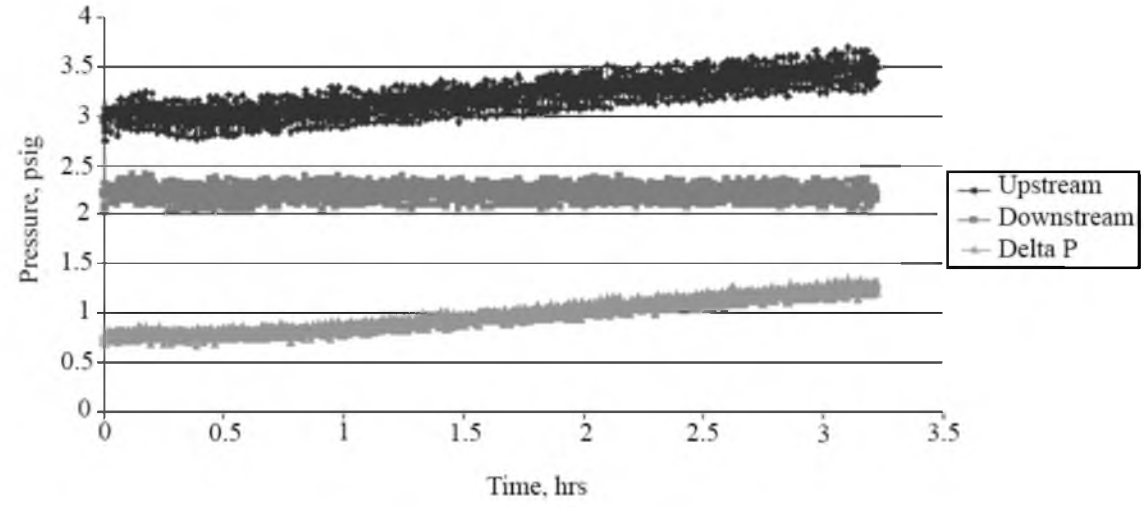

Figure C.3. Pressure profiles and pressure drop for "Hot Flow" test with 5 °C temperature differential. Oil temperature is 20 °C, jacket temperature is 15 °C, flow rate is 0.75 gpm.

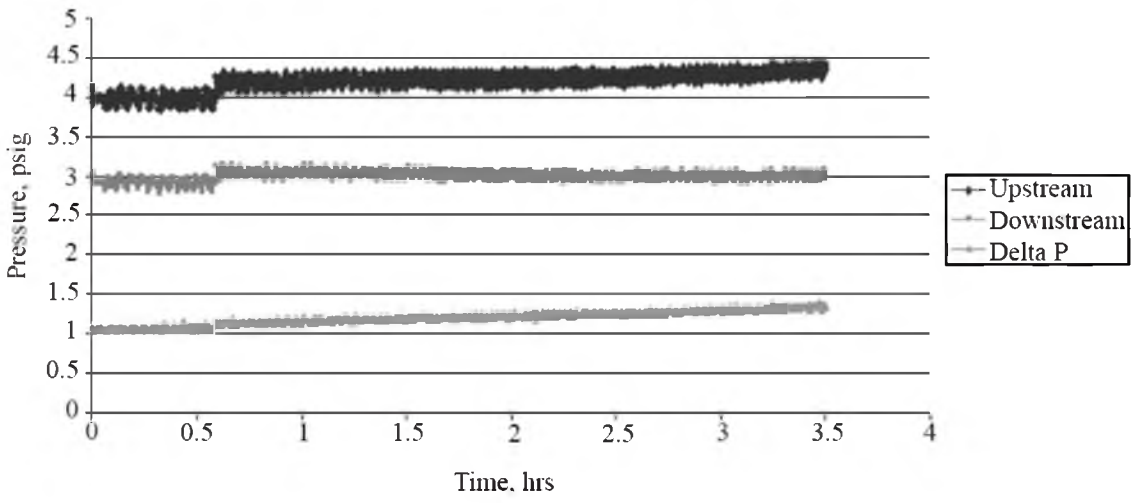

Figure C.4. Pressure profiles and pressure drop for "Cold Flow" test with 5 °C temperature differential. Oil temperature is 16.6 °C, jacket temperature is 11.6 °C, flow rate is 0.9 gpm.

C.2 Heterogeneous Effect On Gel Point

Gel point tests are conducted using the ISCO pump with a flow rate of 80 mL/min (0.035 psi/s, 0.5 Pa/s shear stress loading rate). All gels subjected to 0.33 °C/min cooling rate, 1 hour aging, and atmospheric pressure. All tests conducted using steel test section to avoid any slippage issues, as these can corrupt results and give false impressions of gel presence and behavior. These data comprise Figures C.5-C.17.

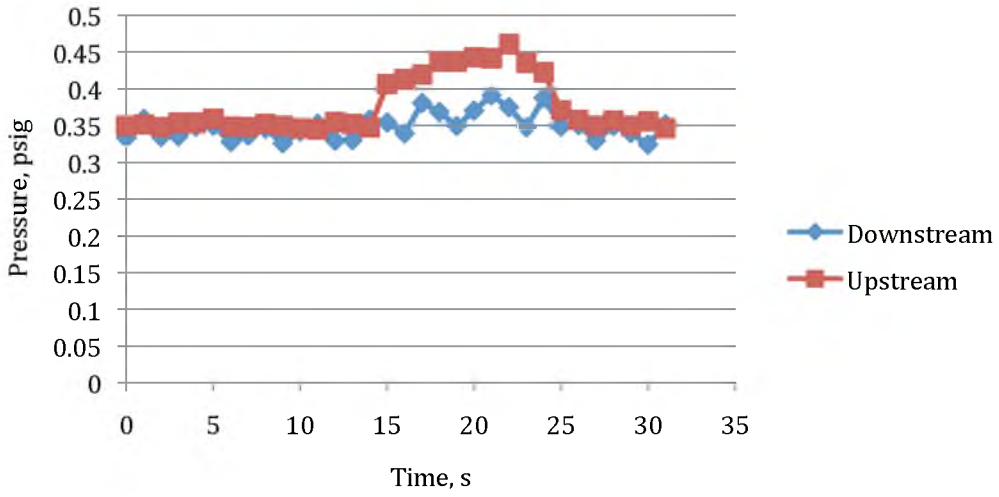

Figure C.5. Gel point test, 17.2 °C slurry conditions at shutdown, 8 °C final temperature. This is a "baseline" type condition as the final temperature is above the homogeneous WAT, meaning no gel is present and pressure response is viscosity-driven.

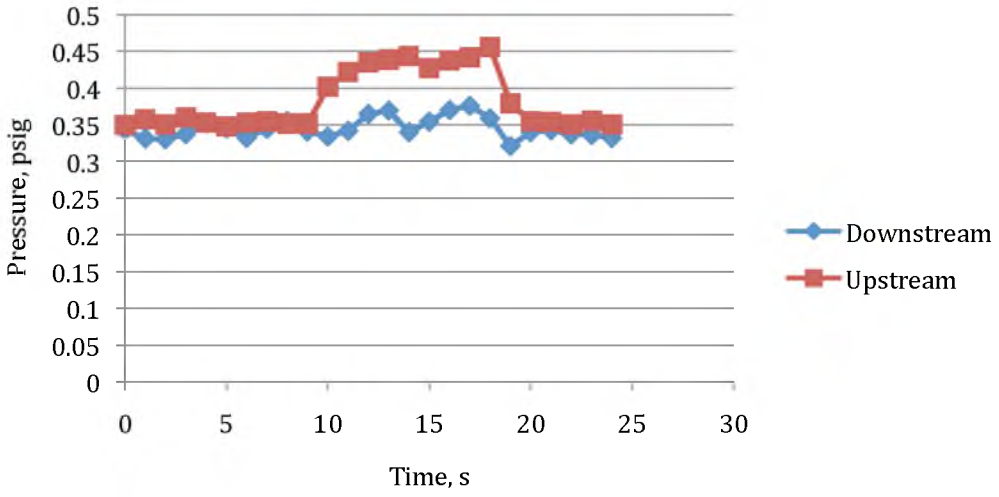

Figure C.6. Gel point test, 17.2 °C slurry conditions at shutdown, 7 °C final temperature. Lack of change from 8 °C test suggests lack of gel formation.

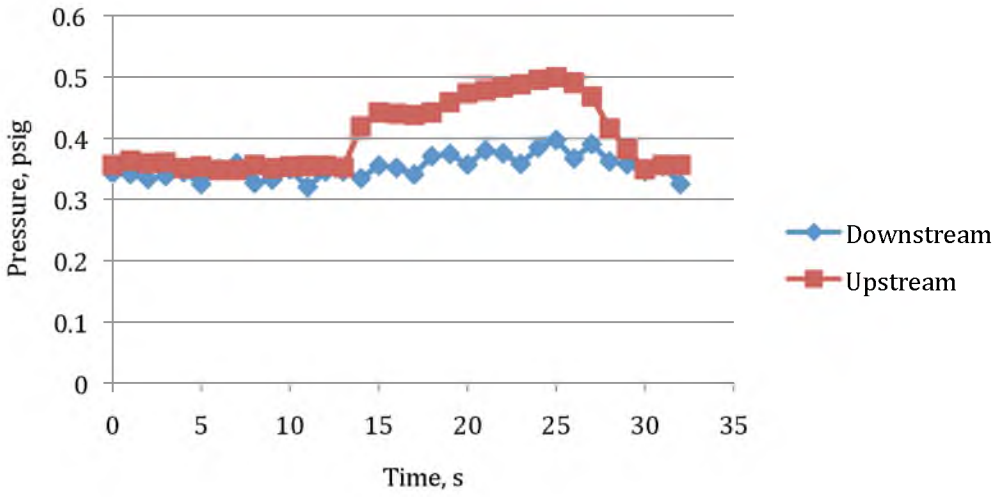

Figure C.7. Gel point test, 17.2 °C slurry conditions at shutdown, 6 °C final temperature. Change in response from 7 °C test suggests early gel formation.

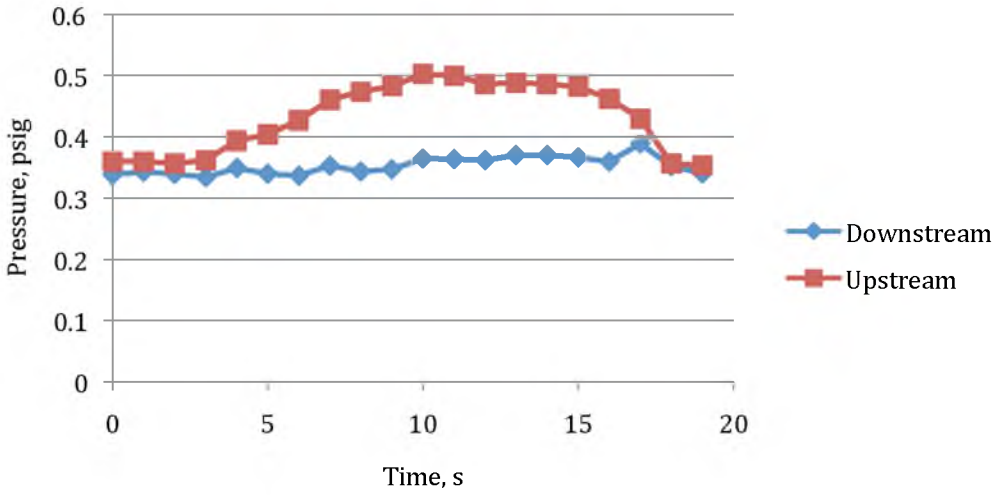

Figure C.8. Gel point test, 17.2 °C slurry conditions at shutdown, 5 °C final temperature. Stable loading response indicatory of presence of gel.

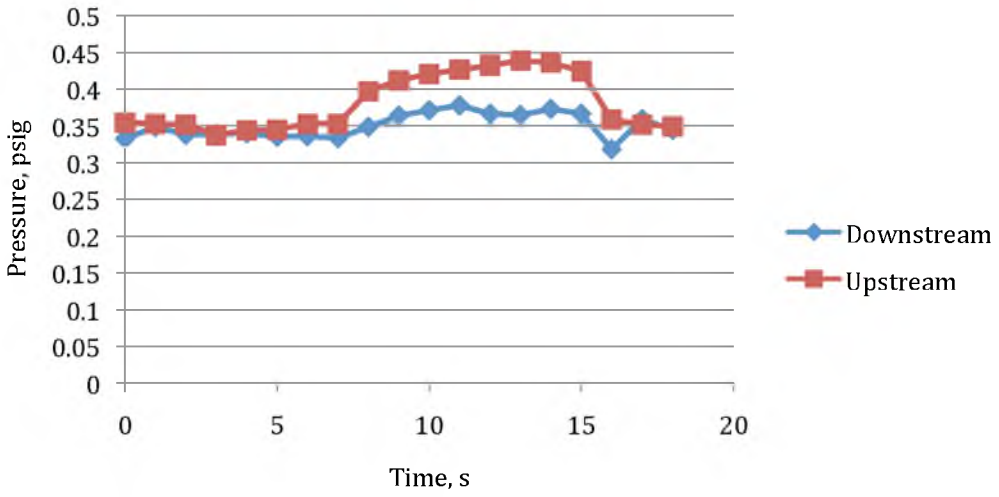

Figure C.9. Gel point test, 16.2 °C slurry conditions at shutdown, 7 °C final temperature.

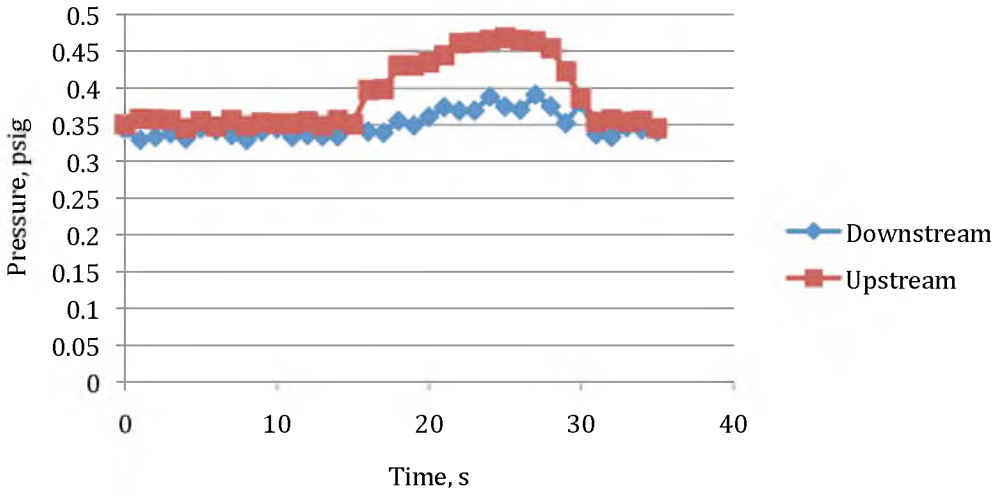

Figure C.10. Gel point test, 16.2 °C slurry conditions at shutdown, 6 °C final temperature.

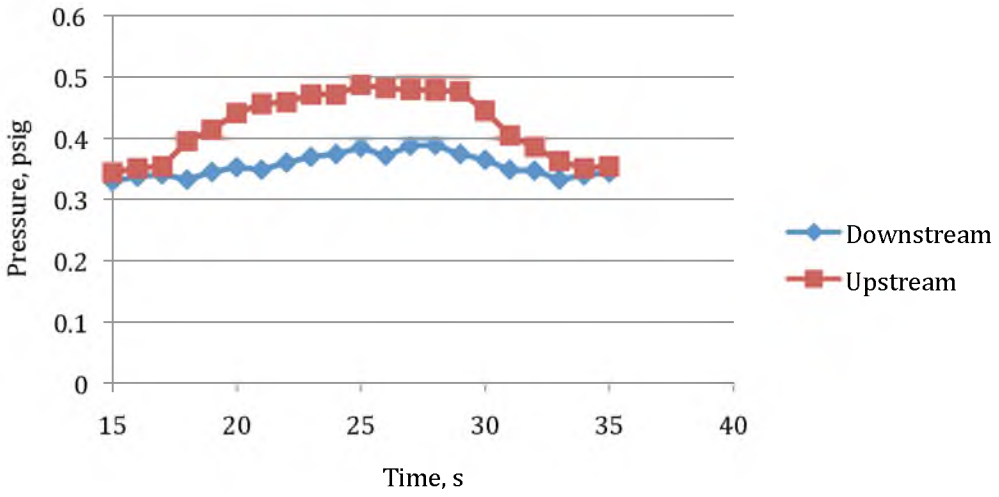

Figure C.11. Gel point test, 16.2 °C slurry conditions at shutdown, 5 °C final temperature.

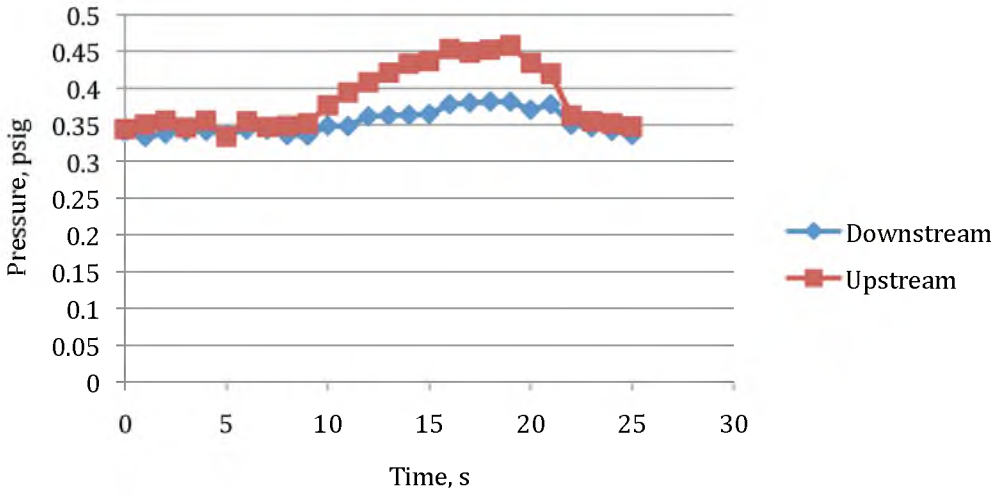

Figure C.12. Gel point test, 15.2 °C slurry conditions at shutdown, 6 °C final temperature. Loading behavior appears to indicate a gel, but more tests are needed to confirm. Run 1 of 2.

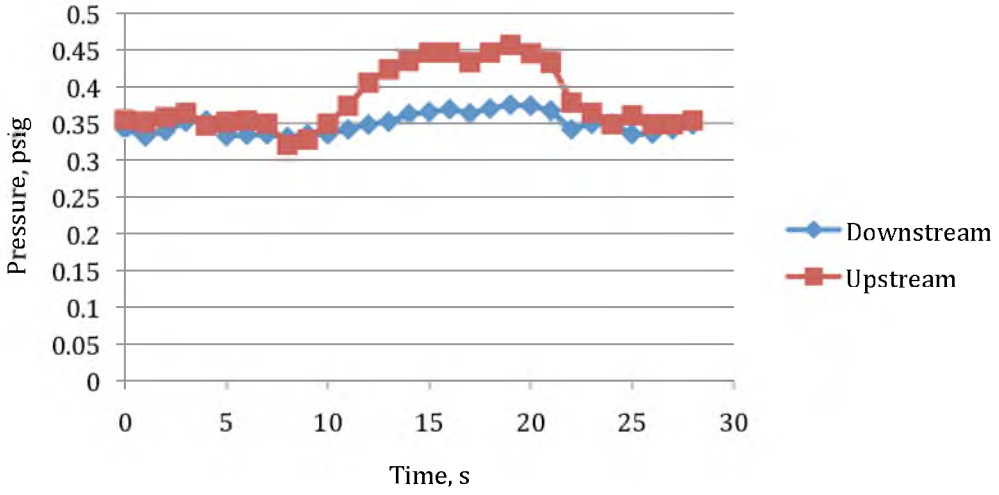

Figure C.13. Gel point test, 15.2 °C slurry conditions at shutdown, 6 °C final temperature. Run 2 of 2.

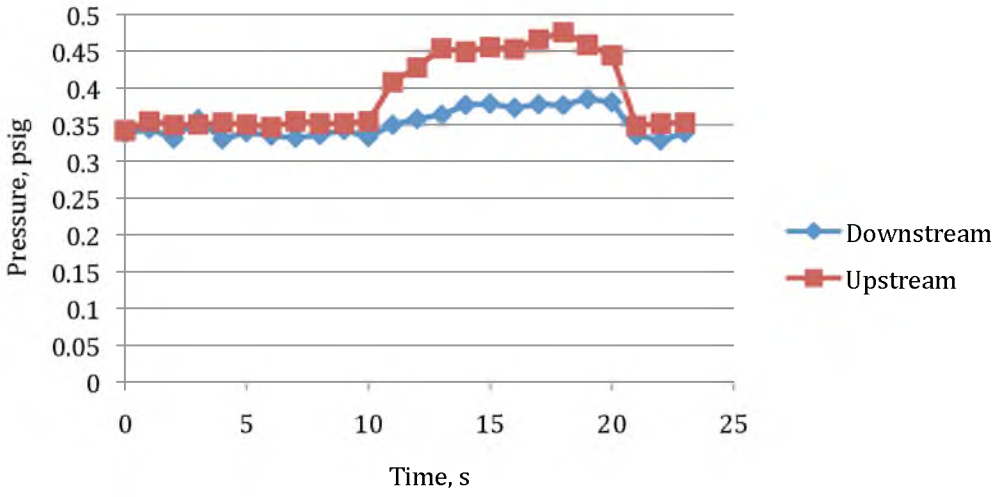

Figure C.14. Gel point test, 15.2 °C slurry conditions at shutdown, 5.75 °C final temperature.

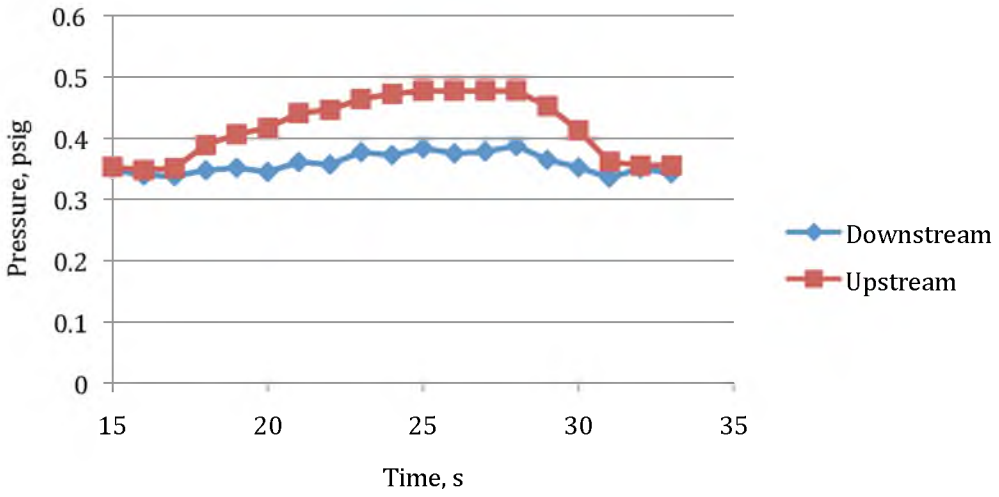

Figure C.15. Gel point test, 15.2 °C slurry conditions at shutdown, 5.5 °C final temperature. Loading behavior and downstream response indicates gel presence.

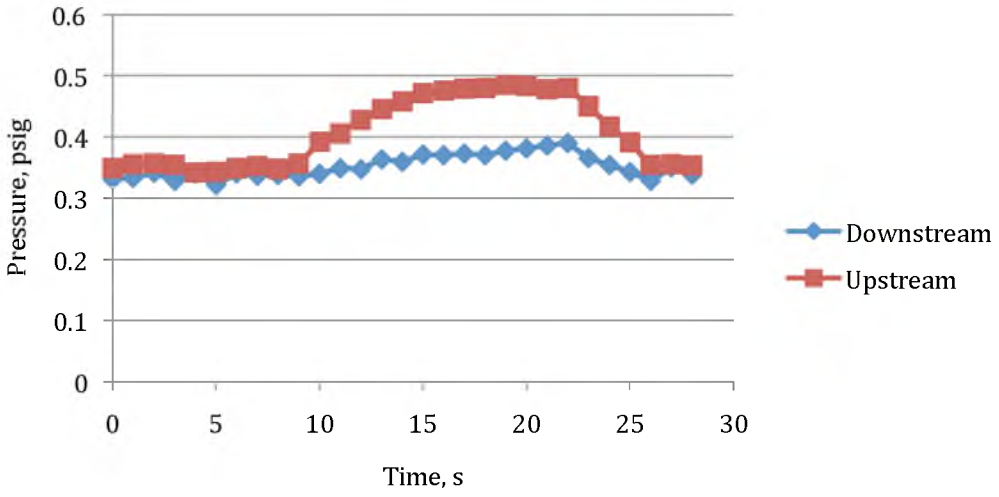

Figure C.16. Gel point test, 15.2 °C slurry conditions at shutdown, 5 °C final temperature. Run 1 of 2.

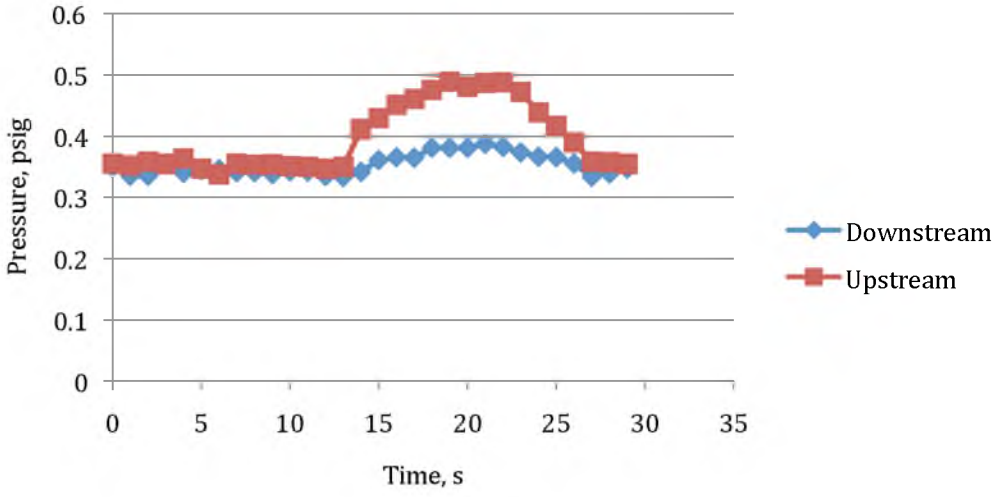

Figure C.17. Gel point test, 15.2 °C slurry conditions at shutdown, 5 °C final temperature. Run 2 of 2.

C.3 Heterogeneous versus Homogeneous Effect on Restart Pressure – Constant Slurry Temperature

All tests subjected to 0.33 °C/min cooling rate and 0.035 psi/s (0.5 Pa/s shear stress) loading rates. All gels aged 1 hour before restart. Both homogeneous and heterogeneous tests were conducted. Both steel and acrylic test sections explored for comparison. These data comprise Figures C.18-C.43. A number of repeated tests due to early errors in procedure were conducted; those not shown were lost due to a hard drive failure.

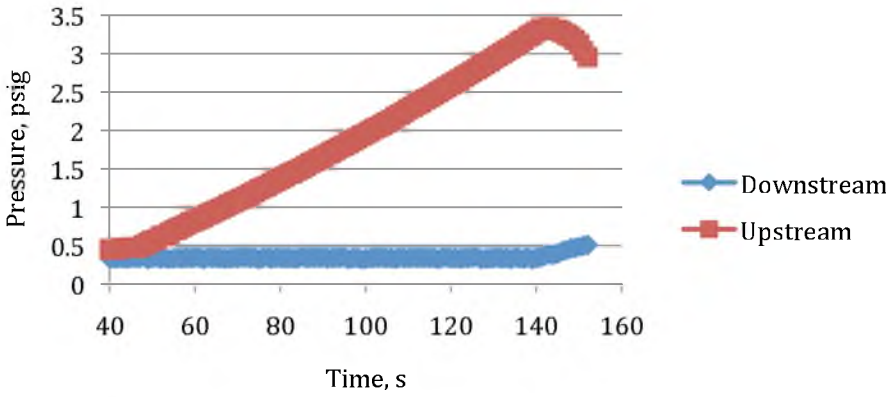

Figure C.18. Steel homogeneous test, 35 °C conditions at shutdown, 0 °C gel temperature.

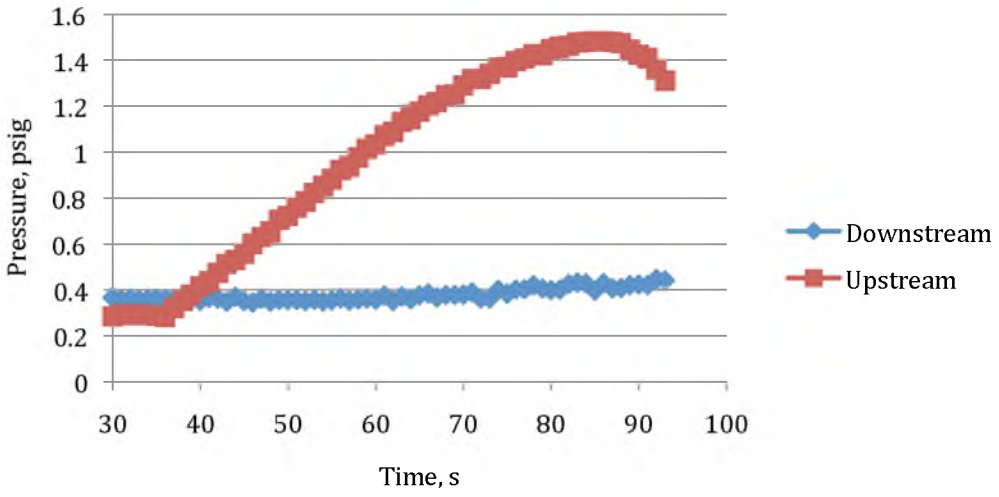

Figure C.19. Acrylic homogeneous test, 35 °C conditions at shutdown, 4 °C gel temperature.

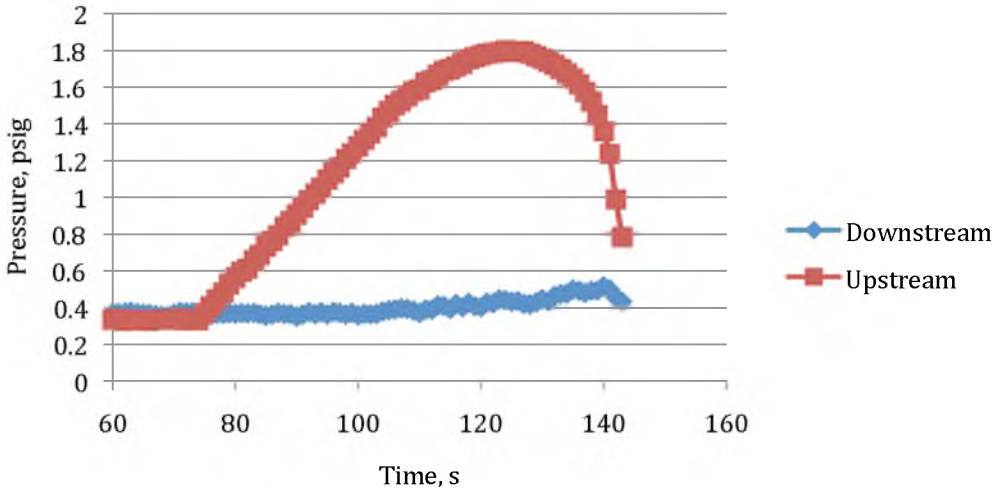

Figure C.20. Acrylic homogeneous test, 35 °C conditions at shutdown, 3 °C gel temperature.

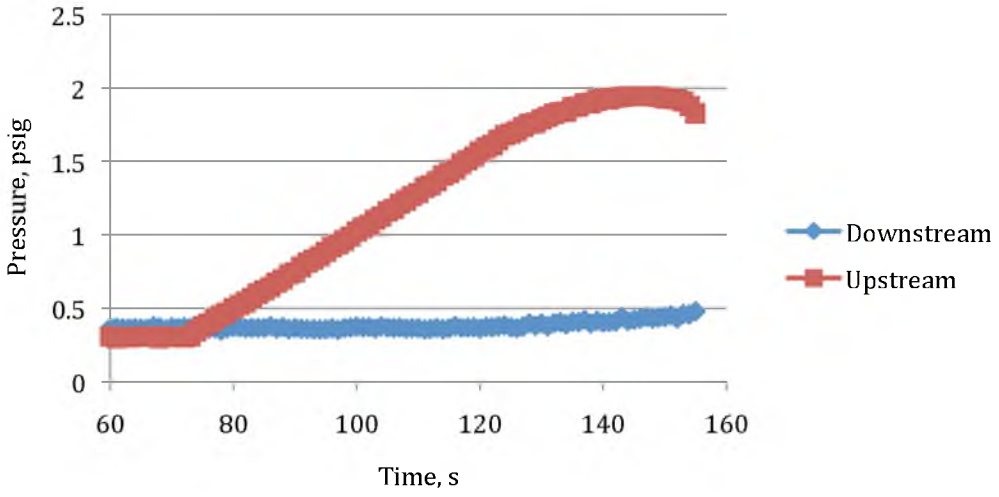

Figure C.21. Acrylic homogeneous test, 35 °C conditions at shutdown, 2 °C gel temperature. Run 1 of 2.

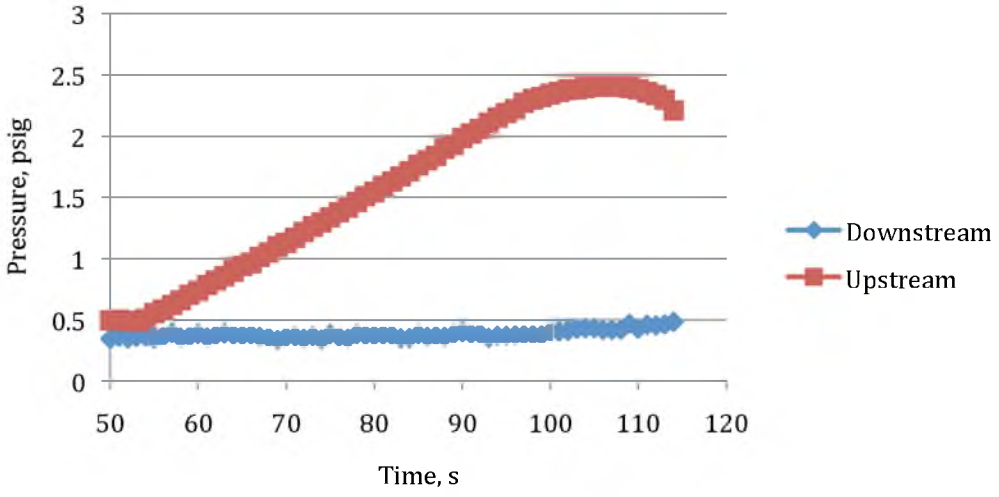

Figure C.22. Acrylic homogeneous test, 35 °C conditions at shutdown, 2 °C gel temperature. Run 2 of 2.

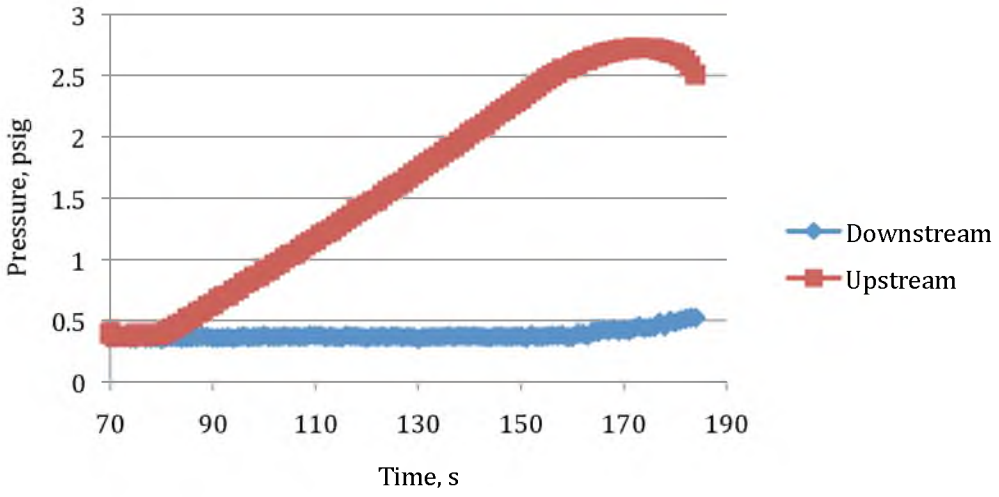

Figure C.23. Acrylic homogeneous test, 35 °C conditions at shutdown, 0 °C gel temperature. Run 1 of 2.

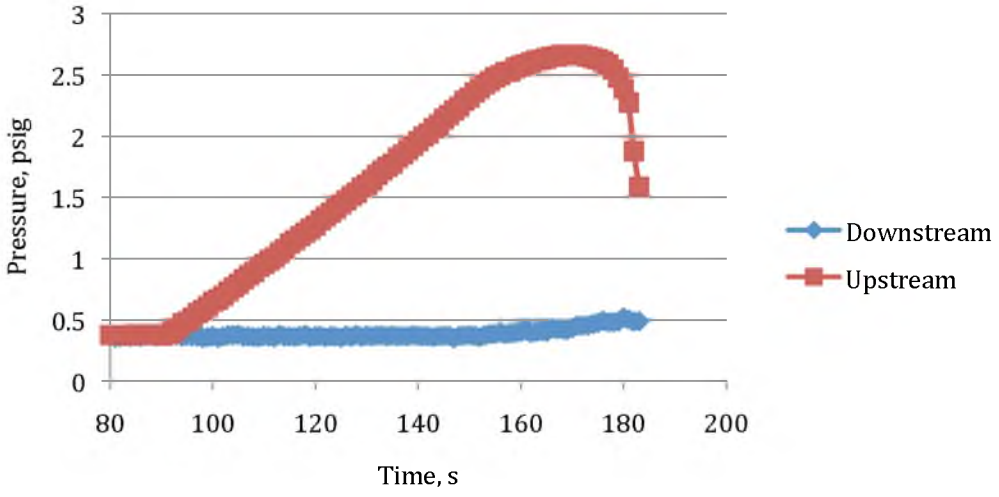

Figure C.24. Acrylic homogeneous test, 35 °C conditions at shutdown, 0 °C gel temperature. Run 2 of 2.

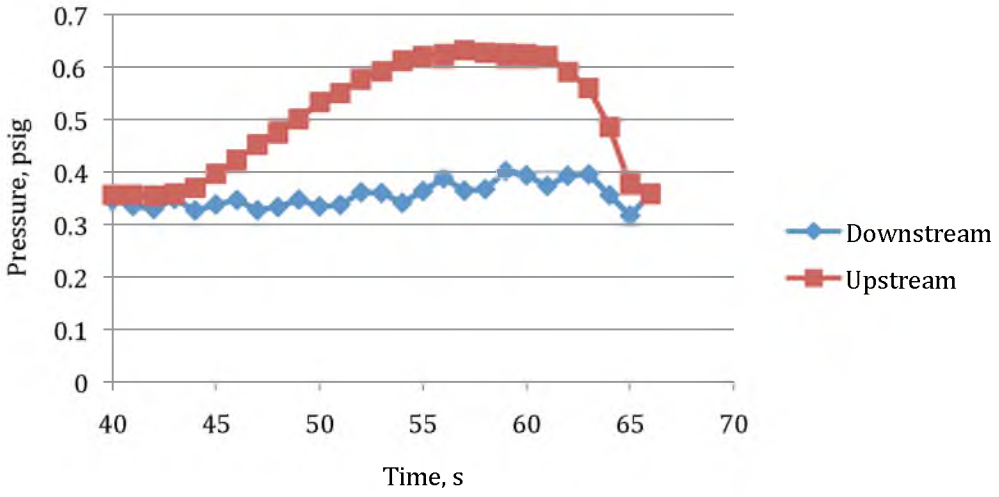

Figure C.25. Steel heterogeneous test, 17.2 °C slurry conditions at shutdown, 4 °C gel temperature.

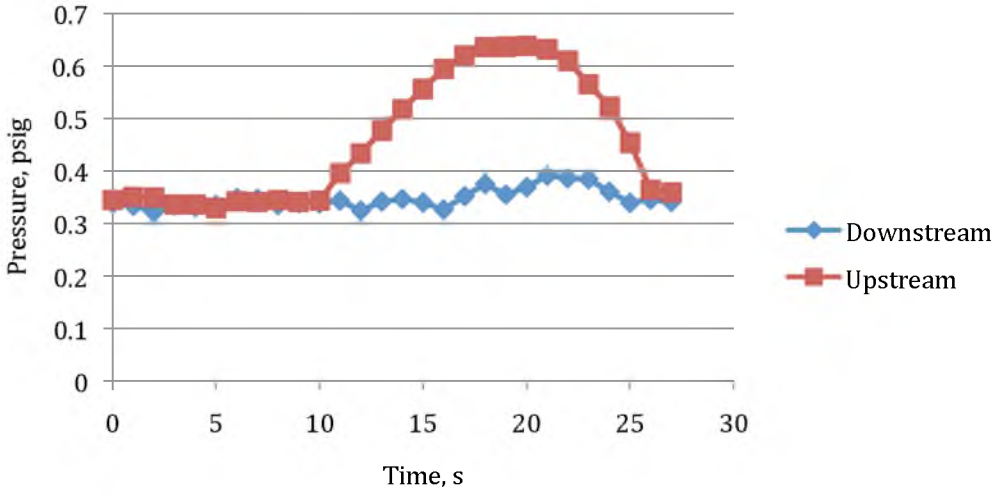

Figure C.26. Steel heterogeneous test, 17.2 °C slurry conditions at shutdown, 3 °C gel temperature.

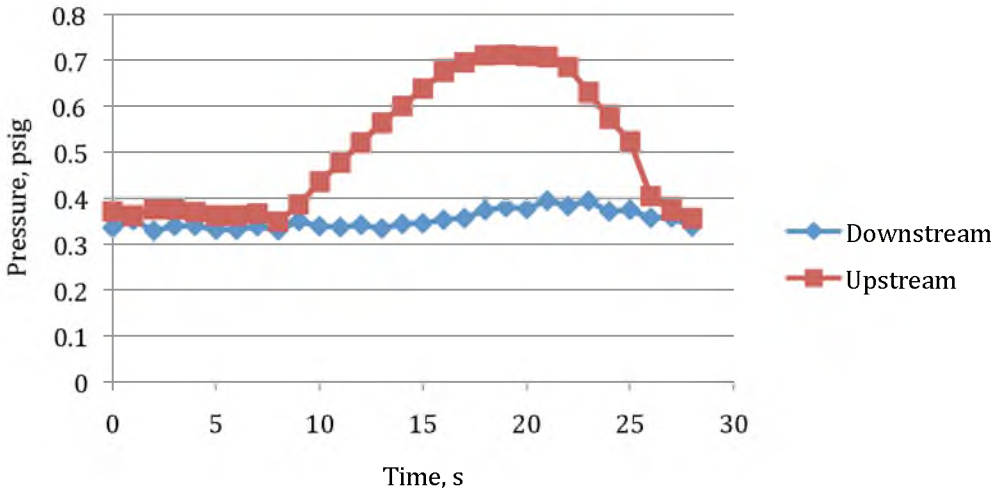

Figure C.27. Steel heterogeneous test, 17.2 °C slurry conditions at shutdown, 2 °C gel temperature.

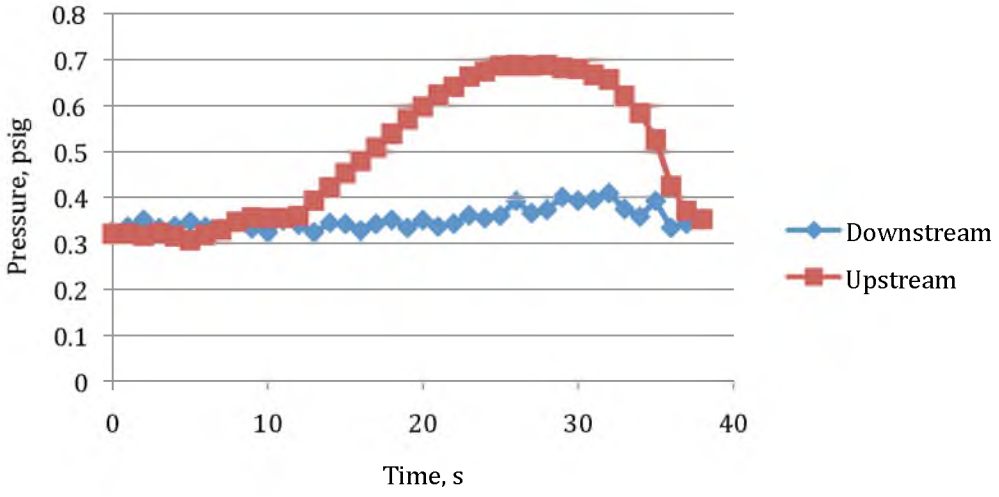

Figure C.28. Steel heterogeneous test, 17.2 °C slurry conditions at shutdown, 1 °C gel temperature.

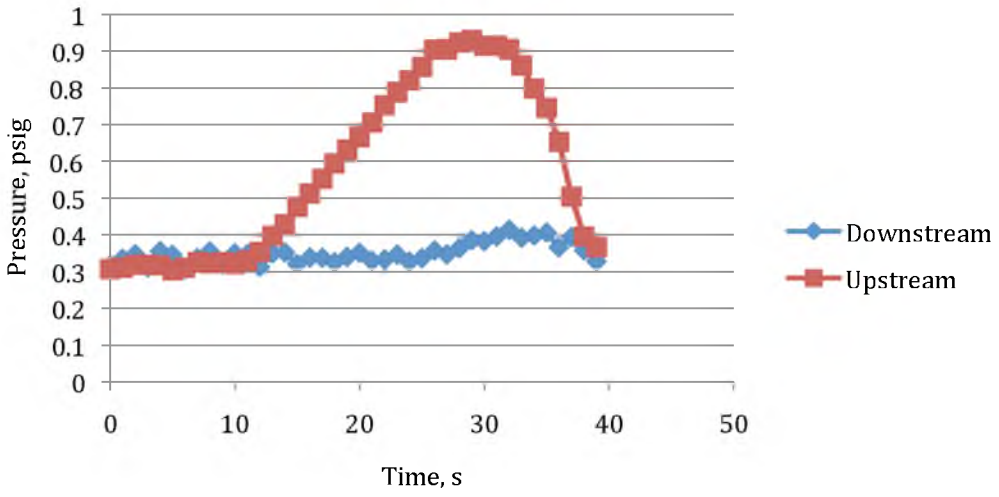

Figure C.29. Steel heterogeneous test, 17.2 °C slurry conditions at shutdown, 0 °C gel temperature.

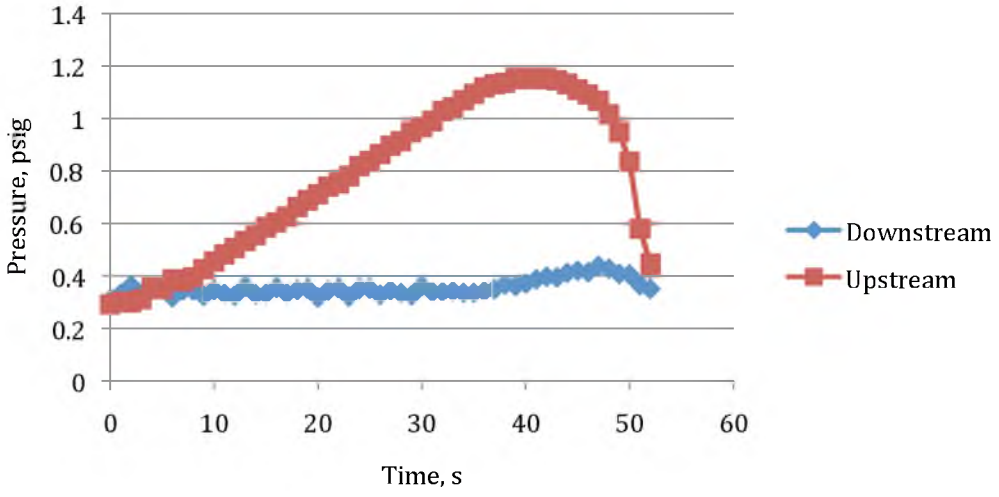

Figure C.30. Steel heterogeneous test, 17.2 °C slurry conditions at shutdown, -1 °C gel temperature. Run 1 of 2.

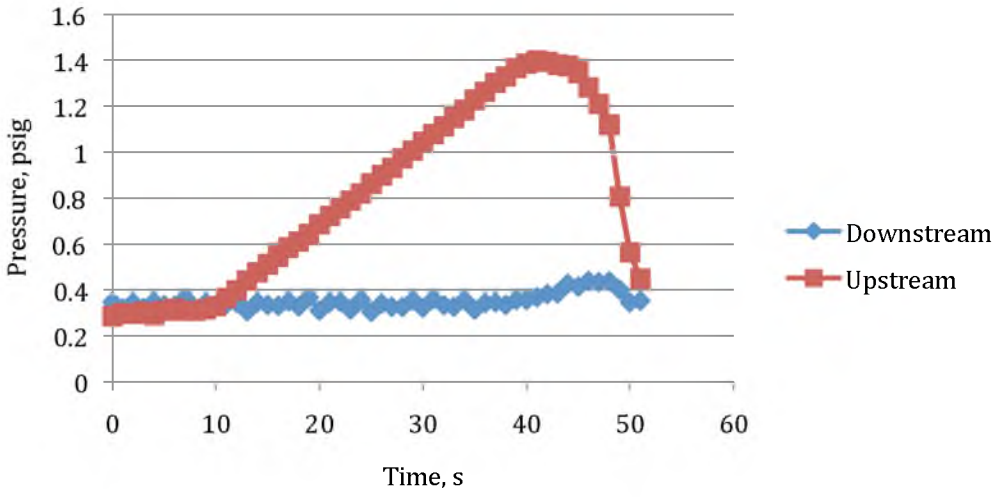

Figure C.31. Steel heterogeneous test, 17.2 °C slurry conditions at shutdown, -1 °C gel temperature. Run 2 of 2.

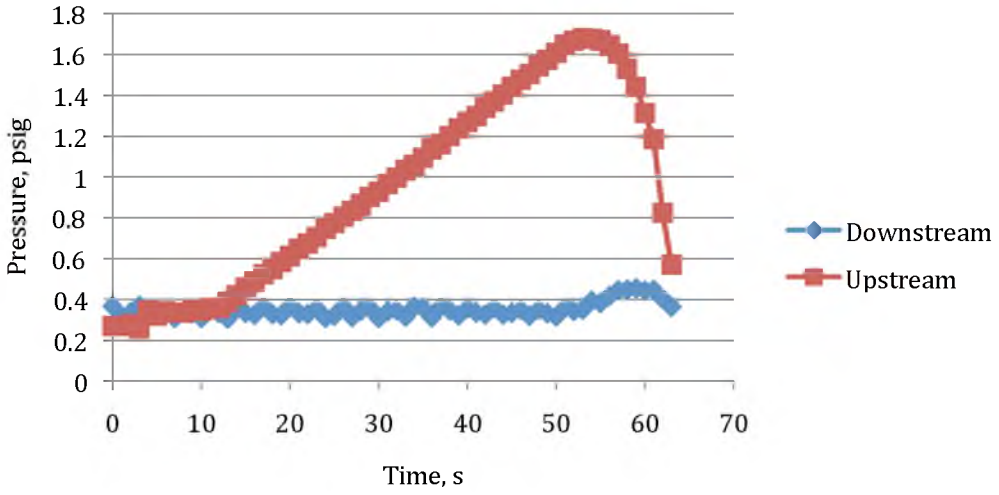

Figure C.32. Steel heterogeneous test, 17.2 °C slurry conditions at shutdown, -2 °C gel temperature.

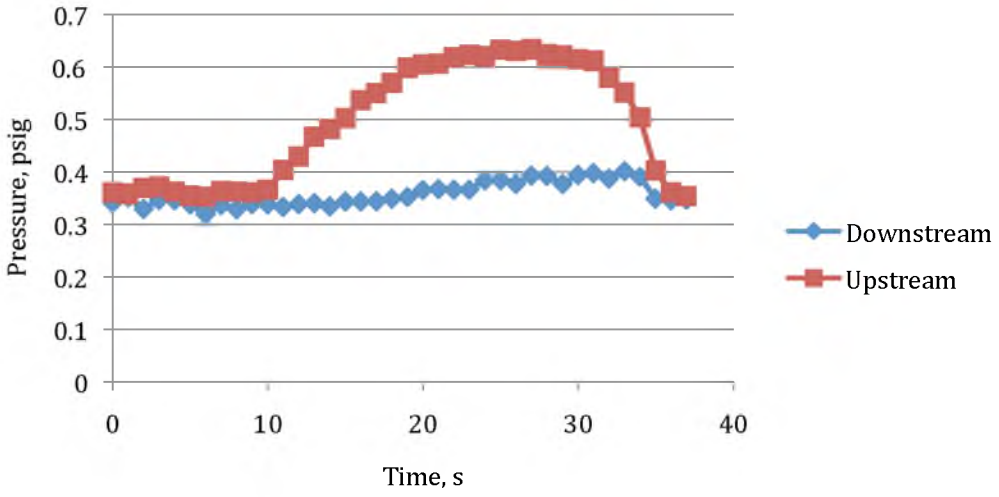

Figure C.33. Steel heterogeneous test, 16.2 °C slurry conditions at shutdown, 1 °C gel temperature.

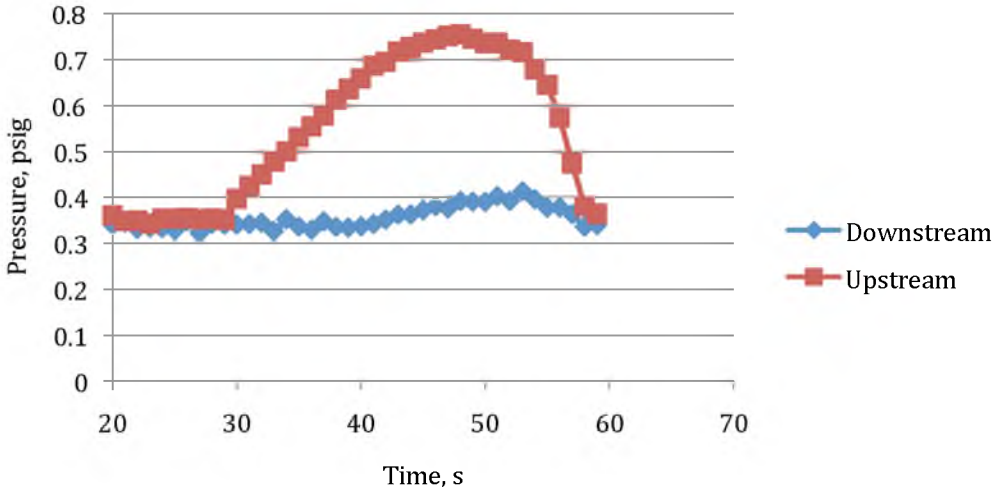

Figure C.34. Steel heterogeneous test, 16.2 °C slurry conditions at shutdown, -1 °C gel temperature.

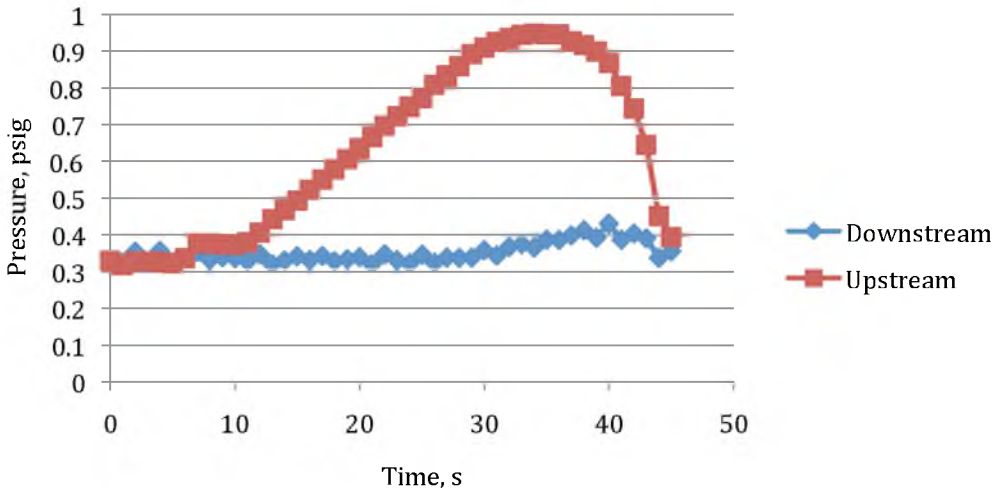

Figure C.35. Steel heterogeneous test, 16.2 °C slurry conditions at shutdown, -3 °C gel temperature.

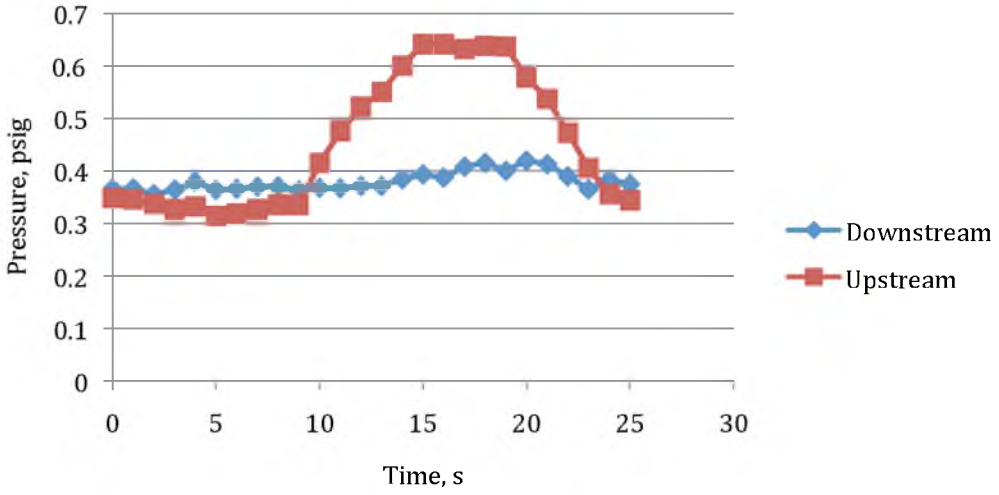

Figure C.36. Acrylic heterogeneous test, 17.2 °C slurry conditions at shutdown, 3 °C gel temperature.

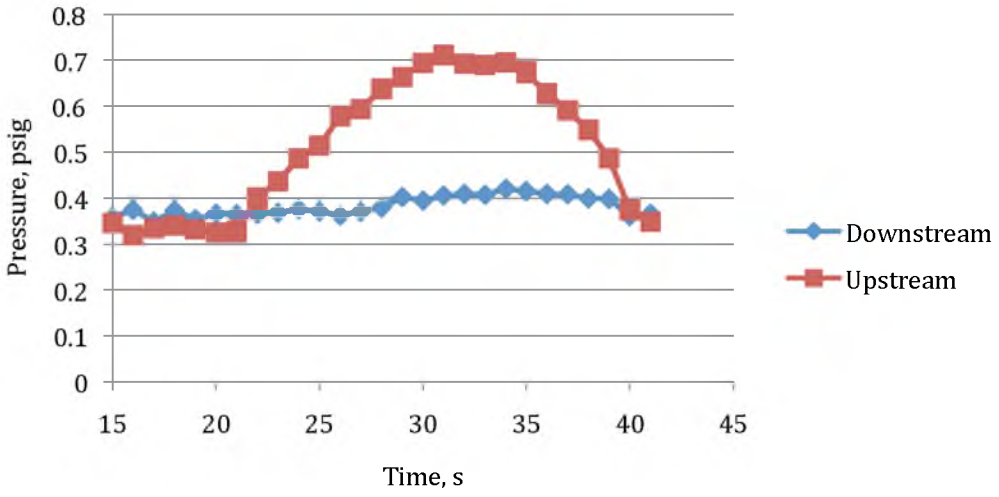

Figure C.37. Acrylic heterogeneous test, 17.2 °C slurry conditions at shutdown, 1 °C gel temperature.

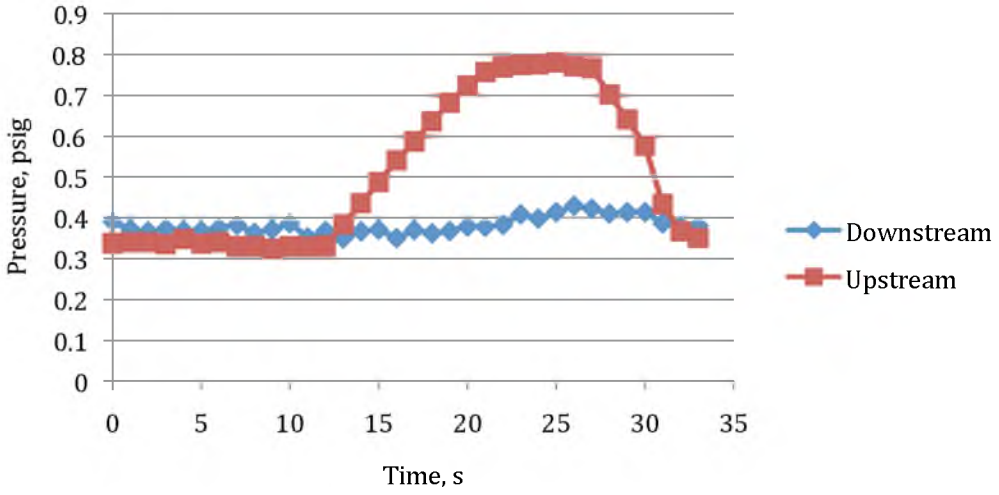

Figure C.38. Acrylic heterogeneous test, 17.2 °C slurry conditions at shutdown, 0 °C gel temperature.

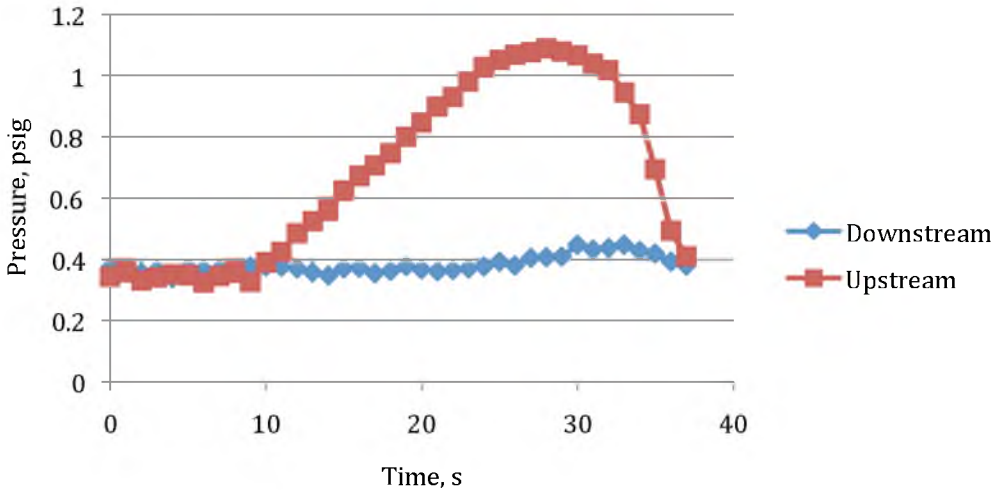

Figure C.39. Acrylic heterogeneous test, 17.2 °C slurry conditions at shutdown, -1 °C gel temperature.

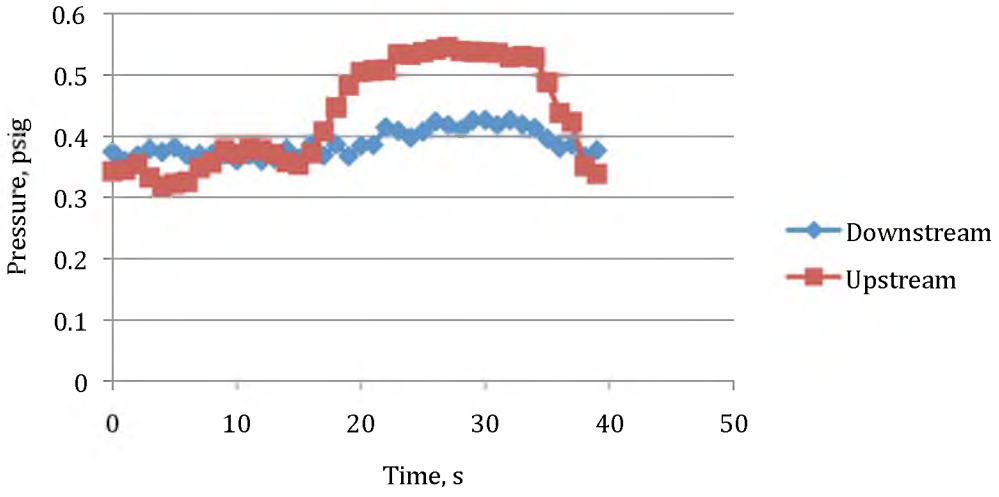

Figure C.40. Acrylic heterogeneous test, 16.2 °C slurry conditions at shutdown, 3 °C gel temperature.

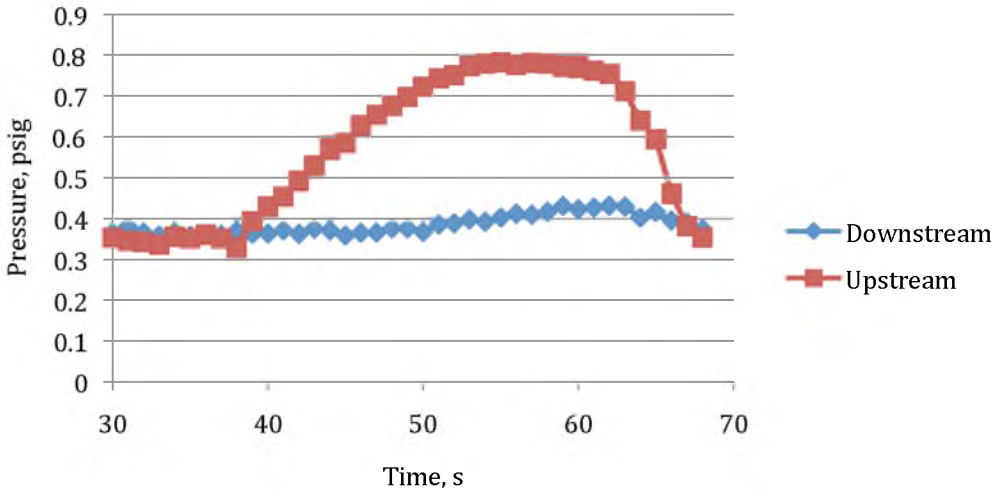

Figure C.41. Acrylic heterogeneous test, 16.2 °C slurry conditions at shutdown, -1 °C gel temperature.

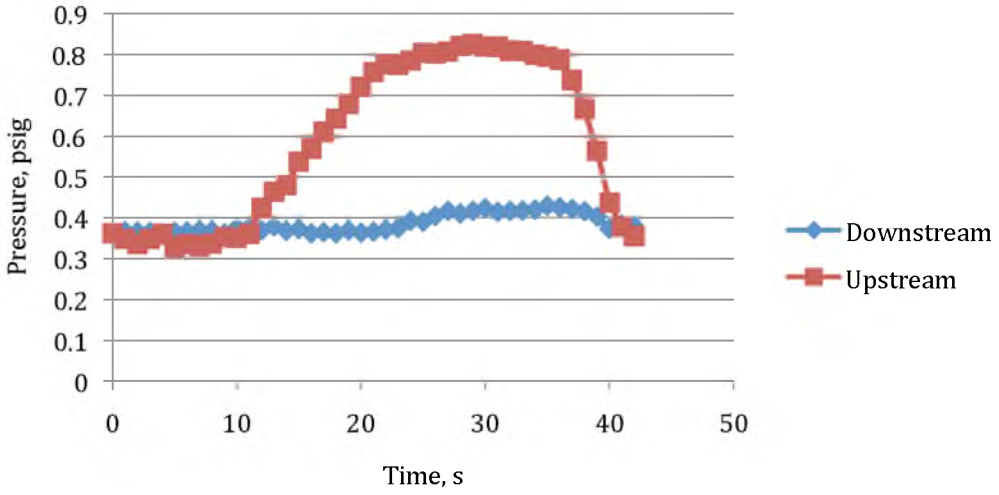

Figure C.42. Acrylic heterogeneous test, 16.2 °C slurry conditions at shutdown, -2 °C gel temperature.

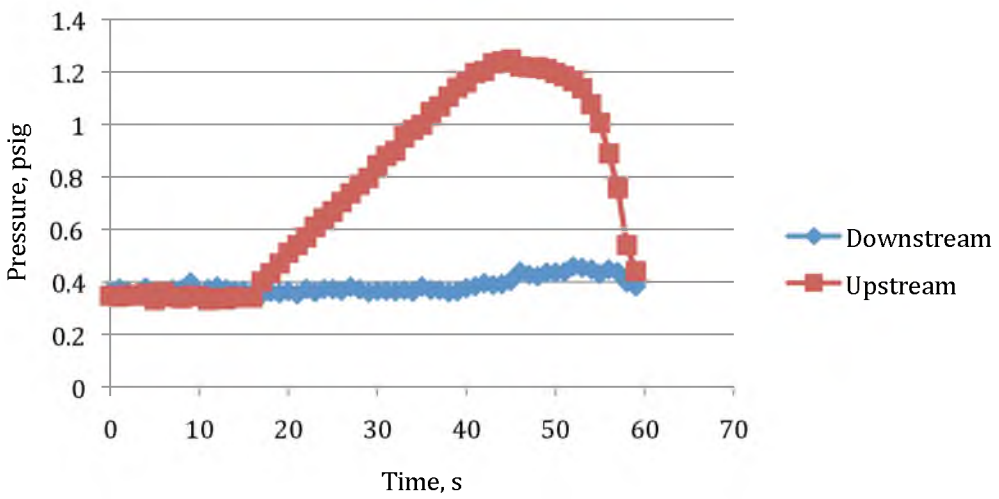

Figure C.43. Acrylic heterogeneous test, 16.2 °C slurry conditions at shutdown, -3 °C gel temperature.

C.4 Solids Loading Effect on Restart Pressure

Some of the tests in this section were conducted using the Moyno pump of the experimental test section as the source of pressure. The rate of pressure increase is estimated to be greater than 4 psi/s, effectively giving an "instantaneous" effect on the gel breakage. All gels subjected to 1 hour aging, 0.33 °C/min cooling rate, and 4 °C final temperature. Both steel and acrylic test sections were used. These data comprise Figures C.44-C.63.

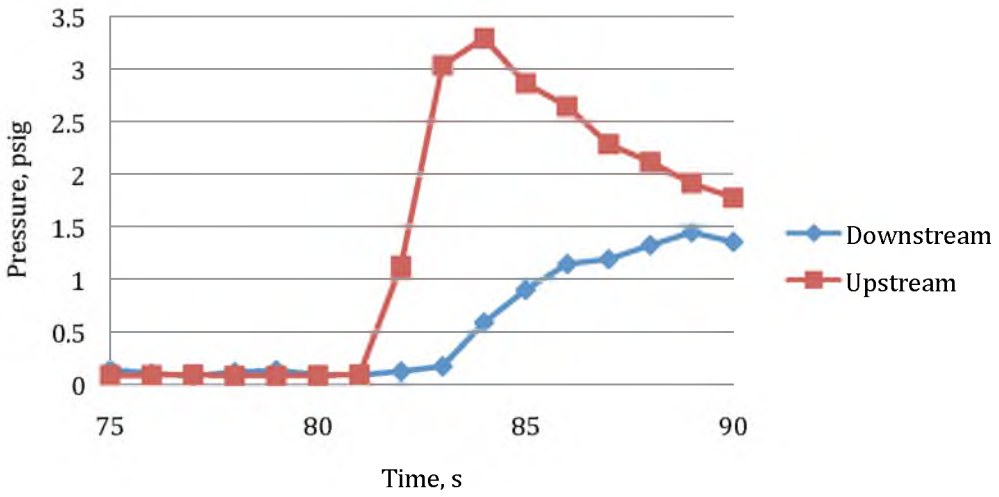

Figure C.44. Steel solids loading homogeneous test, 35 °C conditions at shutdown, Moyno restart (>4 psi/s).

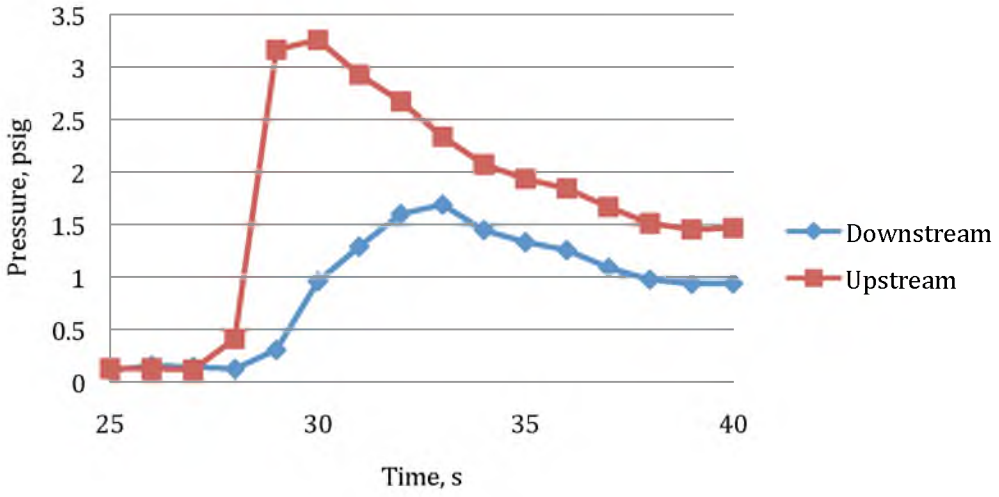

Figure C.45. Steel solids loading homogeneous test, 25 °C conditions at shutdown, Moyno restart (>4 psi/s). Run 1 of 3.

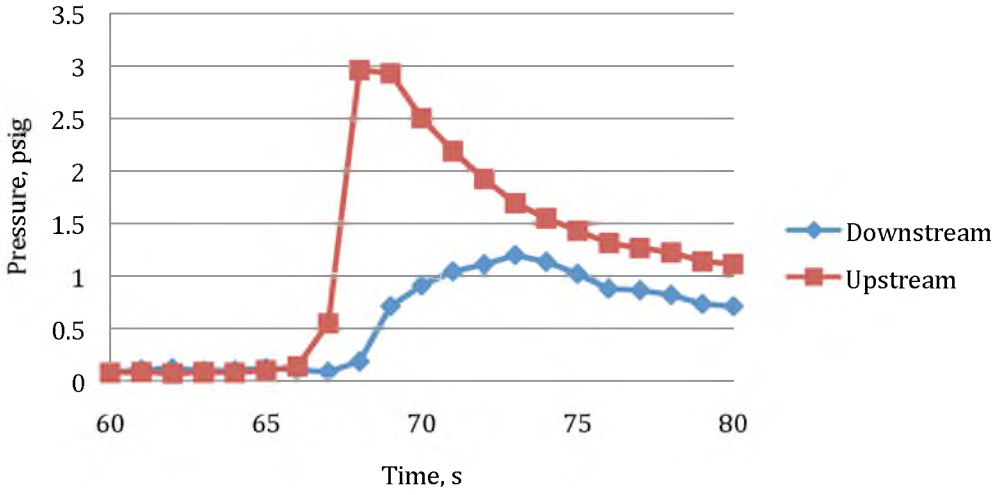

Figure C.46. Steel solids loading homogeneous test, 25 °C conditions at shutdown, Moyno restart (>4 psi/s). Run 2 of 3.

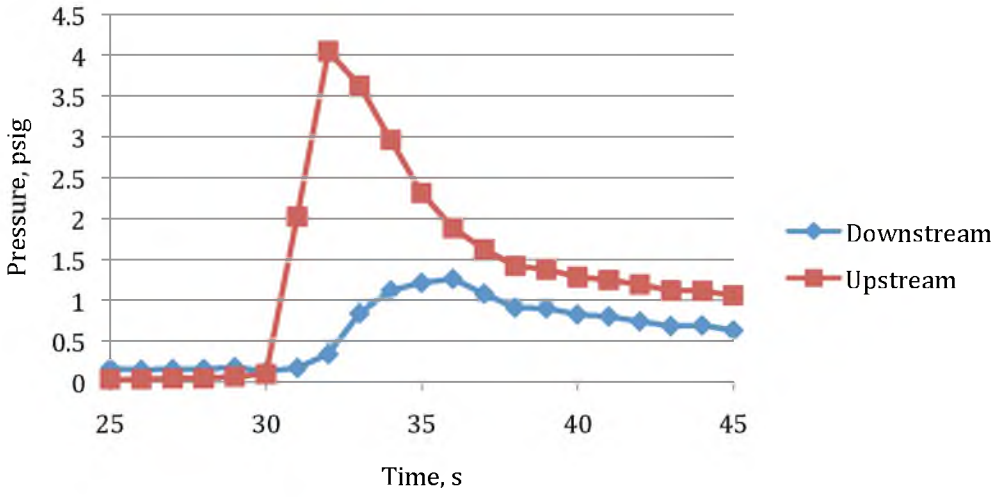

Figure C.47. Steel solids loading homogeneous test, 25 °C conditions at shutdown, Moyno restart (>4 psi/s). Run 3 of 3.

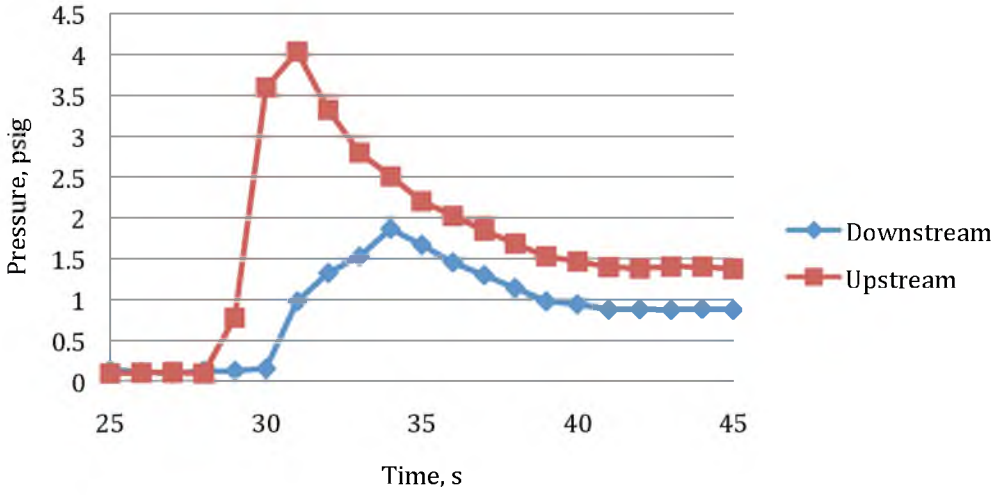

Figure C.48. Steel solids loading homogeneous test, 20 °C conditions at shutdown, Moyno restart (>4 psi/s). Run 1 of 2.

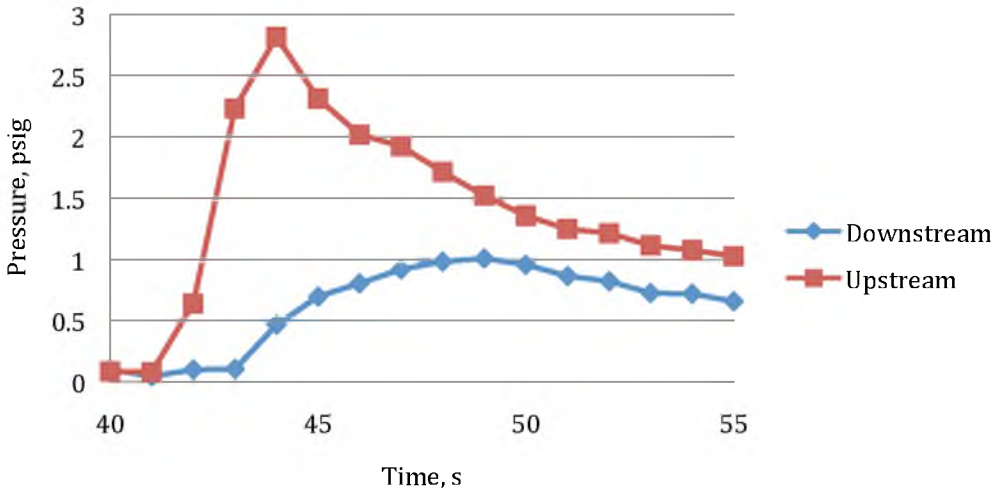

Figure C.49. Steel solids loading homogeneous test, 20 °C conditions at shutdown, Moyno restart (>4 psi/s). Run 2 of 2.

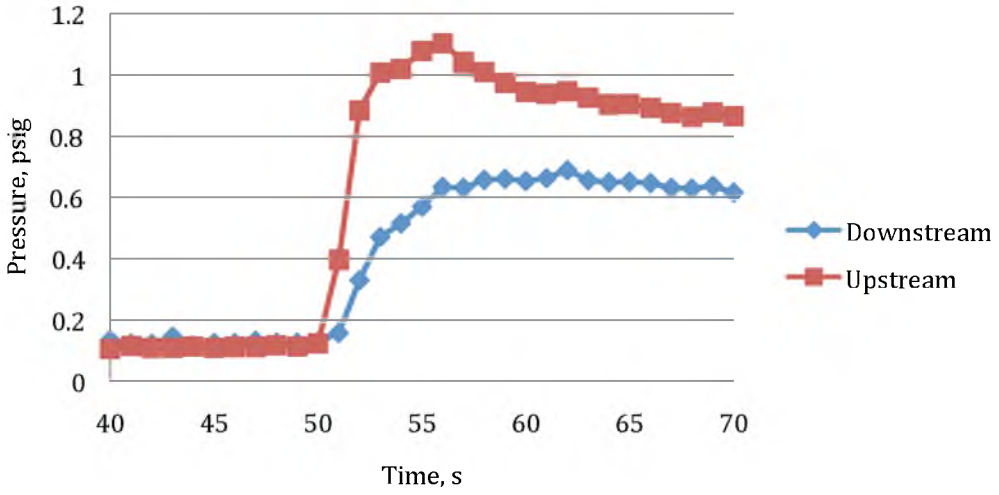

Figure C.50. Steel solids loading heterogeneous test, 15 °C conditions at shutdown, Moyno restart (>4 psi/s).

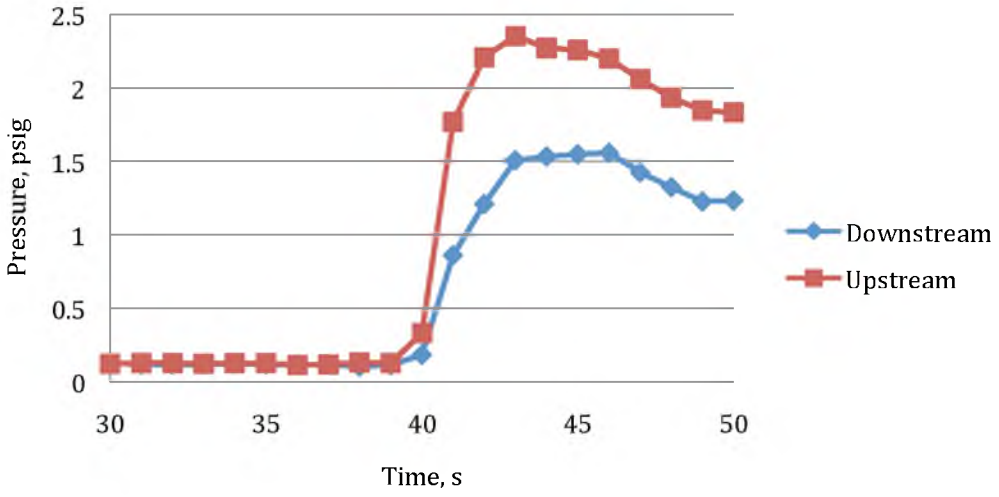

Figure C.51. Steel solids loading heterogeneous test, 10 °C conditions at shutdown, Moyno restart (>4 psi/s).

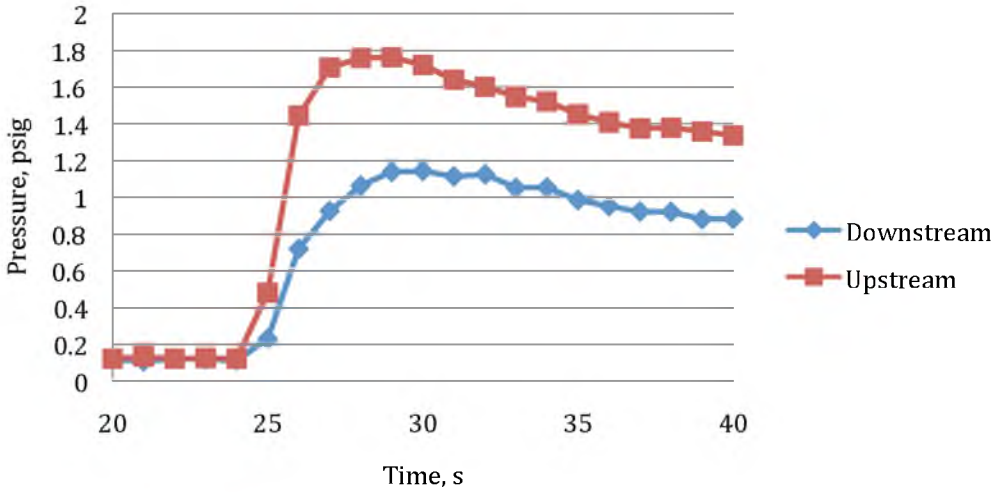

Figure C.52. Steel solids loading heterogeneous test, 8 °C conditions at shutdown, Moyno restart (>4 psi/s).

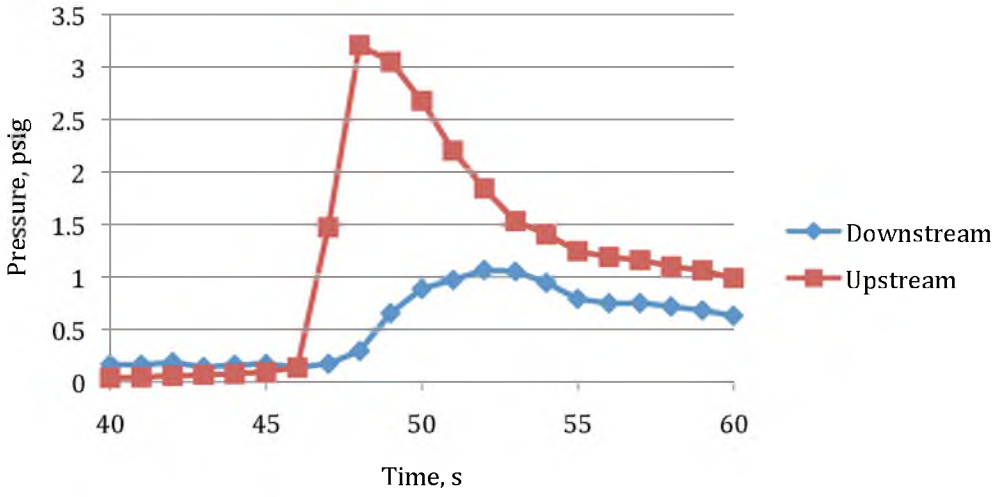

Figure C.53. Acrylic solids loading homogeneous test, 35 °C conditions at shutdown, Moyno restart (>4 psi/s).

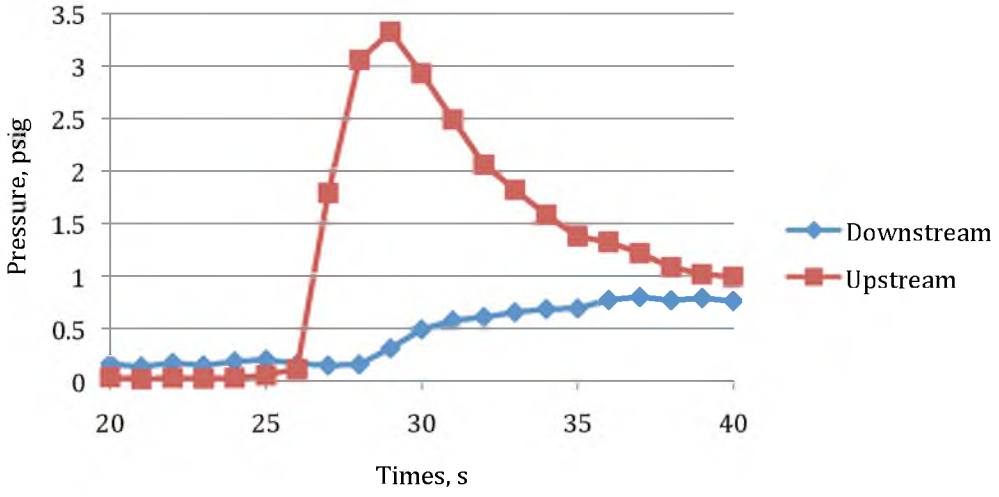

Figure C.54. Acrylic solids loading homogeneous test, 25 °C conditions at shutdown, Moyno restart (>4 psi/s).

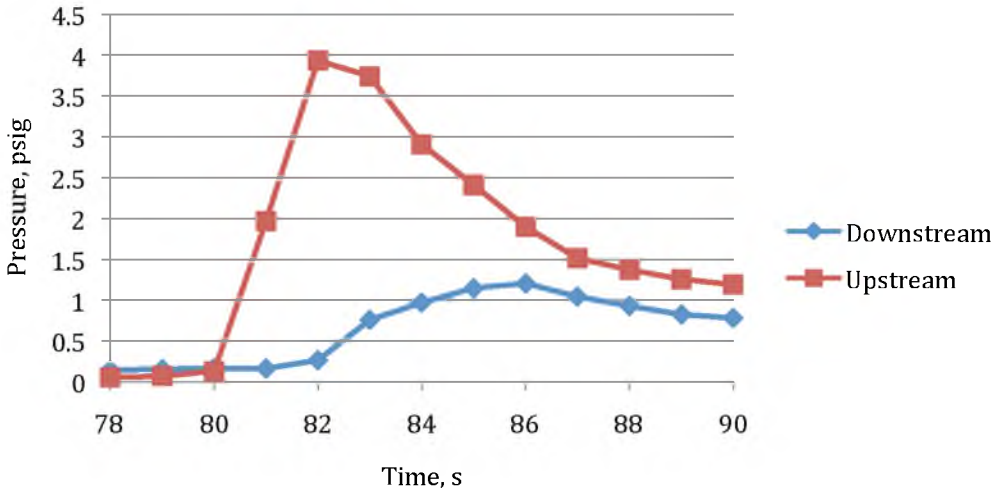

Figure C.55. Acrylic solids loading homogeneous test, 20 °C conditions at shutdown, Moyno restart (>4 psi/s).

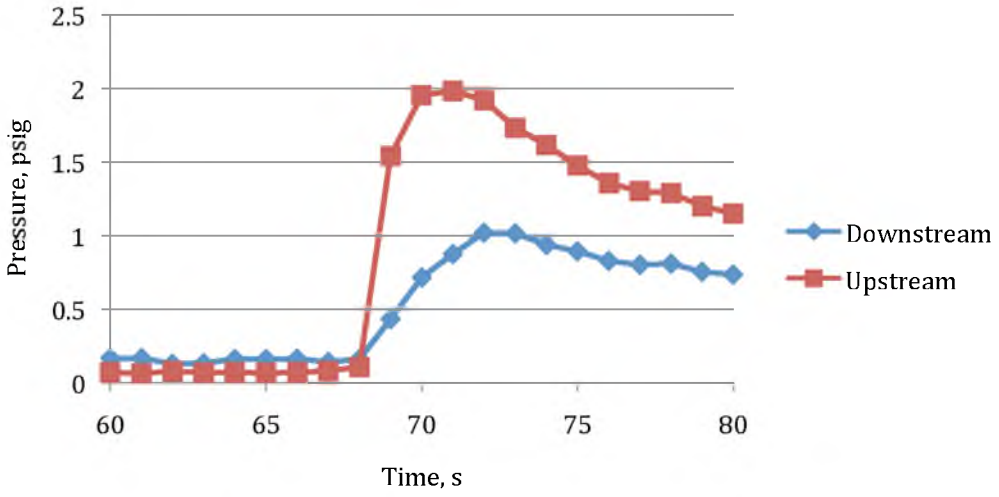

Figure C.56. Acrylic solids loading heterogeneous test, 15 °C conditions at shutdown, Moyno restart (>4 psi/s).

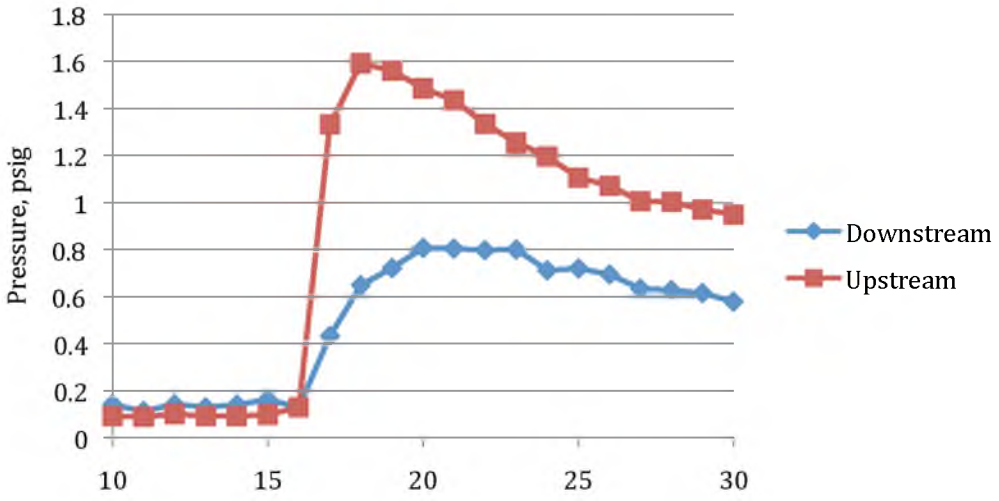

Figure C.57. Acrylic solids loading heterogeneous test, 10 °C conditions at shutdown, Moyno restart (>4 psi/s).

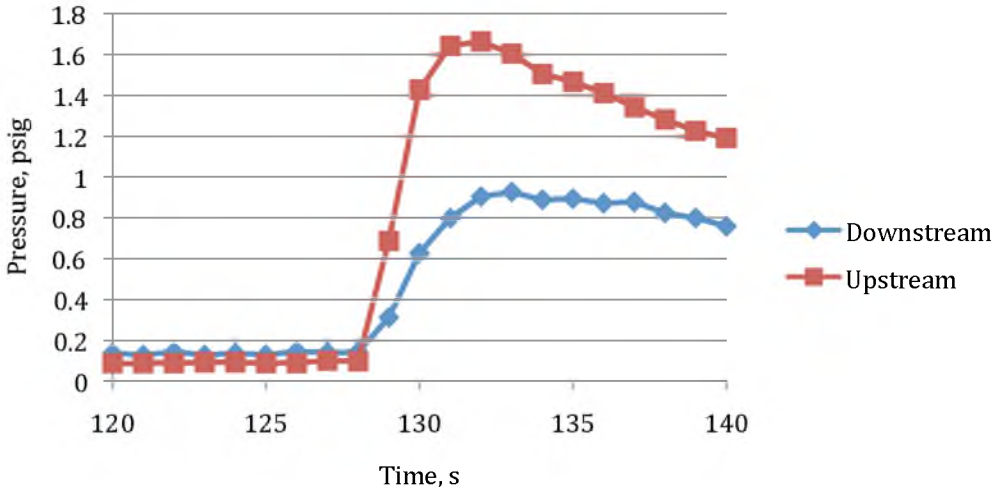

Figure C.58. Acrylic solids loading heterogeneous test, 8 °C conditions at shutdown, Moyno restart (>4 psi/s).

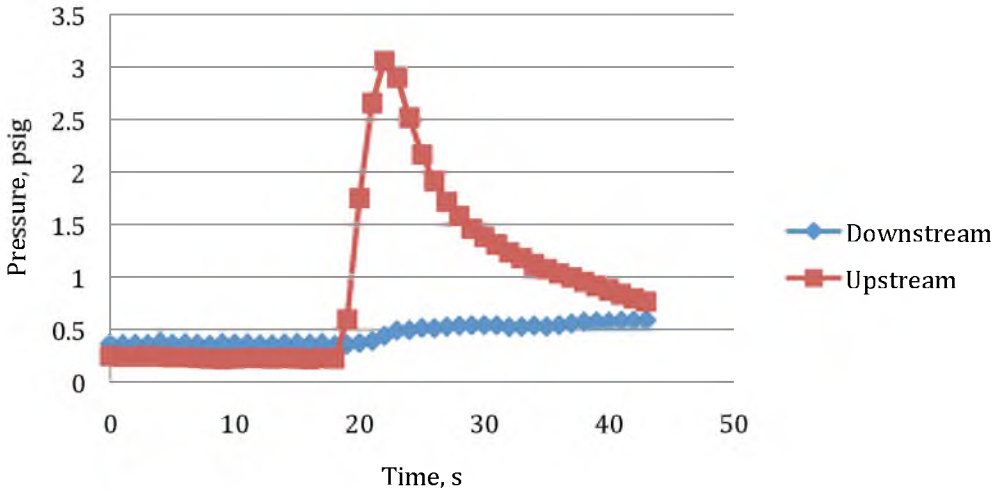

Figure C.59. Acrylic solids loading homogeneous test, 25 °C conditions at shutdown, 1.12 psi/s (16.1 Pa/s shear stress) pressure loading rate.

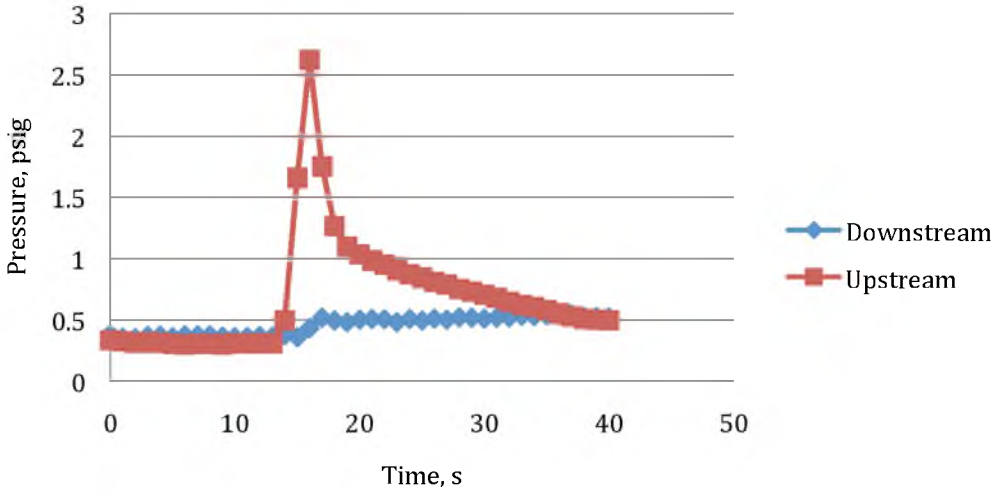

Figure C.60. Acrylic solids loading homogeneous test, 20 °C conditions at shutdown, 1.12 psi/s (16.1 Pa/s shear stress) pressure loading rate.

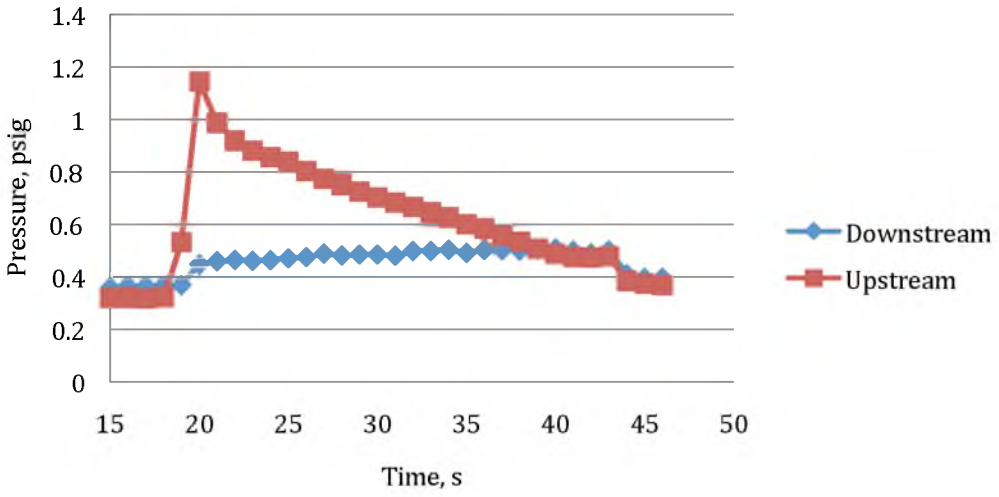

Figure C.61. Acrylic solids loading homogeneous test, 18 °C conditions at shutdown, 1.12 psi/s (16.1 Pa/s shear stress) pressure loading rate.

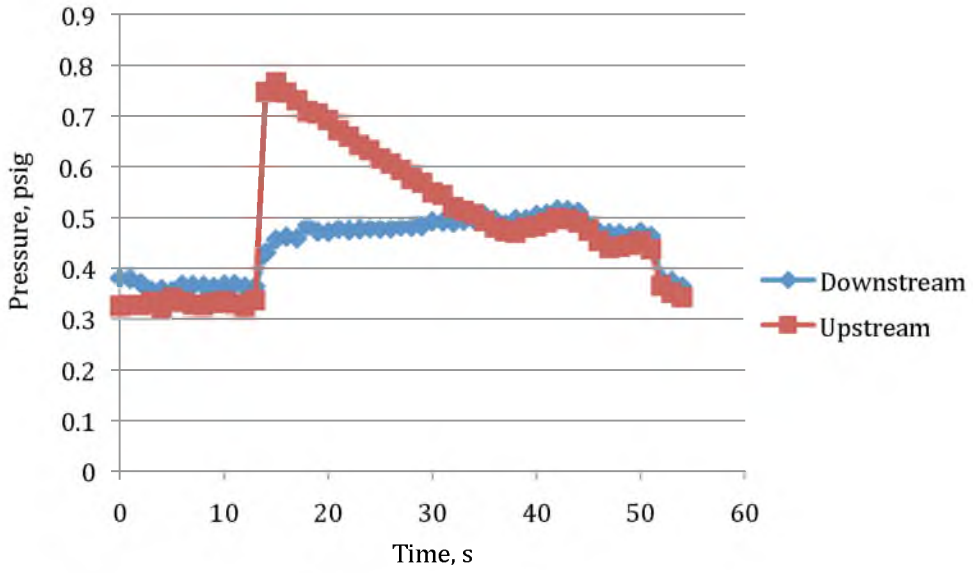

Figure C.62. Acrylic solids loading heterogeneous test, 16.6 °C conditions at shutdown, 1.12 psi/s (16.1 Pa/s shear stress) pressure loading rate.

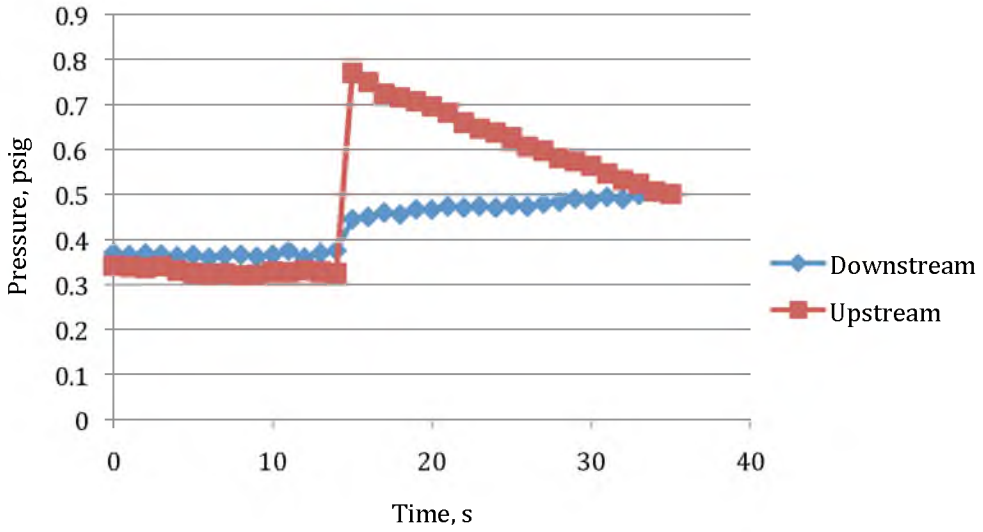

Figure C.63. Acrylic solids loading heterogeneous test, 15.6 ℃ conditions at shutdown, 1.12 psi/s (16.1 Pa/s shear stress) pressure loading rate.

C.5 Particle Size Effect on Restart Pressure

Presented in each subsection are the particle size plots and respective restart plots. Please note that for most tests multiple particle size plots exist; this is to ensure, in the case of poor results from image capture, the best possible mean equivalent circular diameter (MECD) for each test. All tests use identical slurry and final gel temperatures of 16.6 °C and 3 °C, respectively, as well as identical pressurization (atmospheric) and gelation cooling rate of 0.33 °C/min. Both steel and acrylic test sections were used. These data comprise Figures C.64-C.100. Figures C.85-C.88 do not have corresponding distributions due to hard drive failure.

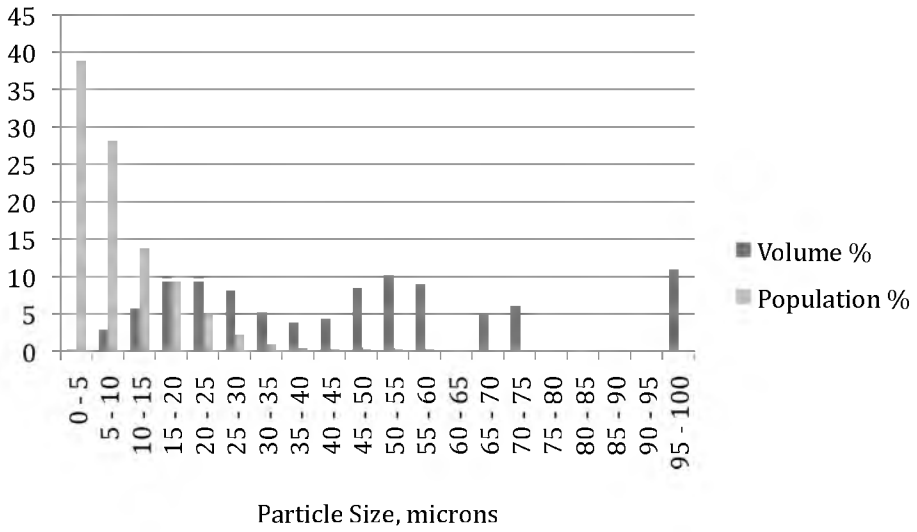

Figure C.64. Volume and Population percents for Steel Section Case 1. Run 1 of 2.

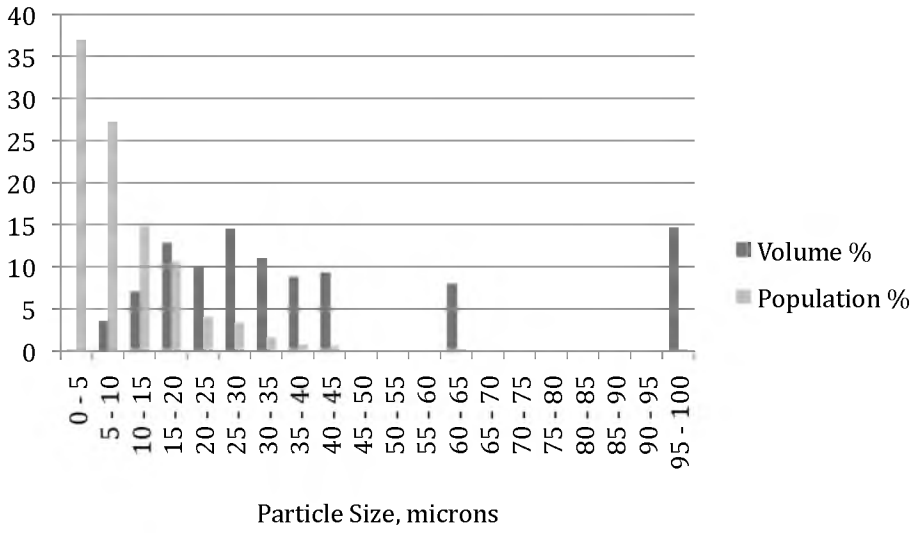

Figure C.65. Volume and Population percents for Steel Section Case 1. Run 2 of 2.

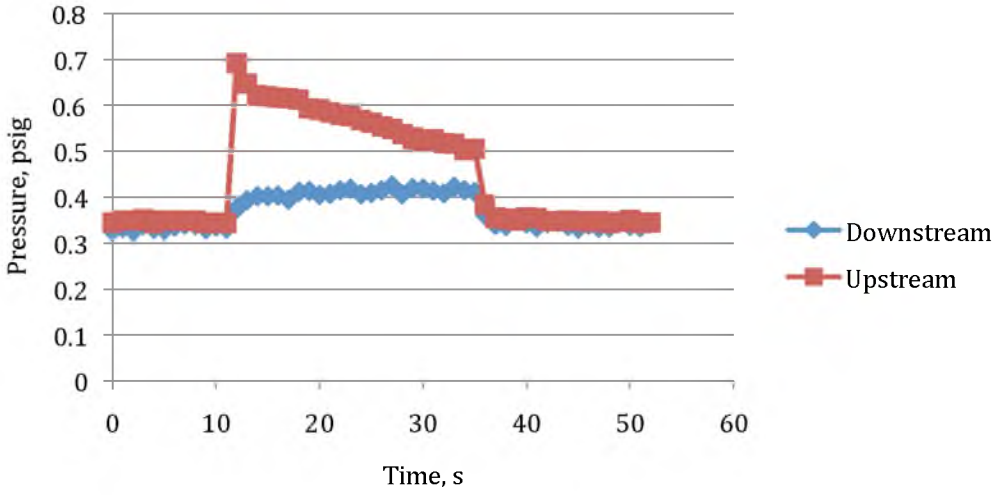

Figure C.66. Mean equivalent circular diameter = 12 microns. 16.6 °C heterogeneous conditions at shutdown, 4 °C gel temperature, 0.33 °C/min cooling rate, 1 hour aging, 1.12 psi/s (16.1 Pa/s shear stress) pressure loading rate, Steel Case 1.

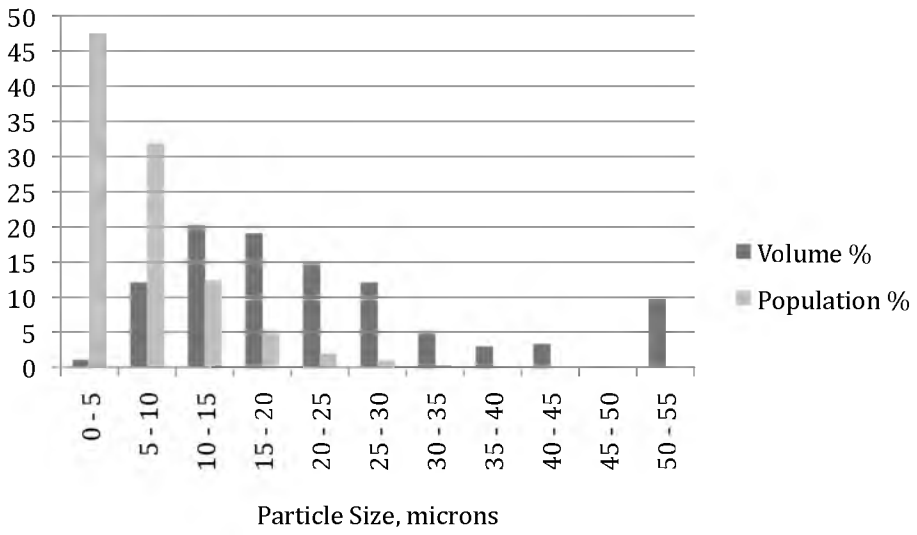

Figure C.67. Volume and Population percents for Steel Section Case 2. Run 1 of 3.

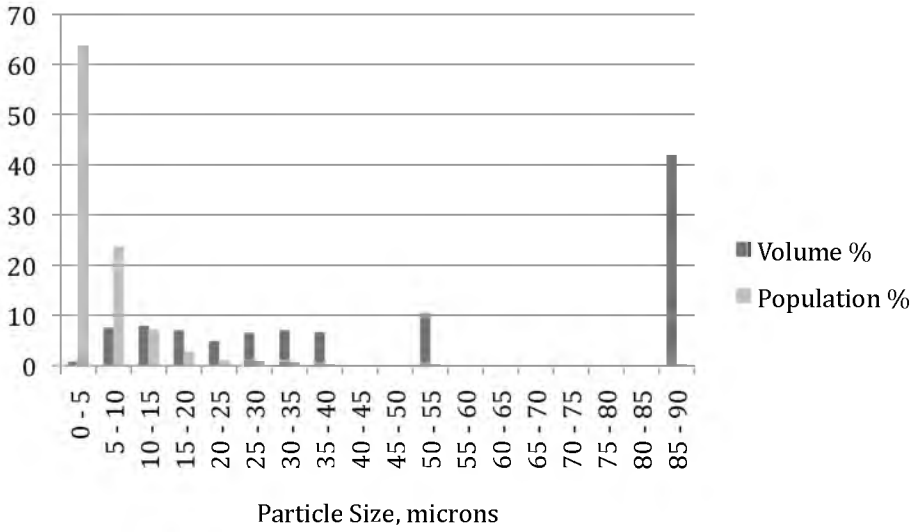

Figure C.68. Volume and Population percents for Steel Section Case 2. Run 2 of 3.

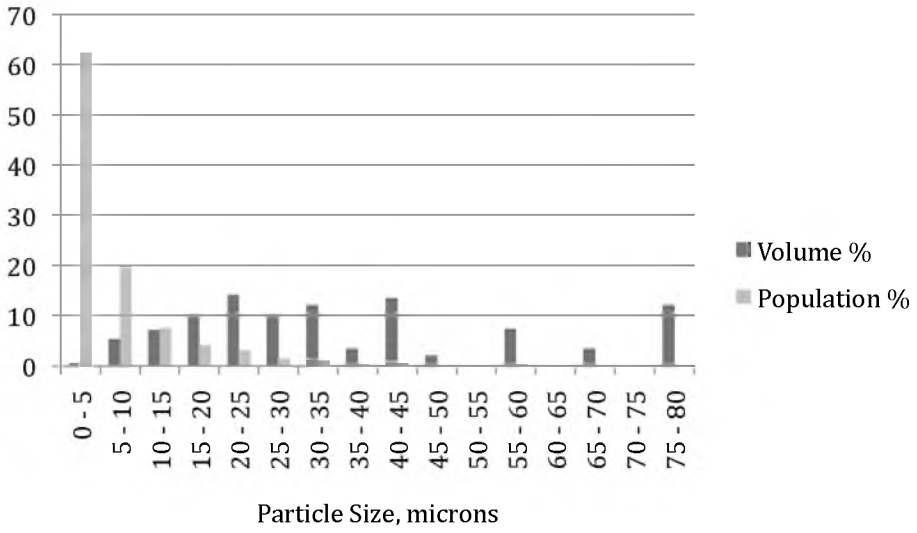

Figure C.69. Volume and Population percents for Steel Section Case 2. Run 3 of 3.

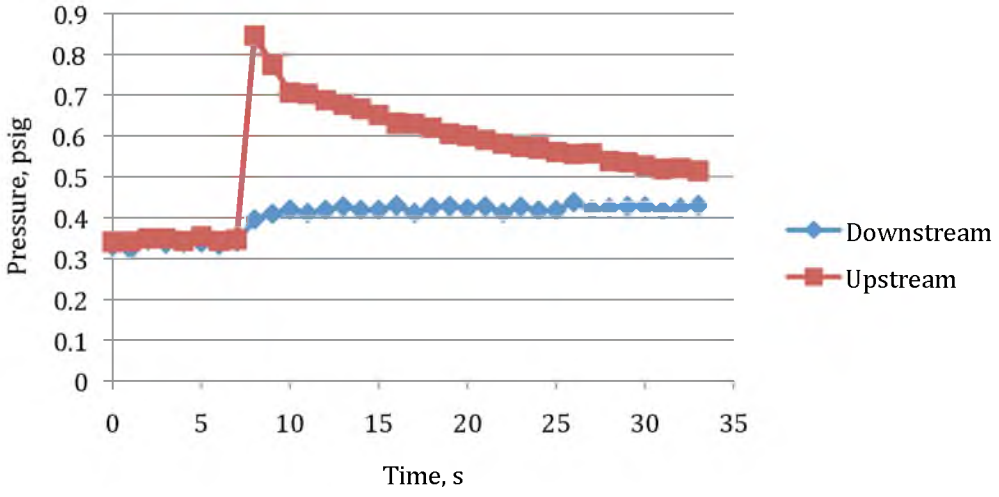

Figure C.70. Mean equivalent circular diameter = 6.7 microns. 16.6 °C heterogeneous conditions at shutdown, 4 °C gel temperature, 0.33 °C/min cooling rate, 1 hour aging, 1.12 psi/s (16.1 Pa/s shear stress) pressure loading rate, Steel Case 2.

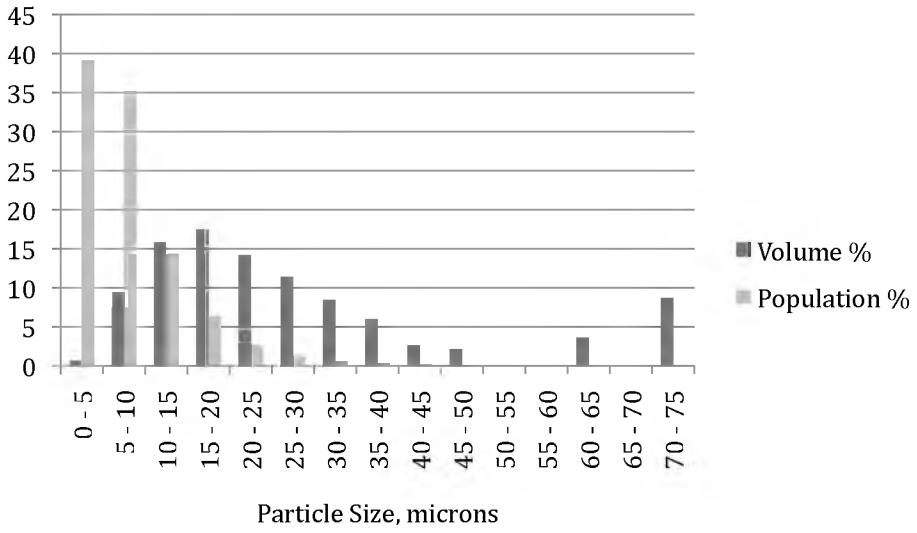

Figure C.71. Volume and Population percents for Steel Section Case 3. Run 1 of 4.

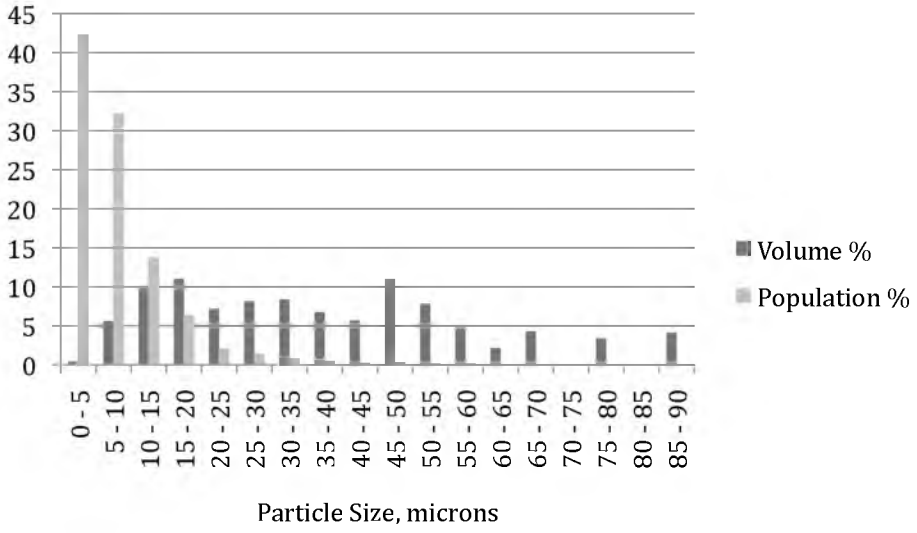

Figure C.72. Volume and Population percents for Steel Section Case 3. Run 2 of 4.

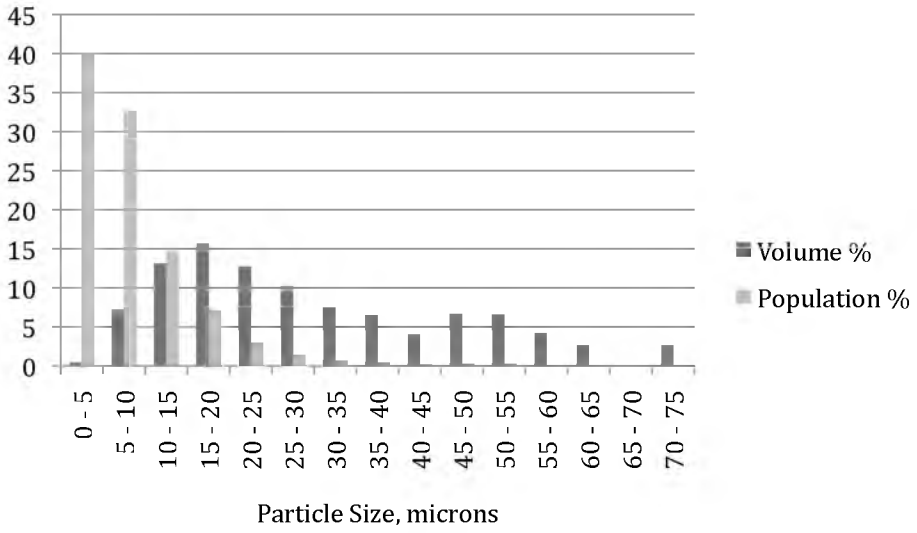

Figure C.73. Volume and Population percents for Steel Section Case 3. Run 3 of 4.

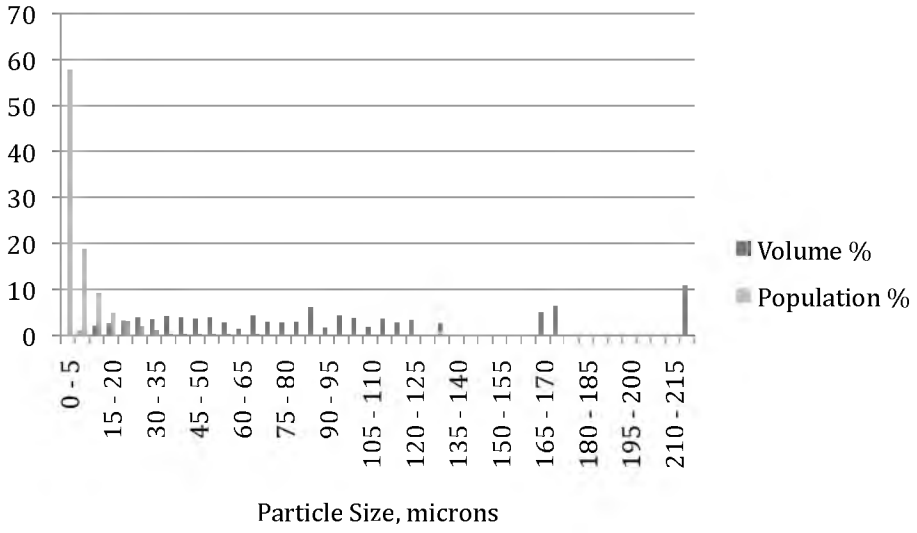

Figure C.74. Volume and Population percents for Steel Section Case 3. Run 4 of 4.

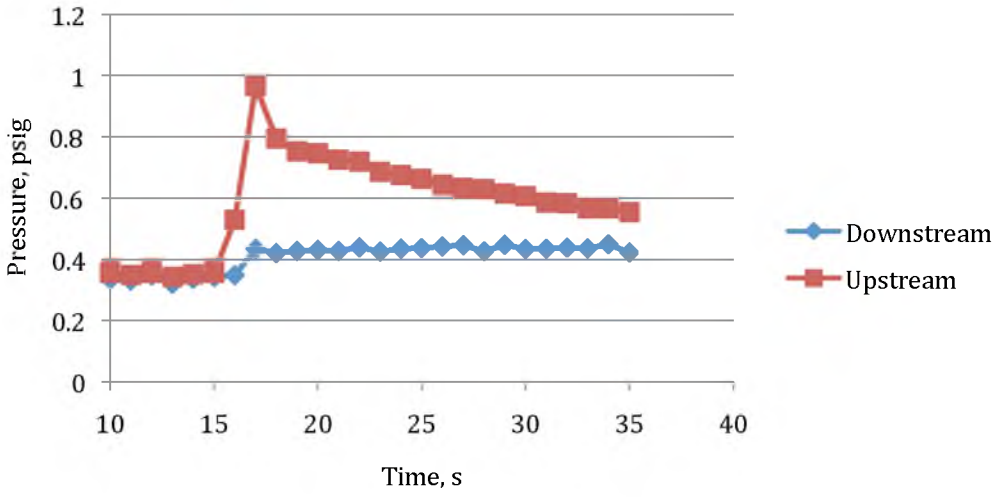

Figure C.75. Mean equivalent circular diameter = 9.7 microns. 16.6 °C heterogeneous conditions at shutdown, 4 °C gel temperature, 0.33 °C/min cooling rate, 1 hour aging, 1.12 psi/s (16.1 Pa/s shear stress) pressure loading rate, Steel Case 3.

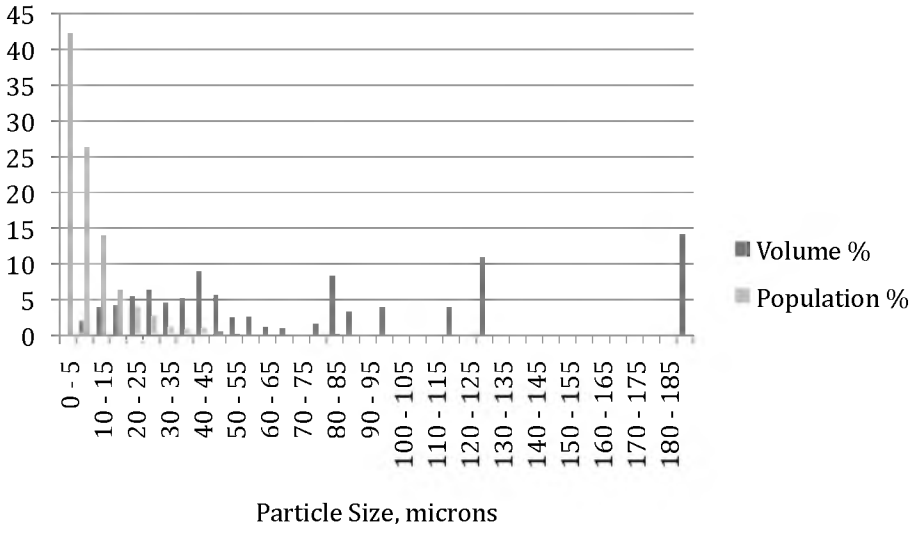

Figure C.76. Volume and Population percents for Steel Section Case 4. Run 1 of 3.

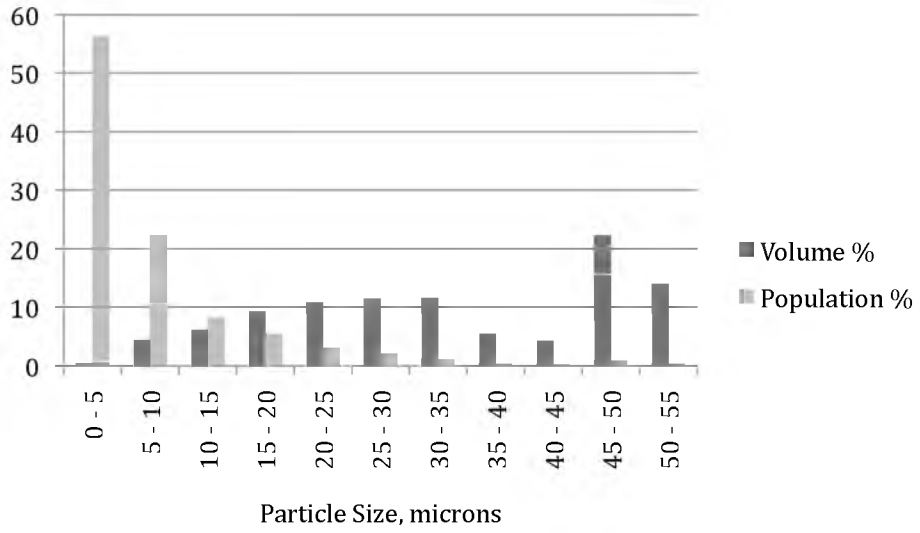

Figure C.77. Volume and Population percents for Steel Section Case 4. Run 2 of 3.

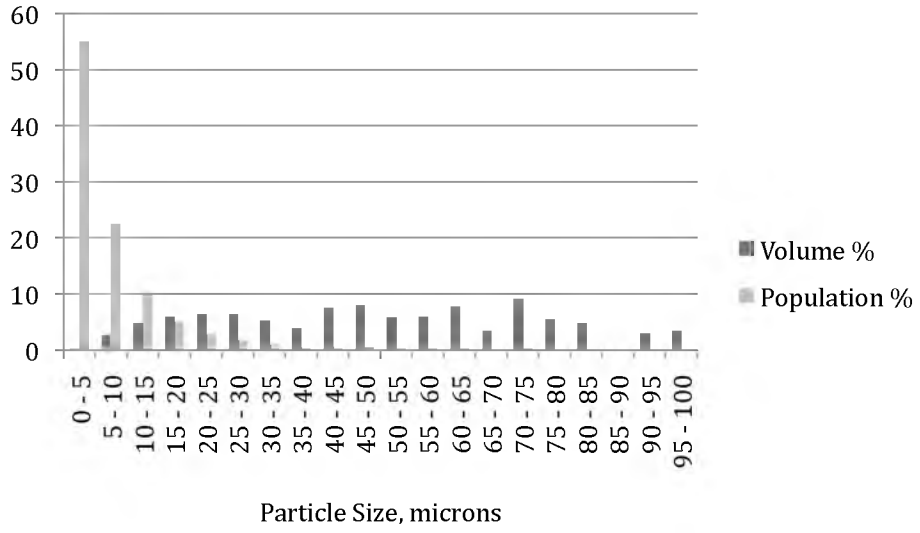

Figure C.78. Volume and Population percents for Steel Section Case 4. Run 3 of 3.

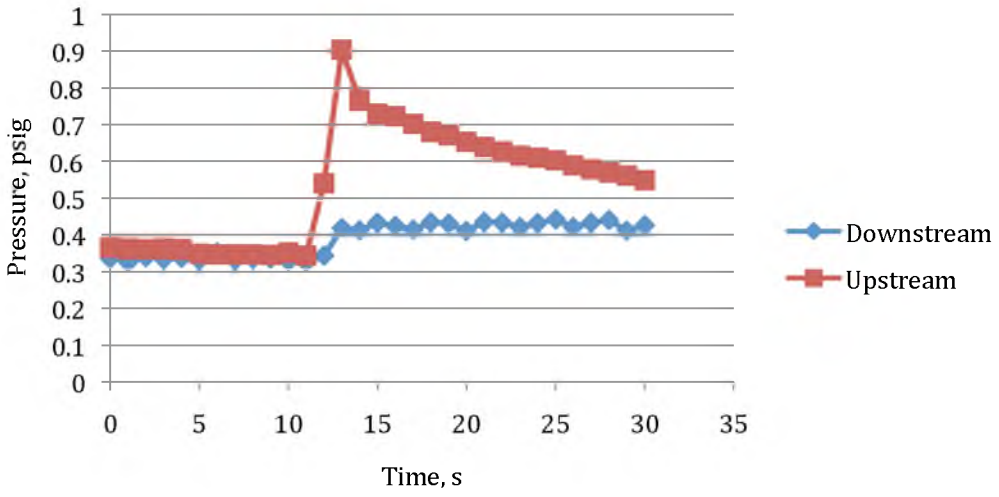

Figure C.79. Mean equivalent circular diameter = 9.0 microns. 16.6 °C heterogeneous conditions at shutdown, 4 °C gel temperature, 0.33 °C/min cooling rate, 1 hour aging, 1.12 psi/s (16.1 Pa/s shear stress) pressure loading rate, Steel Case 4.

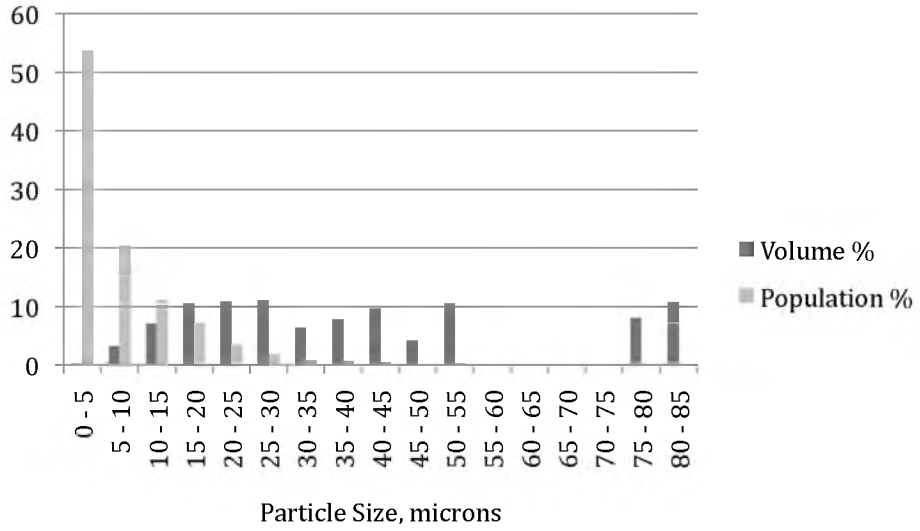

Figure C.80. Volume and Population percents for Steel Section Case 5. Run 1 of 4.

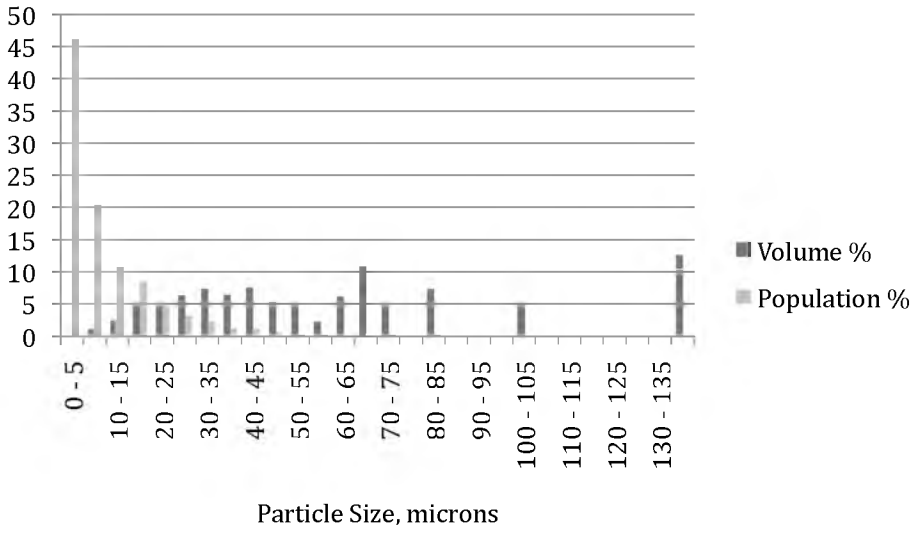

Figure C.81. Volume and Population percents for Steel Section Case 5. Run 2 of 4.

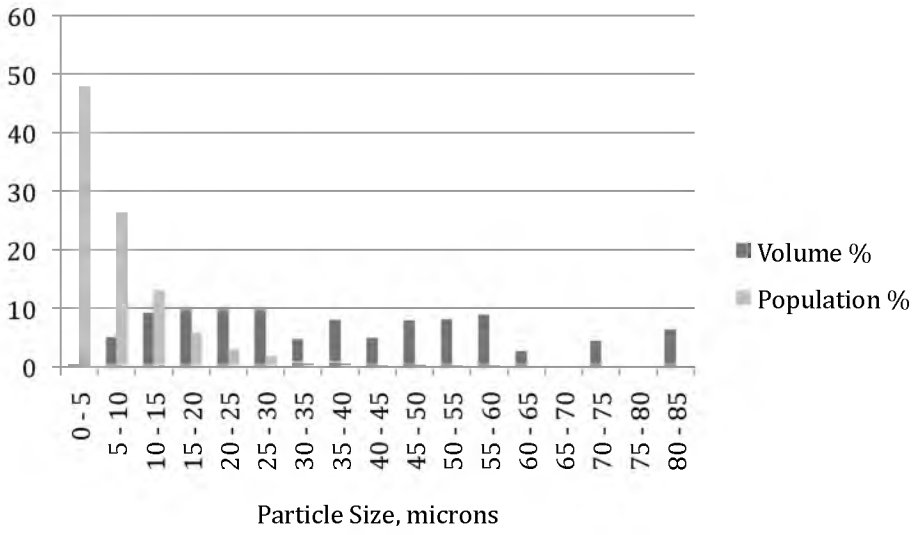

Figure C.82. Volume and Population percents for Steel Section Case 5. Run 3 of 4.

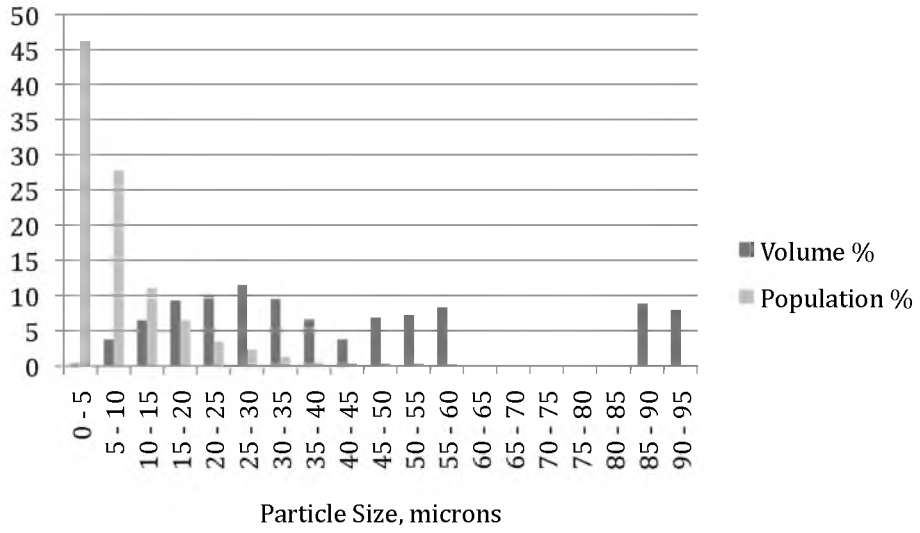

Figure C.83. Volume and Population percents for Steel Section Case 5. Run 4 of 4.

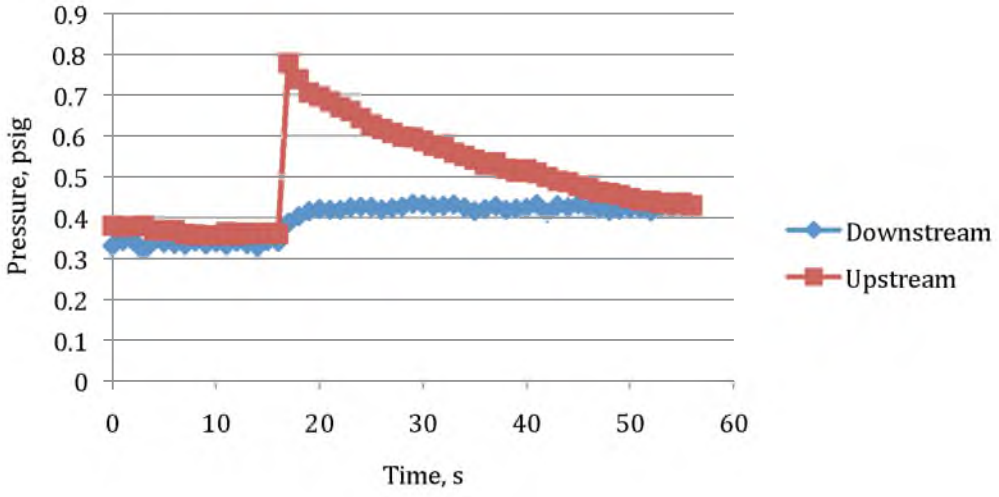

Figure C.84. Mean equivalent circular diameter = 9.4 microns. 16.6 °C heterogeneous conditions at shutdown, 4 °C gel temperature, 0.33 °C/min cooling rate, 1 hour aging, 1.12 psi/s (16.1 Pa/s shear stress) pressure loading rate, Steel Case 5.

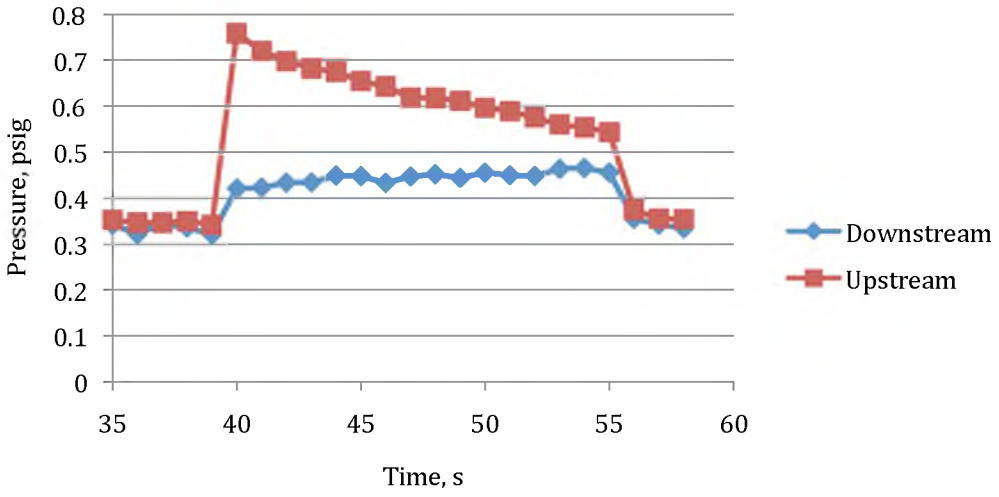

Figure C.85. Mean equivalent circular diameter = 8.0 microns. 16.6 °C heterogeneous conditions at shutdown, 4 °C gel temperature, 0.33 °C/min cooling rate, 1 hour aging, 1.12 psi/s (16.1 Pa/s shear stress) pressure loading rate.

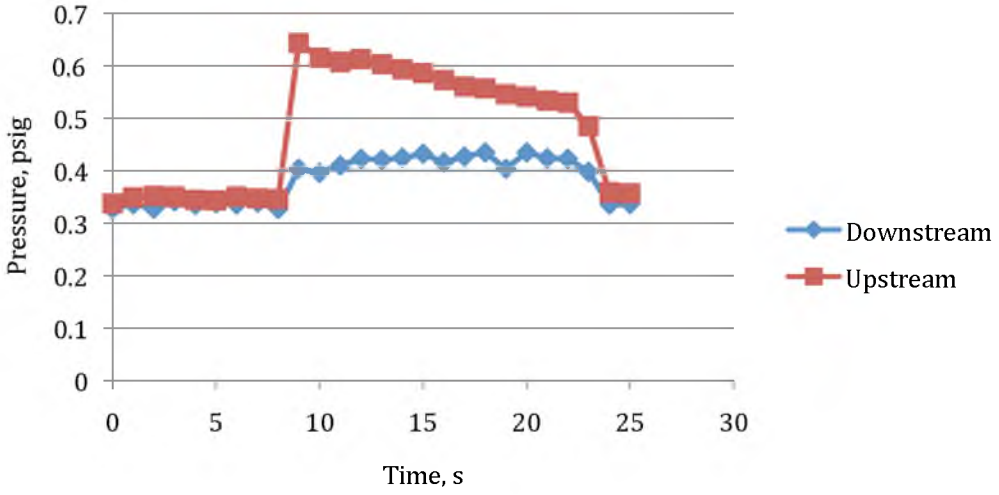

Figure C.86. Mean equivalent circular diameter = 10.7 microns. 16.6 °C heterogeneous conditions at shutdown, 4 °C gel temperature, 0.33 °C/min cooling rate, 1 hour aging, 1.12 psi/s (16.1 Pa/s shear stress) pressure loading rate.

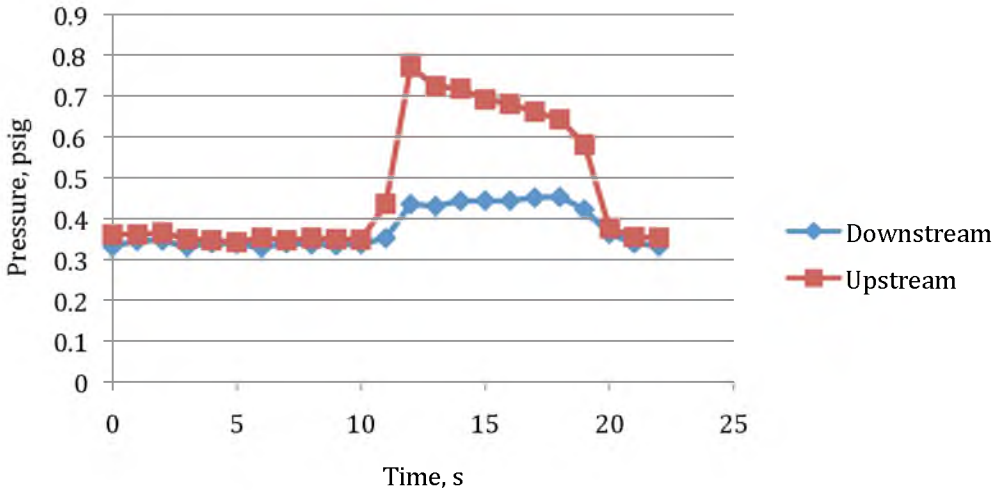

Figure C.87. Mean equivalent circular diameter = 10.0 microns. 16.6 °C heterogeneous conditions at shutdown, 4 °C gel temperature, 0.33 °C/min cooling rate, 1 hour aging, 1.12 psi/s (16.1 Pa/s shear stress) pressure loading rate.

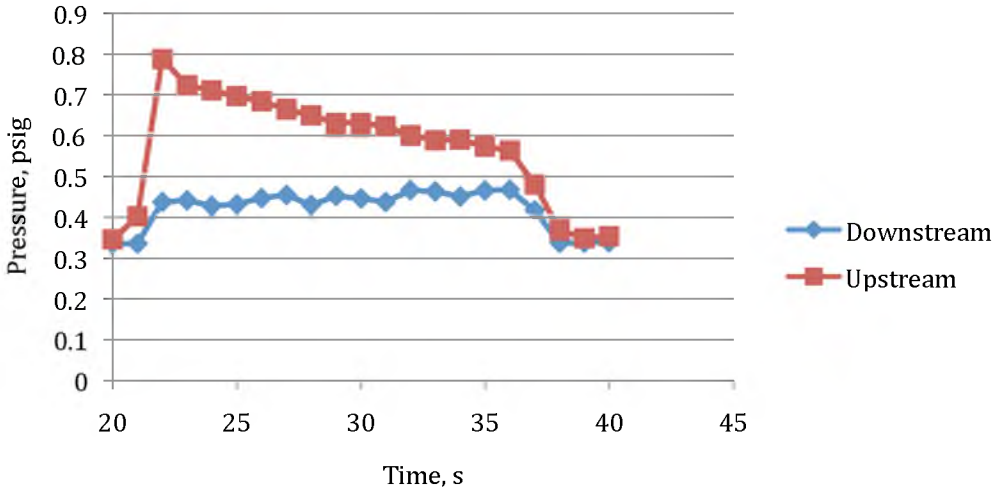

Figure C.88. Mean equivalent circular diameter = 12.4 microns. 16.6 °C heterogeneous conditions at shutdown, 4 °C gel temperature, 0.33 °C/min cooling rate, 1 hour aging, 1.12 psi/s (16.1 Pa/s shear stress) pressure loading rate.

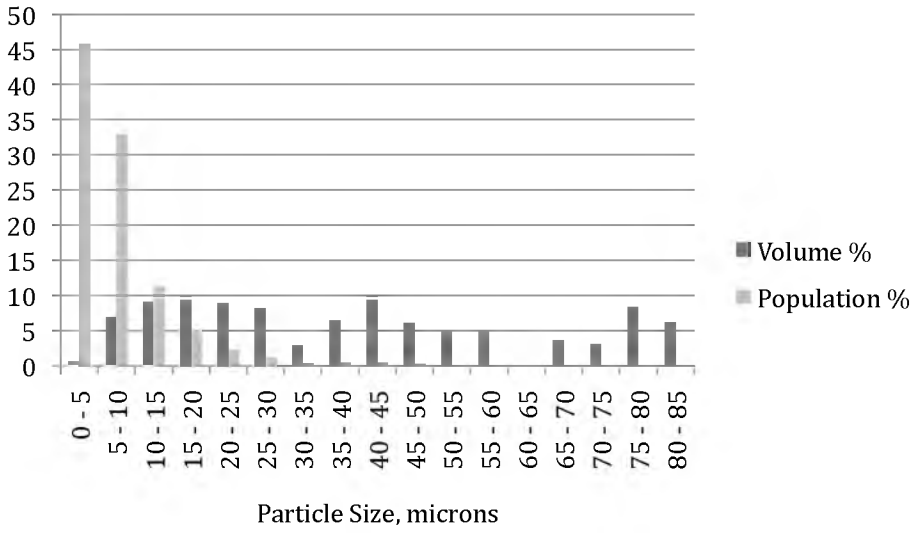

Figure C.89. Volume and Population percents for Acrylic Section Case 1. Run 1 of 2.

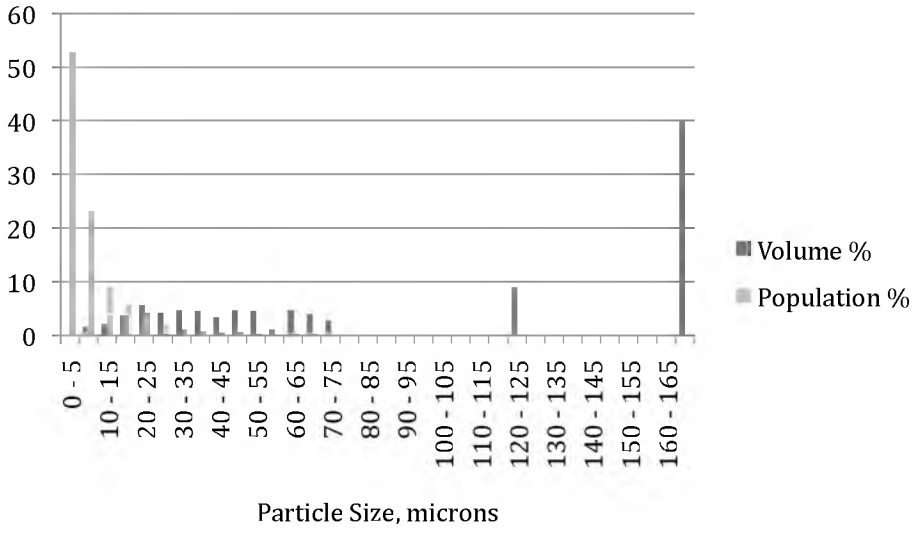

Figure C.90. Volume and Population percents for Acrylic Section Case 1. Run 2 of 2.

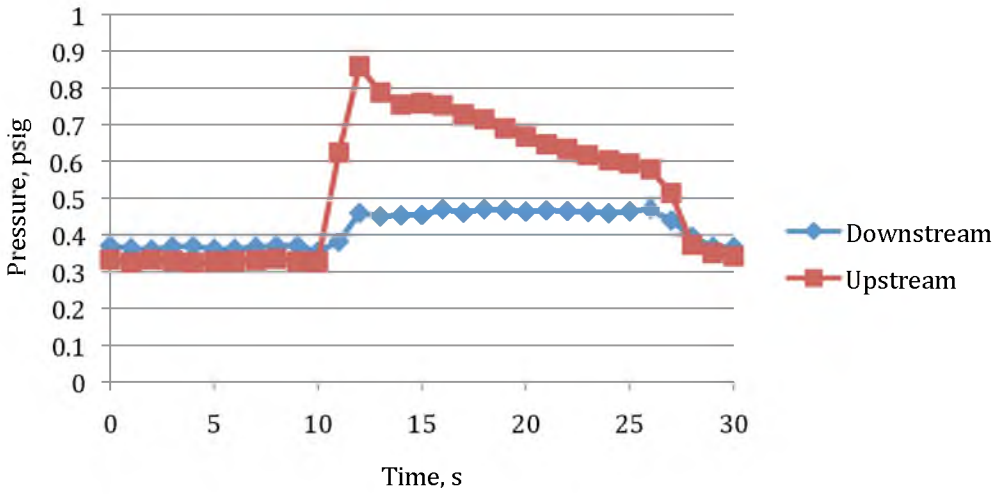

Figure C.91. Mean equivalent circular diameter = 9.1 microns. 16.6 °C heterogeneous conditions at shutdown, 4 °C gel temperature, 0.33 °C/min cooling rate, 1 hour aging, 1.12 psi/s (16.1 Pa/s shear stress) pressure loading rate, Acrylic Case 1.

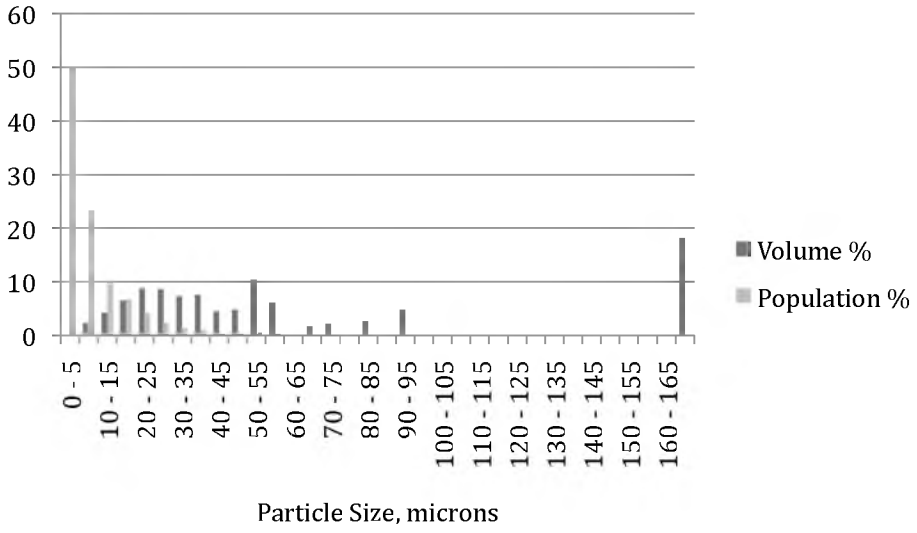

Figure C.92. Volume and Population percents for Acrylic Section Case 2. Run 1 of 2.

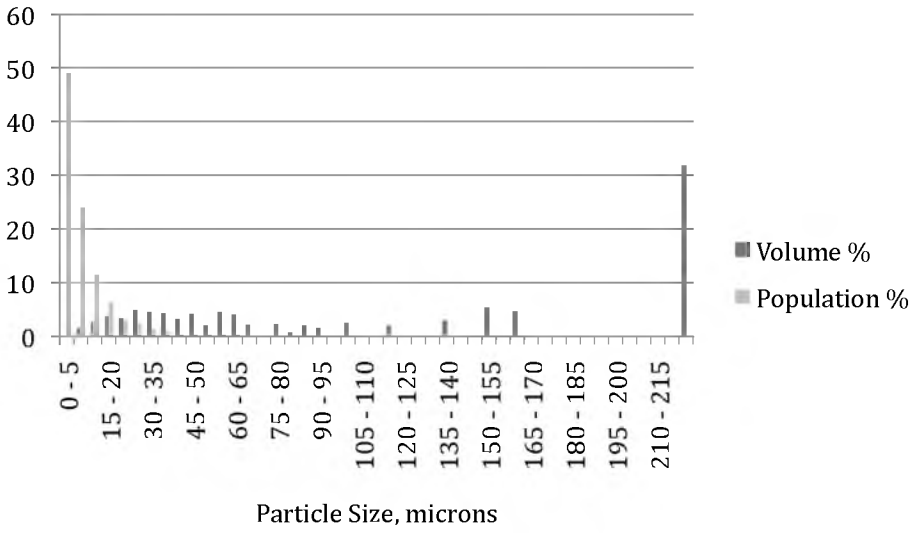

Figure C.93. Volume and Population percents for Acrylic Section Case 2. Run 2 of 2.

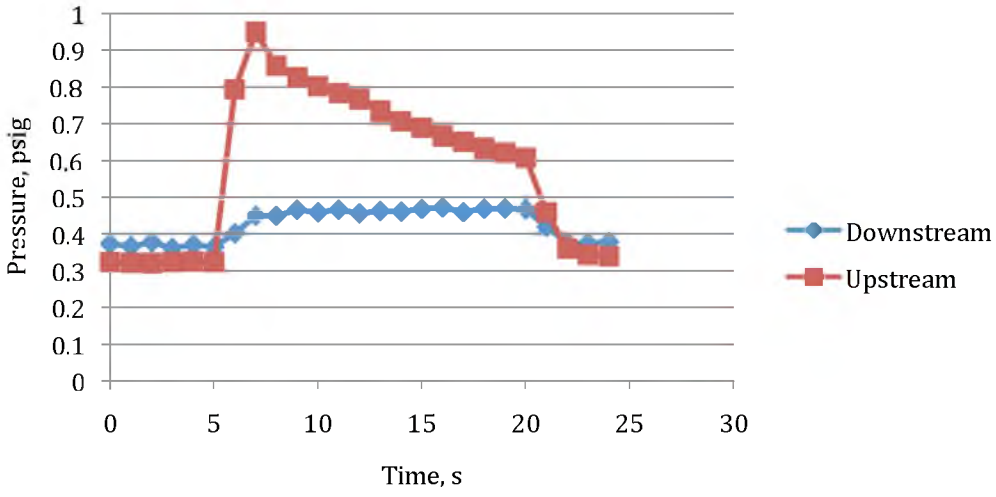

Figure C.94. Mean equivalent circular diameter = 8.5 microns. 16.6 °C heterogeneous conditions at shutdown, 4 °C gel temperature, 0.33 °C/min cooling rate, 1 hour aging, 1.12 psi/s (16.1 Pa/s shear stress) pressure loading rate, Acrylic Case 2.

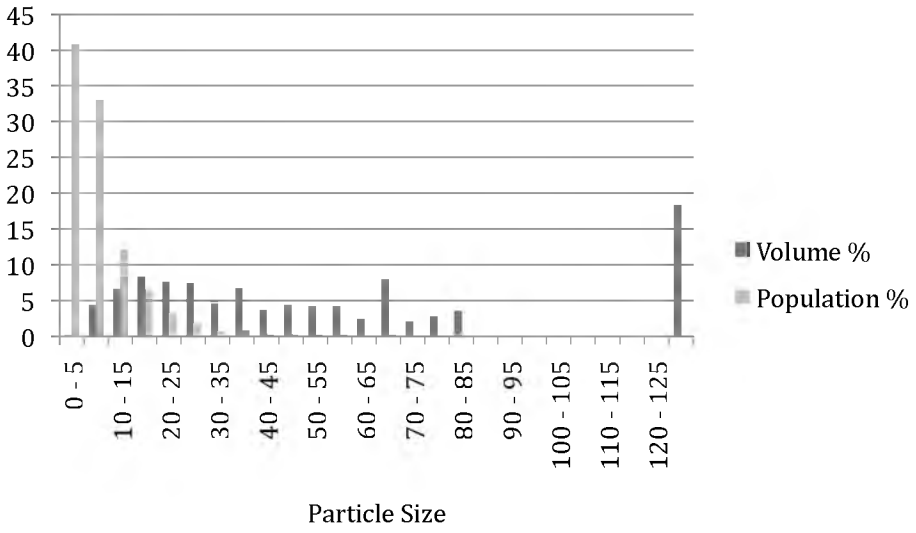

Figure C.95. Volume and Population percents for Acrylic Section Case 3. Run 1 of 3.

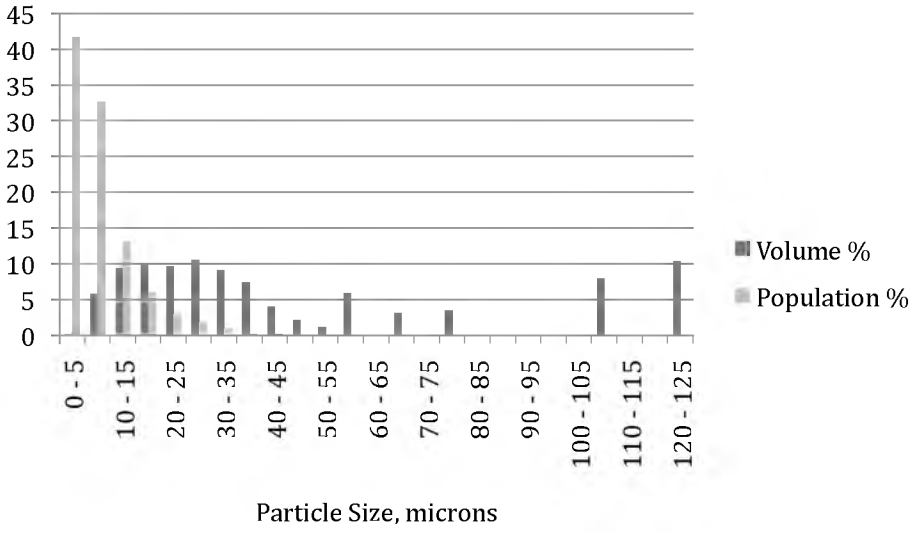

Figure C.96. Volume and Population percents for Acrylic Section Case 3. Run 2 of 3.

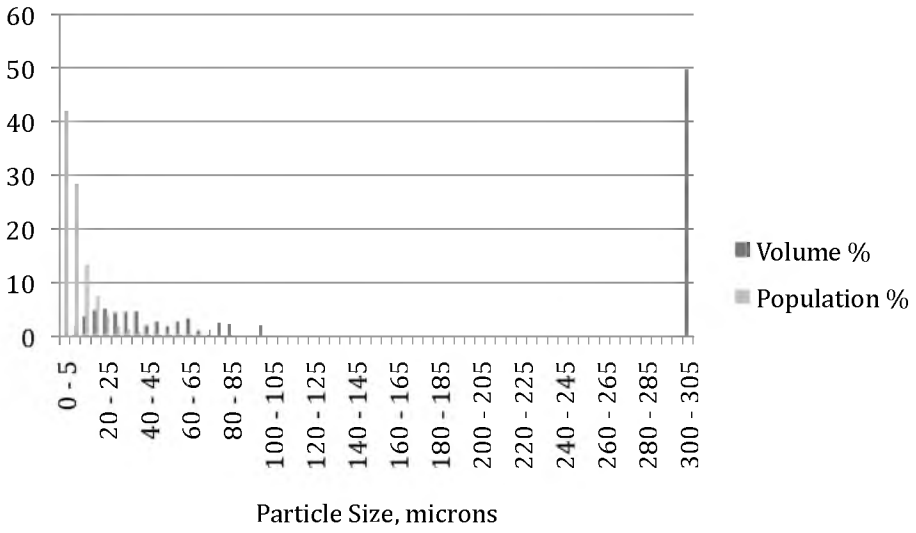

Figure C.97. Volume and Population percents for Acrylic Section Case 3. Run 3 of 3.

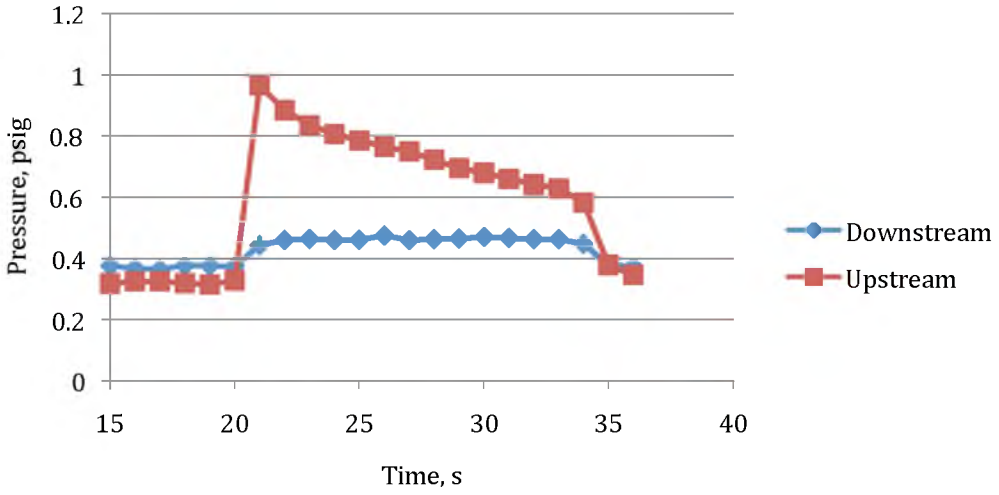

Figure C.98. Mean equivalent circular diameter = 10.5 microns. 16.6 °C heterogeneous conditions at shutdown, 4 °C gel temperature, 0.33 °C/min cooling rate, 1 hour aging, 1.12 psi/s (16.1 Pa/s shear stress) pressure loading rate, Acrylic Case 3.

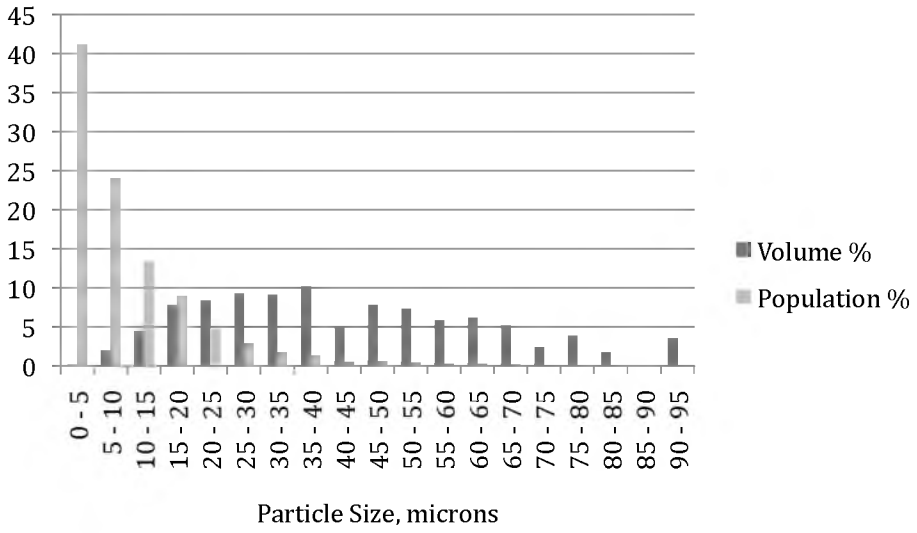

Figure C.99. Volume and Population percents for Acrylic Section Case 3. Run 1 of 1.

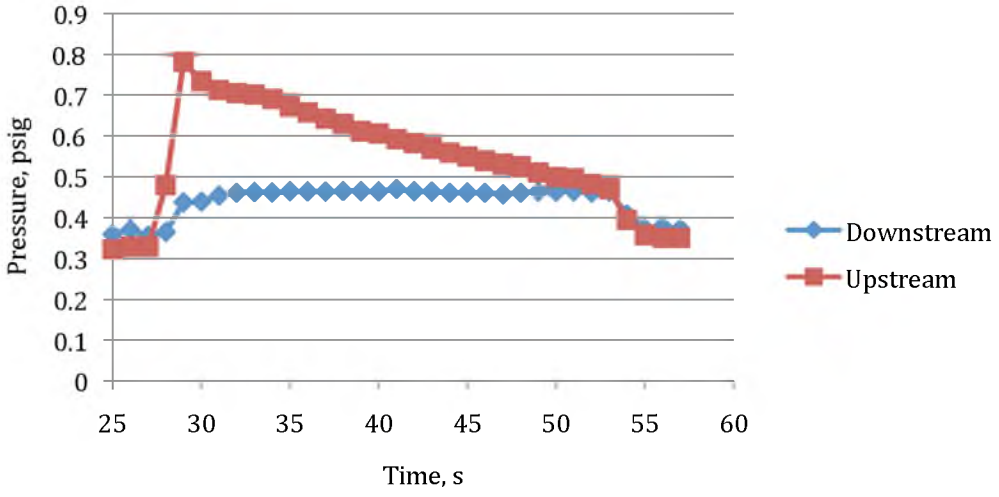

Figure C.100. Mean equivalent circular diameter = 11.2 microns. 16.6 °C heterogeneous conditions at shutdown, 4 °C gel temperature, 0.33 °C/min cooling rate, 1 hour aging, 1.12 psi/s (16.1 Pa/s shear stress) pressure loading rate, Acrylic Case 4.

C.6 Pressure Loading Rate Effect on Restart Pressure

All gels in this section were created identically: 35 °C oil temperature at shutdown for homogeneous gels, 16.6 °C oil temperature at shutdown for heterogeneous gels, 3 °C final cooling temperature, 0.33 °C/min cooling rate, and 1 hour aging time. All oils were mixed and flowed under identical conditions: 500 rpm reservoir mixing rate, 1.5 gpm conditioning flow rate, 1 °C conditioning loop coolant temperature, and 0.75 gpm test section flow rate. These data comprise Figures C.101-C.136. Pleases note that the steel tests are prohibitive towards PIV visualization; as such only pressure data is shown for comparison to acrylic results.

Many of the acrylic section tests involve PIV analysis. As such, each restart with corresponding PIV results includes both the "before" and "after" breakage images. Those PIV images of which software vector analysis was conclusive include the vectors; however, due to the gel's diffusive effect on the laser light software analysis was less than effective in most cases. A simple visual exploration of the images reveals very clearly the breakage profiles. Only one homogeneous gel test was conducted in the clear section, this being to confirm adhesive failure. The PIV images of the two cases presented in the body of this dissertation are not shown.

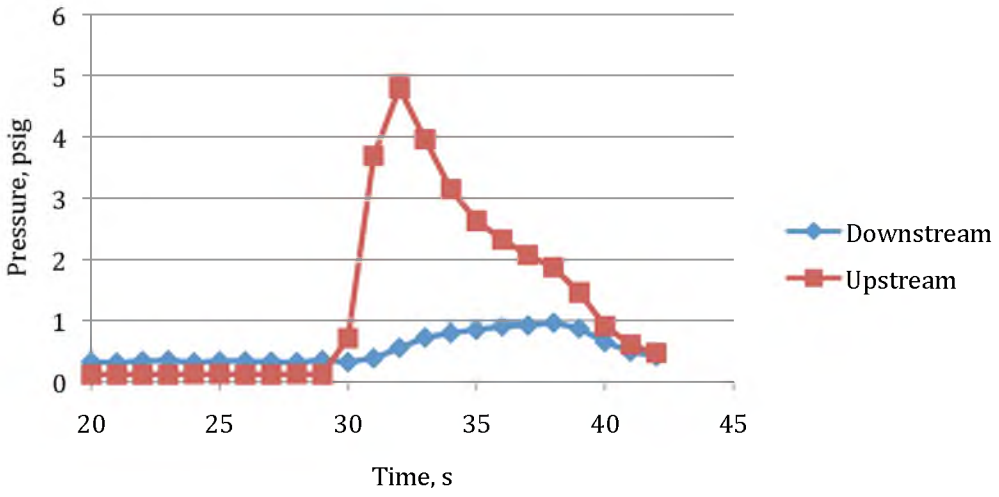

Figure C.101. Homogeneous steel restart at 2.6 psi/s (37.3 Pa/s shear stress).

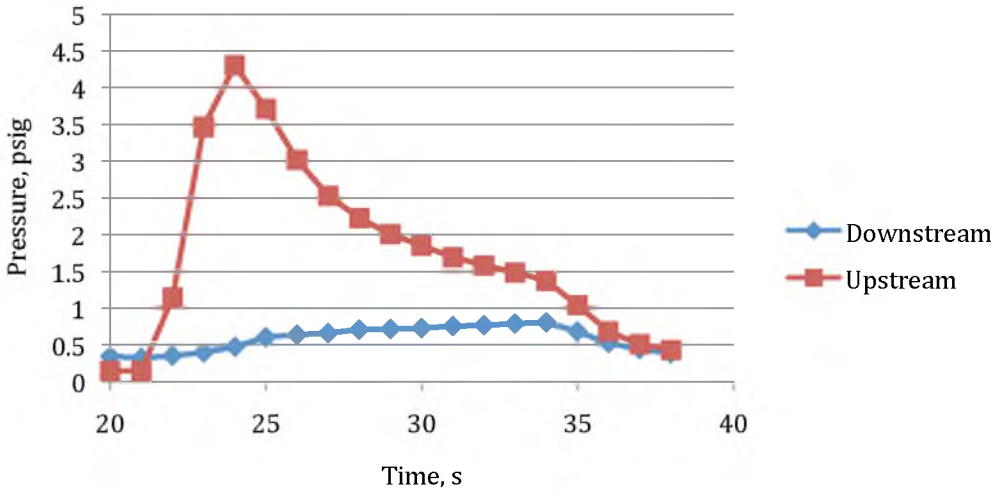

Figure C.102. Homogeneous steel restart at 1.99 psi/s (28.6 Pa/s shear stress).

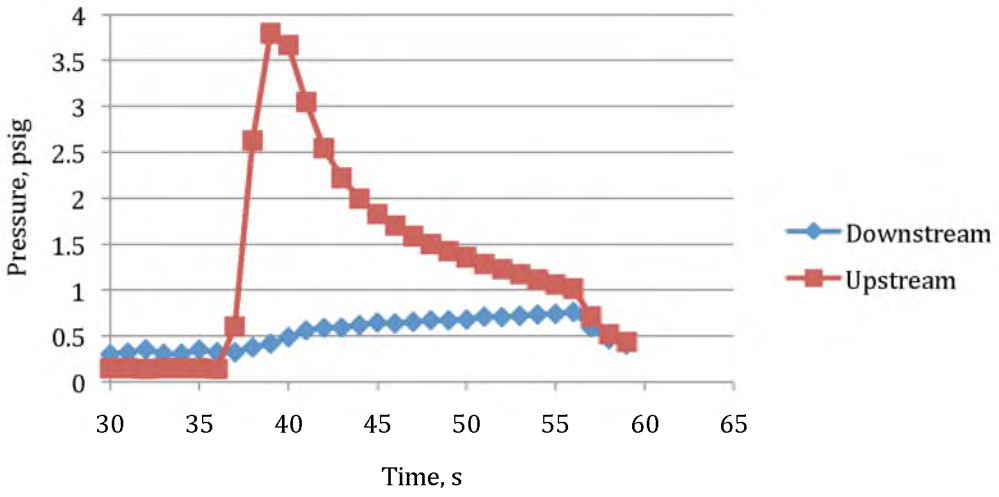

Figure C.103. Homogeneous steel restart at 1.62 psi/s (23.3 Pa/s shear stress).

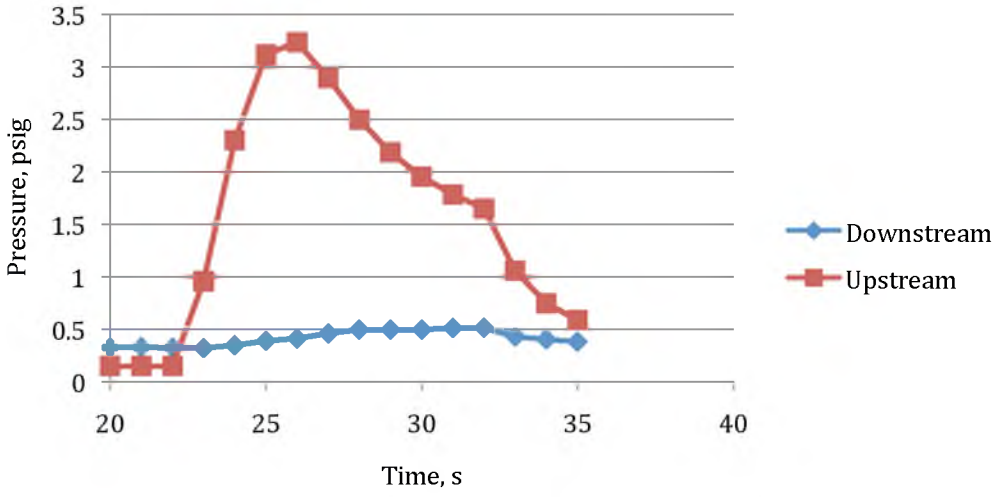

Figure C.104. Homogeneous steel restart at 1.12 psi/s (16.1 Pa/s shear stress).

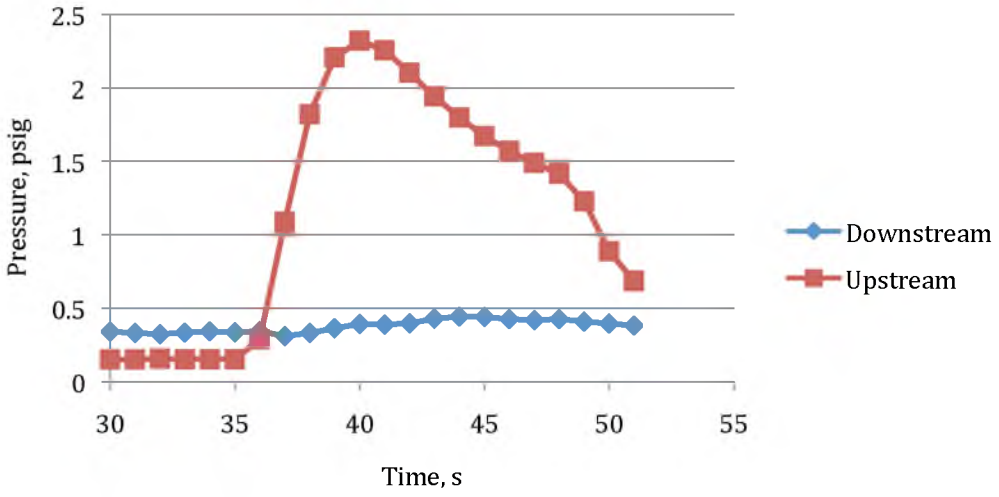

Figure C.105. Homogeneous steel restart at 0.724 psi/s (10.4 Pa/s shear stress).

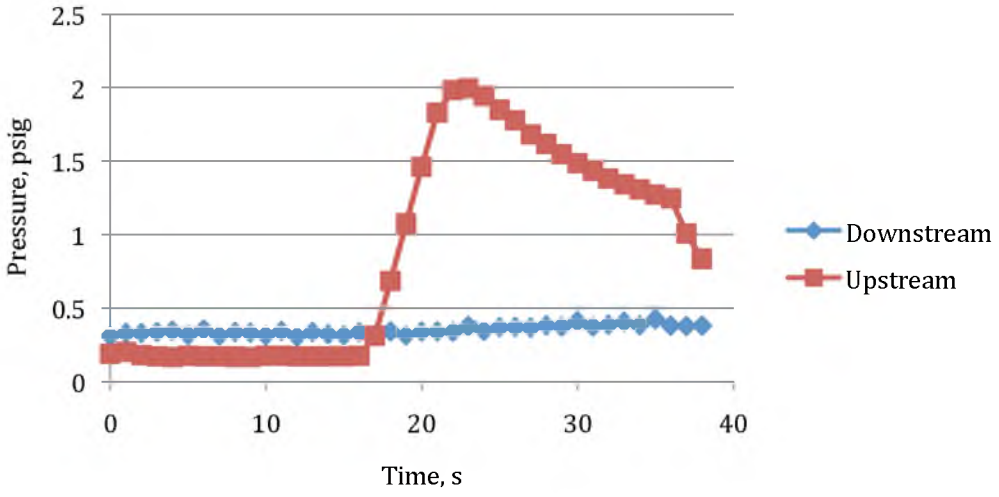

Figure C.106. Homogeneous steel restart at 0.328 psi/s (4.7 Pa/s shear stress).

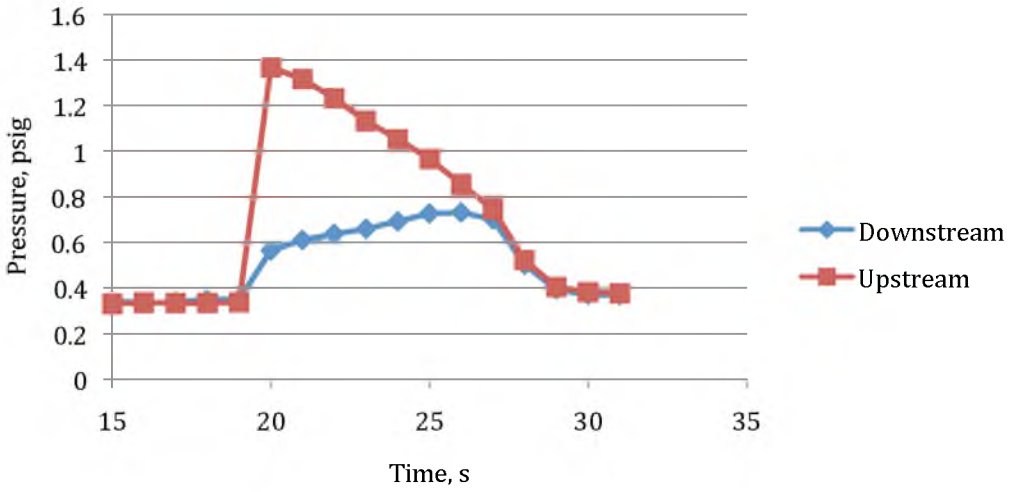

Figure C.107. Heterogeneous steel restart at 2.6 psi/s (37.3 Pa/s shear stress).

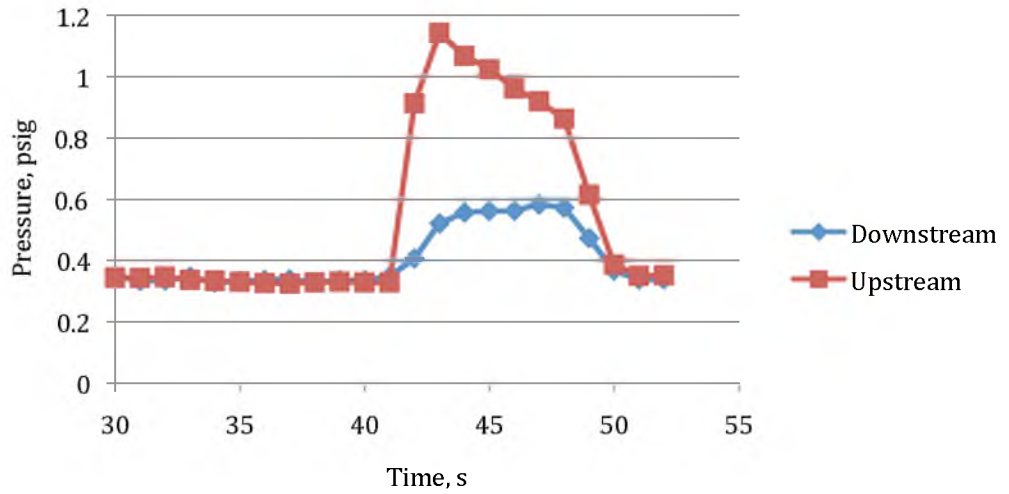

Figure C.108. Heterogeneous steel restart at 1.99 psi/s (28.6 Pa/s shear stress).

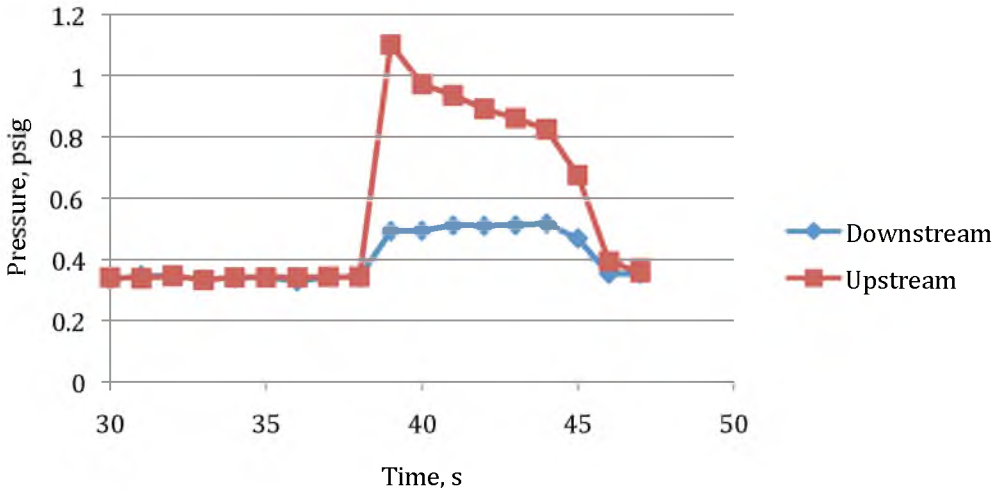

Figure C.109. Heterogeneous steel restart at 1.62 psi/s (23.3 Pa/s shear stress).

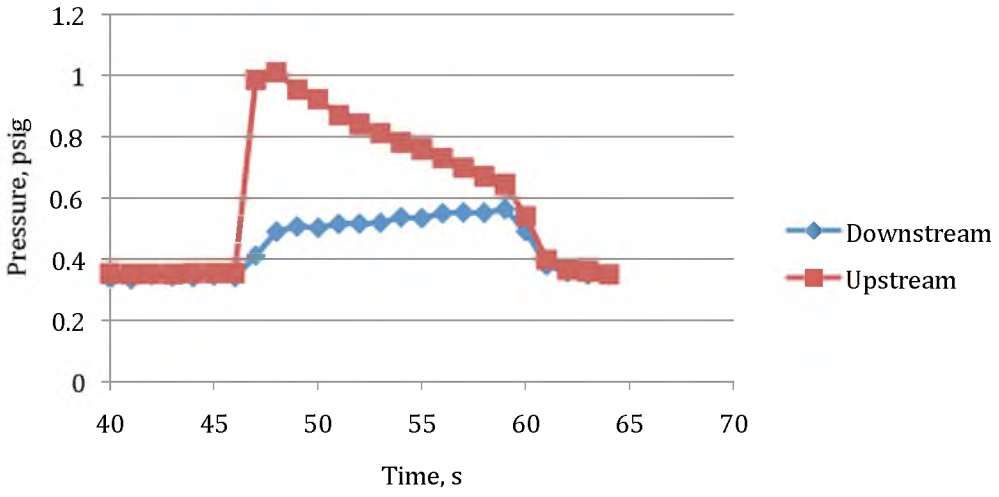

Figure C.110. Heterogeneous steel restart at 1.62 psi/s (23.3 Pa/s shear stress). Run 2.

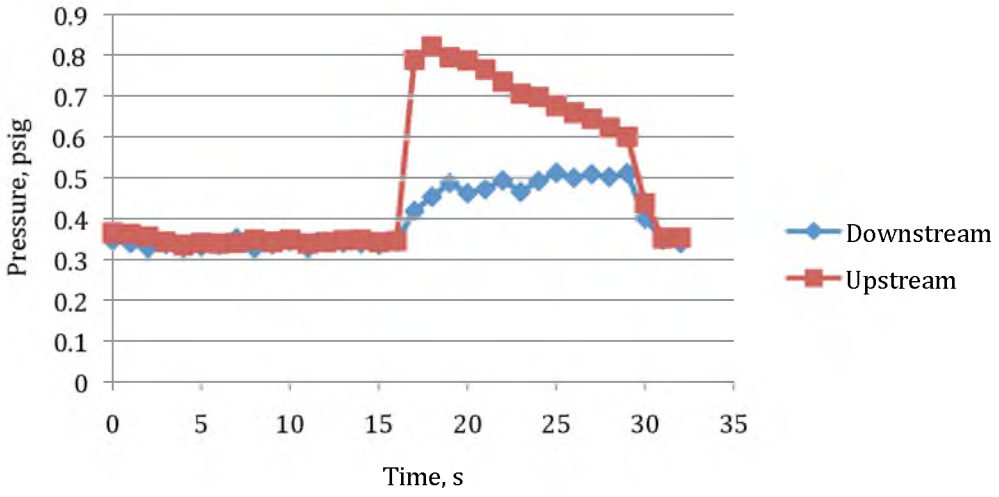

Figure C.111. Heterogeneous steel restart at 1.37 psi/s (19.7 Pa/s shear stress).

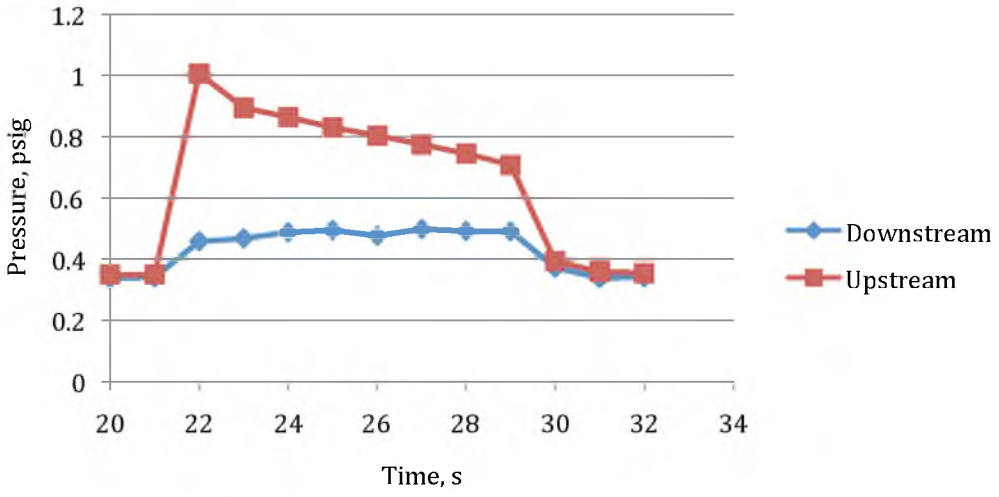

Figure C.112. Heterogeneous steel restart at 1.37 psi/s (19.7 Pa/s shear stress). Run 2.

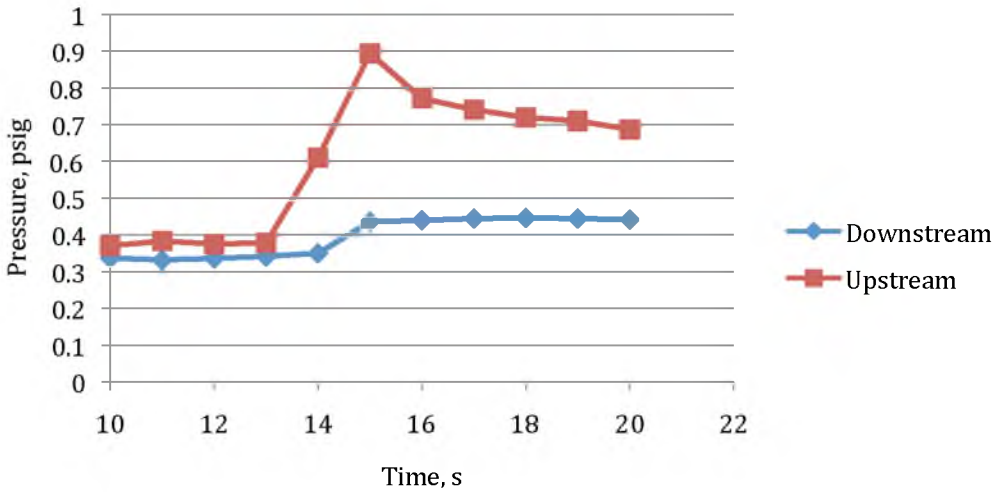

Figure C.113. Heterogeneous steel restart at 1.12 psi/s (16.1 Pa/s shear stress).

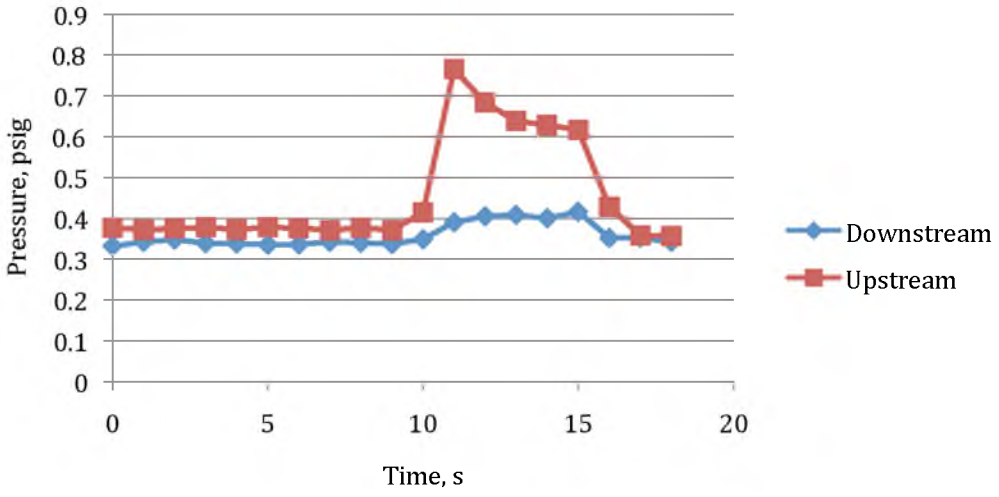

Figure C.114. Heterogeneous steel restart at 0.724 psi/s (10.4 Pa/s shear stress).

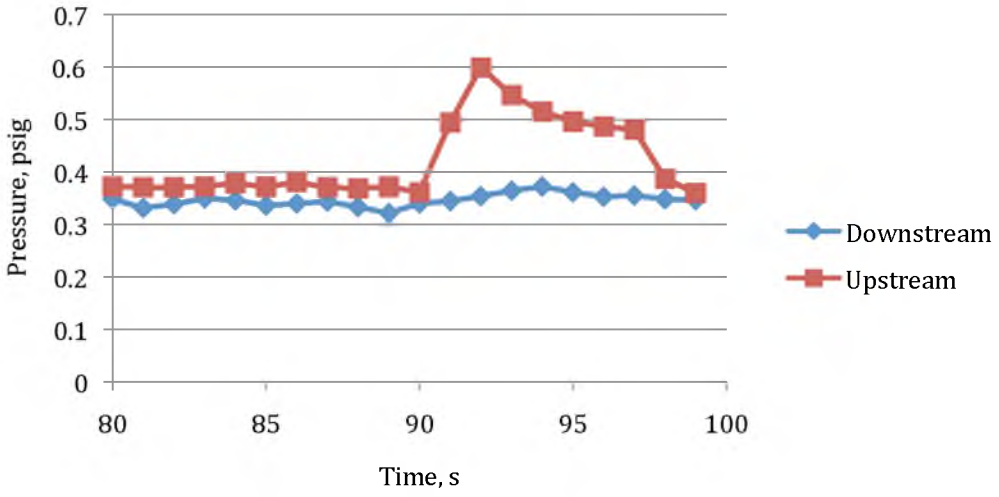

Figure C.115. Heterogeneous steel restart at 0.328 psi/s (1.7 Pa/s shear stress).

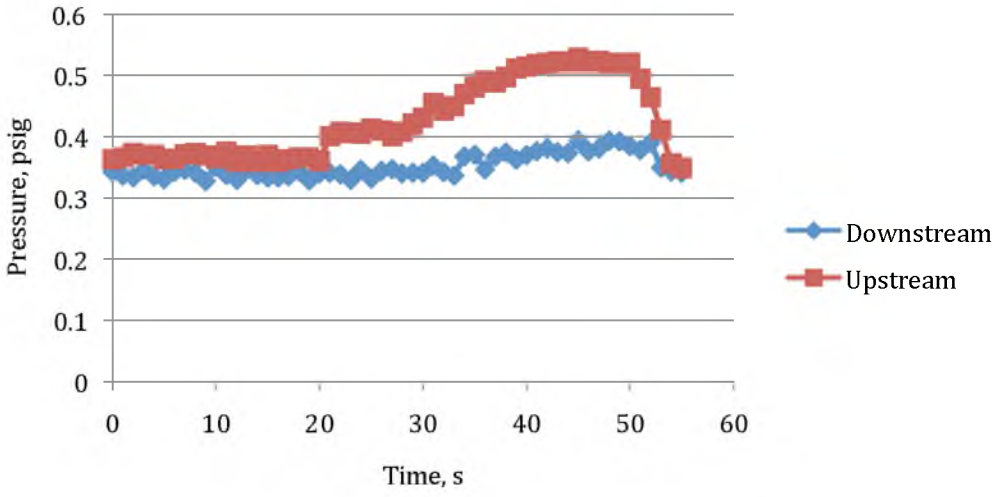

Figure C.116. Heterogeneous steel restart at 0.034 psi/s (0.5 Pa/s shear stress).

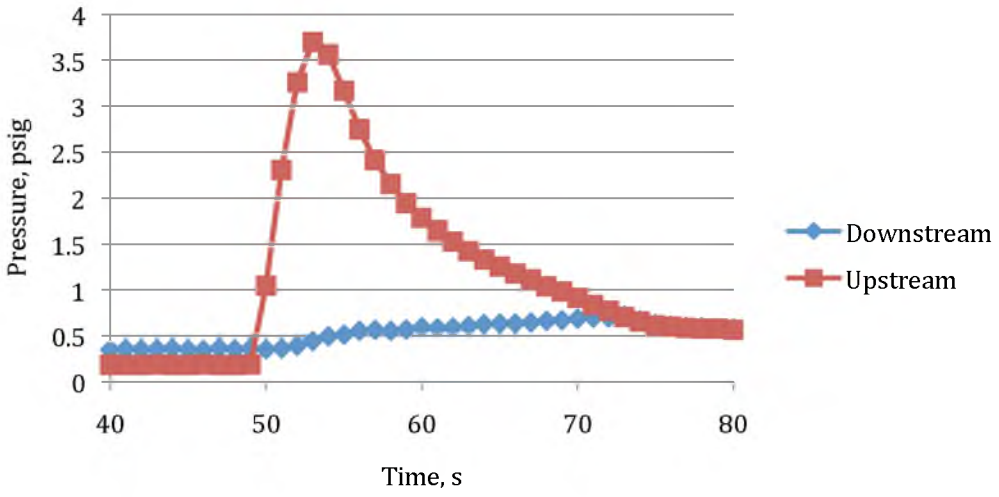

Figure C.117. Homogeneous clear restart at 1.62 psi/s (23.3 Pa/s shear stress).

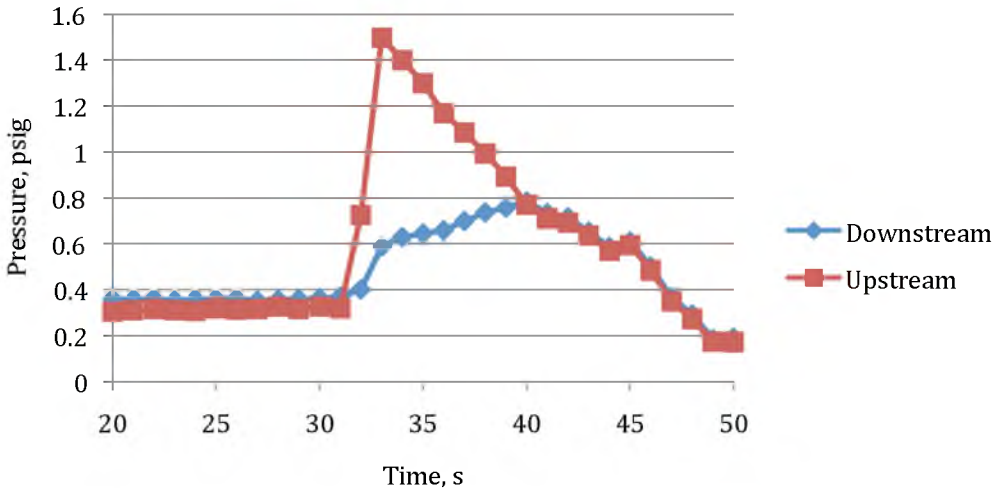

Figure C.118. Heterogeneous clear restart at 2.6 psi/s (37.3 Pa/s shear stress). Run 1 of 2.

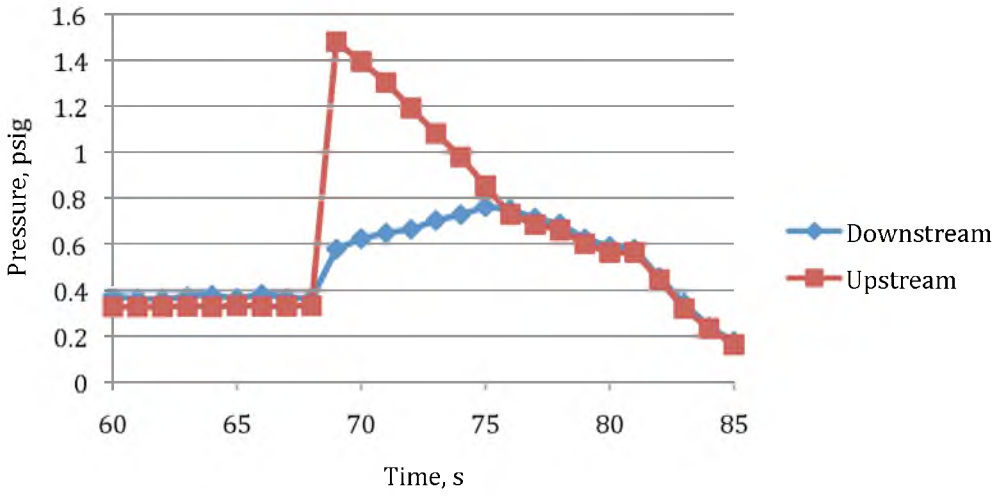

Figure C.119. Heterogeneous clear restart at 2.6 psi/s (37.3 Pa/s shear stress). Run 2 of 2.

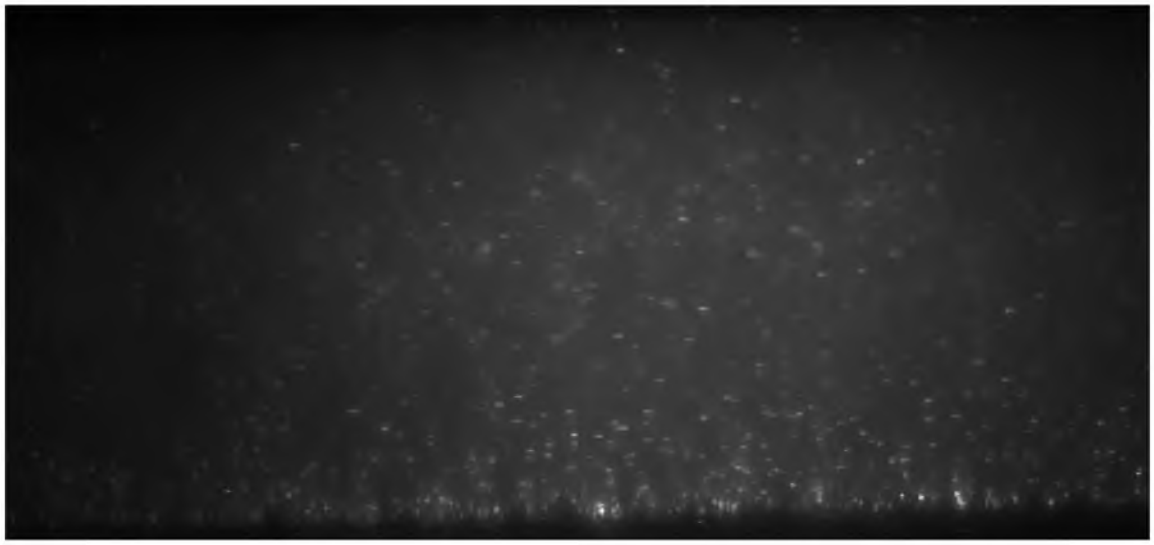

Figure C.120. PIV image of 2.6 psi/s (37.3 Pa/s shear stress) loading case before breakage.

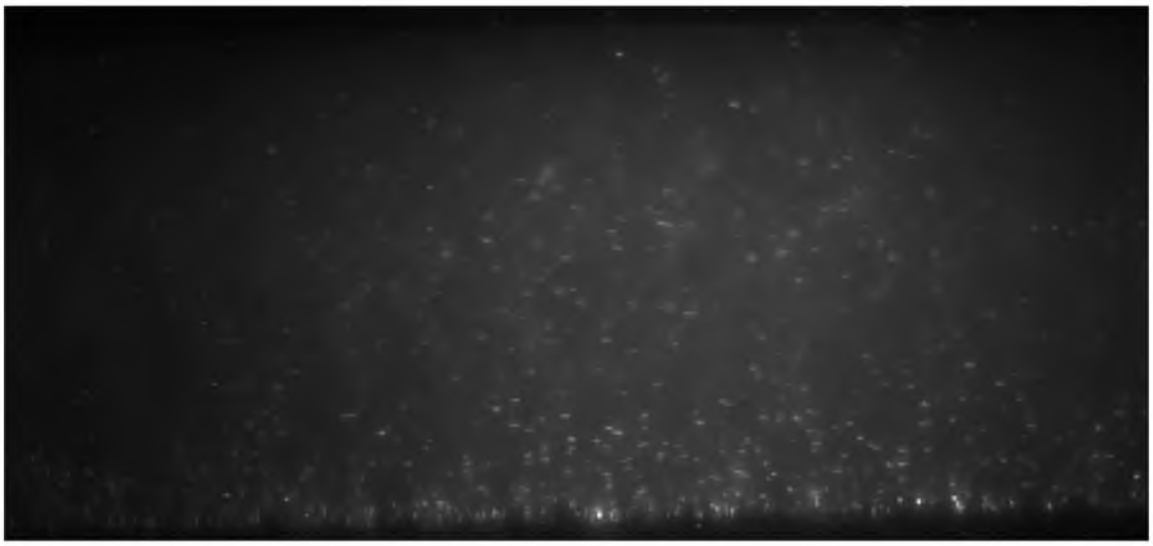

Figure C.121. PIV image of 2.6 psi/s (37.3 Pa/s shear stress) loading case after breakage.

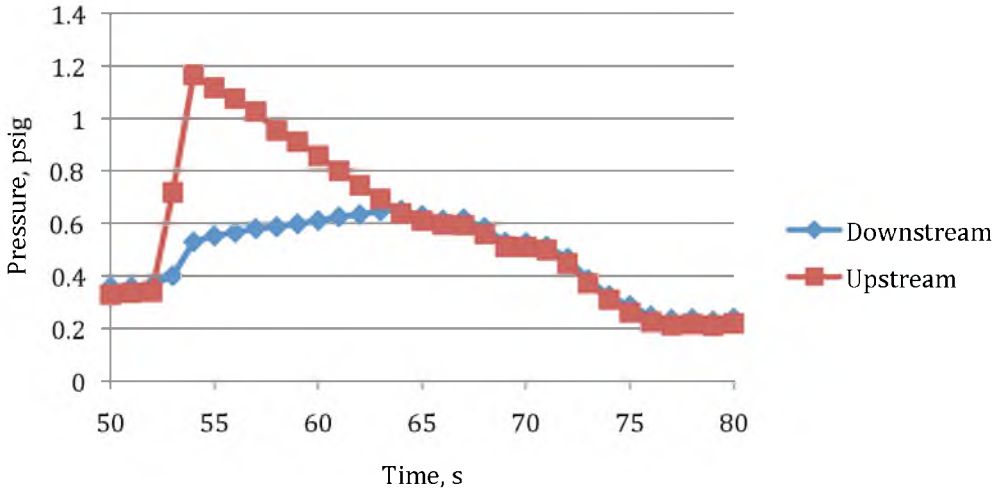

Figure C.122. Heterogeneous clear restart at 1.99 psi/s (28.6 Pa/s shear stress). Run 1 of 2.

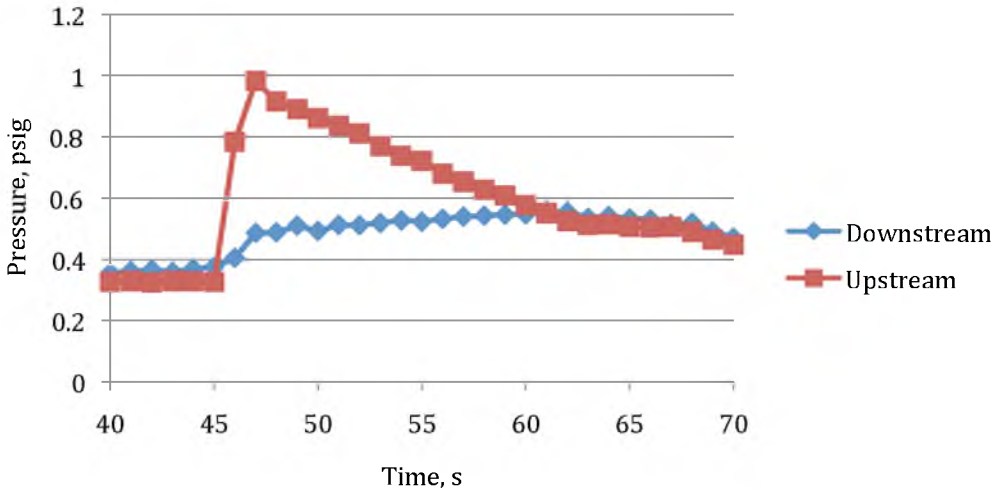

Figure C.123. Heterogeneous clear restart at 1.99 psi/s (28.6 Pa/s shear stress). Run 2 of 2.

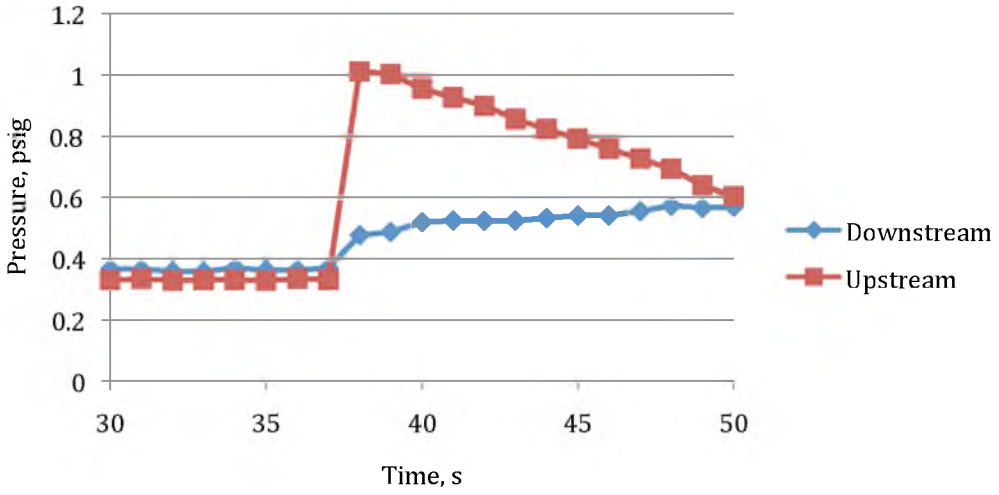

Figure C.124. Heterogeneous clear restart at 1.62 psi/s (23.3 Pa/s shear stress).

Figure C.125. PIV image of 1.62 psi/s (23.3 Pa/s shear stress) loading case before breakage.

Figure C.126. PIV image of 1.62 psi/s (23.3 Pa/s shear stress) loading case after breakage.

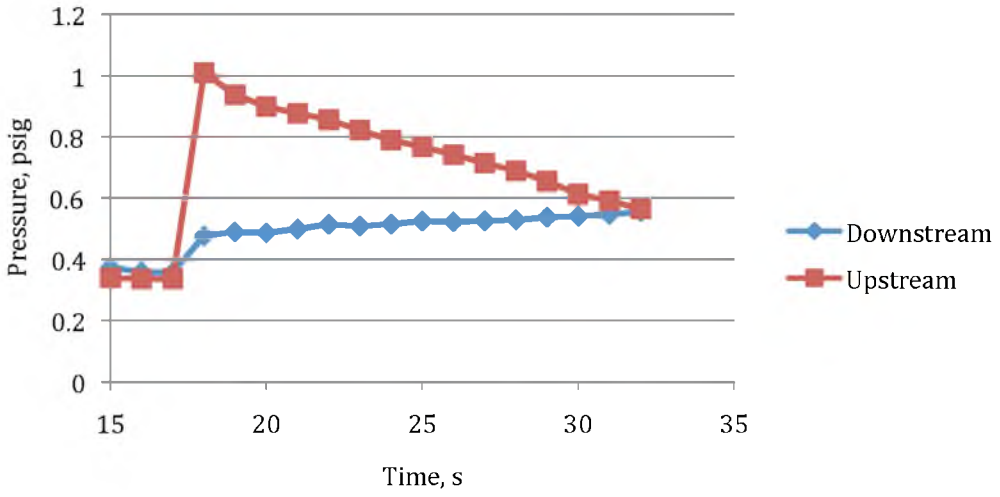

Figure C.127. Heterogeneous clear restart at 1.37 psi/s (19.7 Pa/s shear stress).

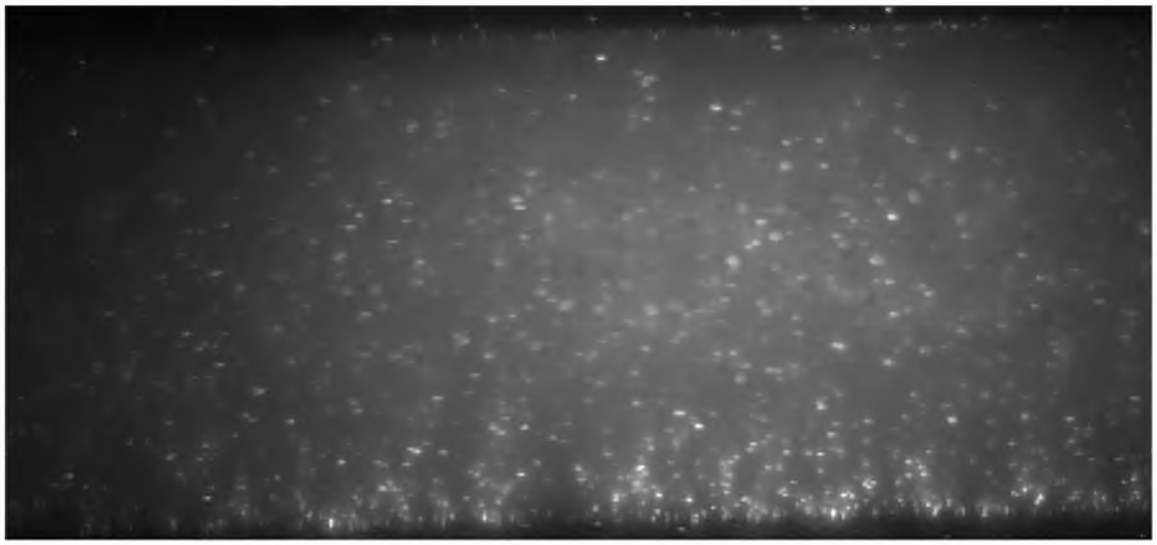

Figure C.128. PIV image of 1.37 psi/s (19.7 Pa/s shear stress) loading case before breakage.

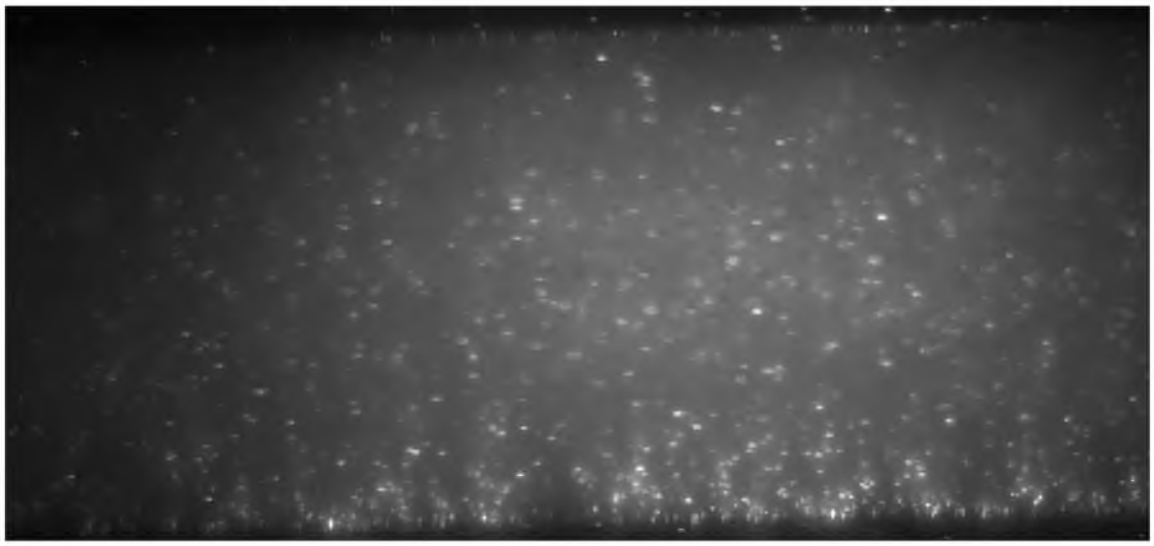

Figure C.129. PIV image of 1.37 psi/s (19.7 Pa/s shear stress) loading case after breakage.

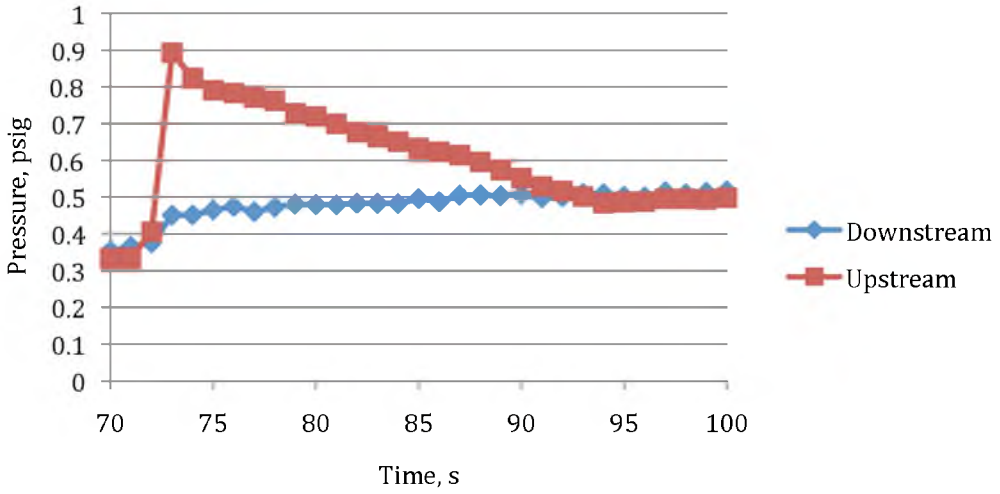

Figure C.130. Heterogeneous clear restart at 1.12 psi/s (16.1 Pa/s shear stress).

Figure C.131. PIV image of 1.12 psi/s (16.1 Pa/s shear stress) loading case before breakage.

Figure C.132. PIV image of 1.12 psi/s (16.1 Pa/s shear stress) loading case after breakage.

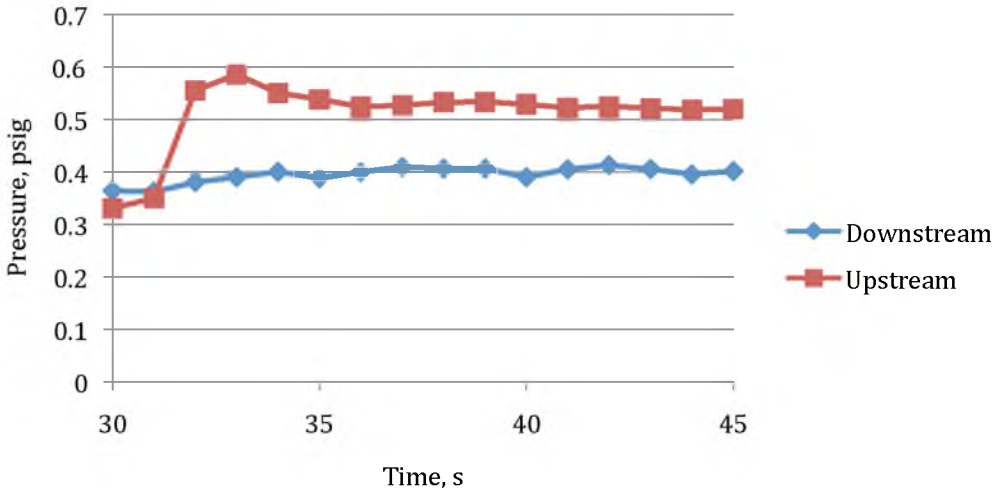

Figure C.133. Heterogeneous clear restart at 0.724 psi/s (10.4 Pa/s shear stress).

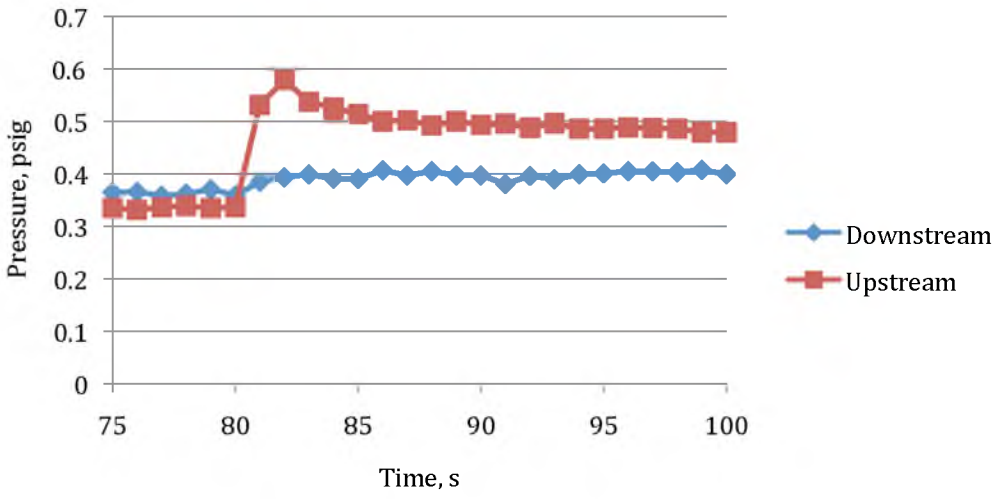

Figure C.134. Heterogeneous clear restart at 0.328 psi/s (4.7 Pa/s shear stress).

Figure C.135. PIV image of 0.328 psi/s (4.7 Pa/s shear stress) loading case before breakage.

Figure C.136. PIV image of 0.328 psi/s (4.7 Pa/s shear stress) loading case after breakage

REFERENCES

[1] K Kvenvolden, K. A. Organic geochemistry – A retrospective of its first 70 years. *Organic Geochemistry* **2006**, 37 (1).

[2] Braun, R. L.; Burnham, l. K. Chemical reaction model for oil and gas generation from type I and type II kerogen. 1993, Lawrence Livermore National Laboratory.

[3] Freund, M.; Mózes, G.; Jakab, E. Paraffin products: properties, technologies, applications. Trans 1982**,** Elsevier, Amsterdam, Netherlands.

[4] Nasser, W. E. Waxes, natural and synthetic. In *McKetta, John J. Encyclopedia of Chemical Processing and Design*, **1999**, *67*, 17.

[5] Camin, D. L.; Raymond, A. J. Chromatography in the petroleum industry. *J. Chromatogr. Sci.*, **1973**, *11* (12), 625-638.

[6] Gaylor, V. F.; Jones, C. N.; Landerl, J. H.; Hughes, E. C. Simultaneous determination of crude oil boiling range distribution and hydrocarbon type distribution by gas chromatography. *Anal. Chem.*, **1964**, *36* (8), 1606–1612.

[7] Jones, W. L.; Kieselbach, R. Units of measurement in gas chromatography. *Anal. Chem.*, **1958**, *30* (10), 1590–1592.

[8] Frysinger, G. S.; Gaines, R. B. Comprehensive two-dimensional gas chromatography with mass spectrometric detection (GC × GC/MS) applied to the analysis of petroleum. *J. High Resol. Chromatogr.* **1999**, *22* (5), 251-255.

[9] Nontechnical guide to petroleum geology, exploration, drilling, and production. Norman J. Hyne, 2nd Edition, PennWell Books, 2001.

[10] Waters, C. C. Petroleum geochemistry – past, present, and future. *Petrophase XIII – 13th International Conference of Petroleum Phase Behavior and Fouling*, Conference Proceedings, June 14, 2012.

[11] Kriz, P.; Andersen, S. I. Effect of asphaltenes on crude oil wax crystallization. *Energy & Fuels*, **2005**, *19* (3), 948–953.

[12] Pan, H.; Firoozabadi, A.; Fotland, P. Pressure and composition effect on wax precipitation: experimental data and model results. *SPE Production & Facilities*, **1997**, *12* (4), 250-258.

[13] Coutinho, J. A. P.; Edmonds, B.; Moorwood, T.; Szczepanski, R.; Zhang, X. Reliable wax predictions for flow assurance. *Energy & Fuels*, **2006**, *20* (3), 1081–1088.

[14] Tiwary, D.; Mehrotra, A. K. Phase transformation and rheological behavior of highly paraffinic 'waxy' mixtures. *Can. J. Chem. Eng.*, **2004,** *82*, 162–174.

[15] Roehner, R. M.; Hanson, F. V. Determination of wax precipitation temperature and amount of precipitated solid wax versus temperature for crude oils using FT-IR spectroscopy. *Energy & Fuels* **2001,** *15,* 756-763.

[16] Jemmett, M. R.; Deo, M.; Earl, J.; Mogenhan, P. Applicability of cloud point depression to 'Cold Flow'. *Energy & Fuels*, **2012**, *26* (5), 2641–2647.

[17] Winter, H.H.; Chambon, F. Analysis of linear viscoelasticity of a crosslinking polymer at the gel point. *J. Rheology,* **1986**, *30* (2), 367-382.

[18] Winter, H. H. Can the gel point of a cross-linking polymer be detected by the *G'* – *G"* crossover? *Polym. Eng, Sci*, **1987**, *27*, 1698–1702.

[19] Thomason, W. H. Proceedings of *2000 Offshore Technology Conference*, Houston Texas, 2000.

[20] Lee, H. S.; Singh, P.; Thomason, W. H.; Fogler, H. S. Waxy oil gel breaking mechanisms: adhesive versus cohesive failure. *Energy & Fuels*, **2008**, *22* (1), 480–487.

[21] Hansen, A. B.; Larsen, E.; Pedersen, W. B.; Nielsen, A. B.; Roenningsen, H. P. Wax precipitation from North Sea crude oils. 3. Precipitation and dissolution of wax studied by differential scanning calorimetry. *Energy & Fuels*, **1991**, *5*, 914–923.

[22] Matsuoka, M.; Ozawa, R. Determination of solid–liquid phase equilibria of binary organic systems by differential scanning calorimetry. *J. Crystal Growth*, **1989**, *96*, 596–604.

[23] Shibuya, H.; Suzuki, Y.; Yamaguchi, K.; Arai, K.; Saito, S. Measurement and prediction of solid–liquid phase equilibria of organic compound mixtures. *Fluid Phase Equilibria*, **1993,** *82*, 397–405.

[24] Han, S.; Huang, Z.; Senra, M.; Hoffmann, R.; Fogler, H. S. Method to determine the wax solubility curve in crude oil from centrifugation and high temperature gas chromatography measurements. *Energy & Fuels*, **2010**, *24* (3), 1753–1761.

[25] Margarone, M.; Bagatin, R.; Busto, C.; D'Olimpio, P; Fusi, L.; Faienza, L.; Fasano, A.; Primicerio, M. A wax crystallization model from DSC experiments. *Petrophase XI – 10th International Conference of Petroleum Phase Behavior and Fouling*, Poster Session, 2010.

[26] Singh, P.; Venkatesan, R.; Fogler, H. S.; Nagarajan, N. .Formation and aging of incipient, thin film wax-oil gels. *AIChE J.* **2000**, *46*, 1059.

[27] Singh, P.; Venkatesan, R.; Fogler, H. S.; Nagarajan, N. Morphological evolution of thick wax deposits during aging. *AIChE J.* **2001**, *47*, 6.

[28] Singh, P.; Youyen, A.; Fogler, H. S. Existence of a critical carbon number in the aging of a wax-oil gel. *AIChE J.* **2001**, *47*, 2111.

[29] Creek, J. L.; Lund, H. J.; Brill, J. P.; Volk, M. Wax deposition in single phase flow. *Fluid Phase Equilib.* **1999**, *801*, 158.

[30] Majeed, A.; Bringedai, B.; Overa, S. Model calculates wax deposition for North Sea oils. *Oil Gas J.* **1990**, *18*, 63.

[31] Svendson, J. A. Mathematical modeling of wax deposition in oil pipeline systems. *AIChE J.* **1993**, *39*, 1377.

[32] Kok, M. V.; Saracoglu, R. O. Mathematical modeling of wax deposition in crude oil pipeline systems. *Pet. Sci. Technol.* **2000**, *18*, 1121.

[33] Ghedamu, M.; Watkinson, A. P.; Epstein, N. Mitigation of wax buildup on cooled surfaces. In *Fouling Mitigation of Industrial Heat Exchange Equipment*; Panchal, C. B., Bott, T. R., Somerscales, E. F. C., Toyama, S., Eds.; Begel House: New York, **1997**, p 473-489.

[34] Mehrotra, A. K.; Bhat, N. V. Modeling the effect of shear stress on deposition from "waxy" mixtures under laminar flow with heat transfer. *Energy & Fuels.* **2007**, *21*, 1277.

[35] Patton, C. C.; Casad, B. M. Paraffin deposition from refined wax-solvent system. *Soc. Pet. Eng. J.* **1970**, *10* (1), 17.

[36] Bott, T. R.; Gudmunsson, J. S. Deposition of paraffin wax from kerosene in cooled heat exchanger tubes. *Can. J. Chem. Eng.* **1977**, *55*, 381.

[37] Jennings, D. W.; Weispfennig, K. Effects of shear and temperature on wax deposition: coldfinger investigation with a Gulf of Mexico crude oil. *Energy & Fuels* **2005**, *19*, 1376.

[38] Wu, C.; Wang, K. S.; Shuler, P. J.; Tand, Y.; Creek, J. L.; Carlson, R. M.; Cheung, S. Measurement of wax deposition in paraffin solutions. *AIChE J.* **2002**, *48*, 2107.

[39] Bidmus, H. O.; Mehrotra, A. K. Heat-transfer analogy for wax deposition from paraffinic mixtures. *Ind. Eng. Chem. Res.* **2004**, *43*, 791.

[40] Parthasarathi, P.; Mehrotra, A. K. Solids deposition from multicomponent wax–solvent mixtures in a benchscale flow-loop apparatus with heat transfer. *Energy & Fuels.* **2005**, *19*, 1387.

[41] Fong, N.; Mehrotra, A. K. Deposition under turbulent flow of wax–solvent mixtures in a bench-scale flow-loop apparatus with heat transfer. *Energy & Fuels* **2007**, *21*, 1263.

[42] Paso, K.; Senra, M.; Yi, Y.; Sastry, A. M.; Fogler, H. S. Paraffin polydispersity facilitates mechanical gelation. *Ind. Eng. Chem. Res.* **2005**, *44*, 7242–7254.

[43] Venkatesan, R. The deposition and rheology of organic gels. Ph.D Thesis, University of Michigan, Ann Arbor, MI, 2004.

[44] Venkatesan, R.; Nagarajan, N. R.; Paso, K.; Yi, Y.; Sastry, A. M.; Fogler, H. S. The strength of paraffin gels formed under static and flow condition. *Chem. Eng. Sci.* **2005,** *60* (13), 3587-3598.

[45] Chang C, Boger DV, Nguyen QD. The yielding of waxy crude oils. *Ind. Eng. Chem. Res.* **1998**, *37*, 1551–1559.

[46] Perkins TK, Turner JB. Starting behavior of gathering lines and pipelines filled with gelled Prudhoe Bay oil. *J. Petroleum Tech*. **1971**, 301–308.

[47] Davenport TC, Somper RSH. The yield value and breakdown of crude oil gels. *J Inst Petroleum.* **1971**, *57*, 86–105.

[48] Chang C, Nguyen QD, Ronningsen HP. Isothermal start-up of pipeline transporting waxy crude oil. *J. Non-Newtonian Fluid Mech*. **1999**, *87*, 127–154.

[49] Magda, J. J.; El-Gendy, H.; Oh, K.; Deo, M. D.; Montesi, A.; Venkatesan, R. Time-dependent rheology of a model waxy crude oil with relevance to gelled pipeline restart. *Energy & Fuels* **2009,** *23*, 1311-1315.

[50] Henaut I, Vincke O, Brucy F. Waxy oil restart: mechanical properties of gelled oils. Paper SPE 56771 presented at the *1999 SPE Annual Technical Conference and Exhibition*, Houston Texas, 1999.

[51] Borghi GP, Correra S. Prediction and scaleup of waxy oil restart behavior. SPE 80259, In *International Symposium on Oilfield Chemistry*, Houston, Texas, 2003: 1–5.

[52] El-Gendy, H., Alcoutlabi, M., Jemmett, M., Deo, M., Magda, J., Venkatesan, R. and Montesi, A. The propagation of pressure in a gelled waxy oil pipeline as studied by particle imaging velocimetry. *AIChE J.* **2012**, *58*, 302–311.

[53] Becker, J. R. Oilfield Paraffin Treatments: Hot oil and hot water compared to crystal modifiers. Proceedings *2000 SPE Ann. Tech. Conf & Exhib. - Prod. Oper. & Eng. Gen.*: Dallas, USA, Oct 1-4, 2000.

[54] Bosch, F. G.; Schmitt, K. J.; Eastlund, B. J. Evaluation of downhole electric impedance heating systems for paraffin control in oil wells. *IEEE Trans. Ind. Applic.* **1992**, *28* (1), 190.

[55] Sarmento, R. C.; Ribbe, G. A. S.; Azevedo, Wax blockage removal by inductive heating of subsea pipelines. *L. F. A. Heat Transfer Eng.* **2004**, *25* (7), 2.

[56] Newberry, M. E.; Addison, G. E.; Barker, K. M. Paraffin control in the Northern Michigan Niagaran Reef trend. *SPE Prod. Eng.* **1986**, *1* (3), 213.

[57] Braden, B. The use of enzymes to control paraffin and asphaltene deposits in the wellbore. Presented at the *SPE Western Regional Meeting*, California, USA, June 25-27, 1997.

[58] Larsen, R., Lund, A., Argo, C., and Makogon, T. Cold Flow – A simple multiphase transport solution for harsh environments. *18th International Oil Field Chemistry Symposium*, 25-28 March, 2007, Geilo, Norway.

[59] Merino-Garcia, D.; Correra, S. Cold Flow: A review of a technology to avoid wax deposition. *Pet. Sci. Technol.* **2008**, *26*, 446.

[60] Bidmus, H. O.; Mehrotra, A. K. Solids deposition during "Cold Flow" of wax−solvent mixtures in a flow-loop apparatus with heat transfer. *Energy & Fuels* **2009**, *23,* 3184-3194.

[61] Wax control in the presence of hydrates, RPSEA 07121-1201. University of Utah Department of Chemical Engineering, submitted to RPSEA October 15, 2011.

[62] Grant I. Particle image velocimetry: a review. *Proc. Inst. Mech. Eng.* Part C **1997**, *211*, 55–76.

[63] Fundamentals of heat and mass transfer, 6th Edition. Frank P. Incropera, David P. DeWitt, Theodore L. Bergman, Adrienne S. Lavine, ISBN 978-0-471-45728-2, March 2006, ©2007, Wiley Publishing.